ULTRAFAST SPECTROSCOPY STUDY OF PHOTOEXCITATIONS DYNAMICS IN ORGANIC-INORGANIC HYBRID PEROVSKITES

by

Yaxin Zhai

A dissertation submitted to the faculty of
The University of Utah
in partial fulfillment of the requirements for the degree of

Doctor of Philosophy

in

Physics

Department of Physics and Astronomy

The University of Utah

August 2017

The University of Utah Graduate School

STATEMENT OF DISSERTATION APPROVAL

The dissertation of **Yaxin Zhai**

has been approved by the following supervisory committee members:

Zeev Valentine Vardeny	, Chair	**05/12/2017** Date Approved
Yong-Shi Wu	, Member	**05/17/2017** Date Approved
Jordan Gerton	, Member	**05/17/2017** Date Approved
Clayton C. Williams	, Member	**05/18/2017** Date Approved
Ajay Nahata	, Member	**05/25/2017** Date Approved

and by **Benjamin Bromley** , Chair/Dean of

the Department/College/School of **Physics and Astronomy**

and by David B. Kieda, Dean of The Graduate School.

ABSTRACT

In the last decade, the organic/inorganic hybrid perovskites have emerged as one of the most promising classes of contenders for low-cost solar cells, owing to extraordinary power conversion efficiencies of more than 22%, and convenient solution fabrication processes. Moreover, the hybrid perovskite systems have found applications in many other fields, such as light emitting diodes, lasers, field effect transistors, and spintronics. In this dissertation, by using a variety of transient and steady-state optical measurements, we have investigated the photoexcitations in different organic/inorganic hybrid perovskite systems, including three- (3D) and two- (2D) dimensional thin films and single crystals.

In 3D hybrid perovskites, we have identified the excitons/photocarriers duality nature in the lead iodine perovskite at room temperature (RT), which is consistent with its small exciton binding energy (E_b) less than k_BT for T=300K. For lead bromide and lead cloride perovskites with larger E_b, excitons have been verified as the the primary photoexcitations. These results show that the branching ratio between the photogenerated excitons and free carriers is determined by the exciton binding energy in the hybrid perovskites. Due to the anistropic teragonal structure phase, we have also observed the polarization memory (POM) dynamics of both excitons and free carriers in the lead iodine perovskite, from which we have estimated the long exciton diffusion length at ~150nm. In addition, the effects of nano-morphologies on photoluminescence and magnetic properites in perovskites have also been studied.

In 2D hybrid perovskites, we have found a strong photoinduced absorption (PA) from the primary exciton state to the upper branch of the Rashba-splitting band, from which we have obtained a giant Rashba-splitting in this compound, with the Rashba-splitting energy, E_R= 40±5 meV and Rashba-splitting parameter α_R=1.6 ±0.1 eV·Å that is among the highest values reported so far.

We have extended our measurements to lead bromide perovskite single crystals, which show much lower trap state densities and longer exciton lifetimes in the bulk than in the film samples. Our observation of a fast photobleaching (PB) and a corresponding rise of PA in the near-surface regime reveals the process of the exciton recombination on the surface and diffusion to the interior of the bulk.

To my family, my husband, and my expecting son…

TABLE OF CONTENTS

LIST OF FIGURES

ACKNOWLEDGEMENTS

I would like to express my deepest gratitude to my supervisor, Prof. Z. Valy Vardeny, for his constant guidance, trust and encouragement during my Ph.D. study. His passion to understand physics has influenced me deeply. I would also like to thank my supervisory committee: Profs. Ajay Nahata, who introduced me to terahertz research, Jordan Gerton, Yong-Shi Wu, and Clayton Williams, for their continuous support. I need to thank Profs. Eitan Ehrenfreund and Chuan-Xiang Sheng, for their patient guidance with their comprehensive understanding of physics. I appreciate the generous help and advice from researchers in our group, Profs. Dali Sun, Chuang Zhang, and Evan Lafalce.

I must thank our collaborators, Profs. Paul M. Haney and Junwen Li from NIST, and Prof. Zhiqun Lin's group from Geotech. I also thank our former group members, Drs. Randy Polson, Ella Olejnik, Uyen Huynh, Bhoj Gautam, and Tek Prasad Basel, for introducing me to the experimental techniques. I need to thank Drs. Matt DeLong and Zhiheng Liu for their instruction and assistance. I would also like to thank the members of my group, Dr. Haoliang Liu, Dr. Jingying Wang, Dr. Ryan McLaughlin, Sangita Baniya, Sandip Aryal, Matthew Groesbeck, Xiaojie Liu, and Qingji Zeng, for their collaboration.

It is impossible to sufficiently express my gratitude to my close family and my husband for their continuous love, patience, and support during my studies.

Finally, I would like to thank the funding agencies of MRSEC, DOE, and MURI.

CHAPTER 1

INTRODUCTION TO ORGANIC/INORGANIC HYBRID PEROVSKITES

Among all the energy sources, solar photovoltaic (PV), which converts solar energy to electricity, is the most promising and clean option because it is pollution-free during use [1-10]. Since the discovery of the photovoltaic effect in the 1830s [4], many PV materials have been extensively studied and applied in our daily life [5-7]. The light to electric power conversion efficiency (PCE) in the most commonly used silicon solar cells starting with 4.5% in the 1950s has now surpassed 25% [8-11]. Other materials with promising PCEs have also been developed, as shown in Figure. 1.1 (a) [11], with the single junction structure PCE record found in GaAs approaching 29%. Along with PCE, the solar cell devices' fabrication cost is also of crucial importance, which means materials with high PCE and low-cost processing are the aims of PV studies [9, 10].

The organic/inorganic hybrid semiconductors methyl-ammonium (CH_3NH_3; MA) lead halide perovskites, $MAPbX_3$ (where X stands for halide) have recently emerged as one of the most promising classes of contenders for PV devices, having extraordinary power conversion efficiencies [9-12]. From 2009 to 2016, the efficiency of the hybrid perovskite solar cells has increased from 3.8% to more than 22% [13-24]. Figure 1.1 (b) shows the open-circuit voltage (V_{OC}) compared to the bandgap (E_g), which indicates the photon energy utilization for the current PV technologies. It is clear to see that the perovskite-

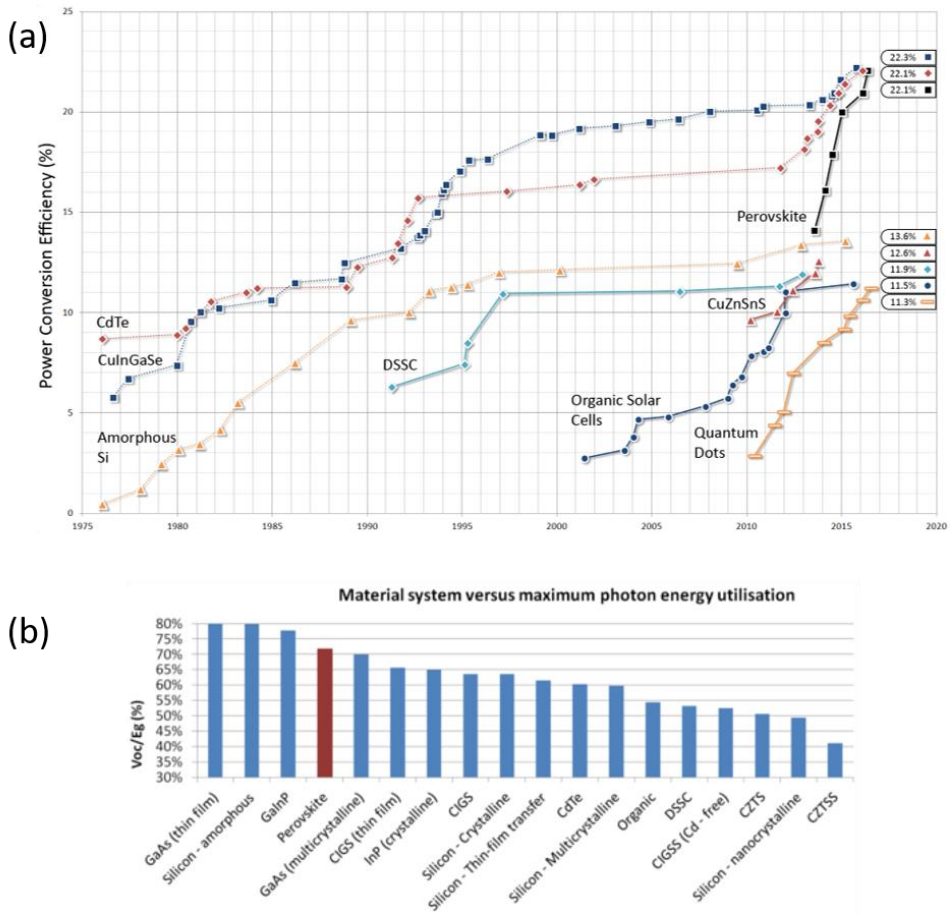

Figure 1.1. Development of perovskite solar cells. (a) Perovskite solar cells have increased in power conversion efficiency at a phenomenal rate compared to other types of photovoltaics. (b) The maximum photon energy utilization (defined as the open circuit voltage V_{oc} divided by the optical bandgap E_g) for common single junction solar cells material systems. Adapted from Ref. [11].

based solar cells are approaching the same level as the current leading monolithic crystalline technologies, such as silicon and GaAs [11]. Importantly, the organic/inorganic hybrid perovskites solar cells can be fabricated through an inexpensive solution process, which makes them more promising to replace the expensive crystalline silicon in the market. Moreover, the hybrid perovskites have also found other promising uses such as light emitting diodes (LED) [25], photo-pumped lasers [26], field-effect transistors [27], and spintronics [28]. However, the origin of the superb opto-electrical performance is still questionable, and understanding of the working mechanism is crucial for the further application of the inorganic/organic hybrid perovskites.

This chapter starts with the crystal and electronic structures of different forms of inorganic/organic hybrid perovskites and discusses their basics optical properties. The nature of the photoexcited species as well as the spin-related properties of this materials, which are fundamental and crucial for their applications, are discussed in detail. This will be followed by a discussion on the promising applications of the inorganic/organic hybrid perovskites.

1.1 Crystal Structures

Technically, perovskite, named after L. A. Perovski (1792–1856), refers to the $CaTiO_3$ mineral; meanwhile, a perovskite structure is anything that has the generic form ABX_3 and the same crystallographic structure as the mineral [29]. In organic/inorganic hybrid halide perovskites such as methyl-ammonium (CH_3NH_3; MA) lead halide perovskites, $MAPbX_3$ (where X stands for halide), a divalent inorganic cation is present and the monovalent metal is replaced by an organic cation of equal charge as illustrated in Figure 1.2 (a) [9].

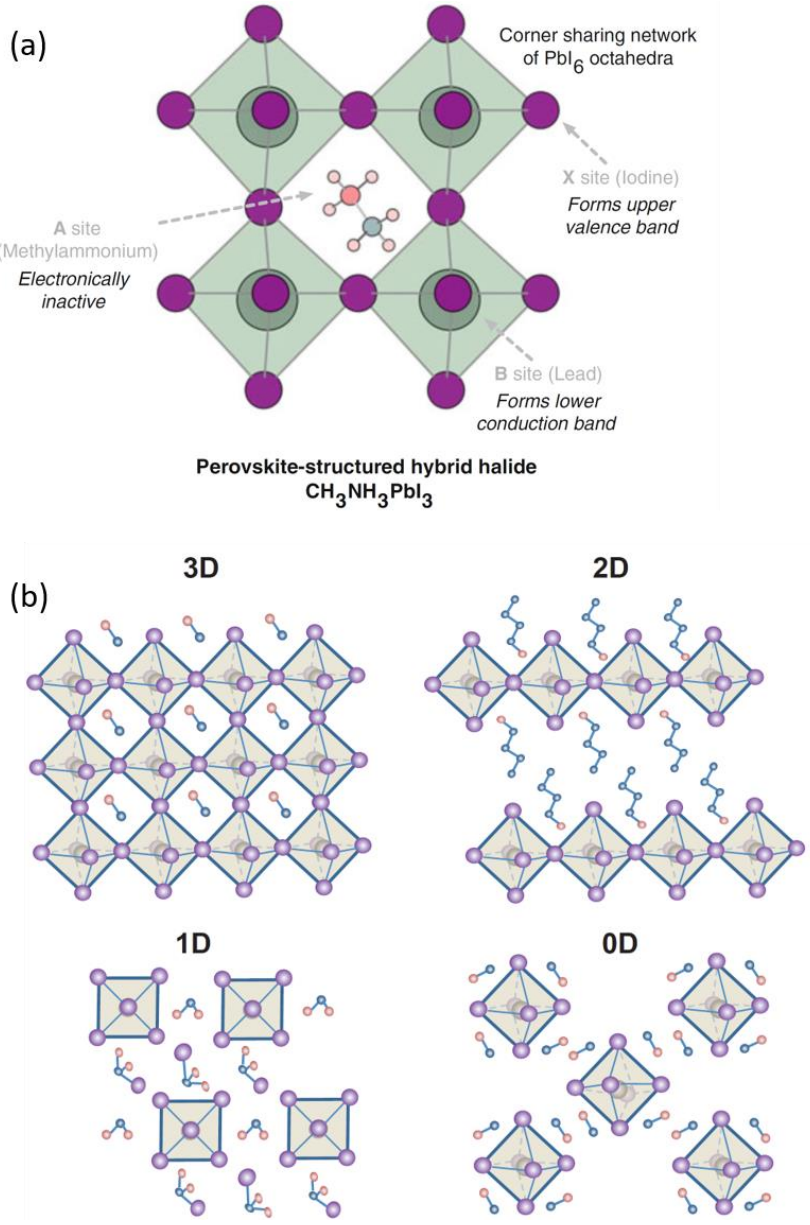

Figure 1.2. Organic-inorganic hybrid perovskites structures. (a) Schematic of the methyl-ammonium (CH_3NH_3; MA) lead halide perovskites, $MAPbX_3$ (where X stands for halide). (b) Perovskites crystal structures in different dimensions: $MAPbI_3$ (3D), $(MA)_2PbI_4$ (2D), $[NH_2C(I)=NH_2]_3PbI_5$ (1D), and $(MA)_4PbI_6{\cdot}2H_2O$ (0D). Adapted from Ref. [9, 30].

The three-dimensional (3D) perovskite can be broken into two-dimensional (2D), one-dimensional (1D), or zero-dimensional (0D) in the inorganic networks if the methyl-ammonium organic cation is large enough, as shown in Figure 1.2 (b) [30]. In all the lower dimensional structures, crystal properties become highly anisotropic and strongly quantum confined. For example, layered 2D structures known as Ruddlesden-Popper phase have strong exciton binding energies, which affects their optoelectrical properties significantly. In the following sections, basic crystal structures of 3D and 2D hybrid perovskites are discussed due to their intensive applications.

1.1.1 Three-Dimensional (3D) Structures

We first consider the $MAPbI_3$ perovskites for the primary interest in solar cells. The crystal structure of this component is similar to other inorganic perovskites; however, the organic cations complicate the structure by their lower symmetry (MA^+ is of C_{3v} point group) and order-disorder transitions [9, 31-36].

As shown in Figure 1.3 (a), the $MAPbI_3$ perovskites possess the cubic phase with the space group *Pm-3m* (O_h symmetry) above 330 K. The MA^+ and halogen ions are disordered at the cubic phase, which leads to a lower symmetry of local structure in $MAPbI_3$.

As the temperature decreases, the cubic phase is transformed into the tetragonal space group *I4/mcm* (D_{4h} point group), as shown in Figure 1.3 (b). In the tetragonal phase, the halogen ions are ordered but not the MA^+ ions.

When the temperature decreases lower than 160K, the tetragonal phase is transformed into the orthorhombic space group *Pnma* (D_{2h} point group), in which the organic MA^+ ions are fully ordered, as shown in Figure 1.3 (c).

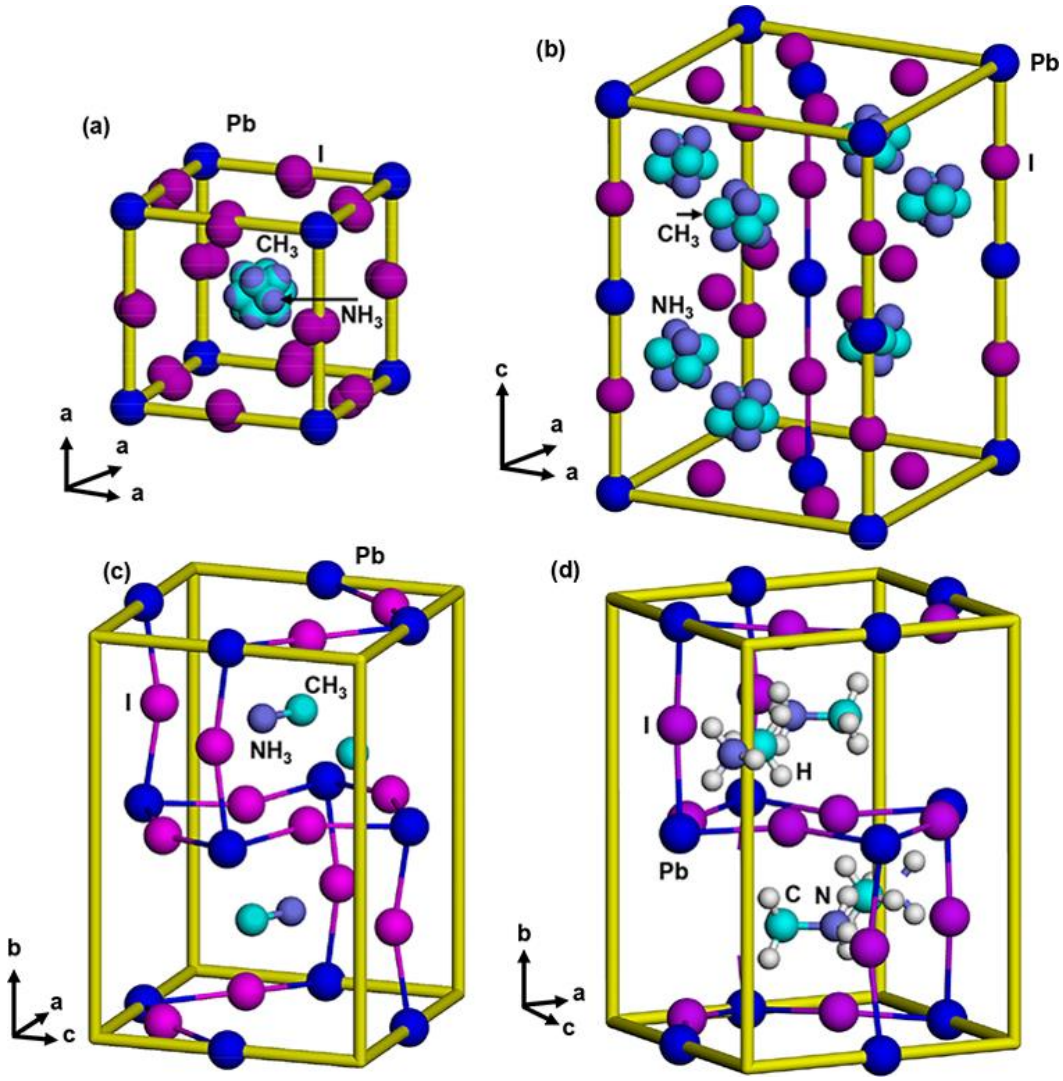

Figure 1.3. Structure models of $MAPbI_3$ with (a) cubic, (b) tetragonal, (c) orthorhombic, and (d) orthorhombic structures with hydrogen positions. Adapted from Ref. [31].

The crystal structure of the bromide and chloride perovskites, namely $MAPbBr_3$ and $MAPbCl_3$, are similar to the $MAPbI_3$ perovskites, except for small differences in the transition temperatures [32-34]. The $MAPbBr_3$ ($MAPbCl_3$) crystal structure transforms from cubic to tetragonal phase at 236 K (177 K) and from tetragonal to orthorhombic phase at 150 K (172K). Thus, both of them possess cubic crystal structure at room temperature.

The ordering may be affected by the material fabrication and/or the cooling rate, and it is possible to find coexistence of multiple phases at a certain temperature.

1.1.2 Two-Dimensional (2D) Structures

By replacing the MAI with larger organic molecules such as butylammonium iodide ($C_4H_9NH_3I$) or $C_6H_5C_2H_4$-NH_3I, the inorganic octahedra layers in 3D perovskites can be separated by the organic moieties and form a lower dimensional Ruddlesden-Popper type 2D structure $(C_4H_9NH_3)_2(CH_3NH_3)_{n-1}Pb_nI_{3n+1}$, where *n* represents the number of octahedra layers (Figure 1.4). Each *n* octahedra layers are separated by two layers of organic moiety and form "multiple quantum wells" due to the different energy gaps in the organics barriers and the inorganic well [37-46]. The structure approaches 3D $MAPbI_3$ perovskites for $n=\infty$.

The 2D perovskite $(C_4H_9NH_3)_2(CH_3NH_3)_{n-1}Pb_nI_{3n+1}$ compounds are reported as orthorhombic and noncentrosymmetric at room temperature [37-40]. The space group are *Cc2m* with a = 8.9470(4) Å, b = 39.347(2) Å, c = 8.8589(6) Å for n=2, *C2cb* with a = 8.9275(6) Å, b = 51.959(4) Å, c = 8.8777(6) Å for n=3, and *Cc2m* with a = 8.9274(4) Å, b = 64.383(4) Å, c = 8.8816(4) Å for n=4. Phase transition from orthorhombic (*Pbca*) to monoclinic ($P2_1/a$) has been reported in another 2D perovskite $(C_{12}H_{25}NH_3)_2PbI_4$ at 317.5K with color change from yellow to orange [37].

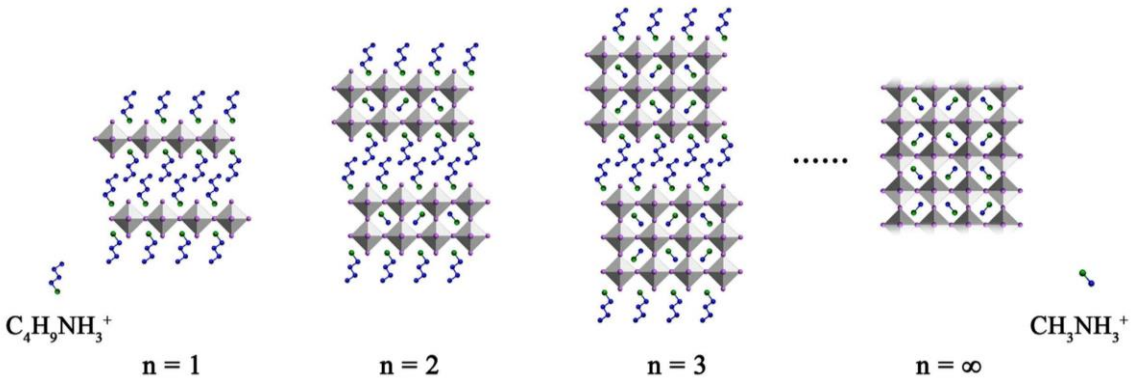

Figure 1.4. Crystal structures of 2D perovskites $(C_4H_9NH_3)_2(CH_3NH_3)_{n-1}Pb_nI_{3n+1}$. Adapted from Ref. [39].

1.2 Linear Optical Properties

The extraordinary power conversion efficiencies (PCE) of organic/inorganic hybrid perovskites solar cells come from their ideal bandgap and high absorption coefficient. The PCE (Shockley–Queisser, SQ limit [47]) is optimized to be ~33% when the bandgap E_g of a material is between 1.1 and 1.4 eV, because of the low photon harvesting for high bandgap materials and energy loss due to thermalization for low bandgap materials. For the $MAPbI_3$ perovskites with bandgap of ~1.55eV, the SQ limit efficiency is about 31% under an AM1.5G solar spectrum at 1000W/m^2 [48-49].

In Figure 1.5 [50], the linear optical absorption spectrum of hybrid perovskite is compared with other typical solar cell materials, such as amorphous silicon (a-Si), GaAs, CIGS, CdTe, and crystalline silicon (c-Si). The absorption spectrum of $MAPbI_3$ covers the entire visible solar emission with coefficient of ~10^{-5} cm^{-1} that is of one order higher than the GaAs that holds the PCE record. The $MAPbI_3$ perovskite is believed to have a direct bandgap and the onset of absorption is much steeper than in crystalline or amorphous Si.

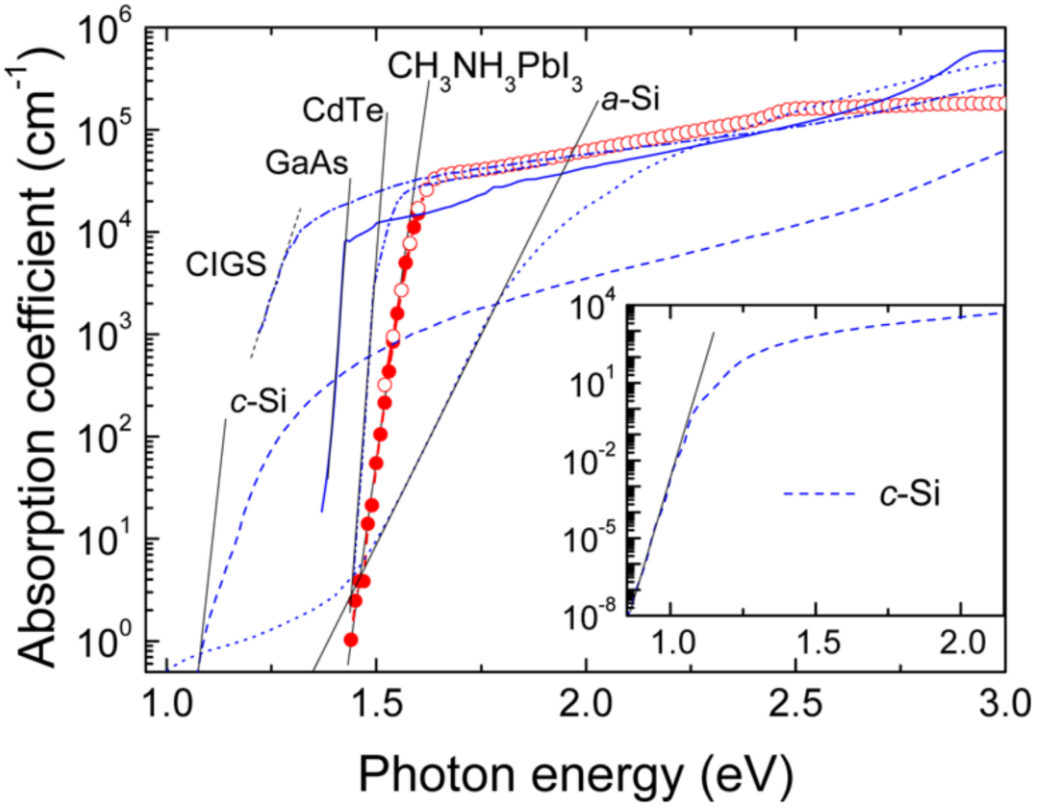

Figure 1.5. Effective absorption coefficient of a $MAPbI_3$ perovskite thin film compared with other typical photovoltaic materials, including amorphous silicon (a-Si), GaAs, CIGS, CdTe, and crystalline silicon (c-Si), all measured at room temperature. For each material, we show the slope of the Urbach tail. For clarity, the inset shows the data for c-Si down to low absorption values. Adapted from Ref. [50].

An important characteristic of perovskite systems is the continuously controllable bandgap [51-56]. This can be done by simply altering the halide content in the solution process (i.e., by mixing I, Br, and Cl) as shown in Figure 1.6 [51]. The composition tuning of the $MAPbX_3$ perovskites can enable the bandgap tuning from 1.6 eV (X = I) to 2.3 eV (X = Br) to 3.1 eV (X = Cl); see Figure 1.6 (a).

Even though increasing the bandgap itself cannot benefit the performance of a single junction solar cell, tuning the bandgap becomes important when making multijunction photovoltaics with the largest E_g employed as the front cell [9]. By stacking solar cells with different bandgaps together, the PCE of multijunction solar cells would be able to overcome the Shockley-Queisser limit [52-56]. For example, a two-junction photovoltaic device (so-called tandem solar cell) of perovskites at preferred bandgap (~1.75eV) combined with silicon (E_g = 1.0eV) could boost the theoretical efficiency from 33% to above 40 % [55, 56].

Besides solar cells, owing to facile solution processing, high color purity, and tunable bandgap, the hybrid perovskites have also found other promising uses such as light emitting diodes (LED) [25], photo-pumped lasers [26], and field-effect transistors [27], which are realized mostly in those perovskites with bandgap in the visible range such as $MAPbBr_3$ (E_b = 2.3 eV). Figure 1.6 (b) [51] shows the photoluminescence (PL) emission spectra on a normalized scale of $MAPbBr_{3-x}Cl_x$ and $MAPbBr_{3-x}I_x$. The PL intensity decreases significantly with increasing x and the maximum emission is observed in $MAPbBr_3$, which makes it most favorable for LED applications. Additionally, by changing the bromide incorporation ratio, a tunable emission color LED based on hybrid perovskites can be realized easily as in organic LED (OLED) [25].

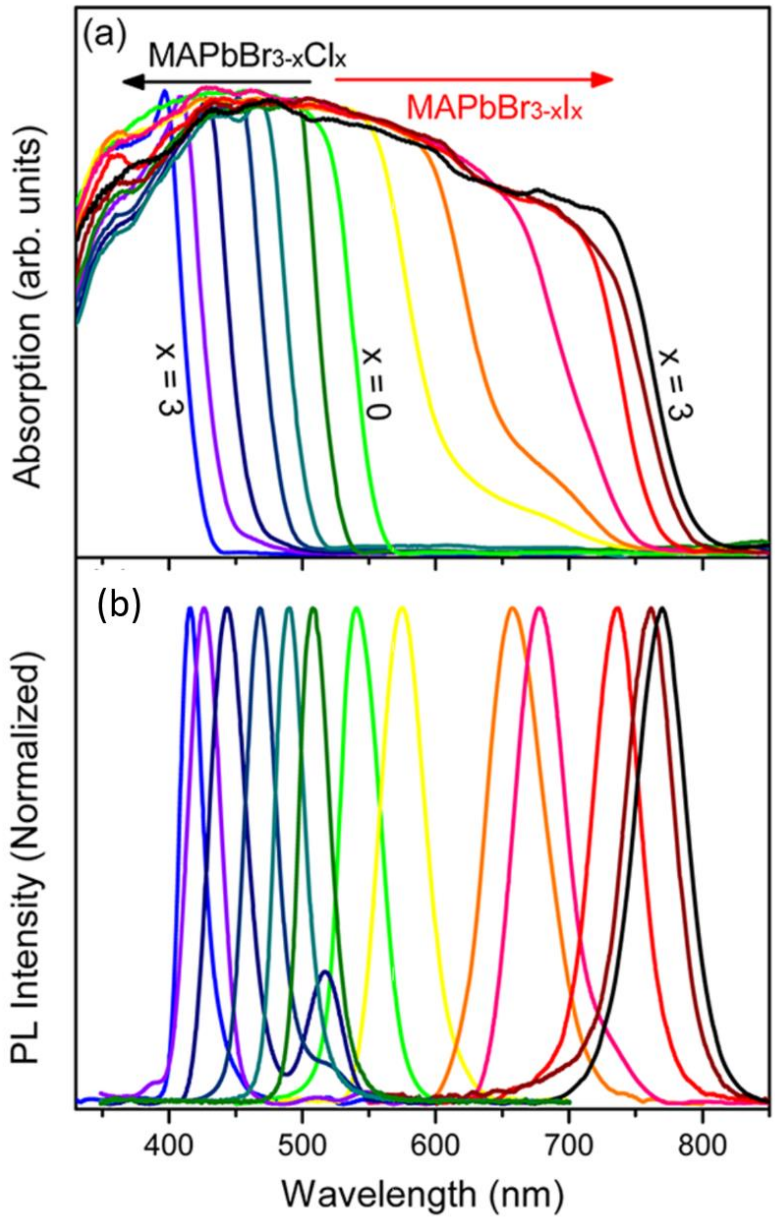

Figure 1.6. Tunable bandgap of organic-inorganic hybrid perovskites. (a) Absorption and (b) photoluminescence spectrum of $MAPbBr_{3-x}Cl_x$ and $MAPbBr_{3-x}I_x$ nanocrystal films, where x = 0, 0.5, 1, 1.5, 2, 2.5, and 3. Adapted from Ref. [51].

By changing the quantum well thickness *n*, the optical properties of two-dimensional (2D) perovskites can also be tuned [37-46], and Figure 1.7 shows the linear absorption and PL spectra in 2D perovskites $(C_4H_9NH_3)_2(CH_3NH_3)_{n-1}Pb_nI_{3n+1}$ from n = 1 to 5 along with 3D $MAPbI_3$ perovskites for comparison [38].

As shown in Figure 1.7 (a) and (b) [38] and summarized in Figure 1.7 (e), the onsets of absorption and the peak of PL spectra in exfoliated crystals decrease linearly from 2.42eV to 1.85eV with *n* increasing from 1 to 5; however, the linewidths of PL spectra keep constant at different *n*. The redshift of spectra is attributed to the larger quantum confinement effect in thinner quantum well layers.

The solution-processed thin film samples; however, show significantly different absorption and PL spectra than their exfoliated crystal counterparts; see Figure 1.7 (c) to (f) [38]. The bandgap of thin films agree well with the single crystals when n=1 and 2, but for *n* larger than 2, a significant redshift is observed and the bandgap does not change with *n*. The PL spectra of thin films also show the same trend and the linewidths get much narrower at larger *n*.

This experiment has ruled out many effects such as modification of the phase during thin film fabrication, changes in dielectric environment, differences in crystallinity, electronic impurities, and different orientations of the perovskite layers, and attributed the optical characteristics in thin film with n>3 to the lower-energy states associated with the local intrinsic electronic structure of the edges (LESs) of the perovskite layers that assist in exciton dissociation [38].

In this dissertation, only single layer quantum well (n=1) 2D perovskite has been studied and therefore, the LESs effect does not influence the results shown in Chapter 4.

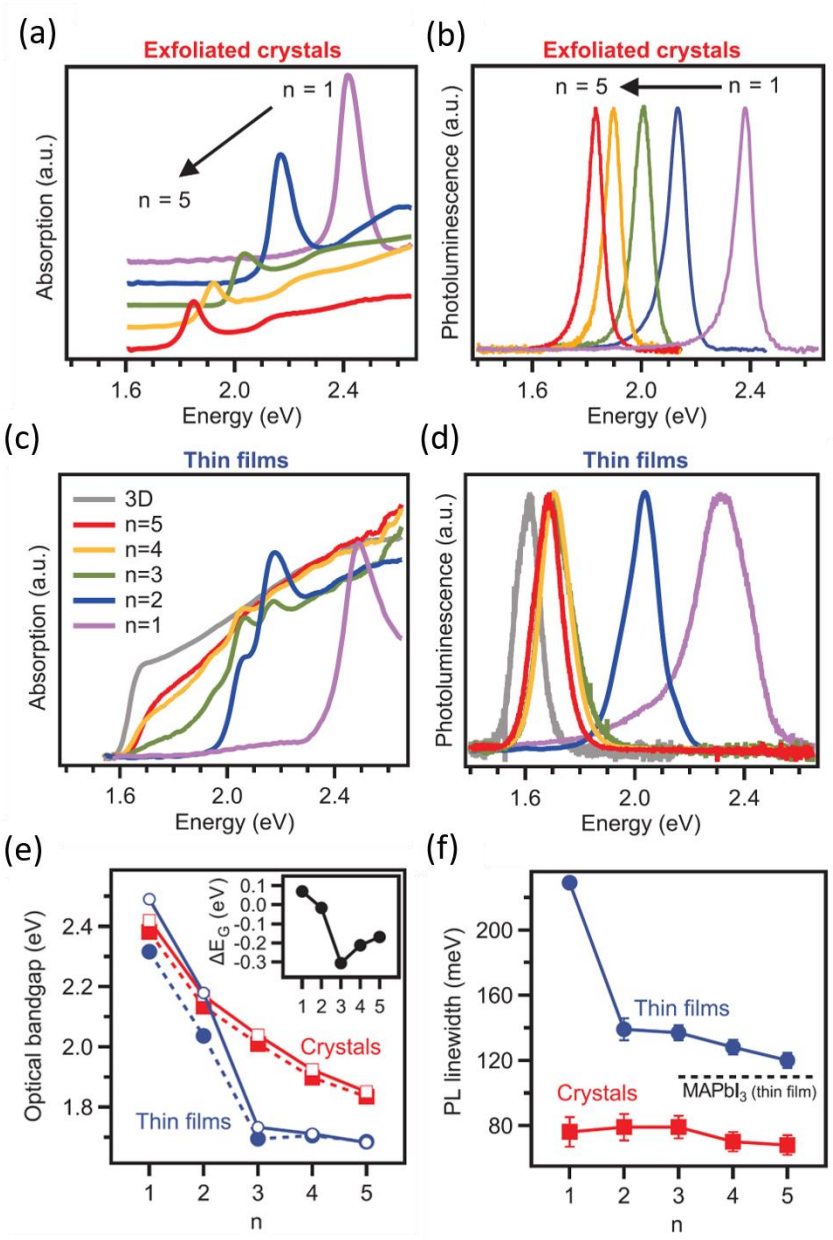

Figure 1.7 Comparison of optical properties of thin films and exfoliated crystals of 2D perovskites $(C_4H_9NH_3)_2(CH_3NH_3)_{n-1}Pb_nI_{3n+1}$ (n = 1 to 5). Absorption and PL of the exfoliated crystals ((a) and (b)) and thin films ((c) and (d)). (e) Optical bandgap derived from absorption (open symbols) and PL (filled symbols) as a function of n. (Inset) Shift of the optical bandgap in thin films with respect to exfoliated crystals (from absorption). (f) PL linewidth versus n. Adapted from Ref. [38].

1.3 Photoexcitations

In optoelectrical applications, a semiconductor operates in its photoexcited state, not the ground state. The photoexcitations must be mobile to facilitate charge transport [57]. As a semiconductor, there are two kinds of primary photoexcitations in the hybrid perovskites (Figure 1.8 (a)); namely photocarriers in the valence band (VB) and/or conduction band (CB); and excitons which are Coulomb correlated electron-hole (e-h) bound pairs [58-61]. An exciton can diffuse in a semiconductor and dissociate into free carriers (electrons and holes), which contribute to the photocurrent eventually. Therefore, the population of excitons and photocarriers as well as the lifetime and diffusion rate of excitons in a perovskites material can determine its performance as an optoelectrical device [58].

1.3.1 Photocarriers

The photocarriers' optical signature is free carrier absorption (FCA), in which a carrier (electron or hole) is excited by a photon from an excited state to another unoccupied state in the *same* band (maybe even a different sub-band) as shown in Figure 1.8 (b). FCA follows the Drude model, and the spectrum can be described by the relation: $FCA \sim N/[1+(\omega\tau_s)^2]$ [62], where N is the photocarriers concentration, τ_s is the momentum scattering time, and ω is the photon angular frequency. Therefore, the FCA contribution to the photoinduced absorption (PA) spectrum is limited to frequencies, ω in the spectral range $\omega\tau_s \approx 1$. We note that for high mobility common semiconductors such as GaAs and Si, the FCA spectrum dominates in the THz range and does not show structured PA bands in the mid-IR spectral range, since τ_s is of the order ~ 1 ps.

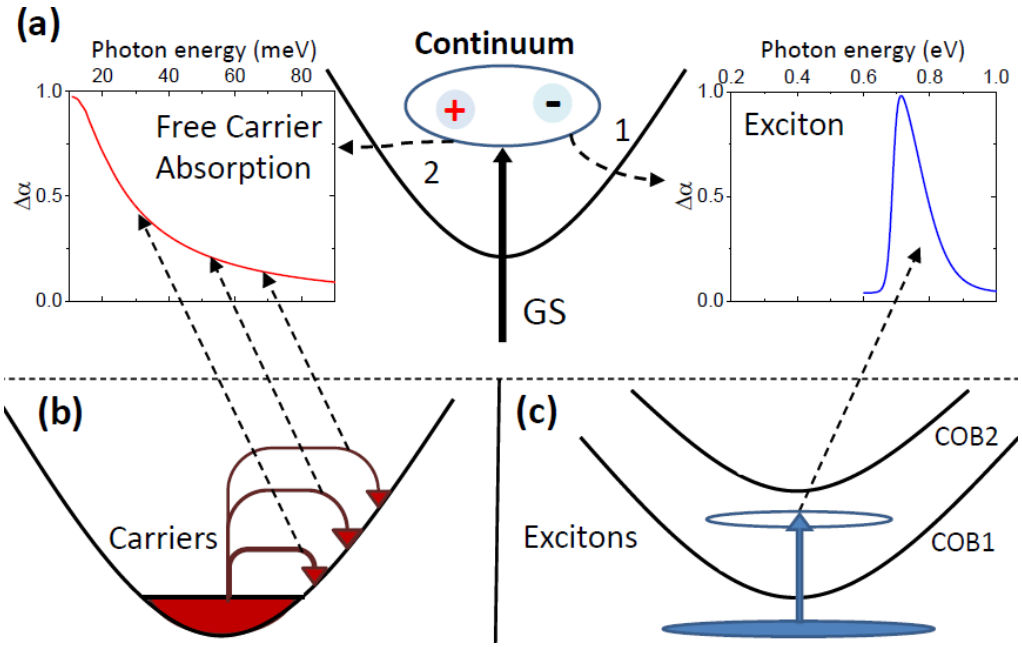

Figure 1.8. Exciton vs. free carrier photoinduced absorption (PA) bands in semiconductors. (a) Schematic presentation of typical PA bands in semiconductors. (b) The free carrier absorption (FCA) process, where energy and momentum cannot be simultaneously conserved due to limited *k*-values of the free carriers in the continuum band in the Brillouin zone (BZ). (c) Exciton PA that is due to optical transitions from low-lying excitons to higher-lying excitons; this occurs in both intraband or interband. In the case presented here (adjusted for $MAPbI_3$), the two excitons belong to two different continuum bands (COB) and thus the exciton transition is *interband*.

From the hole mobility, μ obtained in crystalline methylammonium lead halide perovskites ($\mu \sim 100$ $cm^2V^{-1}s^{-1}$) [63], and $m_{eff} \sim 0.1$ m_e [64], we deduce $\tau_s \approx 10$ fs in the $MAPbI_3$ perovskites, and consequently, the FCA spectrum in these compounds would be relevant only in the spectral range of few tens of meV (see Figure 1.8 (a)).

1.3.2 Excitons

If the photoexcited electron and hole are not fully decoupled from each other, the attractive Coulomb force can lead them to form an exciton, i.e., bound electron-hole pairs. The excitons have lower energy than the bandgap of a material, and the difference is defined as its binding energy [57].

Depending on the materials' properties, excitons can be generated in two limiting cases, so-called Frenkel excitons and Wannier-Mott excitons [62, 65]. A Frenkel exciton as shown in Figure 1.9 (a) has a large binding energy of ~1eV and localizes in a small radius comparable to the size of unit cell. It usually forms in materials with small dielectric constant such as fullerenes, organic aromatic molecular crystals, and alkali halide crystals, in which the Coulomb interaction between the electron and the hole is strong. A Wannier-Mott exciton, on the other hand, has a much larger radius at 40-100 Å and can delocalize over many atoms or molecules, as shown in Figure 1.9 (b). The dielectric constant in semiconductors is generally large, and the electric field screening tends to reduce the Coulomb interaction between electrons and holes, which results in the Wannier exciton. Considering that the effective mass of electrons in semiconductors is usually small, the binding energy of a Wannier exciton is significantly reduced and typically on the order of ~50 meV.

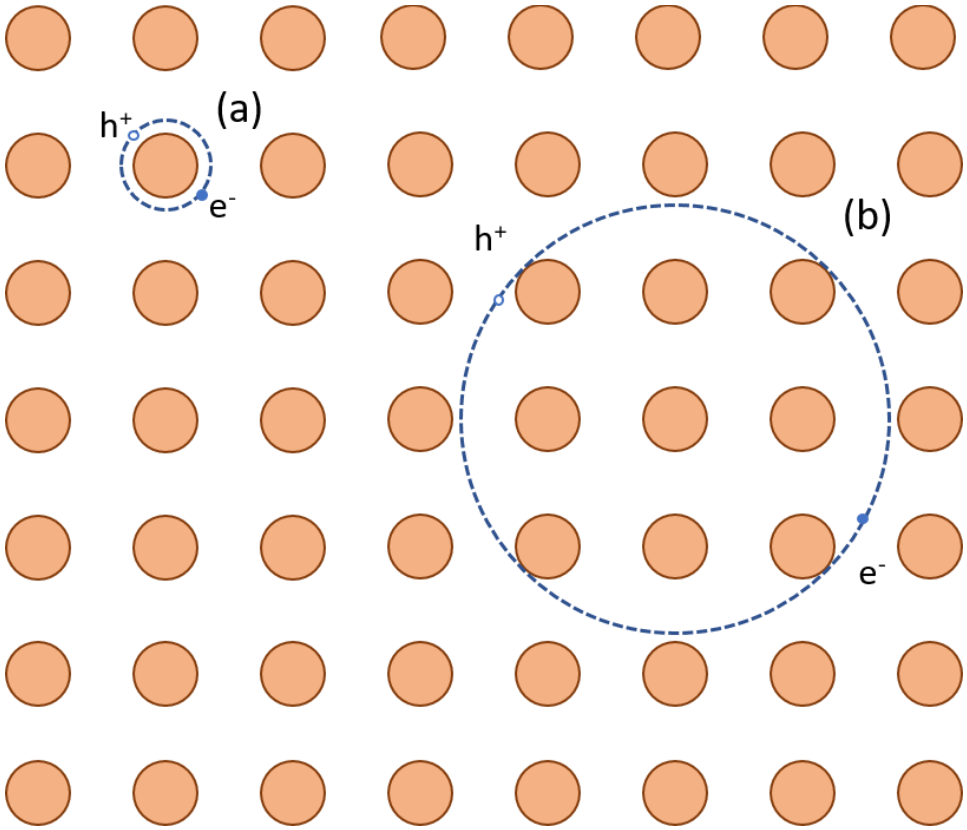

Figure 1.9. Schematic representation of (a) small-radius Frenkel exciton and (b) large-radius Wannier-Mott exciton.

The excitons in a 3D semiconductor can be described as hydrogen-like states [66]:

$$E_{ex}(n_B, \boldsymbol{K}) = E_g - R_y^* \frac{1}{n_B^2} + \frac{\hbar \boldsymbol{K}^2}{2M}, \tag{1.1}$$

in which principle quantum number n_B, exciton Rydberg energy R_y^*, translational mass *M*, wave vector ***K***, and reduced exciton mass are

$$n_B = 1, 2, 3 \ldots \tag{1.2}$$

$$R_y^* = 13.6eV \frac{\mu}{m_0 \varepsilon^2} \tag{1.3}$$

$$M = m_e + m_h, \boldsymbol{K} = \boldsymbol{k_e} + \boldsymbol{k_h} \tag{1.4}$$

$$\mu = \frac{m_e m_h}{m_e + m_h} \tag{1.5}$$

Therefore, the oscillator strength *f* and Bohr radius a_B are given by

$$f(n_B) \propto n_B^{-3}, \qquad a_B \propto a_B^H n_B \tag{1.6}$$

Exciton binding energy usually increases with the bandgap of a semiconductor. For the methylammonium lead halide perovskites $MAPbI_3$, the bandgap is ~1.5eV, which is similar to GaAs [59]; however, the exciton binding energy is still under debate. E_b in $MAPbI_3$ has been reported to be in the energy range from 10 to 55 meV [67-72], with lower values reported in more recent reports [64, 71-73]. Considering thermal energy k_bT = 25 meV at room temperature, the photoexcitations should be mainly free carriers in $MAPbI_3$

perovskites. In $MAPbBr_3$ perovskites with a bandgap at ~2.3eV, however, the binding energy has been reported to be on the order of ~100meV [70-71], and therefore, the photoexcitations are expected to be excitons at room temperature. The relation between Wannier-type excitons and free carriers [58-59] in these components is discussed in detail in Chapter 3.

In a 2D semiconductor, the binding energy can be significantly enhanced due to spatial confinement as

$$E_{ex}(n_B, \boldsymbol{K}) = E_g - R_y^* \frac{1}{(n_B - 1/2)^2} + \frac{\hbar(K_x^2 + K_y^2)}{2M} + E_Q, \tag{1.7}$$

$$f(n_B) \propto \left(n_B - \frac{1}{2}\right)^{-3}, \qquad a_B \propto a_B^H \left(n_B - \frac{1}{2}\right), \tag{1.8}$$

where E_Q is the quantization energy. Thus, the second term of E_{ex} would increase from R_y^* to $4R_y^*$, even without considering the screening effect when the dimension decreases from 3D to 2D. The screening effect caused by the difference in the ε of the quantum wells and barriers would enhance the exciton binding energy more. The oscillator strength f of the 1s exciton in 2D perovskite is also increased 8 times compared to that in 3D [73-75]. The estimated 1s exciton with binding energy at ~200meV [75] and very large oscillator strength in 2D PEPI perovskites is discussed in Chapter 4.

In contrast to free carriers, excitons may have PA bands in the mid-IR range that originate from excitonic intersub-band or/and interband transitions (Figure 1.8 (c)), similar as in nanotubes [76] and π-conjugated polymers [77]; or/and transitions into the continuum band at energies that correspond to high density of states [78] (see Figure 1.8 (c)). The

different PA bands for carriers and excitons may be thus used to thoroughly study their characteristic properties [76-83]. However, one needs to apply broadband spectroscopy in order to access their separate PA bands in the 'pump-probe' photomodulation spectrum, as we have done in the present work.

1.4 Carrier Lifetime and Defects

In semiconductors, the photoexcited free electrons and holes can also recombine with each other. This process in $MAPbI_3$ perovskites, however, is very slow which is one of the reasons contributing to its superior power conversion efficiency (PCE). Carrier lifetime on the order of ~ 10 ns with diffusion length from 100 nm to 1 μm has been reported in $MAPbI_3$ thin films [79-80]. That is extraordinary taking into account the crystalline domains in the solution processed samples. Diffusion length up to ~mm has been measured in single crystals with much fewer defects and boundaries [84].

The mechanism of the long carrier lifetime in hybrid perovskites has been widely studied [85-88]. Edri et al. attribute the successful perovskites solar cell to the different work function between the electron and hole extracting layers inferred from electron beam induced current (EBIC) measurement [85]. Recently, ferroelectric properties have been proposed to explain the long diffusion length in $MAPbI_3$ films since the ferroelectric domains may serve as spatially segregated channels for charge carriers transport [87-88]. The Rashba effect caused by the heavy atoms in hybrid perovskites that induces an indirect bandgap has also been adopted to explain the contradiction between high absorption efficiency and long carrier life time [89-90], which is discussed in the next section.

One of the factors that limit the PCE in the perovskite thin film solar cells should be

the defects, such as point defects and grain boundaries, because these defects can cause non-radiative recombination and reduce the V_{OC} in a photovoltaic device [9]. However, the V_{OC} in $MAPbI_3$ has been reported as high as 1.19eV with $V_{OC}/E_g \sim 77\%$, as shown in Figure 1.1 (b) that is even higher than multi-crystalline GaAs. Such a high V_{OC} performance with a solution processed thin film device indicates that the defects in hybrid perovskites might be very different than those in traditional semiconductors. A DFT calculation revealed the unique property of defects in $MAPbI_3$ perovskites that the point defects with low formation energy values as well as the surfaces and grain boundaries only create shallow levels and do not produce deep levels, which explains the long diffusion lifetime and high V_{OC} performance in polycrystalline $MAPbI_3$ film devices [91].

Experimentally, the performance of perovskite devices including PCE, light emission, and magnetic effect significantly depends on the fabrication processing and the resulting morphology [18, 92-93]. Higher PCE has been achieved in those $MAPbI_3$ devices with fewer defects [18]. In Chapter 3, we have studied $MAPbBr_3$ perovskites with different morphology and found larger bulk defect density in films with larger crystalline domains, which reduces the photoluminescence quantum efficiency via non-radiative decays.

1.5 Rashba-Dresselhaus Effect

The extrema points in the conduction and valence bands are of utmost importance in determining the optical, spin, and transport properties of semiconductors [65]. The electron dispersion relation, $E(k)$ near these extrema points is usually described by the effective-mass approximation, where the electrons and holes are treated as ‘free carriers’ having an effective mass, m*, that leads to spin-degenerate parabolic dispersion (Figure 1.10 (a)).

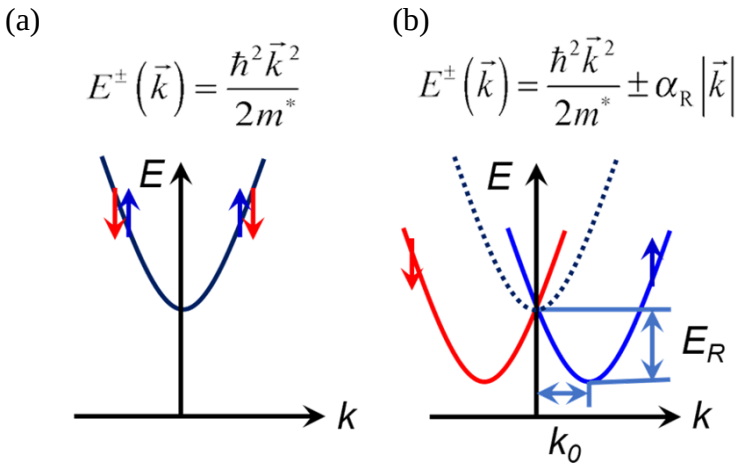

Figure 1.10. Rashba-splitting in semiconductors. (a) Schematic electron dispersion relation of a regular conduction band (CB) that shows a doubly spin-degenerate parabolic band having a single minimum at k=0. (b) Same as in (a) but subjected to Rashba-splitting, in which two parabolic branches having opposite spin sense are formed. The Rashba-splitting energy (E_R) and momentum offset (k_0) are denoted.

However, the spin-degenerate bands can be split in the presence of spin-orbit coupling (SOC) [65], which is a relativistic interaction of a particle's spin with its motion and significantly larger for heavy atoms because SOC increases as the fourth power of the effective nuclear charge Z. If a crystal is centrosymmetric, SOC would not affect the band structure other than generating the heavy holes, light holes, and split-off bands. In a system lacking inversion symmetry, however, SOC can split the spin-degenerate bands into two spin-polarized bands, which is the so-called (i) Rashba effect for systems with uniaxial symmetry or 2D surface [94], and (ii) Dresselhaus effect for bulk systems [95]. More importantly, the SOC is enhanced in reduced dimensions such as in two-dimensional (2D) semiconductors [96]. In this case of Rashba-Dresselhaus effects, the electron (or/and hole) dispersion relation may be described by $E_{\pm}(k)=(\hbar^2k^2/2m^*)\pm\alpha_R|k|$, where α_R is the Rashba-splitting parameter. This formulation yields new extrema at a momentum offset (k_0) and

split energy (E_R) that are related to each other via the relation $\alpha_R = 2E_R/k_0$ [97]; see Figure 1.10 (b). Importantly, the two Rashba-split branches have *opposite spin sense*; therefore, even though it is a small correction to the band structure, the Rashba effect can drive a wide variety of novel physical phenomena of a system and influence the photoexcitations optical and magnetic properties, a situation that may benefit spintronics since it enhances the spin-to-charge conversion efficiency [97-98].

1.5.1 **k·p** Perturbation Theory

In this dissertation, most of the measurements are done by optical methods, thus it would be an advantage if we can adopt a theory to calculate the band structure that uses optical matrix elements as inputs. In solid-state physics, **k·p** perturbation theory is an approximation scheme that was used very successfully for III-V semiconductors with SOC for calculating the band structure (particularly effective mass) and optical properties [65, 99]. In **k·p** perturbation, the band structure over the entire Brillouin zone can be extrapolated from the zone center energy gap and optical elements; therefore, it is very convenient for interpreting optical spectra. In Chapter 4, we used **k·p** perturbation theory to calculate the optical transitions in 2D hybrid perovskites, and the essence of this method is the following.

Under the influence of a periodic potential, V(r), the electronic wave functions are,

$$\varphi_{nk}(r) = \Omega^{1/2} U_{nk}(r) e^{i\vec{k}\cdot\vec{r}} \tag{1.9}$$

where $U_{nk}(r)$ is the cell periodic function (CPF) and Ω is the crystal volume. An important

property of CPF is that for a given *k*, it forms a complete set over the bands *n*.

In this approximation, we deal with small value near the minimum (or maximum) of the band k=0. We therefore write CPF as,

$$U_{nk}(r) = \sum_m c_m U_{m0}(r) \tag{1.10}$$

U_{m0} forms a complete orthonormal set. Substituting it into the electronic Schrödinger equation,

$$[\frac{p^2}{2m} + V(r)]\varphi(r) = E\varphi(r) \tag{1.11}$$

we obtain first

$$[\frac{p^2}{2m} + \frac{\hbar}{m}\vec{k}\cdot\vec{p} + \frac{\hbar^2 k^2}{2m} + V(r)]U_{nk}(r) = E_{nk}U_{nk}(r) \tag{1.12}$$

Since U_{m0} are the solution of Equation (1.12) for k=0,

$$[\frac{p^2}{2m} + V(r)]U_{m0}(r) = E_m U_{m0}(r) \tag{1.13}$$

From Equation (1.10) to (1.13), we obtain

$$\sum_m c_m \left[E_m(0) + \frac{\hbar}{m}\vec{k}\cdot\vec{p} + \frac{\hbar^2 k^2}{2m}\right] U_{m0}(r) = \sum_m c_m\, E_n(k) U_{m0}(r) \qquad (1.14)$$

As usual, we multiply both sides by $U_{j0}^*(r)$ and integrate over the unit cell to obtain a set of linear equations,

$$c_j \left[E_n(k) - E_j(0) - \frac{\hbar^2 k^2}{2m}\right] U_{m0}(r) - \sum_m c_m \frac{\hbar}{m}\vec{k}\cdot\overrightarrow{p_{jm}} = 0 \qquad (1.15)$$

$$\overrightarrow{p_{jm}} = \int U_{j0}^*(r)\vec{p}\, U_{m0}(r) d^3(r) \qquad (1.16)$$

The more bands we use to solve the set of Equation (1.16), the more accurate we will get. This is the essence of the **k·p** approximation. Considering the SOC with Hamiltonian [100],

$$H_{SOC} = \frac{\hbar}{4m^2c^2}\left[\vec{\nabla}V\times\vec{p}\right]\cdot\vec{\sigma} \qquad (1.17)$$

$$\sigma_x = \begin{pmatrix}0 & 1\\ 1 & 0\end{pmatrix};\ \sigma_y = \begin{pmatrix}0 & -i\\ i & 0\end{pmatrix};\ \sigma_z = \begin{pmatrix}1 & 0\\ 0 & -1\end{pmatrix}; \qquad (1.18)$$

where σ is the Pauli spin operator. The Hamiltonian can be written as

$$[\frac{p^2}{2m} + \frac{\hbar}{m}\vec{k}\cdot\vec{p} + \frac{\hbar^2 k^2}{2m} + V(r) + \frac{\hbar}{4m^2c^2}\left[\vec{\nabla}V\times(\vec{p}+\hbar\vec{k})\right]\cdot\vec{\sigma}]U_{nk}(r) = E_{nk}U_{nk}(r) \qquad (1.19)$$

which has been discussed in Chapter 4 by considering spin degeneracy for all the valence

band (s orbital) and triply degenerate conduction bands (p orbitals).

1.5.2 Rashba Effect in Hybrid Perovskites

Rashba effect has been extensively studied [101-104] and observed in various systems, in which ultrathin metallic films [101], the surface of topological insulators such as Bi_2Se_3 [102], and the polar semiconductor BiTeI [103] show large Rashba-splitting with α_R of few eV·Å. In traditional III-V semiconductors, however, the Rashba-splitting is very small; for example, α_R at the interface of InAlAs/InGaAs is ~0.07 eV·Å with E_R ~1 meV [104].

In the case of hybrid perovskites, numerous theoretical studies have predicted Rashba-splitting because of the strong SOC due to the heavy elements (Pb, X) that determine the electron bands near their extrema points, which may lead to large Rashba-splitting if the structure lacks inversion symmetry [105-106]. Recently, the observation of the Rashba effect has been claimed in 3D perovskites by different experimental methods [107-109]. By using the surface-sensitive angle-resolved photoelectron spectroscopy (ARPES), D. Niesner et al. reported a spin splitting of the highest-energy valence band (VB) in single-crystal $MAPbBr_3$ [107]. They found the Rashba-splitting arises when orbitals with SOC are subject to symmetry breaking electric fields, and the Rashba parameters α_R were measured as 7 ± 1 eV·Å and 11 ± 4 eV·Å in the orthorhombic and the cubic phase, respectively, which are amongst the highest values reported. For $MAPbI_3$, an indirect to direct bandgap transition has been reported via optical measurements by tuning temperature [108] or pressure [109], which indicates the presence of Rashba effect.

2D hybrid perovskites, due to the strong SOC and intrinsic quantum well structures with many interfaces, may show Rashba-splitting and be promising candidates for room-

temperature spintronic applications [110]; however, there has been no experimental proof for the spin-related properties in 2D perovskites. Our collaborators from National Institute of Standards and Technology (NIST) have carried out first-principles density functional theory (DFT) calculations and predicated the symmetry breaking and Rashba effect in the 2D perovskites system, as shown in Figure 1.11.

The DFT calculation used the local density approximation (LDA) in the form of ultrasoft pseudopotentials as implemented in QUANTUM-ESPRESSO. Figure 1.11 (a) shows the geometry of the relaxed structure. We find that the inversion symmetry is broken due to the Pb atom displacement from the octahedra center. The displacement is in the 2D plane, roughly in the direction of **a**+**b**, where **a**, **b** are the in-plane lattice vectors. This leads to the Rashba band splitting for states with crystal momentum oriented perpendicular to symmetry breaking direction, as shown in Figure 1.11 (c). The dashed red and blue lines in Figure 1.11 (d) show the optical transition matrix elements within the lowest conduction band, which vanish at the minimum of the energy dispersion. The solid green line denotes the interband matrix element, which does not vanish at this point, indicating that the optical transition is allowed. From the model calculation, we obtain band splitting E_R=160 meV in 2D hybrid perovskites PEPI. We note the LDA method used here may overestimate the Rashba-splitting energy and a calculation at the level of quasiparticle GW would be likely required for more quantitatively accurate description of the electronic structure.

In Chapter 4, we used a variety of transient and steady-state optical spectroscopies and determined the Rashba-splitting energy, E_R = (40 ± 5) meV and Rashba-splitting parameter α_R=(1.6 ± 0.1) eV·Å in PEPI 2D hybrid perovskite, and these values are comparable to the recently measured Rashba parameters in $MAPbBr_3$ [107].

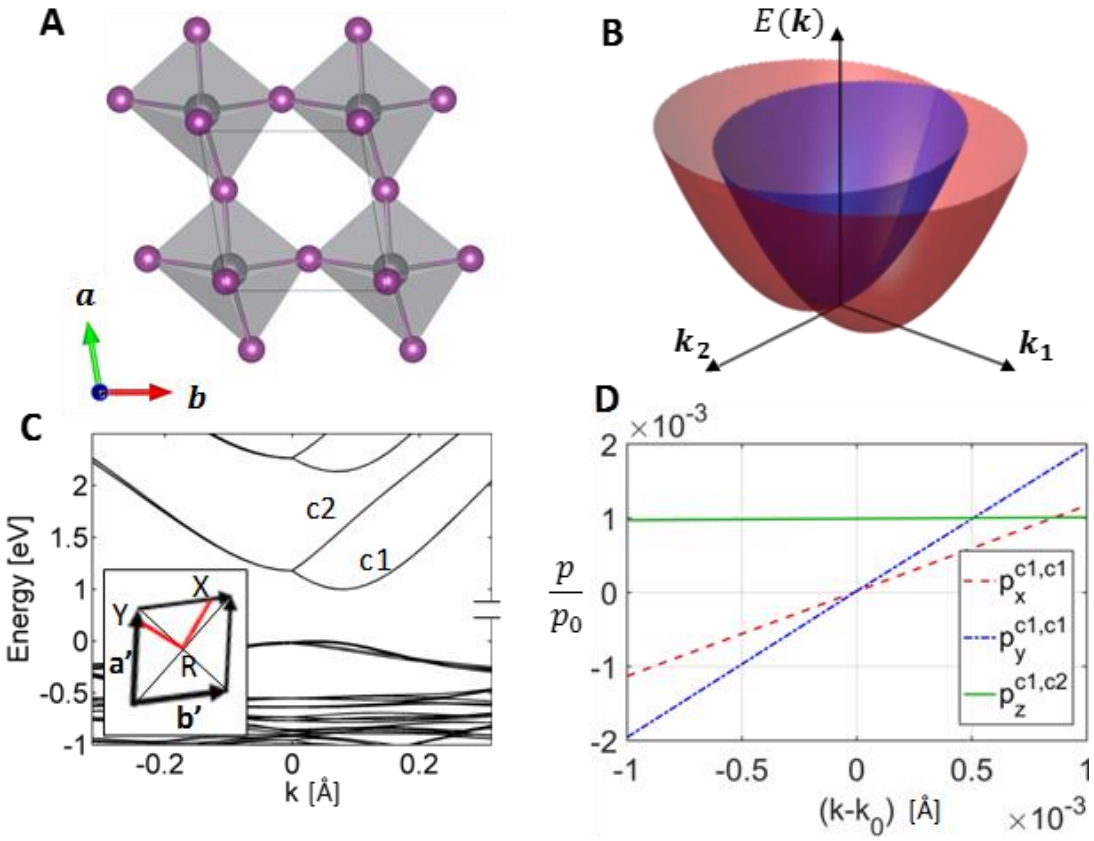

Figure 1.11 Rashba-splitting in PEPI by DFT calculations. (a) The relaxed structure of the PEPI used in the DFT calculations. The unit cell vectors a and b lie in the x-y plane with an angle of 99.7° between them. (b) Schematic of the CB energy dispersion near the R point in the BZ, where $k_{1(2)}$ is directed along the a-(+)b direction. (c) Electronic band structure near the R point, which shows the Rashba-splitting along a direction perpendicular to the symmetry breaking direction; c1 and c2 label the lower and upper Rashba bands, respectively. (d) The DFT-calculated momentum matrix elements vs. *k* in the vicinity of the band minimum (at k_0 =0.07 Å^{-1}) away from the R point along the (1,-1) direction. Red and blue curves correspond to x and y components of the momentum matrix element between the lowest conduction band c1 and itself. The green curve is the z component of the momentum matrix element between the Rashba-split bands c1 and c2, which is nonzero for all *k*. Both y-axes are dimensionless, as the computed momentum p is presented in terms of its value in Rydberg units: p_0=1.99×10^{-24} kg/(m·s).

1.6 Applications of Organic/Inorganic Hybrid Perovskites

As discussed in previous sections, the organic/inorganic hybrid perovskite system has versatile optical and electrical properties and has been used for many optoelectrical applications, including photovoltaics, light emission, lasing, field effect transistors (FETs), and spintronics as shown in Figure 1.12 [25-28, 111-114]. This section discusses those applications as well as the challenges and potential opportunities that hybrid perovskites are facing.

1.6.1 Solar Cells

Figure 1.12 (a) [111] shows the structural evolution of high-performance hybrid perovskite solar cells. Initially, they were developed using the concept of nano-structured excitonic solar cells with mesoscopic structure [16] due to the high absorption coefficient and broad absorption spectrum. However, more recently, it was demonstrated that perovskites are more like the inorganic semiconductors for photovoltaic applications, such as Si or GaAs, and can operate in planar heterojunction configuration, namely, as a solid absorber layer sandwiched in between n- and p-type charge selective contacts. While this structure has led to power conversion efficiencies (PCE) of up to 19.1 % [42], it usually shows an anomalous hysteresis in *I-V* curves [112-113], which is believed to be mainly due to mobile ionic species [114]. Two ways have been shown to reduce this hysteresis. A thin n-type mesoporous TiO_2 layer can provide lager contact surface area and enhance the charge extraction, and therefore offers the highest PCE up to now [115]. An organic n-type layer PCBM is another choice, as shown at the bottom of Figure 1.12 (a) [116-117], which has reduced the hysteresis efficiently.

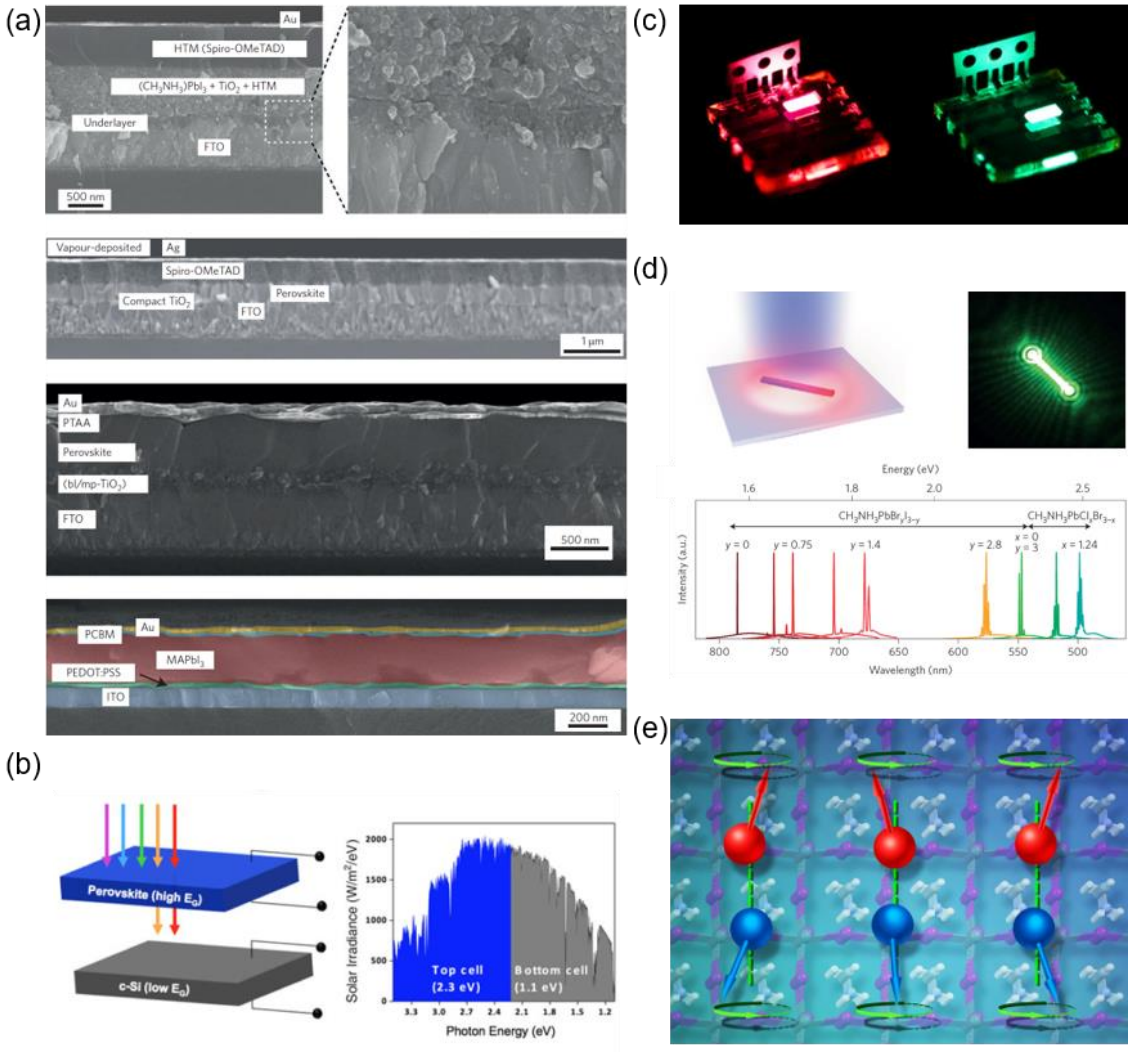

Figure 1.12. Applications of organic/inorganic hybrid perovskites. (a) Structural evolution of high-performance perovskite solar cells. Top to bottom: cross-section SEM images of perovskite solar cells in mesoscopic, planar n-i-p heterojunction, planar–mesoscopic hybrid, and inverted p-i-n planar heterojunction structures. (b) Tandem solar cell by combining perovskites with crystalline silicon. (c) Green and red perovskite LEDs made from $MAPbBr_3$ and $MAPbBr_2I$, respectively. (d) Widely tunable lasing emission wavelength at T=300K from single-crystal nanowire lasers of mixed lead halide perovskites. (e) Perovskites in spintronics. Adapted from Refs. [111], [118], [25], [26], [93], respectively.

As discussed in Section 1.2, the bandgap of perovskites system is continuously tunable by simply changing the halide content. This property opens the way for perovskites in multi-junction solar cell applications [52-56], in which a higher bandgap perovskite solar cell layer can be combined with a lower bandgap silicon or copper indium gallium selenide solar cell working at different photon energy ranges of the solar spectrum, as shown in Figure 1.12 (b) [118]. This structure has been predicted to be the first commercial appearance of perovskites photovoltaic [119].

1.6.2 Light Emitting Diodes (LEDs) and Lasers

The study of light emitting properties of perovskites started well before their application in photovoltaics. In 1990s, Saito and colleagues observed electroluminescence from 2D perovskites layers PEPI, but the device could only operate at low temperature [120-121]. Recently, as the perovskites have received more attention due to their photovoltaic application, researchers once again began to study the light emitting properties of these extraordinary materials [25].

The first light emitting diode (LED) based on 3D hybrid perovskite was in a typical sandwich structure, in which the active thin layer of perovskite was fabricated between an n-type electron-transport layer (ETL) and a p-type hole-transport layer (HTL) [25]. Operating at room temperature, those $MAPbI_3$, $MAPbBr_2I$, and $MAPbBr_3$ LEDs show emission in the near-infrared, red and green, respectively, as shown in Figure 1.12 (c). Later, by controlling the crystal grain size, the external quantum efficiency (EQE) of $MAPbBr_3$ hybrid green LEDs was improved up to 8.5% [122], and the EQE in the near-infrared also achieved 3.5% [123], which were impressive for being solution-processed.

Very recently, perovskite LEDs that operate at EQE of 10.4% for the $MAPbI_3$ and 9.3% for the $MAPbBr_3$ system with significantly improved shelf life and operational stability were realized by coating the nanometer-sized perovskite grains with longer-chain organic cations [124]. Moreover, benefiting from the tunable bandgap, blue LED has been reported in chloride hybrid perovskite even though the EQE was low [125-126]. Therefore, the perovskite system is a very promising candidate for white-light LEDs.

Amplified spontaneous emission (ASE) with large gain and low threshold has also been observed in hybrid perovskite system [127-128], which paved the way for use in optical amplification devices: low-cost optically pumped lasers.

While the first perovskite laser was constructed as a vertical Fabry–Pérot cavity [129], most of the recent perovskite lasers are working in whispering-gallery-mode (WGM) cavities, where optical modes are guided by internal reflection around the circumference of a circular or polygonal resonator provide feedback [130-132]. For example, vapor deposition $MAPbI_3$ thin film lasers exhibited a lasing threshold of 37 $\mu J/cm^2$ [130], and solution-processed single-crystal $MAPbBr_3$ microdisks demonstrated a threshold of 3.6 $\mu J/cm^2$ [131]. Random lasing has also been observed in $MAPbI_3$ perovskite with a threshold as low as 0.32 $\mu J/cm^2$ due to the disorder of the thin film samples [132].

A striking breakthrough of perovskites laser performance was recently made in mixed halide perovskite single crystal nanowires with Fabry–Pérot optical cavities [26]. Compared to thin films, single crystals have low trap-state density and therefore long carrier Auger lifetimes. The nanowire lasers showed extremely high photoluminescence quantum efficiency (PLQE) at nearly 100% and the threshold of ASE as low as 220 $\mu J/cm^2$, with tunability of the color over the whole visible spectrum as shown in Figure 1.12 (d).

1.6.3 Spintronics

Due to the presence of heavy atoms such as lead and halides, the spin-orbital coupling (SOC) has been predicted to be very large in hybrid perovskites by many theoretical methods [89-90, 105-106], which implies the possibility of spintronics application of those materials.

Experimentally, a circularly polarized picosecond pump-probe technique has been used to investigate the highly spin-polarized carrier dynamics and ultra large photoinduced magnetization has been observed in $MAPbI_3$ perovskite thin films [133]. For perovskites-based devices, the magnetic field modulation of the optoelectronic properties such as photocurrent and electroluminescence have also been measured [28, 93]. Recently, our group fabricated hybrid perovskites spintronics devices and measured spin-current in $MAPbI_3$ and $MAPbI_{3-x}Cl_x$ films induced by both spin-pumping and spin-injection from ferromagnetic substrates [134]. Due to the strong SOC and inversion symmetry breaking, large Rashba effect has been reported in 3D and 2D hybrid perovskites via different measurements, as discussed in Section 1.5.2.

Therefore, the interest in the hybrid perovskites for spintronics applications has only recently begun, but promises a great future considering their low-cost and tunable optoelectrical properties.

1.6.4 Challenges and Opportunities

Although organic/inorganic hybrid perovskites have been successfully applied to various optoelectrical fields, they still face challenges for use on a commercial scale.

Compared to the durable silicon solar panels, the primary challenge of $MAPbI_3$

photovoltaic is stability under the outdoor moisture, heat, and extreme light levels, of which moisture is the most detrimental [135]. One way to improve the stability is to replace the organic cation with inorganic cesium ions or organic groups, which has increased stability from less than 100 hours to beyond 1,000 hours [22, 136]. Another promising route is the 2D hybrid perovskites with superior stability at ambient conditions. In 2016, a 2D perovskite photovoltaic has been reported with PCE up to 12.52% and no hysteresis [137]. Importantly, the device showed greatly improved stability in comparison to the 3D solar cells under light, humidity, and heat stress tests. Other ways such as making perovskite films with larger crystals and fewer grain boundaries and industrial encapsulation techniques are also proposed for long-term stability of hybrid perovskite solar cells [135].

Toxicity is the other obvious challenge for lead-based perovskites [138]. Researchers have tried less toxic counterparts such as tin or germanium to replace lead for solar cell fabrications, but much lower PCE were obtained due to the narrower bandgaps [139-140]. If this problem can be solved properly, the hybrid perovskites could become useful for real applications and allay public concerns.

1.7 Organization of This Dissertation

This dissertation is aimed at the ultrafast photoexcitation dynamics in 3D and 2D organic/inorganic hybrid perovskites. The main experimental techniques as well as the sample fabrications and characterizations are introduced in Chapter 2.

In Chapter 3, we investigate the branching ratio between photogenerated carriers and excitons, a key factor for the optoelectronic applications in a series of 3D perovskite films with the ultrafast transient response of photoexcitations using polarized broadband pump-

probe spectroscopy. We show the coexistence of photogenerated carriers and excitons in $MAPbI_3$ perovskite with the ratio tunable by temperature (structure phases). In contrast, $MAPbI_{1.1}Br_{1.9}$, $MAPbI_{3-x}Cl_x$, and $MAPbBr_3$ only show one photoexcitation species, that is excitons. The transient photoinduced polarization memory (POM) for both excitons and photocarriers was observed in $MAPbI_3$ due to the asymmetric tetragonal phase at room temperature. Morphological effect on the optical and magnetic properties of perovskites is also investigated in this chapter.

Chapter 4 focuses on the 2D hybrid perovskite thin film, called $(C_6H_5C_2H_4NH_3)_2PbI_4$ or PEPI, in which a giant Rashba effect has been observed by all optical methods including the electro-absorption (EA) spectrum and transient photoinduced absorption (PA). We obtained Rashba-splitting energy of ~40 meV and Rashba parameter of ~2.7 eV·Å, which are among the highest Rashba-splitting size parameters reported so far. This finding shows that 2D hybrid perovskites have great promise for potential applications in spintronics.

Chapter 5 studies the near-surface region photoexcitation recombination in $MAPbBr_3$ single crystal. A broad PA band has been observed from the surface trapping states, which diffuse to the interior of the crystal very efficiently.

CHAPTER 2

EXPERIMENTAL TECHNIQUES

This chapter discusses the experimental techniques used for fabricating and characterizing the perovskite films and crystals studied in this dissertation. We used the dual source co-evaporation and the one (two)-step solution processes to fabricate the perovskite thin films and a liquid state reaction to synthesize the single crystals. The pump-probe photomodulation (PM) spectroscopy in a broad spectral range from mid-IR to visible (namely 0.2-2.8eV) with 300 fs time resolution has been adapted to study the ultrafast transient response of photoexcitations in different hybrid perovskites. The theory and experimental setup of transient pump-probe spectroscopy as well as other optical measurement systems and techniques, such as steady-state photon-induced absorption and photoluminescence, are discussed in detail.

2.1 Materials Fabrication

2.1.1 Thin Film Fabrication

As discussed in Chapter 1, the optoelectronic and spin-related properties of perovskite thin films are sensitively dependent on the morphology of a sample, and different processing conditions may lead to a substantial difference in the film quality and device performance [18, 92-93].

Unlike most traditional inorganic and organic materials, distinctly different physical and chemical characteristics of the organic and inorganic components make it hard to fabricate high-quality perovskite films. Figure 2.1 shows the main perovskite thin films processing techniques used to date [141-144]; namely (i) dual/single source evaporation, (ii) sequential deposition, (iii) one-step solution process, (iv) sequential two-step solution process (nano-crystal pinning), and (v) vapor-assisted solution process. Even though the record PCE in photovoltaic devices so far was obtained with solution-processed perovskites, there is no preferred method of thin film deposition. Solution process has the advantage of low cost and convenience, while vacuum deposition can present high purity and well-controlled morphology films with large area. In this dissertation, the films were mainly fabricated via the dual source co-evaporation and the one (two)-step solution process as discussed below.

2.1.1.1 Dual Source Co-Evaporation Deposition

Figure 2.1 (a) [144] shows the schematic diagram of the dual-source vapor deposition process, in which an inorganic lead iodide PbI_2 source and an organic methylammonium iodide (MAI) source are thermally evaporated simultaneously in an ultra-high vacuum chamber. The deposition rate as well as the thickness were monitored with two sensors. This method was used to make the first high-efficiency planar $MAPbI_{3-x}Cl_x$ perovskite, and uniform film with large grain sizes was obtained [144]. The dual-source vapor deposition was then widely adopted in a variety of perovskite structures such as layered materials and three-dimensional $MAPbI_3$ because of the advances such as superior centimeter-scale uniformity. Additionally, vapor deposition allows samples to be

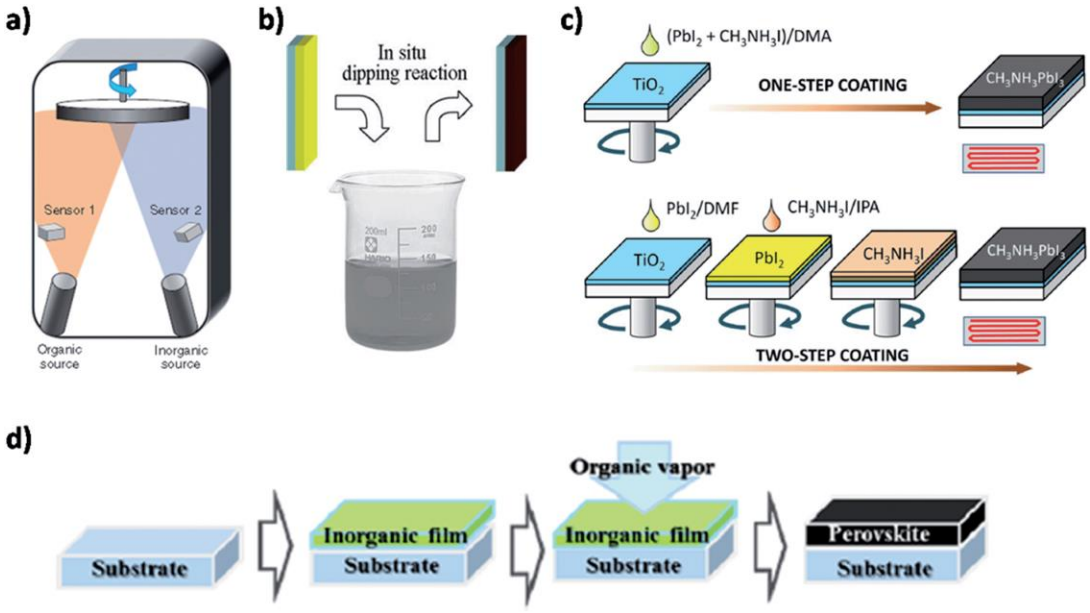

Figure 2.1. The preparation of perovskite devices from different deposition methods: (a) Dual source co-evaporation. (b) Sequential deposition by dipping the PbI_2 film into MAI solution. (c) One-step solution process, and sequential coating of PbI_2 and MAI (nano-crystal pinning). (d) Vapor-assisted solution process using the MAI organic vapor to react with the PbI_2 film. Adapted from Ref. [144].

fabricated at room temperature, which paves the way for devices to be constructed on a wide range of substrates such as soft materials and textiles. We have adopted this deposition method in our spin-related device fabrication; see Figure 2.2. Unlike the inorganic devices that are fabricated via vapor deposition on an industry scale, the thermal deposition of organic materials is hard to precisely control. For example, heating MAI in vacuum usually results in a broader evaporating cone and affects all the sensor readers, resulting in the decomposition or dissociation of the organic component.

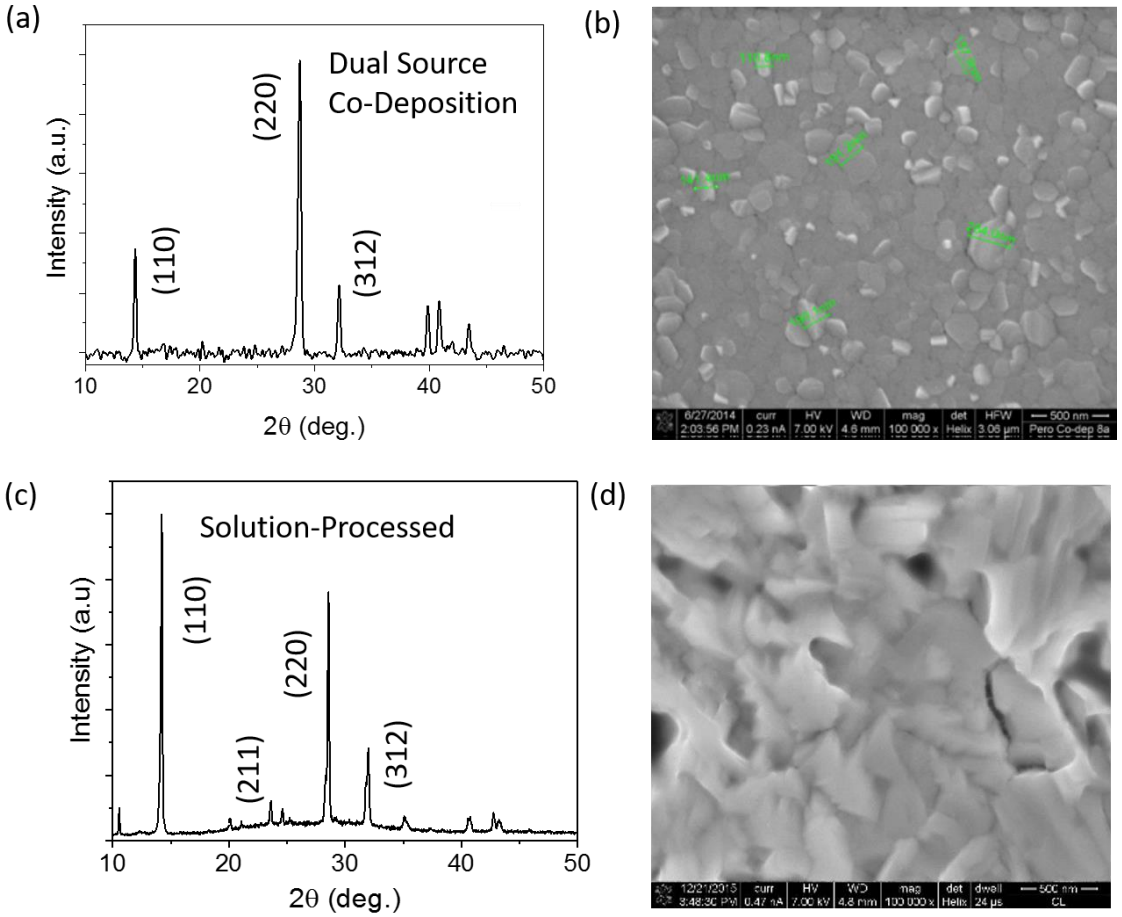

Figure 2.2. The characterization of $MAPbI_{3-x}Cl_x$ perovskite film from different deposition methods: (a) XRD pattern and (b) SEM image of dual source co-evaporated film, (c) XRD pattern and (d) SEM image of one-step solution processed film.

Other vapor deposition methods have been developed to improve the control of perovskite formation, such as single-source vapor deposition, sequential deposition (see Figure 2.1 (b) [142]), and vapor-assisted solution process (see Figure 2.1 (d) [143]). These strategies have shown better control of perovskites morphology with high reproducibility and enhanced optical properties [144].

2.1.1.2 One-Step Solution Process

One-step solution process as shown in Figure 2.3 (upper panel) is the most widely used method for perovskite films due to the ease of fabrication and low cost. In this method, the metal-halide MX_2 (M = Pb, Sn; X = Cl, Br, I) and organo-halide AX (A = methylammonium, MA; formamidinium, FA) species are mixed and dissolved in an organic solvent. The precursor solution is directly deposited on a pretreated substrate and followed by thermal annealing to form the perovskite phase. Because the precursors can fill the space within the pores, solution process is attractive in mesoporous structures, and has been widely adopted and improved to achieve devices with PCEs over 20%.

Figure 2.2 (c) and (d) show the XRD patterns and SEM image of the $MAPbI_{3-x}Cl_x$ films deposited via one-step solution process, and larger crystal grain sizes and more mesoporous structures are obtained than vapor deposition films (~100nm grain size). The XRD patterns of the films fabricated in both methods exhibit peaks at 14°, 29°, and 32° that can be assigned to (110), (220), and (312) planes, respectively, by Bragg's law. The lattice parameter shows a stable cubic phase of $MAPbI_{3-x}Cl_x$ film, which is in accordance with previous reports.

Most of the perovskite samples studied in this dissertation were fabricated via the

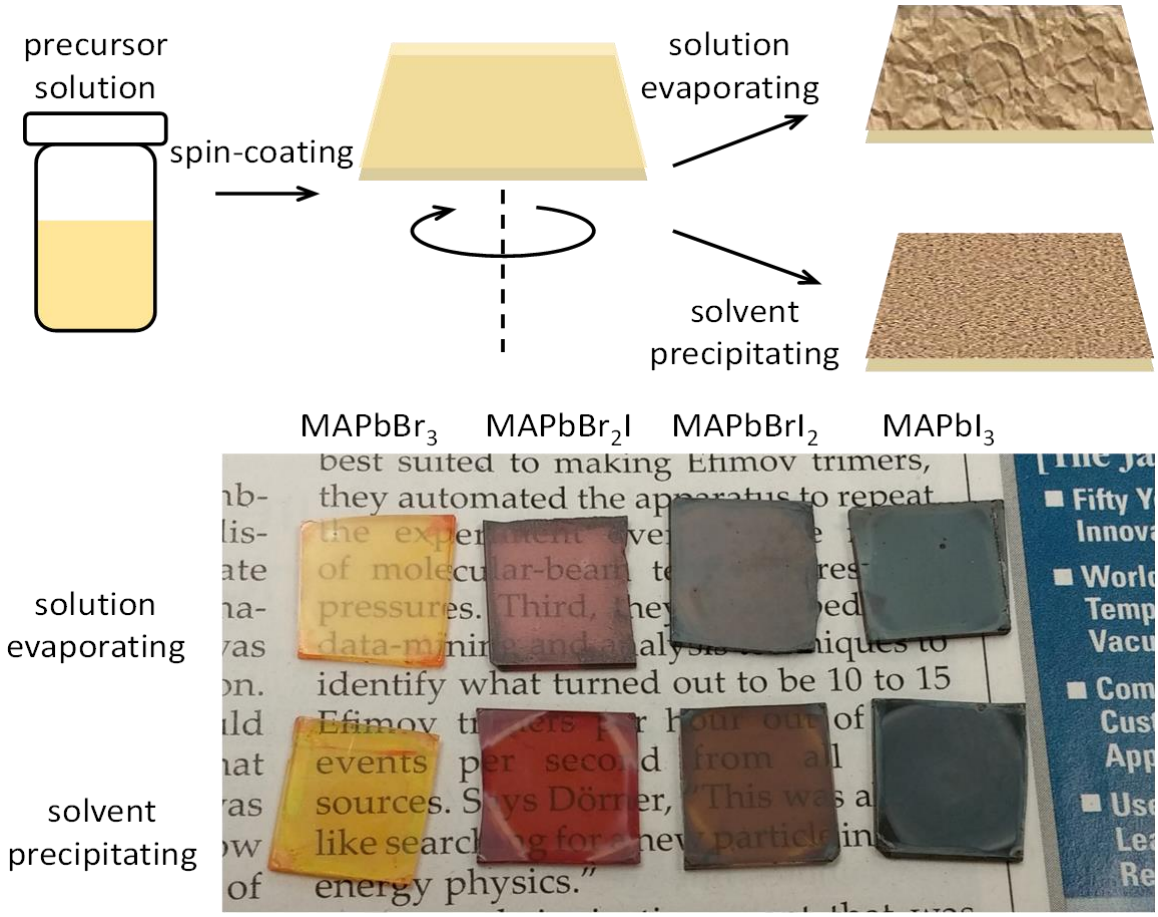

Figure. 2.3. Nano-crystal pinning process (upper panel) and the quality of resulting films (lower panel).

one-step solution process, including $MAPbI_3$, $MAPbI_{1.1}Br_{1.9}$, $MAPbI_{3-x}Cl_x$, and 2D PEPI with details discussed in correlative chapters later.

2.1.1.3 Nanocrystal-Pinning (NCP)

Recently, Cho et al. have achieved greatly improved efficiencies for perovskite LEDs by employing an anti-solvent-induced crystallization method that produces films with well-packed nano-size crystalline grains [122], and this is the so-called "nanocrystal-pinning (NPC)" process or two-step solution process. In this method, a "bad" solvent such as chloroform was used to wash out the "good" solvents [dimethylformamide or dimethyl sulfoxide (DMSO)] during the crystallization and causes pinning of nanocrystals to reduce the size and increase the uniformity of perovskites grains by reducing solvent evaporation time.

We adapted the NCP method to a series of $MAPbI_{3-x}Br_x$ perovskites, which might be important for tandem solar cells, because its optical gap can be tuned from 1.57 eV to 2.3 eV when the composition parameter, x, changes from x=0 to 3. As shown in Figure 2.3, chloroform was used as the anti-solvent and deposited on the sample during spin-coating. It is clear to see from Figure 2.3 (lower panel) that all the NCP-treated films have much smoother surfaces compared to those of as-cast films, which indicates that the large crystallites that form from the usual solvent evaporation process during spin coating are significantly reduced when the crystallization kinetics are increased by the application of the $CHCl_3$ solvent. We further characterized the $MAPbBr_3$ film with optical and SEM images of both NCP and as-cast $MAPbBr_3$ films and revealed the crystallite sizes (<100 nm) in the NCP film, which is 2–3 orders of magnitude smaller than the as-cast films.

2.1.2 Single Crystal Growth

Aside from high PCE films, bulk and low dimensional specific morphological single crystals have attracted certain attention for studying the intrinsic properties of perovskites, such as emission, thermoelectric, and spin-related applications [145-148]. Various methods have been developed in either liquid or solid-state reactions to grow large hybrid perovskites single crystals. Here we used two liquid methods, solvent vapor exchange and solvent evaporation, to synthesize $MAPbBr_3$ and $MAPbI_3$ single crystals.

In a typical solvent vapor exchange procedure, $PbBr_2$ and MABr (molar ratio 1:1.2) are dissolved in dimethylformamide (DMF) (5 mL, 0.5 M), and stirred for 3 hours. The vial with solution is placed in a beaker containing 2-propanol (20 mL) as the anti-solvent. The beaker is covered and placed in a dark place for 3-7 days. Cubic-shape $MAPbBr_3$ crystals are obtained, and used as seeds to repeat the same procedure. Bulk crystals with larger size and better quality could be obtained after several times; see Figure 2.4 (a) and (b). The $MAPbI_3$ crystals can be grown in a similar way, but with ϒ-butyrolactone as the solvent and dichloromethane as the anti-solvent. They are usually obtained on the side of a vial, because dichloromethane diffused slowly into the ϒ-butyrolactone.

In a typical solvent evaporation preparation, PbI_2 and MAI (molar ratio 1:1.5) are dissolved in ϒ-butyrolactone (20 mL, 1 M), and stirred overnight at 70 ºC. The solution is then transferred into a petri dish. The dish is placed on a hot plate in the hood, and heated up to 160 ºC. The solvent evaporates slowly from the surface, and crystal domains appear once the solution reached over-saturation. The crystals could grow larger with the further evaporation of solvent. After that, these thin crystals are filtered and washed with 2-propanol several times; see Figure 2.4 (c) and (d).

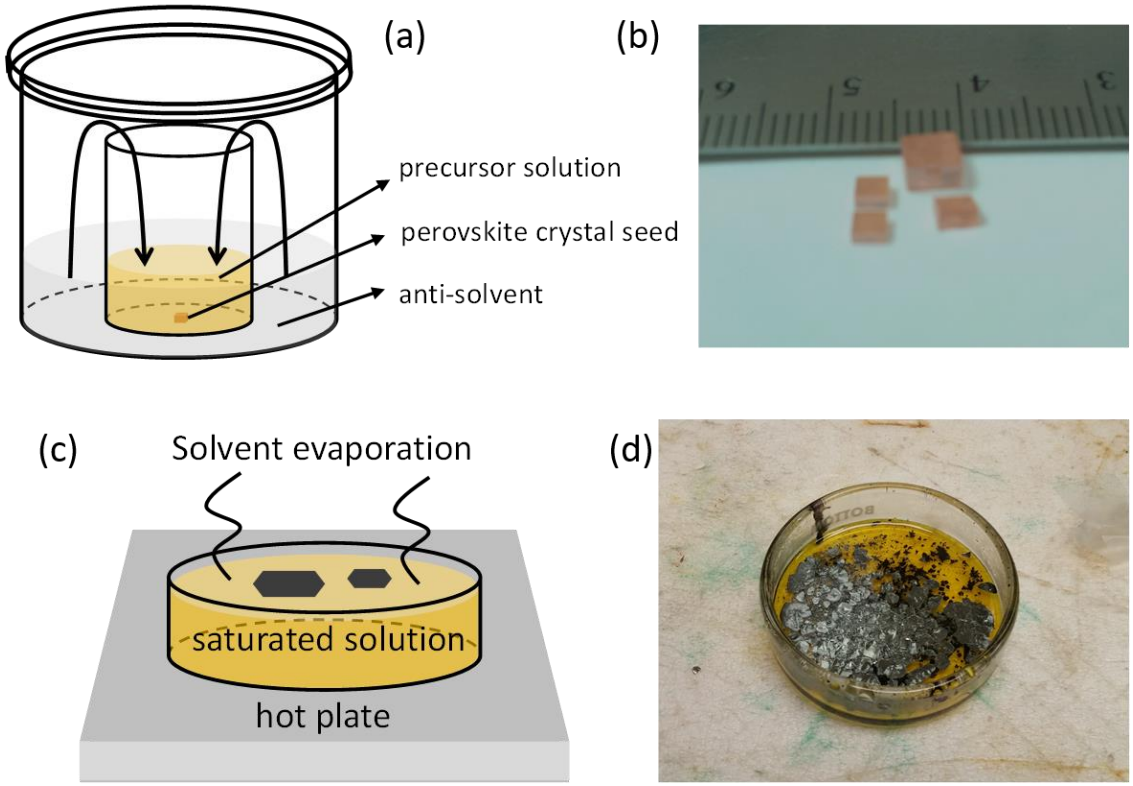

Figure 2.4. Perovskite single crystals growth. (a) Scheme for solvent vapor exchange method and (b) as-grown $MAPbBr_3$ bulk crystals; (c) Scheme for solvent evaporation and (d) as-grown thin pieces of $MAPbI_3$ crystals.

2.2 Theory of Transient Pump-Probe Spectroscopy

Transient pump-probe photomodulation (PM) spectroscopy is perhaps the best way to detect and characterize photoexcitations in perovskites for photovoltaic (PV) and other optical applications [57, 76-77]. In this technique, when a sample absorbs a photon (pumped), a nonequilibrium carrier concentration is created, and we can probe its difference in optical absorption between the two states as a function of time with another photon (probe pulse). A simplified scenario of a pump-probe PM measurement is shown in Figure 2.5. When photoexcited (pumped) by a photon to an allowed optical state, the photoexcitations in the sample will eventually relax back to the ground-state, and the population of the excited state can be monitored by a probe photon with a time delay, which excites the population to higher states. Figure 2.5(b) shows example data of this hypothetical measurement in progress [30, 57].

2.2.1 Linear Absorption (Pump)

When light I_0 is incident a sample with reflectance, R, and transmittance, T, we have $I_0 = I_r + I_t + I_a = RI_0 + TI_0 + I_a$, and the absorbance A is defined as the transmittance loss through a material at a given wavelength as $A = -\ln T$. Transmission T can be expressed with Lambert-Beer law as

$$T = (1 - R)e^{-\alpha d}, \tag{2.1}$$

where α (optical absorption coefficient) is defined by the density of optical absorbers N times the optical cross-section of those absorbers σ at wavelength λ, as $\alpha(\lambda) = N(\lambda)\,\sigma(\lambda)$.

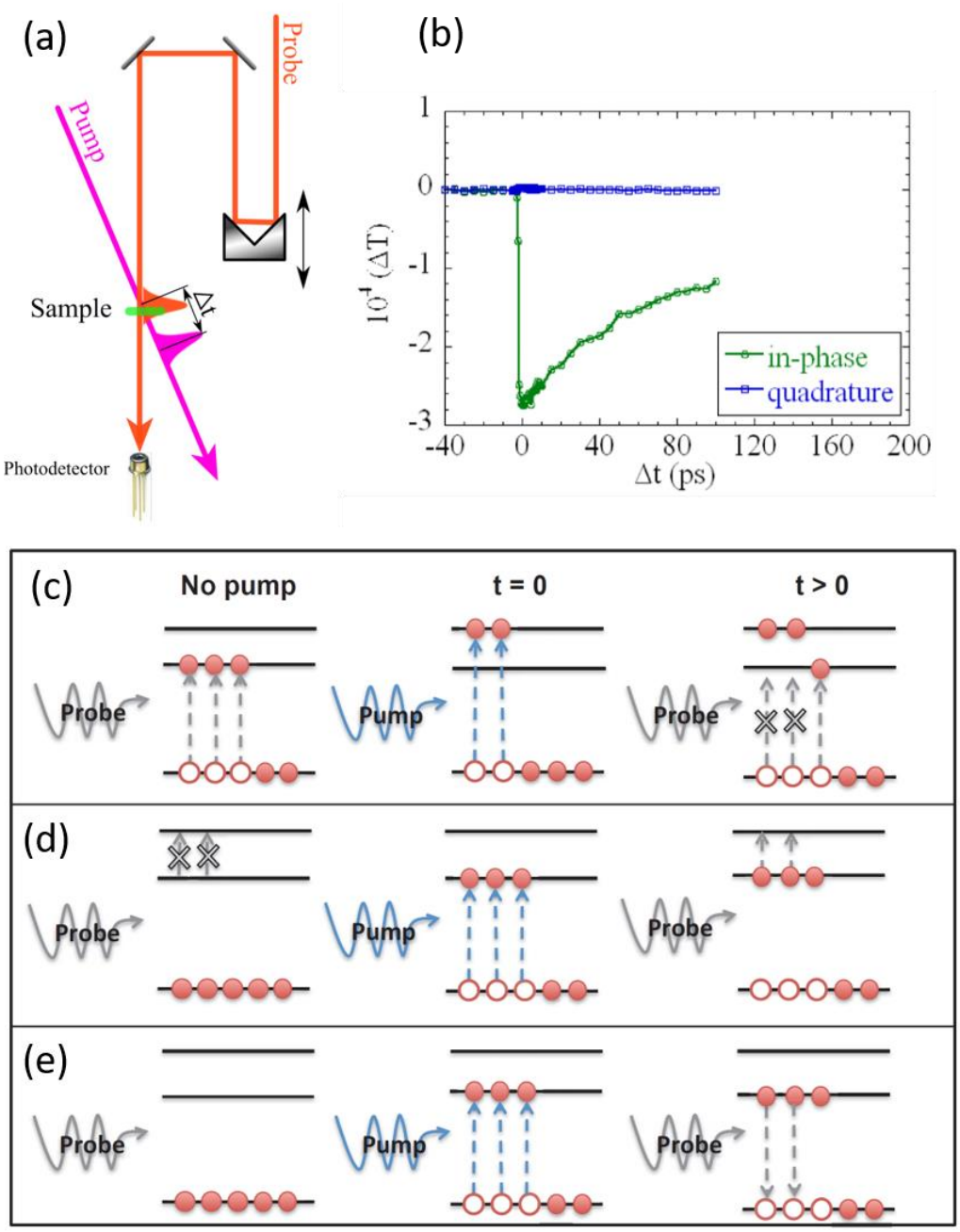

Figure 2.5. Schematics of transitions during pump-probe excitations. (a) Representation of pump-probe experiment illustrating the pump-probe pulse delay. (b) Example data of this hypothetical measurement in progress. (c) to (e) Mechanisms for ground-state band-edge bleaching, photon-induced absorption, and stimulated emission, respectively. Adapted from Ref. [30].

We can find that

$$A = \alpha d - \ln(1 - R) \tag{2.2}$$

When the reflectance is negligible while αd<<1, the absorbance and transmission reduce to

$$A = \ln\left(\frac{I_a}{I_0}\right) = \alpha \mathrm{d}, \text{and } T = e^{-\alpha d} \tag{2.3}$$

Optical density (OD) defined as absorbance per unit length (i.e., divided by the thickness of the sample) is a dimensionless measure of absorption.

2.2.2 Photoinduced Absorption (Probe)

Defining ΔT as the difference of transmission of the sample with and without the pump, namely T_{on}-T_{off}, from Equation (2.3) we get,

$$\Delta T = (e^{-\Delta\alpha} - 1)T \tag{2.4}$$

When $\Delta T << T$, which happens in most of our measurements, we have,

$$\Delta\alpha \approx -\frac{\Delta T}{T} \tag{2.5}$$

In a semiconductor, several features can be observed in a transient PM spectrum [30]:

(1) Ground-state photoinduced bleaching (PB) usually shows as a strong negative signal around the band-edge due to interband transition bleaching as described in Figure 2.5 (c).

(2) Stimulated emission that happens for bright states and resembles the fluorescence spectrum also causes a negative PM signal because of increasing number of photons. It usually happens with a Stokes shift from the PB as shown in Figure 2.5 (e).

(3) Photon-induced absorption (PA) showing positive signal is the most important feature in a PM spectrum. It comes from the absorption of a photoexcited state to higher energy as shown in Figure 2.5 (d) and provides us plenty of information about inter/intraband transitions and dynamics.

(4) It is worth mentioning that the change of absorption spectrum after photoexcitation including shifting and broadening can also contribute to the PM spectrum. The change can be caused by various interactions, for example bandgap renormalization and optical Stark effect. This effect is discussed in Chapter 4.

2.2.3 Kinetic Analysis

Assuming optical cross-section σ is not dependent on time, we have

$$-\frac{\Delta T}{T}(t) = \Delta\alpha(t)d = N(t)\sigma d \tag{2.6}$$

That means the measured PM signal is proportional to the photoexcitation density *N(t)*. By neglecting the saturation effect, we can describe the photoexcitation dynamics

with a simple rate equation as following,

$$\frac{dN}{dt}(t) = G(t) - R(N) \tag{2.7}$$

in which *G* and *R* are the generation and recombination rates, respectively.

Equation (2.6) and (2.7) are the two great equations governing the PA. For steady-state PA, *N* is in equilibrium and therefore $G=R= aI_0$, which is proportional to the pump intensity I_0. In transient absorption, however, *N=N(t)* and *G* is zero after excitation ends.

2.2.3.1 Monomolecular Recombination

Monomolecular recombination (MR) is the simplest channel where only one species is involved in photoexcitation recombination, and therefore $R=N/\tau$.

In steady-state,

$$\frac{dN}{dt}|_{ss} = G - \frac{N_{SS}}{\tau} = 0 \tag{2.8}$$

with the solution

$$N_{ss} = G\tau = aI_0\tau \tag{2.9}$$

which means in the cw-PA measurements, the MR process gives a signal proportional to the pump laser intensity.

In transient spectroscopy, we have

$$\frac{dN}{dt}(t) = -\frac{N}{\tau} \tag{2.10}$$

and therefore, a single exponential decay would be expected as

$$N(t) = N_0 e^{-t/\tau} \tag{2.11}$$

2.2.3.2 Bimolecular Recombination

Bimolecular recombination (BR) happens when two photoexcited states are involved in one recombination and in this case, R=bN^2. In steady-state,

$$\frac{dN}{dt}|_{ss} = G - bN_{SS}{}^2 = 0 \tag{2.12}$$

$$N_{ss} = \sqrt{G/b} = \sqrt{aI_0/b} \tag{2.13}$$

which means in the cw-PA measurements, the MR process gives a signal proportional to the square root of pump laser intensity.

In transient spectroscopy, we have

$$\frac{dN}{dt}(t) = -bN^2 \tag{2.14}$$

$$N(t) = \frac{N_0}{1 + tbN_0} \tag{2.15}$$

2.3 Femtosecond Optical Systems

To realize the broad transient photomodulation (PM) spectral ranging from mid-IR to visible (namely 0.2-2.8 eV), we used two laser systems based on a Ti: Sapphire oscillator. These are a low power (energy/pulse ~0.1 nJ) high repetition rate (~80 MHz) laser for the mid-IR spectral range, and a high power (energy/pulse ~10 μJ) low repetition rate (~1 kHz) laser for the near-IR/visible spectral range. The corresponding spectrum covered by the two systems is show in Figure 2.6 (a).

2.3.1 Mid-IR High Repetition Low Energy OPO System

In this system, we use a commercial CW solid-state laser (Millennia Xs) at 532nm 10W to pump an 80MHz Ti: Sapphire pulse laser (Tsunami), which in turn pumps the optical parametric oscillator (OPO) (Opal). All three optical systems are from Spectra-Physics.

2.3.1.1 Nonlinear Processes: The OPO and Difference Frequency Generation (DFG)

An OPO is a frequency converter, and works via a second-order nonlinear process, parametric down conversion (PDC), in which three photons interact in a temperature-controllable noncentrosymmetric crystal (LiB_3O_5 or LBO here) and transfer the fundamental photon energy and momentum into two photons, signal (higher energy) and idler (lower energy) as

$$\omega_f = \omega_s + \omega_i, \tag{2.16}$$

$$k_f = k_s + k_i. \tag{2.17}$$

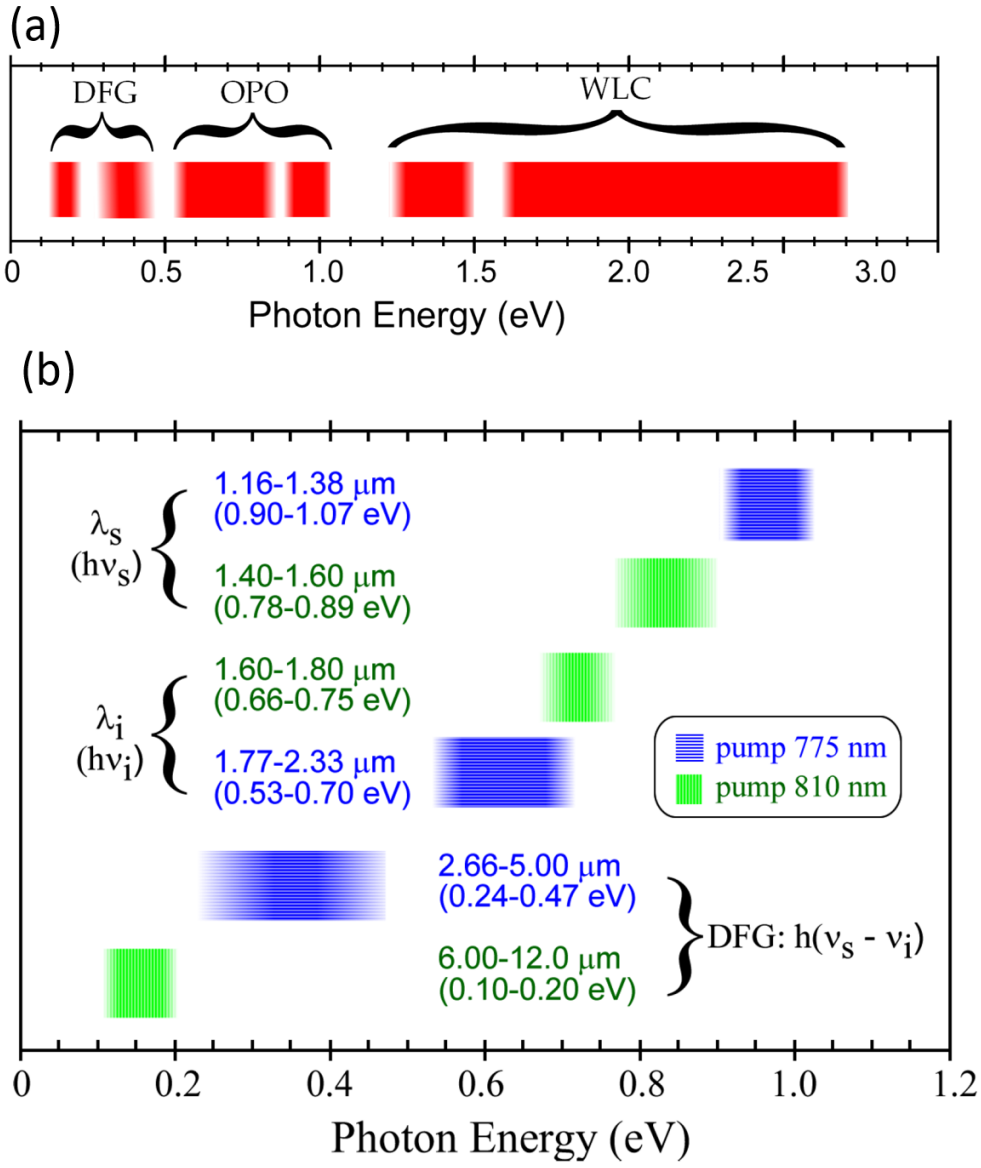

Figure 2.6. Probe optical ranges for ultrafast PM systems. (a) Complete spectrum breadth available from both low-intensity (OPO and DFG) and high-intensity (white-light continuum, WLC) pulsed laser systems. (b) Optical range of OPO probe beam where λ_s and λ_i, respectively, give signal and idler wavelength ranges; the Tsunami fundamental wavelength is tuned as indicated to pump the OPO.

Two cavities are used in the OPO to get a broad spectrum, namely 1.3 μm and 1.5 μm optical range, which are pumped by the Tsunami at 775nm and 810nm, respectively. Along with controlling the temperature of the LBO crystal and the diffraction grating, any desired frequency of signal/idler ranging from 0.53eV (2.33μm) to 1.07eV (1.16μm) can be obtained. Another nonlinear optical process realized in a $AgGaS_2$ crystal, difference frequency generation (DFG), is then used via $\omega_{DFG} = \omega_s - \omega_i$, to generate lower energy from 0.13-0.47 eV (2.66-12.0 μm) [57] as shown in Figure 2.6 (b).

2.3.1.2 OPO System Configuration

The transient pump-probe measurements in mid-IR range are based on the OPO described above. As shown in Figure 2.7(a), a residue beam reflected from and LBO crystal is picked up to pump the sample at fundamental (~1.55eV) or double (~3.1eV) frequency via a second-harmonic generation (SHG) crystal, and modulated with acousto-optic modulator (AOM) at 50KHz to increase the signal-to-noise ratio (S/N) for the low photoexcitations signal. The energy/pulse on the sample is about 0.1nJ and a large beam size ~100-500 μm is usually used to keep the pump intensity below 5μJ/cm^2 per pulse corresponding to 10^{13} cm^{-2} initial photoexcitations to avoid complicated optical processes such as nonlinear effects and exciton-exciton annihilation, or polymer degradation.

The signal/idler probe pulse is delayed through a one-dimentional program-controlled translation stage with an accuracy up to 0.1 μm (or 0.03 fs) and modulated with a mechanical chopper at 310Hz. Even though the probe beam is usually focused on the sample with a much smaller spot size (~30-50 μm) to avoid the effect of its wander caused by the OPO, especially in the DFG case, a step-like out-phase signal at t=0 may

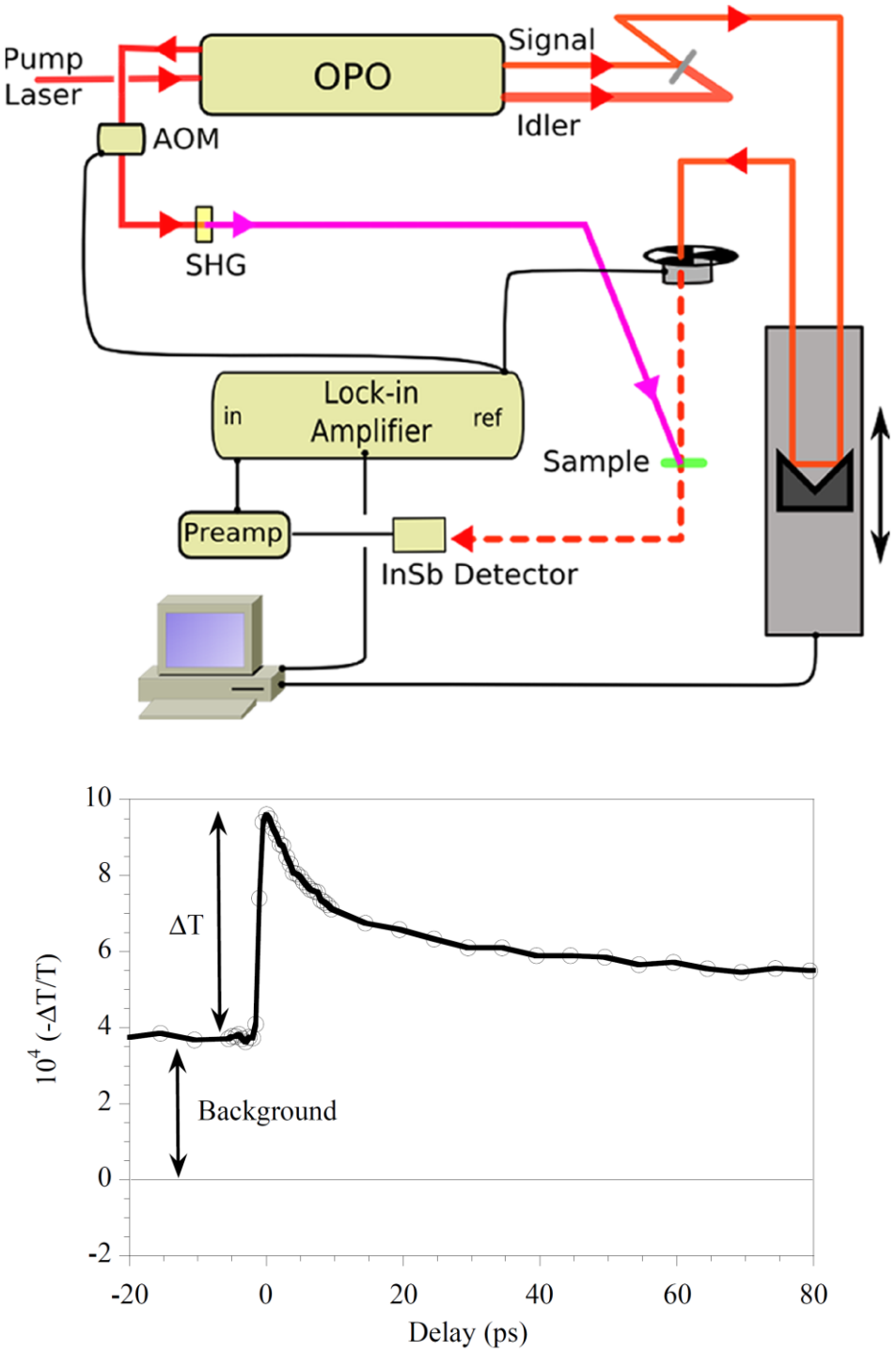

Figure 2.7. OPO system configuration. (a) Experimental schematic for transient pump-probe IR spectroscopy. (b) Example of a measurement showing transient PA (ΔT) atop PA background.

still show up in the lock-in amplifier (LIA) indicating a “beam-walk” happened. This has been fixed with fine aligning the optics or eliminated with the program.

In practice, the probe transmission T is measured using the optical chopper with the pump beam blocked, and photomodulation $\Delta T/T$ is measured regarding the AOM while the chopper is removed from the probe path. By using a LIA, the minimum $\Delta T/T$ can be measured down to 10^{-7}, that is ~10^{-14} cm^{-3} photoexcitations for a ~100nm thin film with $\sigma=10^{-16}$ cm^2. Proper optics such as mirrors and optical band filters are chosen for certain wavelengths to filter all but the desired probe wavelength and eliminate any scattering light. The CaF_2 substrate with wide vis/IR transmission are used for various samples, which are measured in a dynamic vacuum of ~150 μtorr to prevent degradation and oxidation in the presence of intense laser light. Two photodetectors are used in this setup, namely liquid nitrogen (LN)-cooled indium antimonite (InSb) detector for 0.8 μm to 5.5 μm and LN-cooled mercury cadmium telluride (MCT) for 5.5 μm to 9.5 μm.

2.3.1.3 Ultrafast Background

In our high repetition OPO system (80MHz), a background signal is usually measured at t=0ps with the PA sitting on top of it because the long-lived photoexcitations do not have enough time to completely recombine before the next pulse arrives and accumulate together. Therefore, the background signal equals the steady-state in-phase PA signal modulated at the AOM frequency and should be analyzed separately from the transient spectrum. Figure 2.7 (b) shows an example of a measurement with transient PA (ΔT) atop a background. The background is not completely flat during the delay time and the PA signal can only be qualitatively analyzed if the background is significantly large.

2.3.2 Vis/NIR Low Repetition High Energy Ti: Sapphire System

2.3.2.1 Home-Made Ti: Sapphire Laser System

Unlike the OPO system used in IR, the vis/NIR high energy picosecond system is mainly home-made and requires full understanding for daily operation. It was assembled at the University of Utah Laser Institute and consists of two parts, namely Ti: Sapphire oscillator and Ti: Sapphire regenerative amplifier.

The Ti: Sapphire oscillator is a self-mode-locked laser system based on "Kapteyn-Murnane 11 fs scheme" [149]. A horizontal polarized cw beam at 5W and 532 nm by Millenia Pro (Spectra-Physics) diode laser is used to pump a 4.75mm path-length Ti: Sapphire crystal (0.015% doped) and generates a seed beam with the center wavelength at 800nm as shown in Figure 2.8. The position of the crystal need to be carefully adjusted to minimize the reflection (Brewster angle needs to be achieved). Two fused silica prisms in the cavity are used to compensate the dispersion, and can be fine adjusted in order to get to mode-lock pulse mode. The output power and spectrum of the oscillator can be measured with a thermal power meter and an ultrafast spectrometer from Ocean-Optics, respectively. For our daily single wavelength pump and WLC probe operation, a ~200-300mW laser output is good enough, but to pump the traveling-wave optical parametric amplifier of white-light continuum (TOPAS-C) and get tunable pump wavelength, higher and more stable power is needed and can be achieved by fine aligning the optical path.

The output beam from the oscillator at ~ 80MHz (800 ± 30 nm) is then fed into the Ti: Sapphire regenerative amplifier, in which its energy/pulse would be amplified 5 orders higher. The Ti: Sapphire regenerative amplifier system was built based on the configuration provided by the Positive Light Inc. and contains three parts: stretcher,

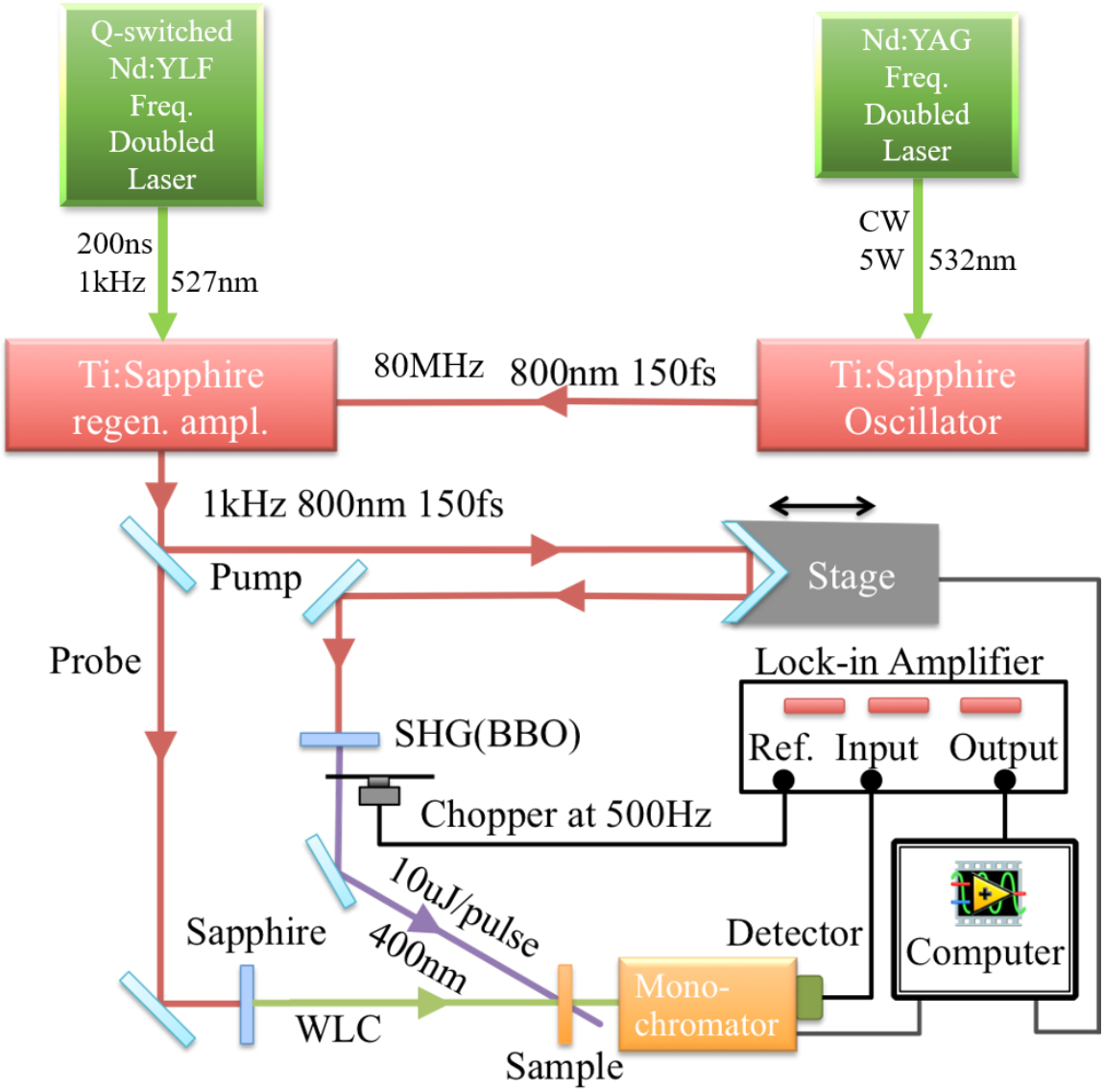

Figure 2.8. Schematic diagram of ultrafast high intensity transient pump-probe setup.

amplifier, and compressor. The stretcher and compressor are designed to protect the amplifier and other optics from the high peak power during the amplification. They work complementarily based on the group velocity dispersion at different frequencies, meaning the stretcher stretches the short pulses into long pulses with a grating and feeds the beam into the amplifier, after which the compressor compresses the pulses into short pulses again. Because the pulse duration is crucial in this system (both the SHG and the WLC generation), it is necessary to make sure the grating and the optical path are identical in the stretcher and compressor. We use a technique called autocorrelation to measure the pulse duration, which will be discussed in the next section.

The amplification takes place as the optical pulse from the stretcher passes through the Ti: Sapphire rod in the amplifier, which has been optically excited by a nanosecond Q-switched Nd: YLF laser at 527 nm and 1kHz repetition rate (Coherent, Evolution-15). Normally, the amplification of the rod is small; however, the regenerative technique enables the pulse to multi-pass the rod, resulting in an overall amplification of over 10^5 by precise timing control via the synchronization delay generator (SDG). Therefore, the output beam from the Ti: Sapphire regenerative amplifier has repetition at 1kHz, center wavelength 800 nm, time resolution ~150 fs, and energy/pulse up to mJ.

It is important to notice that the Ti: Sapphire crystals are very sensitive to the environment and the white light continuum system is not sealed as in the OPO system. Thus, temperature and humidity level need to be monitored in the lab during daily operation. It is also crucial to make sure the closed circle cooling equipment for all the crystals and lasers are working normally at set parameters to guarantee the stability of both the oscillator and amplifier.

2.3.2.2 Autocorrelation

Since the pulse duration is crucial to generate other nonlinear processes in the pump-probe experiment such as SHG and WLC, a technique called autocorrelation is used to measure the temporal profile of the fundamental pulses. The output beam from the Ti: Sapphire laser system is separated into two beams with equal intensity and one of them goes through a delay stage. The two beams are focused together at a BBO crystal and a sum-frequency spot can be observed when they have identical optical paths. The autocorrelation signal can be measured by controlling the delay between the two pulses as shown in Figure 2.9. By a Gaussian fitting, FWHM at 240 fs is obtained in the autocorrelation profile indicating a 170 fs pulse of the fundamental 800nm laser.

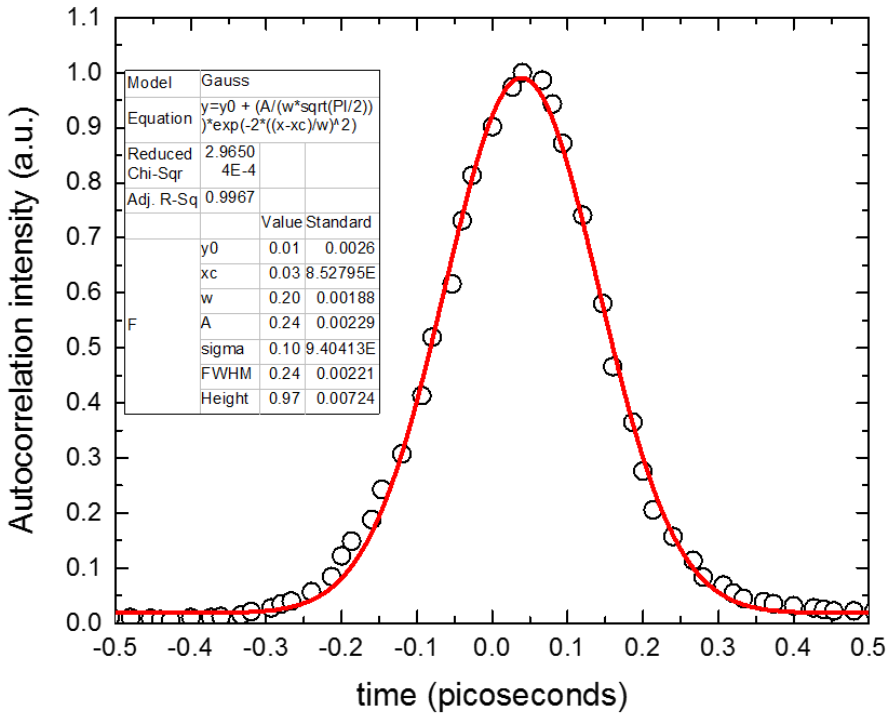

Figure 2.9. Temporal profile of fundamental pulses measured by autocorrelation.

2.3.2.3 White Light Continuum (WLC) System Configuration

The pump-probe setup in WLC system shown in Figure 2.8 is like the OPO system discussed in Section 2.3.1. In this setup, a 1:3 beam splitter is used to separate the 800nm fundamental beam into pump (3/4) and probe (1/4) beams. The time delay between pump and probe ultrashort pulses is controlled by delaying the pump beam to guarantee the stability of WLC generation during measurements. The pump beam can be used directly at 1.55eV (800nm) or double frequency at 3.1eV (400nm) with a BBO crystal. The 1kHz repetition signal from SDG is fed as a reference frequency to a mechanical chopper and modulates the pump beam at exactly half frequency (500Hz). The energy/pulse of the pump beam can be 100uJ and adjusted by a continuous density filter to measure the excitation intensity dependence of PM. The pump beam is usually focused on a sample at ~500 μm diameter, and beam walk must be checked before measurements.

The probe beam is used to generate broadband 1.2–2.8 eV WLC with a 1 mm thick sapphire plate; see details in the next section. The 800nm notch pass filters are used to block the fundamental pulses, and the WLC beam is focused on a sample at ~100um and overlaps with pump spot concentrically. The WLC allows us to measure the photomodulation in two modes: PM spectrum $\Delta T/T$ (λ) with a monochromator at fixed time and photoexcitation dynamics $\Delta T/T$ (t) with delay stage at fixed wavelength. Therefore, the WLC system is more efficient than the OPO system that only operates in the second mode.

The samples are measured in a cryostat that can reduce the temperature down to 80K/4K by transferring liquid nitrogen/helium and increase the temperature by an electrical heater.

2.3.2.4 WLC Generation

The white-light supercontinuum, so-called WLC, is a startling effect that converts one color laser into an intense, collimated, and coherent light source with broadband spanning the ultraviolet (UV) to the near infrared (NIR). WLC can be realized by the nonlinear interaction of an ultrafast pulse and a transparent material that causes the change of index of refraction in material with intensity. In our setup, the 800nm fundamental beam (<10mW) is focused on a 1mm sapphire plate and yields a broad spectrum from 450 nm (2.8eV) to 1050 nm (1.2eV) as shown in Figure 2.10 (a). The fundamental beam is blocked with a notch pass filter in measurements to avoid saturation of the photodetector.

Due to the group velocity dispersion, the higher energy pulses arrive at the sample earlier than those at lower energies, which is what we called “chirp”. Chirp doesn’t influence the dynamics measurements but would change the transient spectrum significantly at a fixed pump delay. A calibration program runs to compensate for the group velocity dispersion, which needs the real “zero” position at each probe wavelength.

A nonlinear optical process, two-photon absorption (TPA), is used to calibrate the zero position because there is no real intermediate electronic level involved in TPA and this makes the transition instantaneous. Figure 2.10 (b) shows TPA time-resolved response in DOOPPV film using 1.55 eV pump and various probe beams. It is clear to see that the PA signals follow the autocorrelation response in Figure 2.9 and different wavelengths reach maxima at different times. By plotting the wavelength vs. its zero position and fitting the plot with a second-order polynomial function as shown in Figure 2.10 (c), we get a series of coefficients that is further used in the program to calibrate the chirp effect.

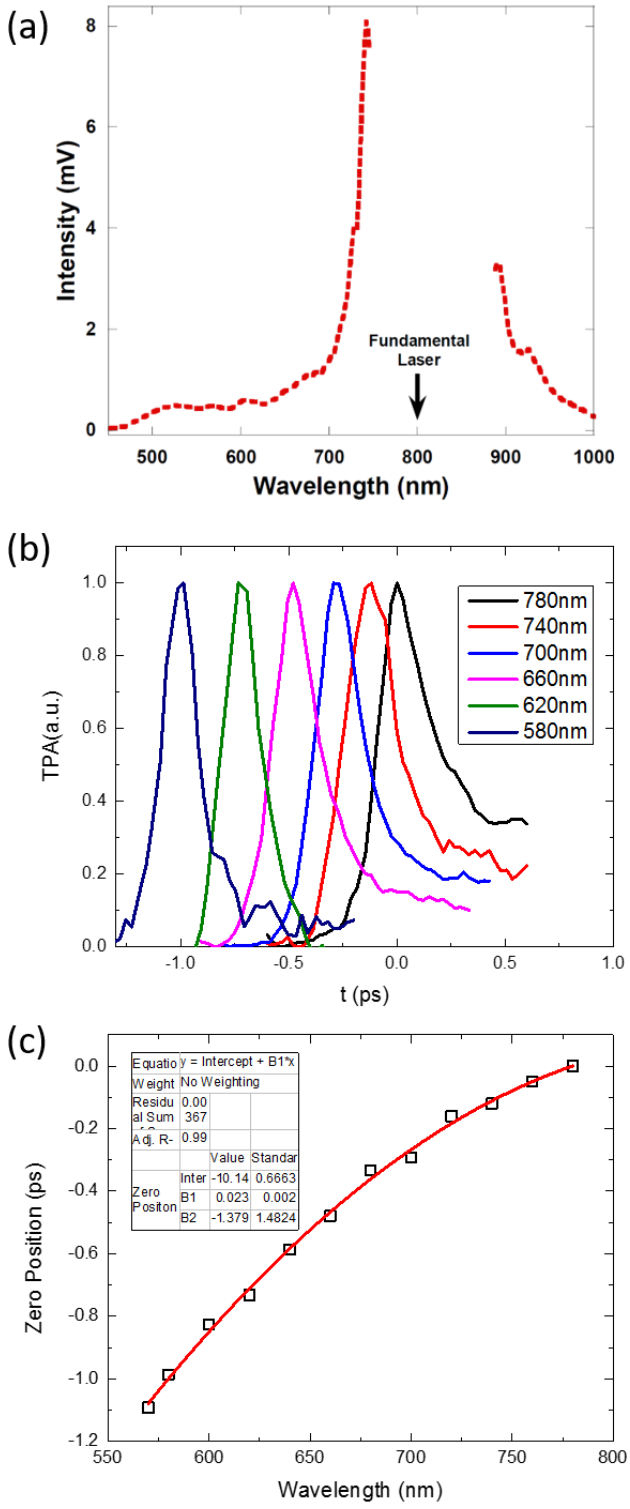

Figure 2.10. Characterization of white light continuum (WLC) source. (a) Spectrum of WLC generated by 800 nm fundamental laser. (b) Chirp of WLC at different wavelength measured by two-photon absorption in DOOPPV polymer pumped at 1.55eV. (c) Chirp of WLC against wavelength fitted with second-order polynomial function.

2.3.3 Polarization Memory (POM)

In pump-probe measurement, the polarization of the two beams can be parallel (||), perpendicular (⊥), or with a random angle to each other. To study polarization anisotropy dynamics in a sample, both the parallel and perpendicular components of the probe beam with respect to the pump beam should be analyzed and compared. In our OPO and WLC system, to rotate the pump beam so that its polarization has a 45^0 angle with respect to the probe beam is the simplest way to do the POM. The change of transmission in parallel $\Delta T_{\|}$ or perpendicular $\Delta T_{\perp}$ can therefore be measured with a a broad wavelength range of polarizer/analyzers before the detector, and the polarization memory is defined as $P(t) = (\Delta T_{\|} - \Delta T_{\perp})/(\Delta T_{\|} + \Delta T_{\perp})$ in thin films. POM study is helpful to understand the transient photoexcitation dynamics within the sample and its transient dipole moment reorientation.

2.4 Other Optical Measurement Systems and Techniques

2.4.1 Steady-State Photoinduced Absorption (PA)

For the steady-state photoluminescence (PL) and PA measurements, we use a standard cw pump/probe photo-modulation setup as shown in Figure 2.11. The samples are photoexcited by a modulated laser beam from different pump sources (laser or UV lamp), whereas the probe beam is extracted from a tungsten incandescent lamp that covers the spectral range from 0.25 to 3 eV. The pump beam is blocked by a suitable filter before the probe wavelength is selected using a monochromator. Photoinduced absorption, $\Delta T/T$, is recorded with a phase-sensitive LIA technique. Typically, the $\Delta T/T$ signal sensitivity is of the order of 10^5.

This arrangement can be modified to other measurements such as PL by turning off

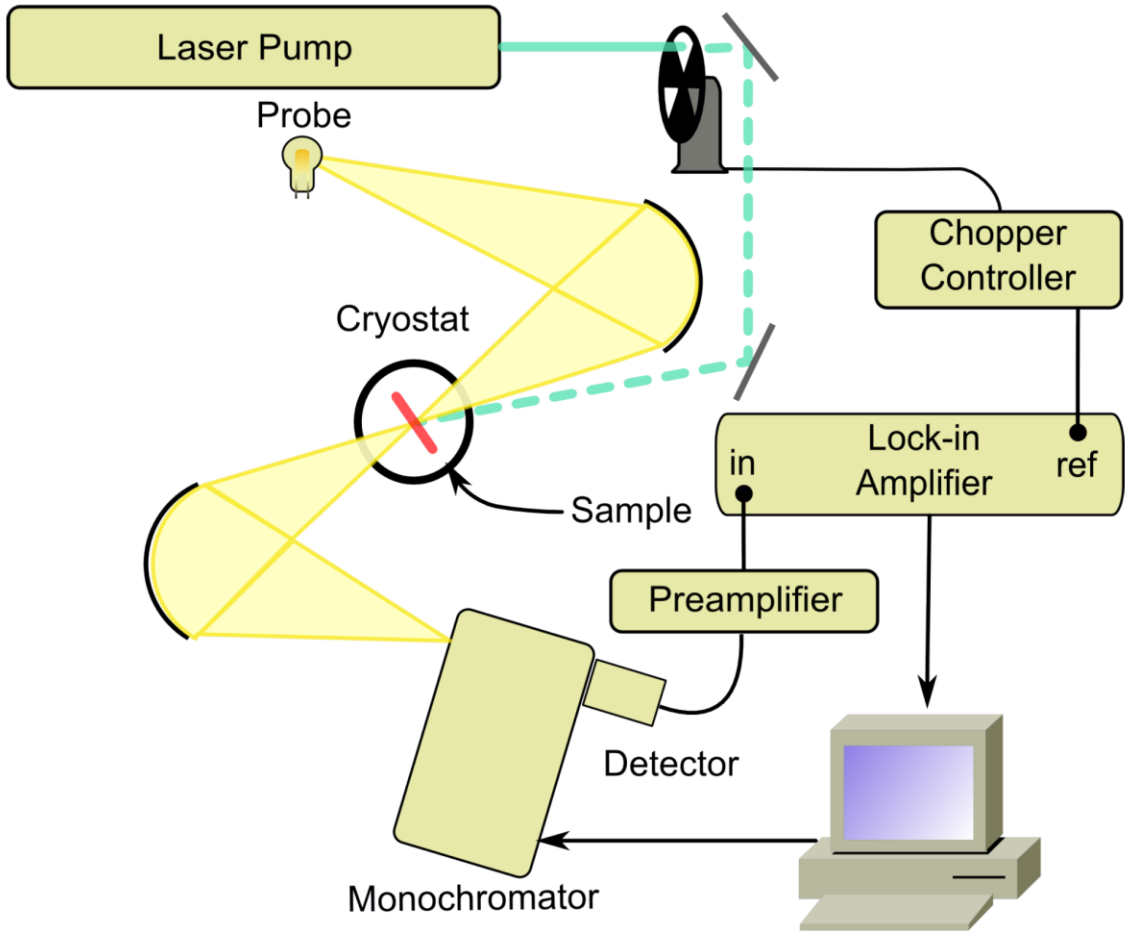

Figure 2.11. Experimental setup for steady-state PM measurement.

the probe source, frequency dependence PA by tuning the pump modulation, and magneto-PA (MPA) by adding a magnetic field. For the MPA measurements, the samples are placed in a temperature-controllable cryostat between two poles of an external magnetic field, B up to B=±2000 Gauss. By sweeping the magnetic field back and forth, we can obtain the PA magnetic field response defined as

$$MPA(B) = \frac{PA(B) - PA(0)}{|PA(0)|} \tag{2.18}$$

2.4.2 Excitation Dependence of Photoinduced Absorption (EXPA)

The EXPA measurement setup shown in Figure 2.12 is also based on the steady-state PA technique. In this technique, we fix the probe photon energy, $\hbar\omega$, at appropriate PA using band-pass filters, and vary the pump excitation photon energy, $E = \hbar\omega$, between 1.8 and 3.6 eV using a Xenon lamp and a monochromator equipped with an appropriate short-pass filter. The pump beam is modulated at frequency, f ~300 Hz, using a mechanical chopper. The resulting PA amplitude is monitored as a function of the pump $\hbar\omega$ having intensity, I(ω). To get the PA per absorbed photon, we normalize I(ω) by the photon energy ($\hbar\omega$) and the appropriate density of absorbed photons at ω that changes according to the optical density of the sample at ω. Subsequently, the EXPA(ω) spectrum can be normalized per absorbed photon by dividing by sample absorption:

$$EXPA(\omega) = \frac{\hbar\omega \cdot PA \cdot \xi(\omega)}{I_L(\omega)(1-R)(1-e^{-\alpha d})} \tag{2.19}$$

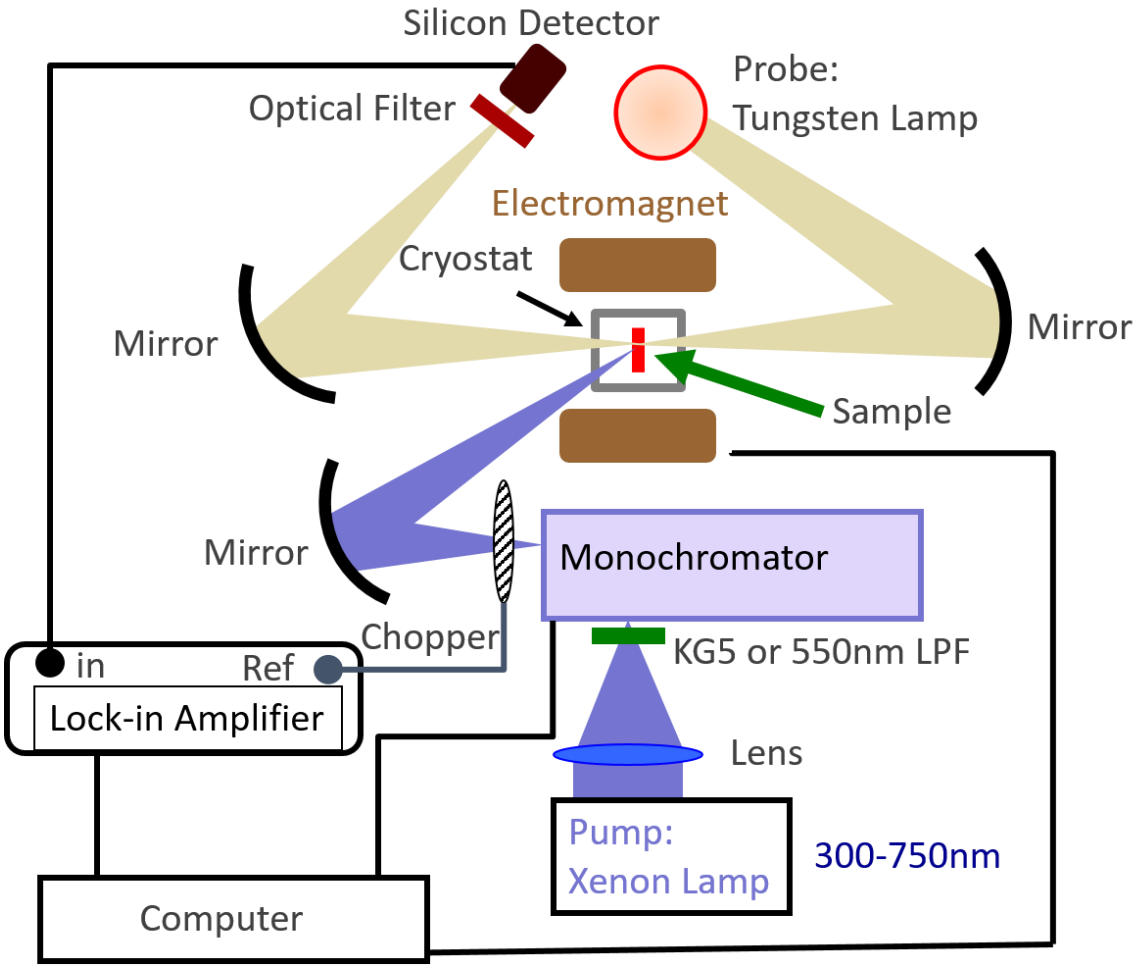

Figure 2.12. Experimental setup for excitation dependence of photoinduced absorption (EXPA) measurements.

in which $\xi(\omega)$ is the system response including detector, monochromator, etc., α is the absorption coefficient at ω, and d is the film thickness. An electro-magnet can also be added to the setup to measure the corresponding magnetic field effect (MEF) at certain pump energy.

2.4.3 Electroabsorption (EA)

The electroabsorption (EA) measuring changes in the absorption spectrum as a function of an applied electric field is a very important method to study optical energy levels in a sample, and has been used extensively to understand the excited states energy and related transitions. The EA signal is proportional to the imaginary part of the third-order nonlinear susceptibility χ^3 [57].

$$\frac{\Delta T}{T} \cong -\Delta\alpha d = \frac{4\pi\omega}{nc} Im[\chi^3(-\omega;\omega,0,0)]F^2 d \qquad (2.20)$$

in which *F* is the applied electric field, *d* and *n* are film thickness and refractive index, respectively. The modulation frequency of the electric field, *f*, should be set much lower than the optical frequency.

The two basic manifestations exist in EA spectrum, namely the Stark effect, which originates from mixing of discrete statese by changing the polarizability of excited states, and the Franz-Keldysh (FK) effect, which arises from acceleration of a free particle by the electric field through a continuum of states. The FK effect requires high mobility and large spatial coherence over tens of unit cells. The Stark effect, on the other hand, is observed in many materials as redshift of the fundamental excitonic transition.

EA spectroscopy of bulk samples often accesses the polarizability and the quadratic field response. Linear Stark shifts in isotropic bulk materials usually average out because the permanent dipole required for the effect cancels [150]. Confined excitons exhibit a quadratic Stark effect, where the EA signal scales with F^2 and proportional to the derivative of the absorption with respect to the photon energy ($d\alpha=dE$). In contrast, the EA of the continuum band scales with $F^{1/3}$ and shows FK-type oscillation in energy [151].

For the experimental EA measurements, we fabricate thin film samples on a substrate with patterned metallic electrodes. As shown in Figure 2.13 (a), the EA substrate consisted of two interdigitated sets of a few hundred of 10 μm wide gold electrodes, which are patterned on a sapphire substrate. The device is placed in a cryostat for low-temperature measurements.

By applying a potential, V, to the electrodes, a typical electric field, $F \sim 10^5$ Volt/cm, can be easily generated with V = 300 Volts and f = 1 kHz parallel to the film. For probing the EA spectrum, we use an incandescent light source from a Xenon (Xe) lamp, which is dispersed through a monochromator, focused on the sample, and detected by a UV-enhanced silicon photodiode. If a sample is not preferentially aligned with respect to the electrodes, the modulation ΔT of the transmission T is expected to be the same for positive and negative F. Thus, the EA signal occurs, and is measured at twice the frequency ($2f$) of the applied field, $F(f)$, and EA signals at the fundamental frequency f and $3f$ are usually absent. We can therefore measure the changes, ΔT, in the transmission spectrum, T, using a lock-in amplifier, set to twice the frequency ($2f$) of the applied field. The absence of an EA signal at f or $3f$ should be verified. ΔT and T spectra are measured separately using a Si photodiode and the EA spectrum is obtained from the ratio $\Delta T/T$.

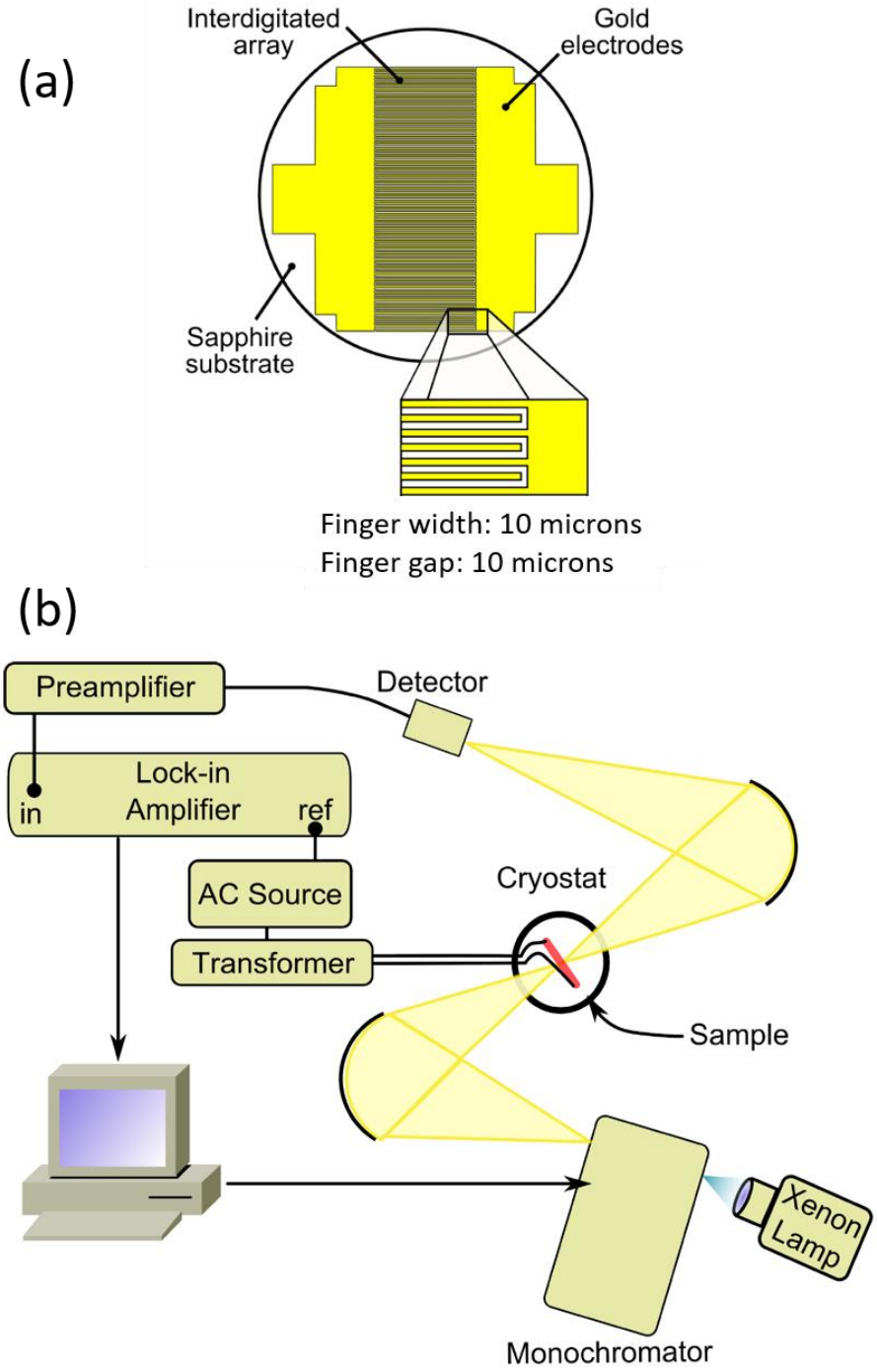

Figure 2.13 Experimental apparatus for electroabsorption spectroscopy (a) Interpenetrating finger electrode design for substrates used for EA measurements. (b) Experimental configuration.

2.4.4 Photoluminescence Quantum Efficiency (PLQE)

The photoluminescence quantum efficiency (PLQE) of luminescent materials is defined as the ratio of number of emitted photons/absorbed photons, and provides information about radiative versus nonradiative channels. Figure 2.14 shows the experimental setup for measuring the PLQE. A laser beam modulated by a mechanical chopper enters the integrating sphere (IS) that distributes and reflects light homogeneously. The sample is placed in the path of the light inside the IS, and the emission is collected by a solid-state detector. The PLQE can be then calculated using the following equation:

$$PLQE = \frac{I_{PL} - (R+T)I_{PL,corr}}{(1-R-T)I_L}\frac{D_L}{D_{PL}}\frac{S_L}{S_{PL}}\frac{E_L}{E_{PL}}\frac{1}{T_F(PL)} \tag{2.21}$$

The first term includes the intensities that need to be measured and the last four terms are the measured system corrections to eliminate the contribution to the collected light emission by spurious photons that excite the sample indirectly (due to reflection from the IS walls). The three intensities are I_L, the reflected laser intensity without the sample; I_{PL}, the reflected, uncorrected PL intensity when the sample is in the path of the excitation laser; and a correction term $I_{PL,corr}$, the reflected PL intensity when the sample is not in the path of laser. The *D, S, E* terms indicate the photodetector sensitivity, IS sensitivity, and photon energy at the laser (L) and PL wavelengths, respectively, and $T_F(PL)$ is the transmission of the optical long pass filter employed in the measurement at the PL wavelength.

The sample should be thick enough to keep *T* small, but not too thick to keep self-

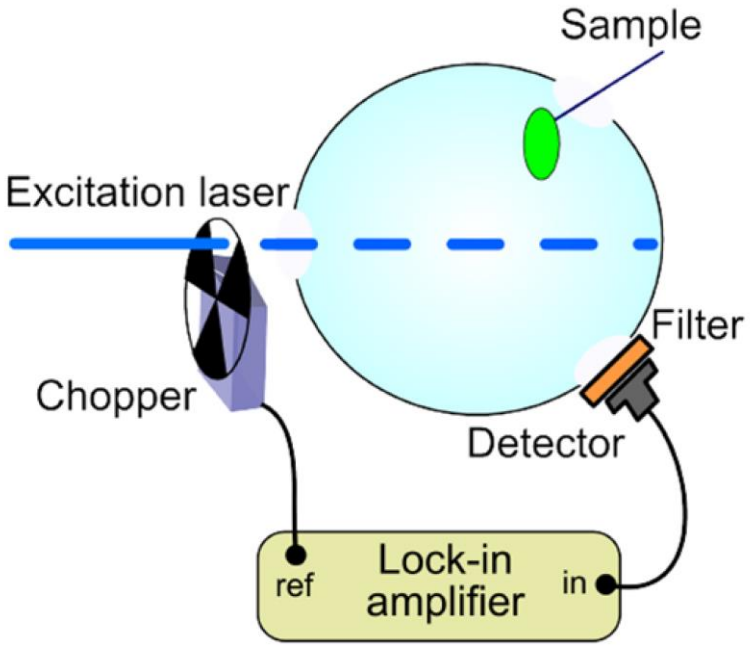

Figure 2.14. Experimental setup for the measurement of photoluminescence quantum efficiency (PLQE).

absorption of the PL small (especially if the absorption and PL spectra significantly overlap). It is recommended to use films with OD of 1 to 2 at the laser wavelength.

The radiative lifetime of the singlet exciton can be calculated by the relation

$$\tau_{rad} = \frac{\tau_{exc}}{PLQE} \tag{2.22}$$

in which the exciton lifetime τ_{exc} can be measured by transient photomodulation as discussed in Section 2.2. The radiative lifetime of a singlet exciton is usually of the order of a nanosecond.

CHAPTER 3

ULTRAFAST SPECTROSCOPY OF PHOTOEXCITATIONS IN THREE-DIMENSIONAL (3D) ORGANOMETAL TRIHALIDE PEROVSKITES

In the present chapter, we studied the ultrafast transient response of photoexcitations in a series of three-dimensional (3D) perovskite films using polarized broadband pump-probe spectroscopy, which unravels the branching ratio between photogenerated carriers and excitons, a key factor for the optoelectronic applications. At T=300K, we found both photogenerated carriers and excitons in $MAPbI_3$ with above-gap excitation, but only carriers with below-gap excitation. When the temperature of the sample was reduced below 160K, a clear phase transition from tetragonal to orthorhombic has been observed in $MAPbI_3$ as well as a dramatic increase in decay dynamics indicating the change of the ratio between carriers and excitons. In contrast, all bands in $MAPbI_{1.1}Br_{1.9}$ and $MAPbI_{3-x}Cl_x$ share the same dynamics, and are therefore due to the same species, photogenerated excitons. The transient photoinduced polarization memory (POM) for both excitons and photocarriers as well as the steady-state photoluminescence (PL) emission have been observed in $MAPbI_3$, but not in $MAPbI_{1.1}Br_{1.9}$ and $MAPbI_{3-x}Cl_x$ because they possess cubic symmetry at T=300K. The estimated long excitons diffusion length (~150 nm) in $MAPbI_3$ opens up the possibility of photocarriers generation at interfaces and grain boundaries even when the exciton binding energy is large compared to k_BT. The optical

and magnetic properties affected by nano-scale crystal size distribution in 3D perovskite films have also been studied, which would be beneficial for lasing and spintronics applications of these semiconductors.

3.1 Introduction

The organic/inorganic hybrid semiconductors methyl-ammonium (CH_3NH_3; MA) lead halide perovskites, $MAPbX_3$ (where X stands for halide), have recently emerged as one of the most promising classes of contenders for photovoltaic (PV) devices as discussed in Chapter 1. Initially, the hybrid perovskite solar cell was developed using the concept of a nano-structured excitonic solar cell [15]. However, more recently, it has been demonstrated that these solar cells are capable of operating in planar heterojunction configuration, namely as a solid absorber layer sandwiched in between n- and p-type charge selective contacts. This points to photogenerated free carriers as the dominant primary photoexcitations underlying the effective photovoltaic effect in these materials [17]. Despite the stunning advance achieved in device applications, several fundamental properties of the photoexcitations in the hybrid perovskites remain unclear, and this hampers further development of optoelectronic applications. For example, the binding energy of the excitons (E_b) in the prototype material, $MAPbI_3$, has been reported to be in the energy range from 10 to 55 meV [67-72], with lower values reported in more recent reports [64, 71-72]. In a recent estimation of E_b in $MAPbI_3$ using magneto-absorption at very high magnetic fields, E_b was found to be ~16 meV [72] at low temperature (in the temperature range in which this perovskite takes on the orthorhombic crystal phase); however, at room temperature (in the tetragonal phase), E_b was measured to be only a

few meV. In another analysis of the temperature-dependent absorption, it was concluded that E_b ranges from 30 meV at 13K to 6 meV at room temperature [67]. In contrast, E_b in another chemically modified hybrid perovskite, $MAPbBr_3$, has been reported to be ~100 meV [70-71]. Therefore, the organic lead halide perovskites form a unique system for studying the relation between Wannier-type excitons and free carriers [58-59]. We note that E_b is the dominant factor that determines the branching ratio of photocarriers/excitons and thus is one of the main ingredients for optoelectronic applications of the hybrid perovskites; for example, it determines whether a particular perovskite compound is more suited for PV or LED applications. As discussed in Section 1.3, the different PA bands for carriers and excitons may be used to thoroughly study their characteristic properties [76-83]. However, one needs to apply broadband spectroscopy to access their separate PA bands in the 'pump-probe' photomodulation spectrum, as we have done here.

Moreover, while the ease and versatility of fabrication afforded by organic lead halide perovskites provides great advantages, placing them as active competitors with π-conjugated polymers and colloidal quantum dots for future components in low-cost lighting and Si-compatible micro-photonics, optoelectronic properties of perovskites have been shown to depend sensitively on the underlying morphology [92-93], such as crystal quality and grain boundaries. Thus, an investigation of how morphology determines the device properties is also warranted to realize the potential application of these materials.

In this chapter, we first studied the ultrafast transient response of photoexcitations in thin films of three different hybrid perovskites at room temperature, namely $MAPbI_3$, $MAPbI_{1.1}Br_{1.9}$, and $MAPbI_{3-x}Cl_x$ using the pump-probe photomodulation spectroscopy in

a broad spectral range from mid-IR to visible (namely 0.3-2.7 eV) with 300 fs time resolution. We demonstrate the existence of photogenerated exciton/carrier duality response in these three perovskites. With above-gap pulse excitation, we found in $MAPbI_3$ both photogenerated carriers and excitons, but only carriers are photogenerated when excited below the gap (i.e., into the film's Urbach absorption tail). When temperature was reduced below 160K, a clear phase transition from tetragonal to orthorhombic has been obeserved in $MAPbI_3$ as well as a dramatic increase in decay dynamics indicating a larger contribution of excitons recombination in the orthorhombic phase. In $MAPbI_{1.1}Br_{1.9}$ and $MAPbI_{3-x}Cl_x$, however, we only detected photogenerated excitons, consistent with the larger exciton binding energy E_b in these hybrid perovskites. Our results show that a broadband ultrafast optical probe is crucial for revealing the characteristic hybrid perovskite photophysics properties. We also found transient photoinduced polarization memory (POM) for both excitons and photocarriers PA bands in $MAPbI_3$, as well as in cw photoluminescence (PL) emission from this compound; the POM originates from the tetragonal crystal anisotropy of this hybrid perovskite at RT. On the contrary, $MAPbI_{1.1}Br_{1.9}$ and $MAPbI_{3-x}Cl_x$ with $x>0.6$ lack optical anisotropy due to their cubic crystal structure at RT, and thus do not show photoinduced POM. From the POM decay dynamics and nano-crystallites size distribution in the $MAPbI_3$ film, we estimate the exciton diffusion constant to be $D=0.01$ cm^2s^{-1}, which corresponds to a typical exciton diffusion length of ~150 nm in films of this perovskite.

We then investigated the optical properties and excited state dynamics of $MAPbBr_3$ films of markedly different nano-morphologies, and obtained higher PL quantum efficiency (PLQE) that results from a reduced non-radiative decay in the smaller

crystalline grains, as revealed by the excited state dynamics. To extend the morphology studies in the 3D perovskites, we further measured the ps dynamics and magneto-photoluminescence (MPL) on the same film, respectively, and obtained shorter average lifetimes in those films with broader and weaker MPL(B) response, which would be beneficial for the spin-related applications of perovskites.

3.2 Materials

3.2.1 One-Step Spin-Coating $MAPbX_3$ Films

The one-step spin-coating technique introduced in Chapter 2 was used to fabricate the organometal trihalide perovskite ($MAPbX_3$) films for the photoexcitations study. The crystal structure is shown in Figure 3.1 (a) as discussed in detail in Chapter 2.

The $MAPbI_3$ precursor solution was made by mixing 1.16 g PbI_2 (Sigma Aldrich) with 0.4 g CH_3NH_3I (or 0.92 g $PbBr_2$ with 0.4 g CH_3NH_3I, and 0.7 g $PbCl_2$ with 1.2 g CH_3NH_3I for $MAPbI_{1.1}Br_{1.9}$ and $MAPbI_{3-x}Cl_x$, respectively) (Sigma Aldrich) in anhydrous N, N-Dimethylformamide (DMF, 3 ml), and allowed to stir overnight on a hot plate at 60°C. A bright yellow solution was obtained in all cases and cooled down to room temperature. Glass slides or CaF_2 substrates were pretreated with O_2 plasma for 30 mins., so that the hydrophilic surface could allow for more uniform perovskite layers. The precursor solution was then spin coated at 2000 RPM for 30 seconds, and annealed at ~100°C for 15 mins. (120 mins. for $MAPbI_{3-x}Cl_x$ due to its slower crystallization).

The $MAPbI_{3-x}Cl_x$ pristine films were also grown on sapphire substrates and annealed at different temperatures for varying the film morphology and MPL measurements. All processes were done in a nitrogen glovebox with O_2 and $H_2O < 1$ ppm.

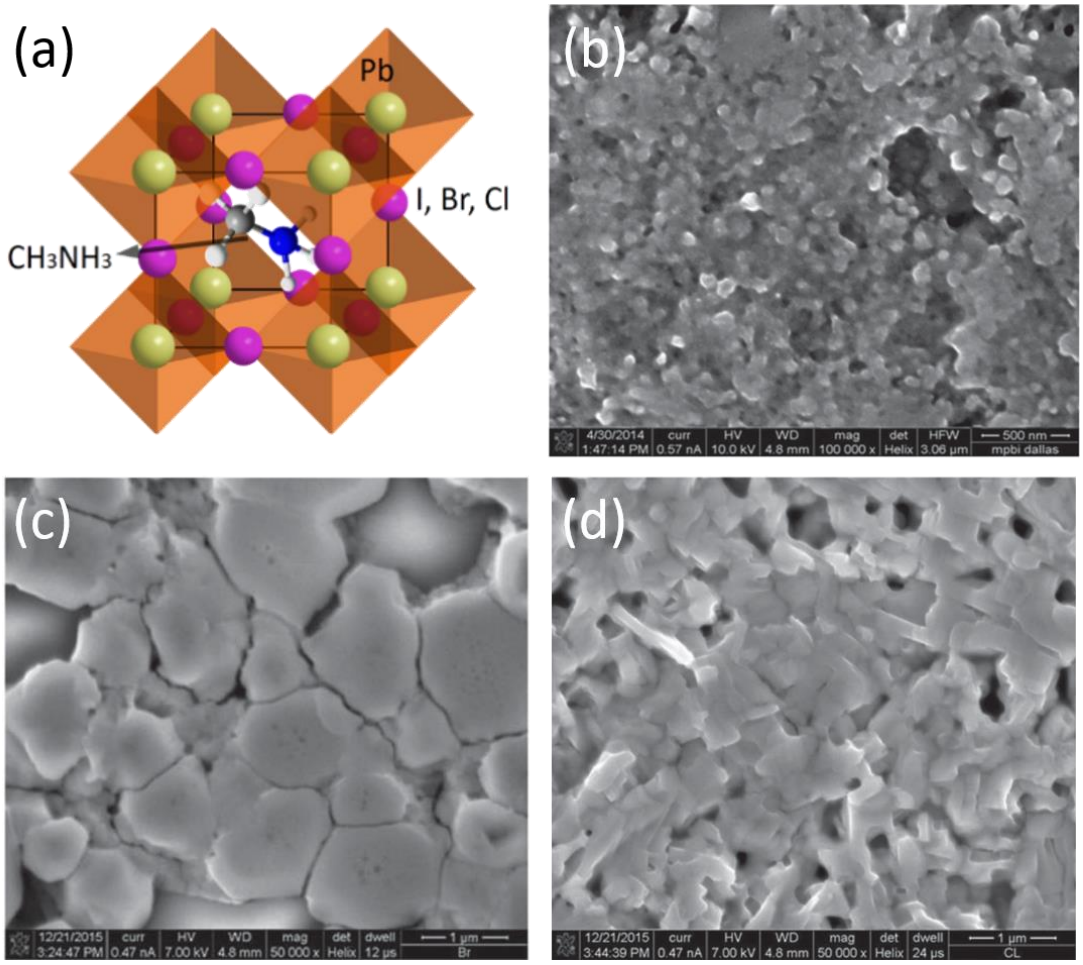

Figure 3.1. $MAPbX_3$ perovskite films. (a) Crystal structure of $MAPbI_3$ films. (b) SEM image of (b) $MAPbI_3$ with scale of 500 nm for grain size measurements, (c) $MAPbI_{1.1}Br_{1.9}$, and (d) SEM image of $MAPbI_{3-x}Cl_x$ with scale of 1 μm for grain size measurements.

Smooth perovskite films were obtained and the scanning electron microscope (SEM) images in Figure 3.1 (b) to (d) show the existence of crystalline domains in all the three perovskite films with different grain size. The grain sizes of $MAPbI_3$ will be calculated and discussed in detail later in this chapter.

Figure 3.2 shows the SEM image of the four $MAPbI_{3-x}Cl_x$ films used for MPL and picosecond dynamics characterization, which were annealed at 90, 110, 120, and 130 ºC, respectively. The change of crystal quality and grain size can be clearly observed. This may serve as an explanation for the structure-property relation between the perovskite film morphology and the e-h pair lifetime, which will be discussed later in this chapter.

3.2.2 Nanocrystal-Pining $MAPbBr_3$ Films

The $MAPbBr_3$ films were fabricated by spin-coating from a precursor solution in DMSO (Dimethyl sulfoxide). The 0.5 mol/ml solution was made from MABr (Sigma Aldrich) and $PbBr_2$ (Sigma Aldrich) with a molar ration of 1.05:1. The excess amount of MABr could increase the solubility and consequently slow down the crystallization process, as well as minimize the photoluminescence quenching by Pb atom impurities [122]. The solution was then spin-coated on to O_2 plasma cleaned glass slides with a speed of 3000 rpm. To control the crystalline morphology of $MAPbBr_3$ films, the anti-solvent ($CHCl_3$) treatment was applied during the spin-coating process, which is referred to as nanocrystal-pinning (NCP) [122] as discussed in Chapter 2.

Figure 3.3 shows optical and SEM images of both NCP and as-cast $MAPbBr_3$ films. It is clear to see that the large crystallites that form from the usual solvent evaporation process during spin coating are significantly reduced when the crystallization kinetics are

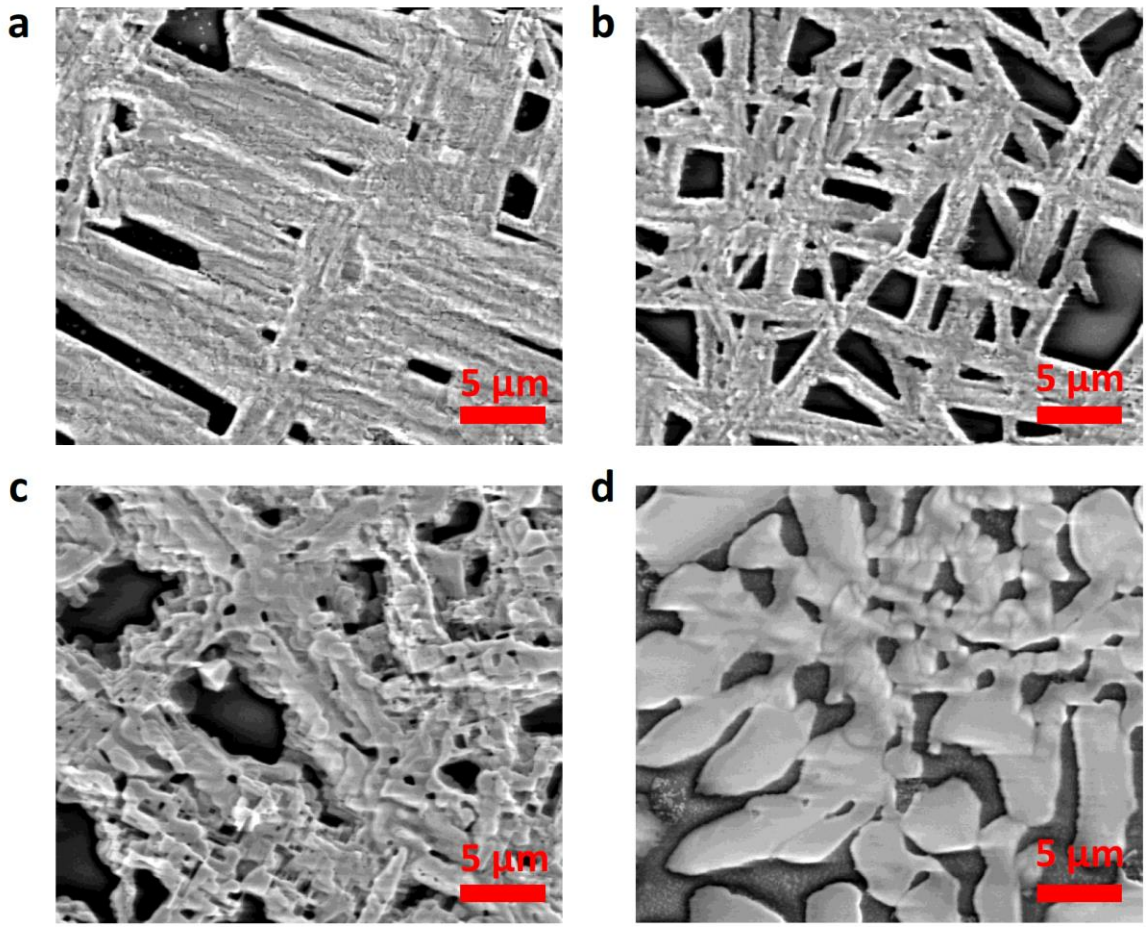

Figure 3.2. SEM images of various $MAPbI_{3-x}Cl_x$ films for morphology dependence of MPL and ps dynamics characterization. (a) to (d), Microscopic morphology of films 1-4 (corresponding to Fig. 3.19 (c) and (d)), which were annealed at 90, 110, 120, and 130 ºC, respectively. The change of crystal quality and grain size can be clearly observed.

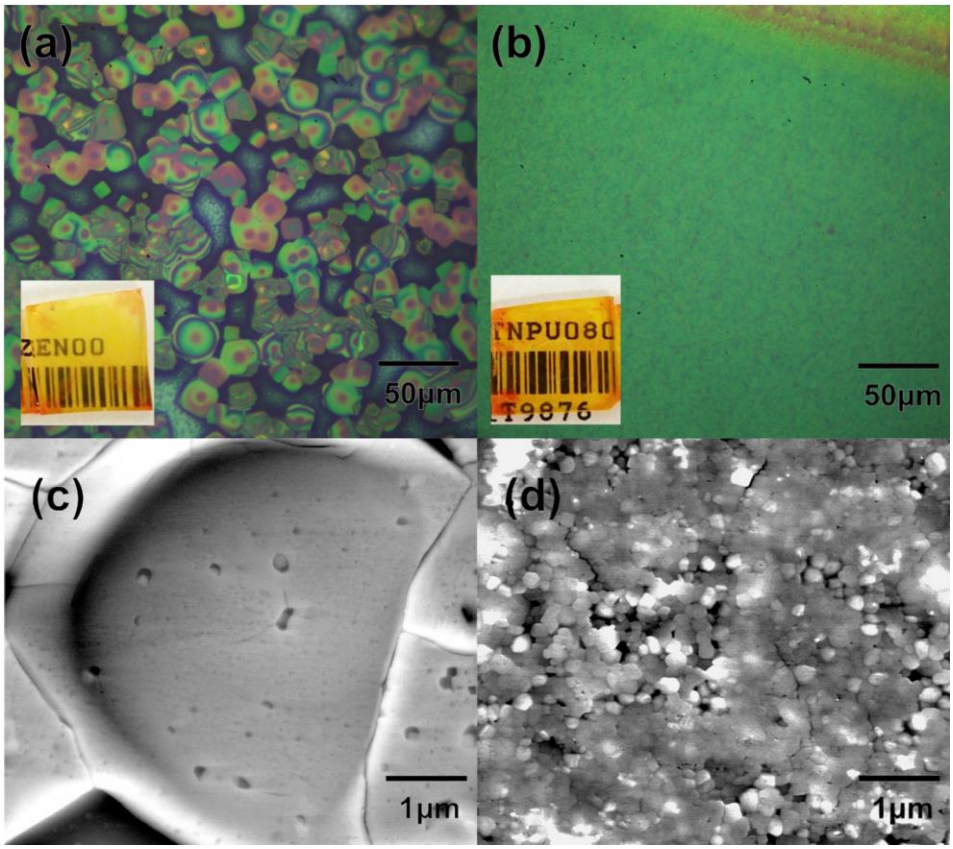

Figure 3.3. Morphology of $MAPbBr_3$ films. (a) and (b) Optical microscopic and (c) and (d) SEM images of $MAPbBr_3$ films without (a) and (c) and with NCP treatment (b) and (d), respectively. The insets to (a) and (b) show macroscopic images of the grown films.

increased by the application of the $CHCl_3$ solvent. The resulting films have much smoother surfaces compared to those of as-cast films. As shown in the optical microscopic images (Figures 3.3 (a) and (b)), the as-cast film contains isolated plate-like microcrystals with widely-distributed sizes from several to ~100 μm. In comparison, the NCP film shows smooth and uniform surfaces under the microscope, which indicates better coverage and smaller sizes of $MAPbBr_3$ nanocrystals. A closer look at these films from SEM images in Figures 3.3 (c) and (d) reveals the crystallite sizes (<100 nm) in the NCP film, which is 2–3 orders of magnitude smaller than that in the as-cast films.

3.3 Transient Photomodulation Spectroscopy and Polarization Memory Dynamics in $MAPbI_3$ Film

3.3.1 Above Bandgap Excitation

Figure 3.4 summarizes the picosecond transient photomodulation (PM) spectroscopy results of a $MAPbI_3$ film with above-gap excitation (~3.1eV) at room temperature (RT). At t=0, the PM spectrum contains three main spectral features (Figure 3.4 (a)). In the visible/near-IR range, there is a large PB band at ~1.65 eV (PB) which is correlated with a neighboring PA band (PA_2) that extends to larger energy; both bands share the same decay dynamics. PB and PA_2 bands have been recently observed in the picosecond and nanosecond time domains, as well as in continuous wave (cw) PM spectroscopy [16-17, 26, 79-80]. Although the origin of these bands is still under debate, it has been widely accepted that PB is photo-bleaching due to band-filling effect caused by the photocarriers [16-17, 26, 79-80]; but the origin of PA_2 is still debated. We note, however, that excitons may also cause the PB-PA_2 spectral feature [79-80]. We propose here an alternative explanation for these two correlated bands, and other similar bands at photon energies above these.

It is known from band structure calculations that include e-h interaction and spin-orbit coupling that there are two types of excitons in the hybrid perovskites, namely optically allowed (having irreducible representation, IRR; Γ_4) and optically forbidden (IRR; Γ_1) from the ground state (IRR; Γ_1). The energies of these excitons are very close to each other [69] (E_1 in Figure 3.4 (a) inset). The pump excitation is not absorbed homogeneously in the film, which is especially true for the hybrid perovskites known to have larger absorption coefficient, α. Therefore, the initial photoexcitations density varies

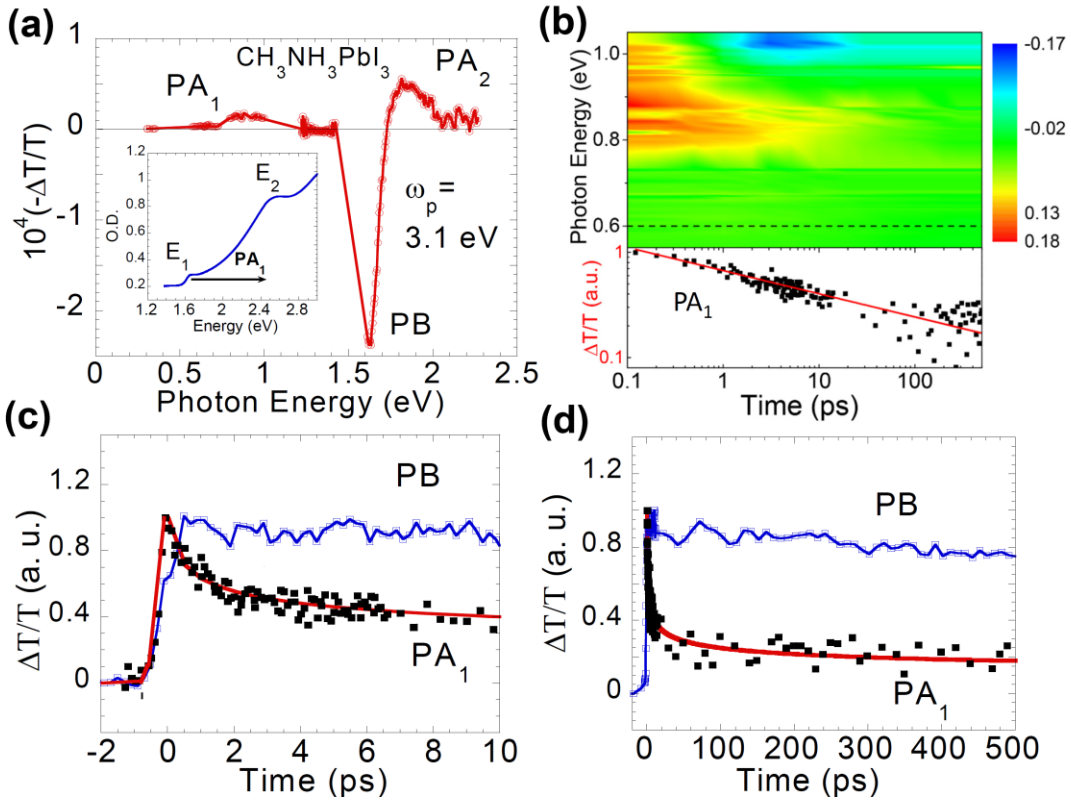

Figure 3.4. Room temperature photomodulation (PM) spectroscopy of a $MAPbI_3$ film excited at 3.1eV. (a) Transient PM spectrum measured at t = 0 ps; various bands are assigned. The inset shows the film absorption spectrum, where two different excitons, E_1 and E_2, and the interband PA_1 transition between them are assigned. (b) PA_1 decay dynamics plotted with false colors (upper panel), and on double logarithmic scale (lower panel) measured at 0.6 eV. The line through the data points is a power law decay in the form of $(t/t_0)^{-\alpha}$, with α = 0.21. (c) and (d) Decay dynamics of PB and PA_1 bands up to 10 ps and 500 ps, respectively. The red lines through the data points are calculated using the same power law decay described in (b).

with z away from the film's surface according to the density of the absorbed photons in the form of $exp(-z/z_0)$, where z_0 is the pump laser penetration depth ($z_0 \sim 1/\alpha_L$ at the laser frequency). These photoexcitations create strain in the film due to the change in the deformation potential between the ground and excited states, which also varies with z following the same exponential form as that of the absorbed laser intensity. In turn, the photoinduced static strain associated with the photoexcitations, being spatially inhomogeneous, breaks the inversion symmetry in the illuminated sample, in the same way as does an applied electric field [152]. Consequently, some oscillator strength is taken from the allowed exciton (Γ_4) and given to the forbidden exciton (Γ_1) that lies above the former, resulting in a derivative-like feature, or PB and PA_2 correlated feature. The virtue of this explanation is that the derivative-like optical feature is generated regardless of the photoexcitation type; free carriers and excitons may form *similar* derivative-like feature at the band-edge. Moreover, higher-lying excitons that are associated with other transitions into higher energy continuum bands may also show similar optical features (not shown in Figure 3.4 (a)); this may explain the existence of a derivative-like feature known to exist at ~ 2.3 eV [153], as discussed below.

The third feature in the transient PM spectrum of $MAPbI_3$ is a prominent PA band in the mid-IR range that peaks at ~0.8eV (PA_1; Figure 3.4 (a) and (b)); this band has been observed and reported recently [60-61]; however, here we present its in-depth study. PA_1 decay dynamics are shown in Figure 3.4 (b) and compared to that of the PB feature at the band-edge in Figure 3.4 (c) and (d), at comparable pump intensities. It is clearly seen that the decay dynamics are very different for these two bands, indicating that they originate from two different photoexcitations. We also see (Figure 3.4 (c)) a delay of ~1 ps at the

onset of PB(t) transient, which is not seen in $PA_1(t)$ dynamics. PB(t) dynamics in a $MAPbI_3$ film at various excitation intensities are shown in Figure 3.5. The linear excitation dependence and the excitation independent decay show monomolecular kinetics.

We thus conclude that PA_1 is generated instantaneously within our time resolution, whereas PB generation is delayed. Therefore, PA_1 and PB originate from two different species, suggesting the coexistence of two types of primary photoexcitations in this hybrid perovskite at RT.

Being a band-like transition, PA_1 cannot be explained as due to FCA of thermalized photocarriers, since such a spectrum does not contain a pronounced band as discussed in Chapter 1. In addition, the FCA spectrum of photocarriers in the perovskites should be mostly pronounced for probe energy below ~ 60meV, which is outside the probe spectral range here. We therefore assign PA_1 as due to photogenerated *excitons*. There are two clear exciton transitions in $MAPbI_3$ absorption spectrum, namely E_1 at 1.66 eV and E_2 at 2.48 eV as shown in Figure 3.4 (a) inset [69]. These two transitions are separated by about 0.8 eV that is the same as PA_1 peak, which strongly indicates that PA_1 may be an optical transition from photogenerated excitons at E_1 into excitons at E_2, similar to the transient PA between two adjacent bands in nanotubes [76], as shown in Figure 3.4 (b). In fact, from band structure calculations that include electron-hole interaction [69], the allowed high-energy exciton (Γ_4) is accompanied by a forbidden exciton at even higher energies (Γ_3 and Γ_5) of which transitions from the lower lying exciton (Γ_4) are dipole allowed.

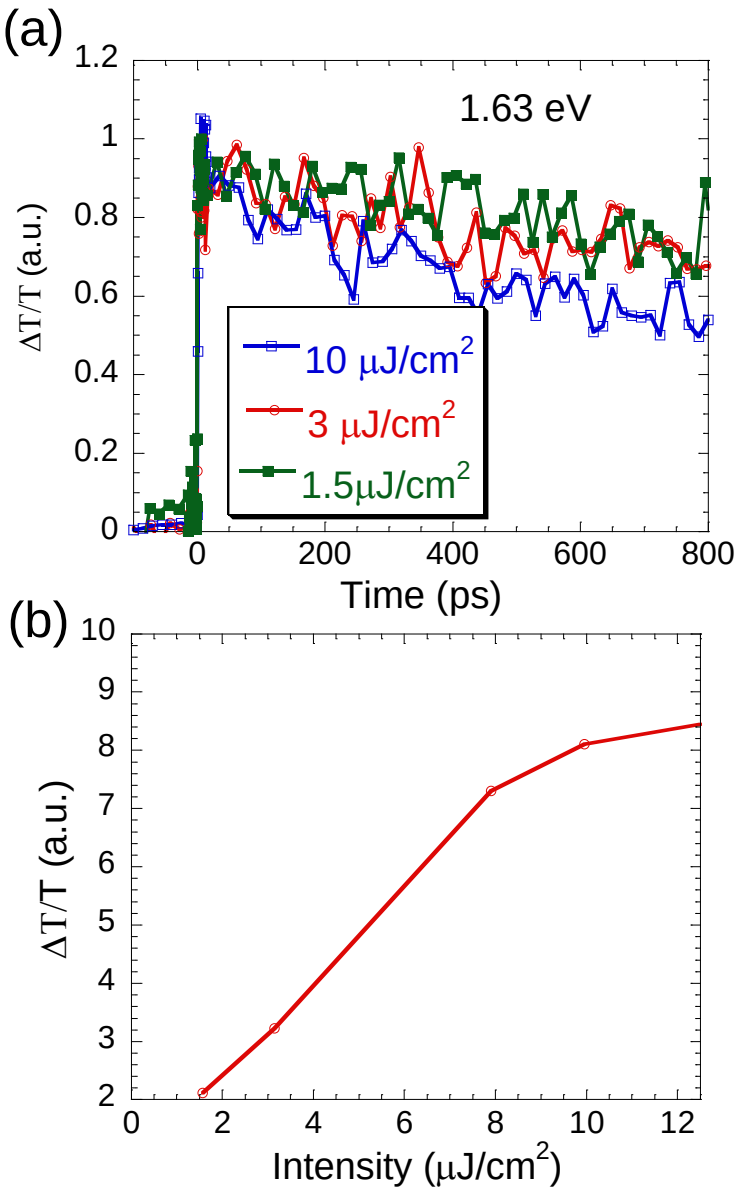

Figure 3.5. Pump excitation dependence of PM in $MAPbI_3$ films at 3.1eV. (a) PB(t) dynamics in a $MAPbI_3$ film at various excitation intensities. (b) $\Delta T/T$ at t=0 ps vs. pump excitation intensity. The linear excitation dependence and the excitation independent decay show monomolecular kinetics.

PA_1 appears to be instantaneously generated within the time resolution of the experiment of ~300 fs. This shows that the exciton excess energy thermalization rate, $R=\Delta E/\Delta t$, in the perovskite is quite large. The largest possible thermalization rate is: $R_{max}=h\nu^2$, where ν is a phonon frequency averaged over the phonon density of states in the material [156]. Since the hybrid perovskites also contain an organic moiety, namely the MA molecule, the available vibration frequencies may reach ~1500 cm^{-1} (C-N stretching vibration) and even ~3200 cm^{-1} (C-H and N-H stretching vibrations) [155]. If we take the average available phonon frequencies in the organic molecule at 2350 cm^{-1}, then R_{max} in the hybrid perovskites may be estimated to be as large as 20.5 eV ps^{-1}, which is similar to other organic semiconductors. The excess energy, ΔE, of excitons due to the pump excitation at 3.1 eV is ~1.5 eV; thus the exciton thermalization time, $\tau_{th}=\Delta E/R_{max} \approx$ 75 fs. This is below our experimental time resolution of ~300 fs, and explains the apparent instantaneous PA_1 response here.

It is interesting to compare the exciton thermalization time to that of photocarriers which is revealed via the PB formation time (Figure 3.4 (c)). Photocarriers first form hot charge plasma by e-e collisions, which is established much faster than their thermalization time caused by electron-phonon scattering. Subsequently the generated hot plasma cools down to the lattice temperature by emitting LO phonons via the relatively weak Froehlich interaction [156]. This usually takes a few picoseconds, which is in agreement with the PB formation time (Figure 3.4 (c)). We thus conclude that the different thermalization times of excitons and photocarriers fit well the formation times of PA_1 and PB, and this unravels the photoexcitations duality of this hybrid perovskite.

Figure 3.4 (b) (lower panel) shows that PA_1 decays as a power law, $(t/t_0)^{-\alpha}$, where α

~0.21. This explains the relatively fast decay of PA_1 seen in the first few picoseconds (Figure 3.4 (c)); it is simply a part of the power law decay, rather than fast photocarriers thermalization as advanced before [80]. This non-exponential PA_1 decay may originate either from a dispersive transport type process [157], where the exciton diffusion towards recombination centers is time dependent [158], or is due to a distribution, $g(\tau)$ of lifetimes, τ having a tail towards longer lifetimes of the form $\tau^{-(1+\alpha)}$ with $\alpha \sim 0.21$ [159].

As a consequence of our PA_1 assignment due to excitons, and based on the different decay dynamics of PA_1 and PB, we thus assign the PB/PA_2 feature as due to symmetry breaking caused by the spatially inhomogeneous photon absorption in the hybrid perovskite film, which leads to spatially inhomogeneous photogenerated free carriers in $MAPbI_3$. The larger PB feature in the spectrum can be explained as an additional contribution caused by ground state absorption bleaching. This assignment does not mean that the optical feature of PB/PA_2 is a signature of free carriers per se, since photogenerated excitons may also produce an optical modulation at the absorption edge (see below), based on the same process as that of free photocarriers, namely photoinduced spatially inhomogeneous strain. We thus conclude that the derivative-like feature at the band-edge may be produced by a symmetry breaking process, in addition to PB contribution caused by phase-space filling [160-161].

We also observed transient photoinduced dichroism for band PA_1 (Figure 3.6), namely $-\Delta T_{\parallel} \neq -\Delta T_{\perp}$, where $-\Delta T_{\parallel}$ ($-\Delta T_{\perp}$) is the PA measured for the pump-probe polarizations parallel (perpendicular) to each other [60-61]. The degree, P of 'linear polarization memory' (POM) is defined as $P(t) = (\Delta T_{\parallel} - \Delta T_{\perp})/(\Delta T_{\parallel} + \Delta T_{\perp})$ as discussed in Chapter 2. As clearly seen, P at t=0 [namely $P(0)$] is relatively small (we obtain $P(0) \approx$

0.11), but is clearly observable. The measured photoinduced dichroism indicates an underlying *anisotropic* crystal structure, which is consistent with the tetragonal Bravais lattice structure of $MAPbI_3$ at RT [162]. In order to best display the physics associated with the POM dynamics, we first fit $\Delta T_{\parallel}(t)$ and $\Delta T_{\perp}(t)$ decay dynamics using a power law form (see Figure 3.6). Subsequently, we calculated $P(t)$ from the fitting functions of $\Delta T_{\parallel}(t)$ and $\Delta T_{\perp}(t)$. We define the POM lifetime, $\tau(POM)$ as the time for $P(t)$ to decay to $P(0)/3$ value; consequently, we find $\tau(POM) \approx 150$ ps for PA_1.

We may understand the existence of POM in the pump/probe measurements as due to two successive optical transitions (Figure 3.6 inset). When linearly polarized light pulses are absorbed by the medium, the resulting photoexcitations may preserve (or 'memorize') certain information about the excitation optical field. This effect, the so-called 'polarization memory' as discussed in Chapter 2, may exist for longer time than the pulse duration. For pump-probe measurements, there are two incident plane waves: the pump beam at frequency ω_1 and the probe beam at frequency ω_2. A number of excited oscillators with resonance at ω_1 are generated upon absorption of the pump pulse. To describe the resulting PA, a model with a second oscillator attached to the first oscillator is introduced (Figure 3.6 inset), which describes two successive optical transitions in the system. The dipole mpoment of the second oscillator does not have to be in the same direction as that of the first oscillator, because the wave function of the excited state in the hybrid perovskites may be very different from that of the ground state due to the strong spin-orbit coupling in these materials [93]. The different direction of the induced dipole can be simply expressed by an angle, θ, between the two transitions as shown in Figure 3.6 inset.

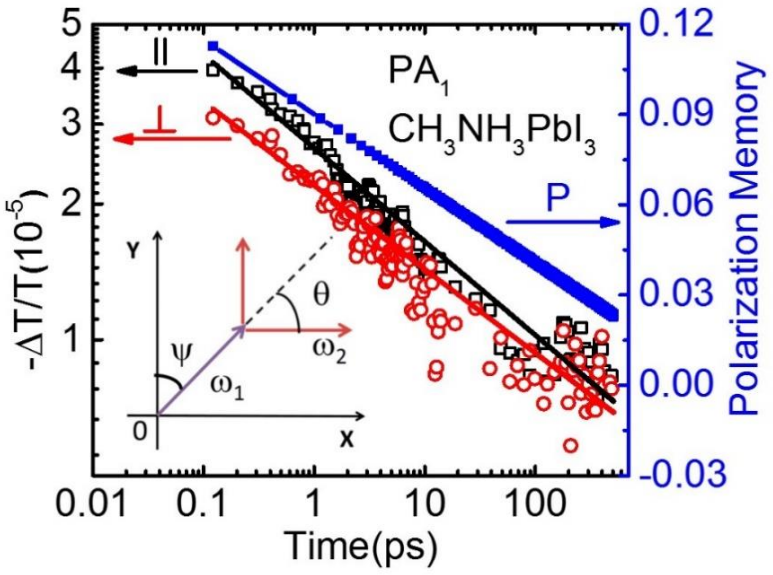

Figure 3.6 Polarization memory (POM) dynamics of PA_1 bands in $MAPbI_3$ film excited at 3.1eV, where $\Delta T_{\parallel}$, $\Delta T_{\perp}$, and POM(t) decay dynamics are shown. The back and red lines through the data points are fittings using power law decay $(t/t_0)^{-\alpha}$ with α=0.21 and α=0.19 for $\Delta T_{\parallel}$(t) (black) and $\Delta T_{\perp}$(t) (red), respectively. The POM response was calculated using these fits (see text). Inset: The pump-probe dipole approximation in a 2D medium that may help explain the POM in the PM spectrum.

When a dipole at ω_1 is excited in an anisotropic medium such as the hybrid perovskite grain having tetragonal symmetry, but with a random orientation, ψ with respect to the pump electric field, it can induce an absorption by a second dipole with ω_2 in two possible orientations, (ψ+θ) and (ψ-θ) [163]. Consequently, the PA components for the probe beam polarization in X and Y laboratory axes, namely ΔI_Y and ΔI_x may be expressed as:

$$\Delta T_y = <\Delta I_Y> = c\int_0^{2\pi} cos^2\psi[\cos^2(\theta+\psi)+\cos^2(\theta-\psi)]d\psi = c\pi\left(1+\frac{cos2\theta}{2}\right) \quad (3.1)$$

$$\Delta T_x = <\Delta I_X> = c\int_0^{2\pi} cos^2\psi[\sin^2(\theta+\psi)+\sin^2(\theta-\psi)]d\psi = c\pi\left(1-\frac{cos2\theta}{2}\right) \quad (3.2)$$

The polarization memory, *P*, in 2D is defined by the relation:

$$P = \frac{\Delta T_y - \Delta T_x}{\Delta T_y + \Delta T_x} \quad (3.3)$$

From Equation (3.1) to (3.3), we then get:

$$P(\theta) = \frac{cos(2\theta)}{2} \quad (3.4)$$

We note that if θ varies from 0 to π, P(θ) may vary between -0.5 to 0.5.

In an anisotropic crystalline environment, the exciton P(0) cannot be lost because the structure is rigid, and therefore, exciton diffusion would not change its polarization in space. However, the hybrid perovskite film is composed of crystalline grains in random orientations (see Figure 3.1 (a) for an SEM image); in fact, we obtain from the image an average crystalline grain size D_{ave}= 82 ± 22 nm as shown in Figure 3.7 (a). In this case, *P*(0) may change only if a photogenerated exciton reaches the crystalline grain boundary by diffusion, and then crosses to an adjacent crystalline grain having different orientation in space relative to that of the initial grain as in Figure 3.7 (b). Consequently, we may extract the exciton diffusion constant, *D* from *P*(t) decay, assuming that an exciton randomizes its initial dipole orientation with respect to the pump polarization when it crosses the initial grain boundary (Figure 3.7 (b)). This can be rationalized since the grain

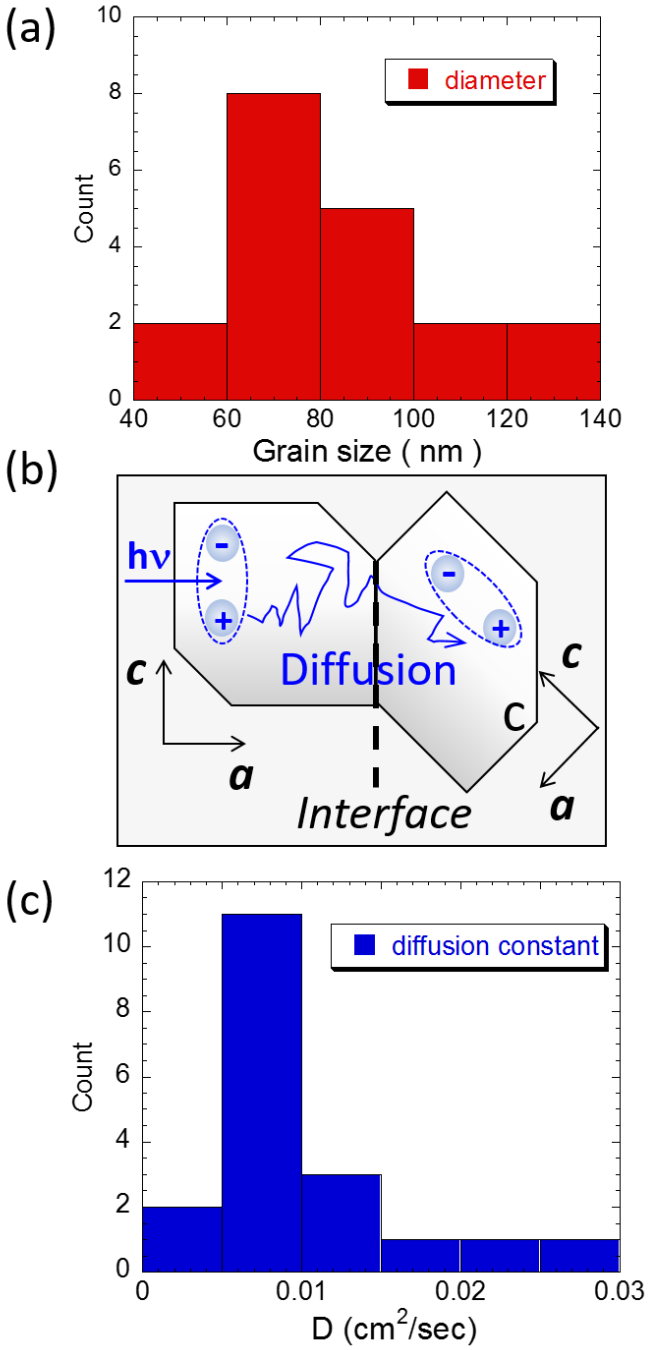

Figure 3.7. Exciton diffusion in $MAPbI_3$ films. (a) The obtained distribution of the grain size. (b) Schematic representation of the model used to analyze the POM(*t*) decay in the perovskite film. To lose the initial POM, a photogenerated exciton diffuses to the closest interface and crosses to a neighboring crystalline grain with different tetrahedral crystal orientation. (c) The average exciton diffusion constant calculated from Equation (3.6) and the size distribution in (b).

boundaries are oriented in all directions, given that the crystalline domains are arranged randomly in the 'as-grown' film. In addition, there may also be a disordered perovskite phase in between adjacent grains, in which a photogenerated exciton completely disorients. In this model, *P*(t) decay can be calculated based on the distribution in the exciton arrival times to the grain boundary, caused by a distribution of grain sizes and initial exciton positions with respect to the closest grain boundary, where we assume that a photogenerated exciton loses its polarization memory when it reaches the circumference of the perovskite crystalline grain.

For simplicity, we describe the hybrid perovskite crystalline grain as a 2D disk having radius, R_0, which is half of the measured grain size, D_{ave} in the SEM of Figure 3.1 (a). We further assume that the excitons are photogenerated with the same probability anywhere within the disk. Therefore, the probability, *P(r)*, that an exciton is photogenerated at a distance, *r*, from the disk center may be written as $2\pi r(dr)/\pi R_0^2$ (i.e., the ring area at *r*, normalized by the disk area). An exciton at *r* travels the shortest distance $L(r)=R_0-r$ to the circumference of the disk, in order to lose its acquired POM. This is achieved via a diffusion process, where *L(r)* is given by the diffusion relation: $(L(r))^2= (R_0-r)^2=2Dt(r)$. Here *D* is the diffusion constant, and *t(r)* is the diffusion time for an exciton to reach the disk edge at distance *L(r)*.

From this relation, we can calculate the average time *t*(aver) by integration:

$$t(\text{aver}) = \int_0^{R_0} t(r)P(r)dr = \frac{(R_0 - r)^2}{2D}\frac{2\pi r}{\pi {R_0}^2}dr \tag{3.5}$$

From Equation (3.5), we then obtain:

$$t(\text{aver}) = (R_0^2)/(12D) \quad (3.6)$$

Considering the distribution of grain sizes (Figure 3.7(a)), we averaged *t*(aver) over the grain size distribution. Consequently, we calculated *D* from Equation (3.6) and the obtained τ(POM) = 150 ps from *P*(t) decay (Figure 3.6) to be *D*=0.010 cm^2s^{-1}, with a standard deviation of 0.005 cm^2s^{-1} (see Figure 3.7(c)). This value is in agreement with the exciton diffusion coefficient in $MAPbI_3$ estimated by an alternative method [80]. Using the photoexcitation lifetime, τ_0~10 ns, estimated in Ref. 164, we obtain an exciton diffusion length, L_D ~150 nm, in $MAPbI_3$ at RT using the relation $L_D=(2D\tau_0)^{1/2}$. This large exciton diffusion length at room temperature indicates that photocarriers may be generated in the perovskite active layer of PV devices via exciton dissociation at interfaces and grain boundaries even in perovskites where the exciton binding energy, $E_b > k_BT$, as in mixed perovskite compounds such as $MAPbI_{1-x}Br_x$ and $MAPbI_{1-x}Cl_x$ (see Section 3.4 and 3.5).

We also found transient photoinduced POM for the PB band in the visible range as shown in Figure 3.8 (a). In contrast to the polarization memory of PA_1, however, POM of PB is *negative* (namely $\Delta T_{\parallel} < \Delta T_{\perp}$), and much longer-lived. In addition, POM initial value for PB, $-P(0)= 0.04$, is much smaller than that of PA_1 ($P(0) = 0.11$). The different POM properties obtained for PA_1 and PB again show that these two bands do not originate from the same photoexcitation species, in agreement with our interpretation that PA_1 is due to excitons whereas PB in this perovskite is mainly caused by photogenerated carriers. In this case, the much slower *P*(t) decay for PB indicates that free carriers do not easily cross the boundary between the neighboring crystalline grains, which suggests that

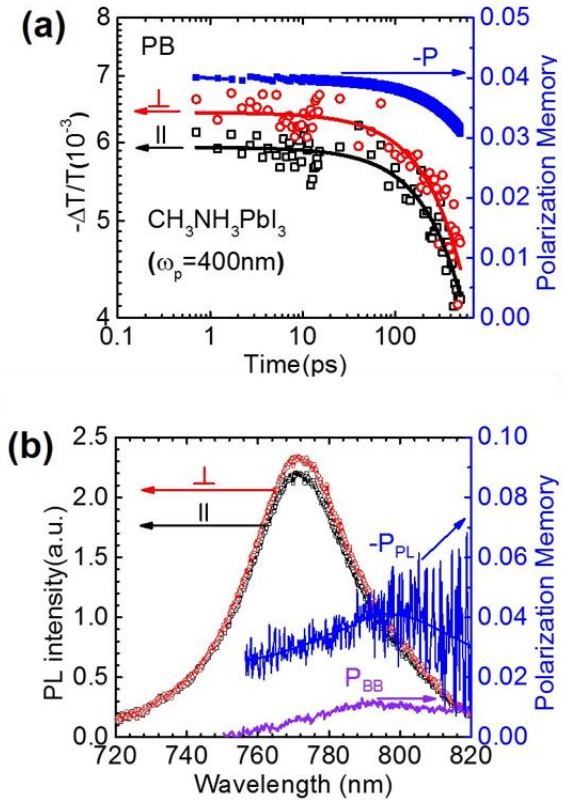

Figure 3.8. POM of PB and PL in $MAPbI_3$ films. (a) Dynamics of the PB band in $MAPbI_3$ film excited at 3.1eV for both $\Delta T_{\parallel}$ and $\Delta T_{\perp}$, and POM(t). The black and red lines through the data points are fittings using a single exponential decay ($\sim e^{-t/\tau}$) with τ=1.47 ns and τ = 1.4 ns for $\Delta T_{\parallel}(t)$ (red) and $\Delta T_{\perp}(t)$ (blue), respectively. The calculated POM(t) decay obtained from these fitting functions is also shown. (b) The RT photoluminescence (PL) emission spectrum measured parallel ($PL_{\parallel}$) and perpendicular ($PL_{\perp}$) with respect to the pump linear polarization in $MAPbI_3$. Also shown are the calculated spectra of the PL polarization degree, P_{PL}, and the system polarization degree, P_{BB}, measured using the emission from a blackbody radiator.

grain boundaries are an important factor that may limit the charge mobility in the perovskites [165]. It is tempting to interpret the negative $P(0)$ value obtained for PB as due to two successive transitions with an angle $\theta_0 > \pi/4$ (which gives negative $P(0)$ when using Equation (3.1)). However, this is elusive, since the PB/PA_2 feature cannot be interpreted as an optical transition of a photogenerated excitation with a certain dipole moment orientation. Instead, we interpret $P(0)$ for PB as due to the polarization

properties of the optical transition at the band-edge. In this case, the photoluminescence (PL) should also show similar POM properties.

To check this hypothesis, we measured the RT polarization properties of the steady-state PL emission in $MAPbI_3$, excited by a linearly polarized cw pump beam from an Ar^+ laser at 488 nm. The PL emission passed through a polarizer followed by a polarization scrambler, and was measured with polarization parallel, $PL_{\parallel}$, and perpendicular, $PL_{\perp}$, to the polarization of the pump beam. Figure 3.8 (b) shows the spectrum of the two PL components and the PL polarization memory, P_{PL}, defined by the relation: $P_{PL} = (PL_{\parallel} - PL_{\perp})/(PL_{\parallel} + PL_{\perp})$. It is clearly seen that the PL emission is polarized; in fact, P_{PL} remains approximately constant at $P_{PL} \sim -0.035 \pm 0.005$ across the entire PL spectrum. In addition, we also measured the polarization degree, P_{BB}, of the emission from a blackbody radiator at the sample position, where $P_{BB} = (BB_{\parallel} - BB_{\perp})/(BB_{\parallel} + BB_{\perp})$, and $BB_{\parallel}$ ($BB_{\perp}$) have the same meaning as $PL_{\parallel}$ ($PL_{\perp}$) above. We found that $P_{BB} < 0.007$ (see Figure 3.8 (b)), much smaller than the obtained P_{PL}. The rather surprising POM result for the cw PL emission from the perovskite film shows that PL originates from the optical transition at the band-edge, but not necessarily from excitons. This is consistent with the PL spectrum which peaks at 1.6 eV, very close to PB band in the transient PM spectrum (Figure 3.4 (a)). In addition, since P_{PL} is very close to that of the PB caused by photocarriers (but smaller than $P(0)$ because of the $PL(t)$ decay), we speculate that the PL at RT is due to interband transition of photogenerated electrons and holes, rather than due to excitons. This assumption is in agreement with the general belief in the field of hybrid perovskite photophysics [166-168].

3.3.2 Below Bandgap Excitation

In Figure 3.9, we show the transient PM spectrum of $MAPbI_3$ film with below-gap excitation, at ω_{pump}=1.55eV, i.e., into the Urbach edge of the film [169]. One of the two possibilities for the pump excitation in this case is an optical transition from the VB edge to the CB tail inside the gap, as schematically shown in Figure 3.9 (c) (the other possibility is VB tail to the CB edge). Under these conditions, exciton photogeneration is impossible, since $\omega_{pump} < E_1$ ~1.65eV. Indeed, no PA band in the mid-IR has been observed in this case (Figure 3.9 (a)), and *this justifies our assignment of PA_1 band as due to excitons*. In contrast, the PB/PA_2 feature at the band-edge is still clearly seen. Surprisingly the overall PM spectrum shows the same dynamics across the entire measured spectral range (see Figure 3.9 (b) for the decay dynamics at 0.63eV and 1.63 eV). This is consistent with our interpretation that the PB/PA_2 feature in $MAPbI_3$ is due to photogenerated carriers, since excitons are simply not generated with below-gap excitation (see below). Another interesting phenomenon is that the abnormal transient photoinduced POM at the band-edge is also obtained using below-gap excitation (Figure 3.9 (d)), but with larger initial value $P(0)$=-0.08 compared to $P(0)$=-0.04 that is obtained with above-gap excitation. This suggests that $P(0)$ is excitation energy dependent, and may be partially lost during the hot carriers thermalization process associated with $\hbar\omega_{pump}$ =3.1eV. The fact that the decay dynamics of PB kinetics shown in Figure 3.10 are independent on the excitation intensity (which determines N(0)) shows that bimolecular recombination is not involved in the photoexcitation dynamics, probably due to the small N(0) caused by the low absorption coefficient for below-gap pump excitation.

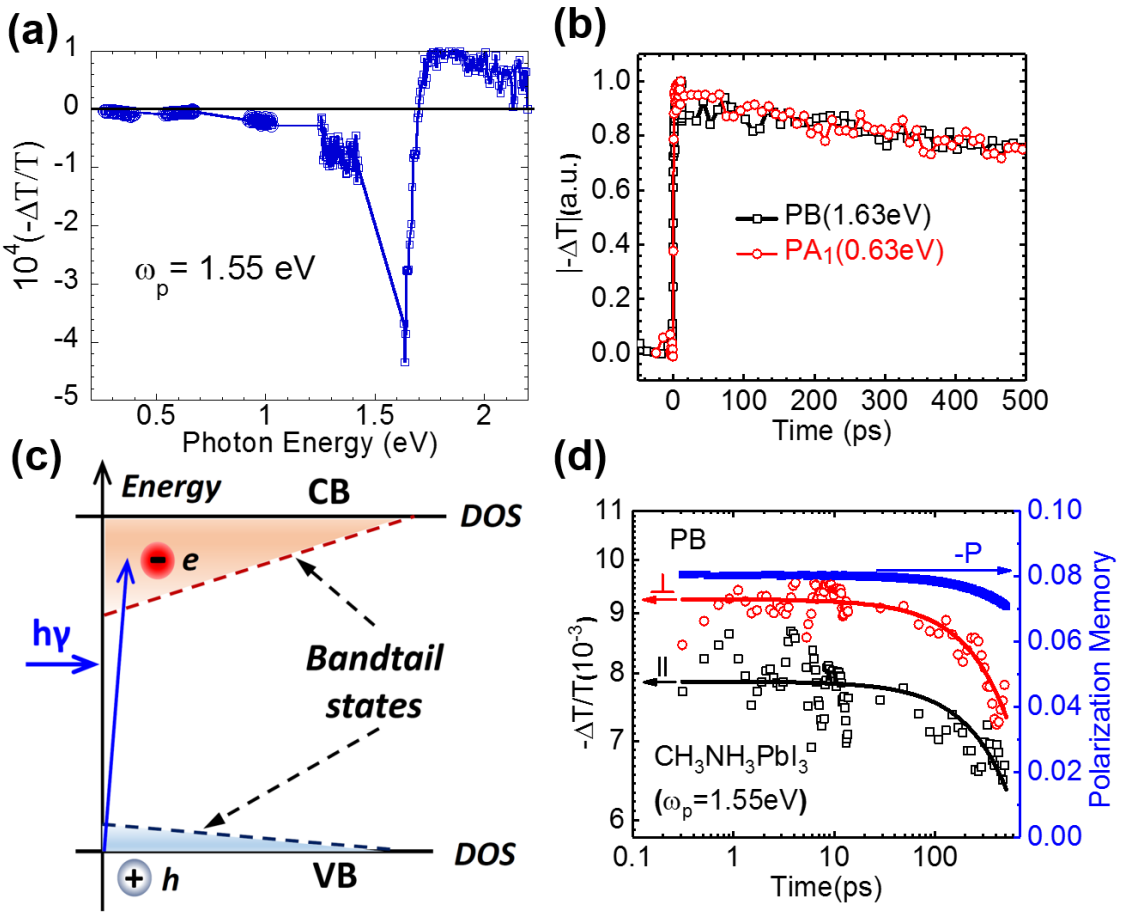

Figure 3.9 Photomodulation spectroscopy of $MAPbI_3$ film excited below-gap at 1.55eV. (a) PM spectrum at t = 0 ps, where various bands are assigned. (b) Decay dynamics of the PB bands at 1.63eV and 0.63eV up to 500 ps. (c) Schematic energy diagram that explains the process of photogenerated free holes using a pump of below-gap photon energy. The film exponential band tails due to disorder are also shown. (d) Transient polarized photomodulation response of the PB band probed at 1.63eV. The lines through the data points are fitting using a single exponential decay ($\sim e^{-t/\tau}$) with τ=2.4 ns and τ=2.2 ns for $\Delta T_{\parallel}$ and $\Delta T_{\perp}$ transients, respectively; the calculated polarization memory (P) decay obtained from these fitting functions is also shown.

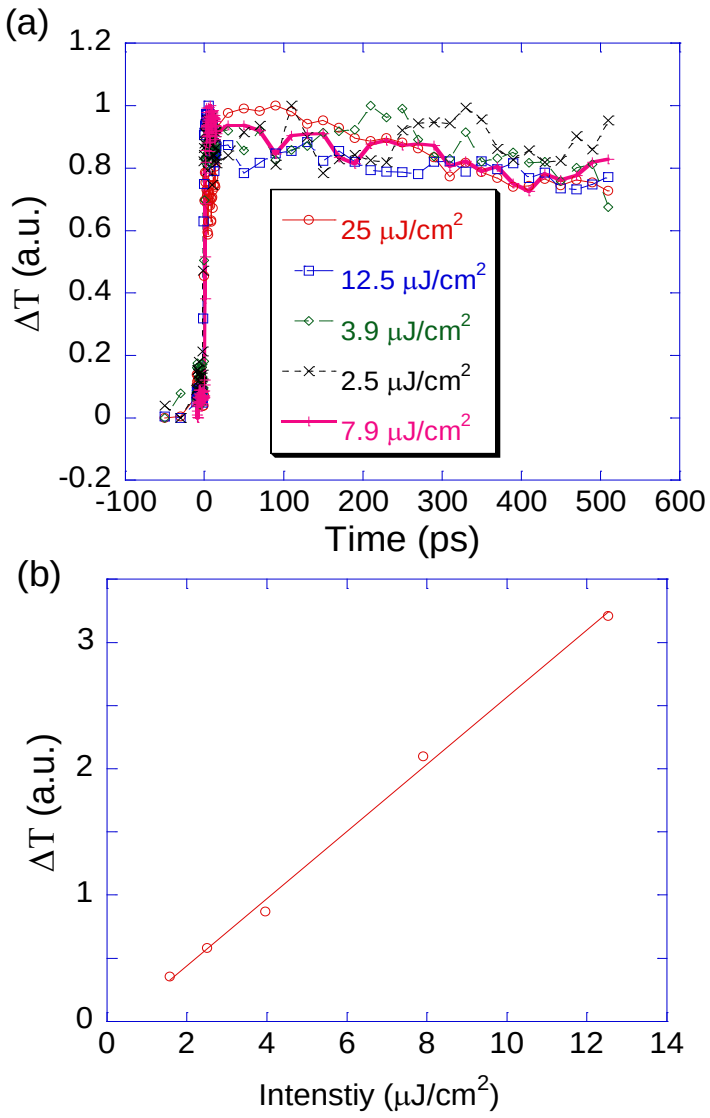

Figure 3.10. Pump excitation dependence of PM in $MAPbI_3$ films at 1.55 eV. (a) PB dynamics in $MAPbI_3$ film photoexcited at 800nm (1.55 eV) at various pump excitation intensities. (b) ΔT at t=0 ps vs. the pump excitation intensity.

3.3.3 Temperature Dependence and Phase Transition

The relationship between the exciton binding energy and the crystal structure could be crucial for photovoltaic devices as discussed in Chapter 1, and in $MAPbI_3$, the crystal structure can undergo phase transitions with temperature leading to the change of the exciton binding energy. It is therefore useful to explore the effect of this transition on the photoexcitation ratio between carriers and excitons in the $MAPbI_3$ perovskite.

3.3.3.1 Below Room Temperature: Tetragonal to Orthorhombic Phase

Figure 3.11 shows the visible range transient PM spectroscopy results of $MAPbI_3$ film with above-gap excitation (~3.1eV) below room teperature. At T=300K in Figure 3.11 (a), the PB/PA_2 spectral feature, which is due to band-filling effect caused by the coexistance of photocarriers and excitons as discussed in the previous section, decays slowly within 2ns. At low temperature as shown in Figure 3.11 (b), however, the PB peak appears at ~1.68eV correlated with the PA_2 band peak at ~1.73eV, both of which are significantly enhanced and shifted with respect to that at room temperature. The derivative PB/PA_2 spectral features share the same decay dynamics over the whole range as emphasized by the similiar shape of the normalized spectra shown in Figure 3.12.

Figure 3.11 (c) shows the transient PM spectrum changing with temperature. Right at 160 K, we observed two PB peaks (Figure 3.11 (c) inset) suggesting that both tetragonal and orthorhombic phases coexist at this temperature. The whole PM spectrum shows blue shift with temperature for both phases, and this trend is consistent with previous reports results showing the positive thermal expansion coefficient of the bandgap, dE_g/dT~0.25 meV/K for the tetragonal phase and ~0.28 meV/K for the orthorhombic phase [170].

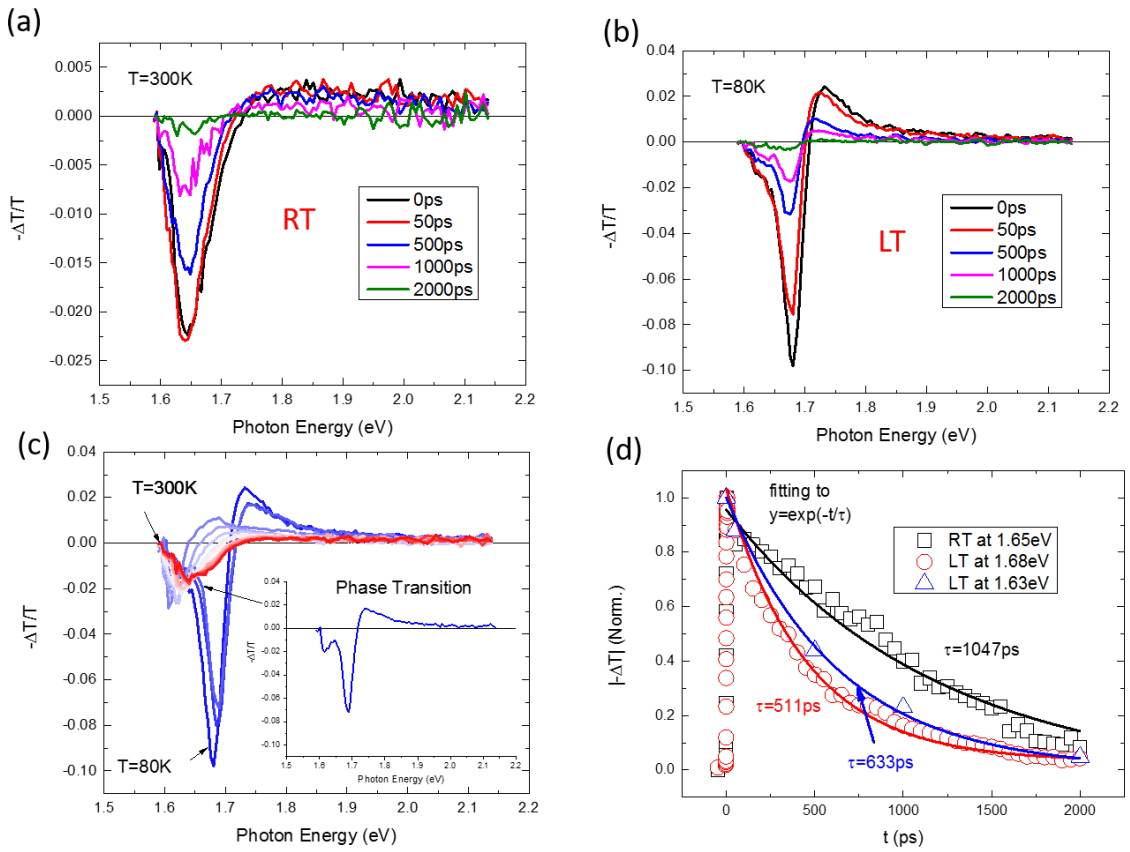

Figure 3.11 Temperature dependence of photomodulation spectroscopy of $MAPbI_3$ film excited at 3.1eV below room temperature. (a) PM spectrum at T=300K, (b) PM spectrum at T=80K, (c) PM spectrum vs. Temperature from 80K to 300K. Inset: Phase transition with PB features from both phases has been observed at 160K. (d) PB decay dynamics can be fit with single exponential decay in both phases. The recombination lifetime at low temperature is 511 ps, which is significantly shorter than that at room temperature 1047 ps. The slow decay shoulder at 1.63eV when T=80K has also been fit with single exponential decay and the lifetime obtained is 633 ps.

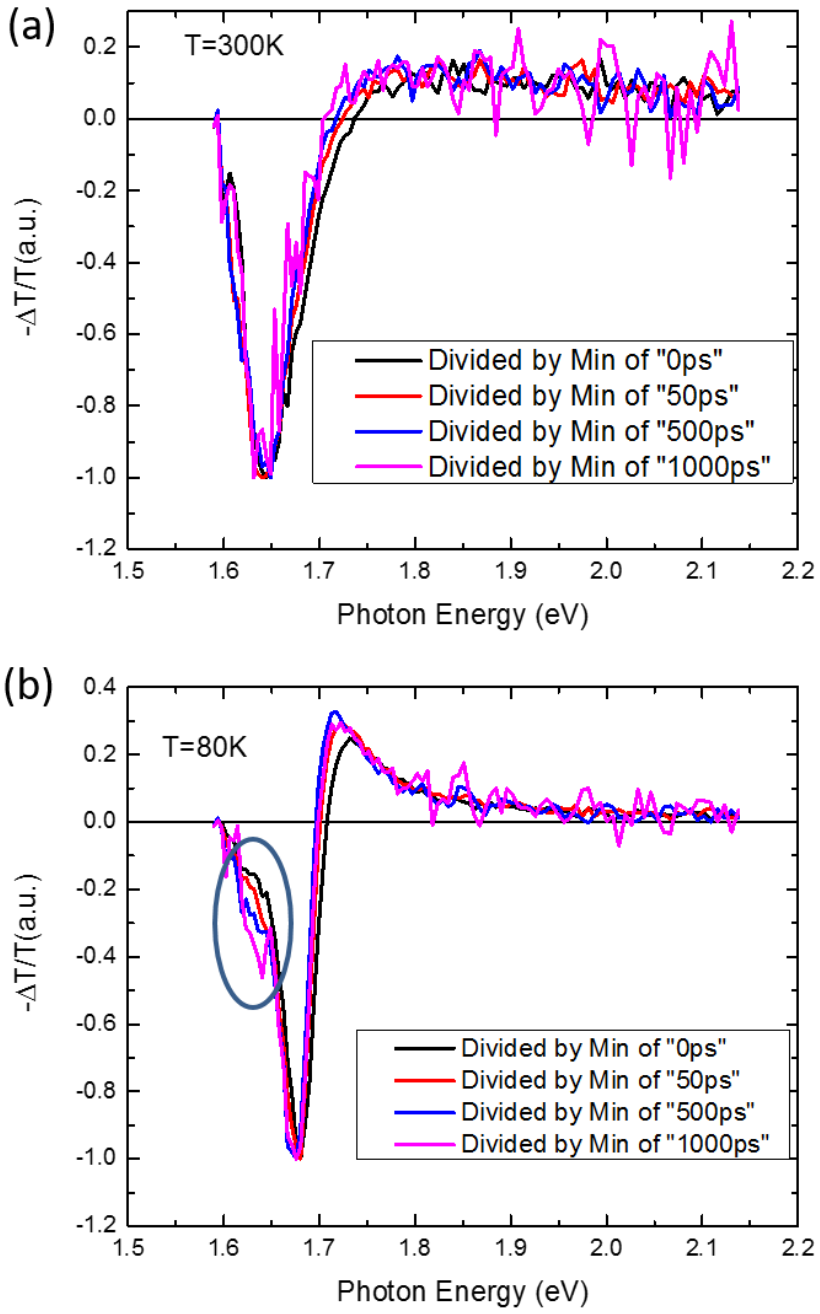

Figure 3.12 Normalized photomodulation spectra of $MAPbI_3$ film excited at 3.1eV at (a) room temperature and (b) low temperature. A slow decay shoulder at 1.63eV has been observed at low temperature.

Figure 3.11 (d) displays representative decay dynamics and fits probing at the center of PB peak for the tetragonal phase at 300K and orthorhombic phase at 80K, respectively. The PB/PA_2 feature shows significant difference at low temperature compared to room temperature. We observed a long-lived PB signal with a center around 1.58-1.65eV for the tetragonal phase, and the single exponential fitting gives a lifetime longer than 1 ns. In orthorhombic phase, however, the PB peak is located around 1.68-1.70eV and has a much shorter lifetime of ~ 511ps. The different decay rates in the two phases are consistent with previous reports [170]. As demonstrated in the previous section and other works [58-61], typically the lifetime of the free charges is orders of magnitude larger than that of excitons, and we attribute the shorter lifetime at low temperature to the fact that the exciton recombination becomes the dominant process in orthorhombic phase.

This result is not surprising considering the larger exciton binding energy in the orthorhombic phase compared to the tetragonal phase as mentioned in Section 3.1. Exciton binding energy E_b in $MAPbI_3$ was found to be tens of meV [71] at low temperature (in the orthorhombic phase) but only a few meV at room temperature (in the tetragonal phase) [64]. On the other hand, it is known that exciton binding energy is inversely proportional to the dielectric constant ε. Onoda-Yamamuro and co-workers compared ε of both the tetragonal and orthorhombic phases [171], and found that the real ε of $MAPbI_3$ in the orthorhombic phase (35 below 150 K) is much smaller than that of the tetragonal phase (135 above 160 K). They attributed this to the permanent dipole of the methylammonium cation which is predominantly disordered in the tetragonal phase and ordered in the orthorhombic phase [170]. Therefore, the larger E_b of the orthorhombic phase in turn gives a larger contribution of excitons to the dynamics as we have obtained.

Another feature of the time-resolved results in Figure 3.11 is the slow decaying shoulder at round 1.63eV for the orthorhombic phase at 80 K, which has not been observed in the tetragonal phase at room temperature. This feature becomes more pronounced when the spectra are normalized at the PB peaks as shown in Figure 3.12 (b). The lifetime of this shoulder was extracted from the fit as 633 ps (blue curve in Figure 3.11(d)). The origin of this feature is still unclear, and it could be due to the coexistence of the two phases even at low temperature as discussed in Chapter 1. Another possibility is related to the Rashba effect as discussed in Section 1.5 indicating that the low energy decay (indirect transition) is indeed slower that the high energy decay (direct transition). This may be another indication that the Rashba effect modifies the photocarriers (or exciton) dynamics in this material, which needs more sophisticated study.

3.3.3.2 Above Room Temperature: Tetragonal to Cubic Phase

Figure 3.13 shows the visible range picosecond transient PM spectroscopy results of $MAPbI_3$ film with above-gap excitation (~3.1eV) above room temperature. The band-filling derivitive-like PB/PA_2 spectral feature caused by the photocarriers is weakened and blueshifts with temperature up to 350K. This trend is consistent with previous reports results showing the positive thermal expansion coefficient of the bandgap, dE_g/dT~0.257 meV/K, for the tetragonal phase and cubic phase from 310 to 400 K [172]. Although the signal-to-noise ratio gets worse with increasing temperature, the broader of the PB peaks and a faster decay dynamics can still be discerned at temperature above 332K, which agrees well with the reported phase transition temperature at 330K.

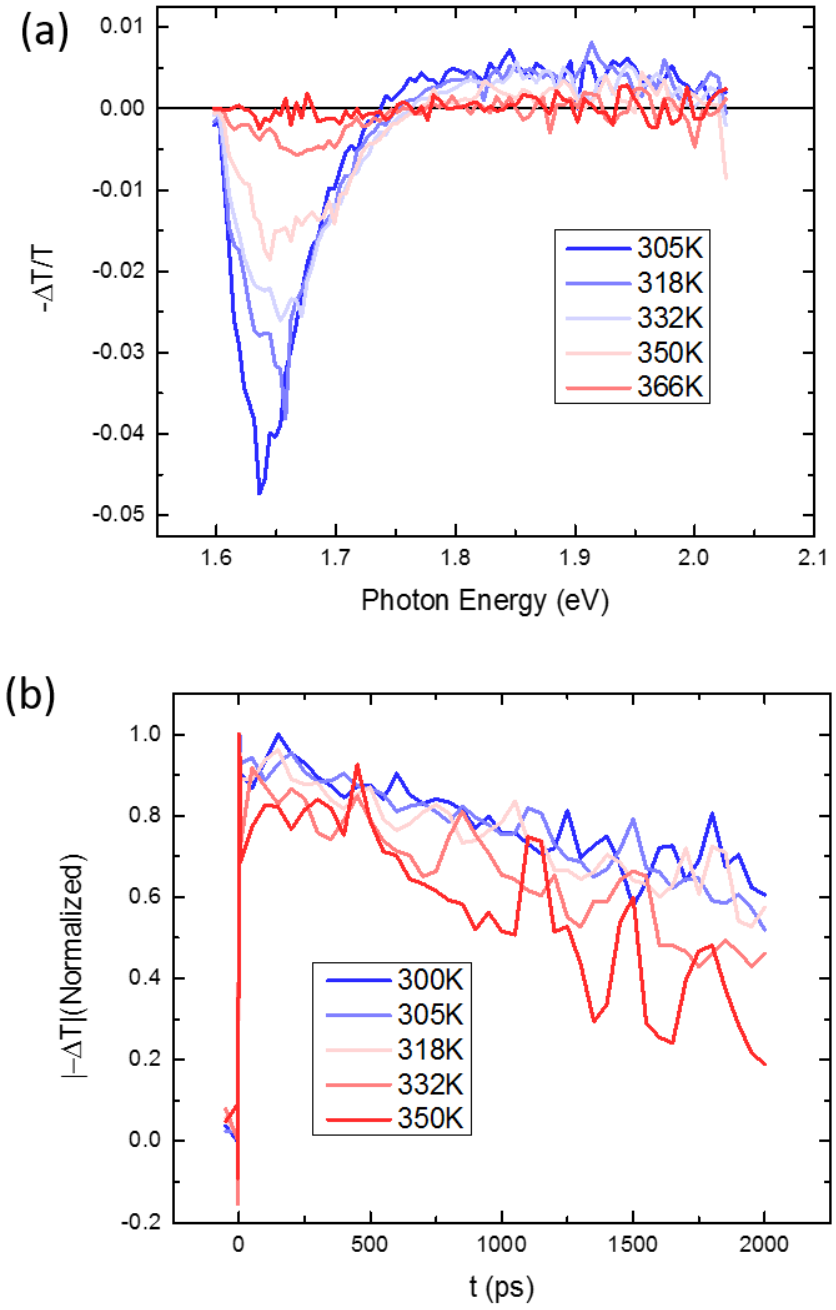

Figure 3.13 Temperature dependence of photomodulation spectroscopy of $MAPbI_3$ film excited at 3.1eV above room temperature. (a) PM spectrum vs. temperature from 305K to 366K. Phase transition has been observed between 332K to 350K. (b) PB decay dynamics.

3.4 Transient Photomodulation Spectroscopy of $MAPbI_{1.1}Br_{1.9}$ Mixed Films

We have extended our transient spectroscopy measurements to mixed perovskite films, namely $MAPbI_{3-x}Br_x$. The $MAPbI_{3-x}Br_x$ system might be important for tandem solar cells, because its optical gap can be tuned from 1.57 eV to 2.3 eV when the composition parameter, x, changes from x=0 to 3. From the absorption edge of this film at ~2.1eV (Figure 3.14 (a) inset), we estimate x=1.9 [173]. For $MAPbBr_3$, the exciton E_1 transition is at 2.34 eV [174], and the binding energy was estimated to be 80-150 meV [70-71], much larger than in $MAPbI_3$. We thus expect that most primary photoexcitations in this hybrid perovskite would be *excitons* rather than free carriers. If this is correct, then the comparison of the transient PM spectra of $MAPbI_3$ and $MAPbI_{1.1}Br_{1.9}$ films should be instructive.

In Figure 3.14 (a), we present the transient PM spectrum of the $MAPbI_{1.1}Br_{1.9}$ film at t = 0 ps. Like the PM spectrum of $MAPbI_3$ shown in Figure 3.4 (a), the PM spectrum here also contains three features: PA_1 at ~0.5 eV, and PB and PA_2 at ~2.1 eV and 2.3 eV, respectively. We attribute PA_1 to exciton transition between adjacent bands (interband), similar to the analysis of this PA band in $MAPbI_3$. From the absorption spectrum (Figure 3.14 (a) inset), we identify two exciton transitions, E_1 at 2.1 eV and a broader transition, E_2 with a shoulder at 2.7 eV. Thus, there is a possible interband exciton transition from E_1 to E_2 at similar energy as PA_1 in this perovskite. In contrast to $MAPbI_3$, however, the dynamics of the PM feature at the band-edge up to t=500 ps are *the same* as that of PA_1; this also includes their formation dynamics at t~0 ps (see Figure 3.14 (c) inset). This shows that spatially inhomogeneous density of excitons may also induce symmetry breaking in the film via photoinduced static strain (similar to the photocarriers in $MAPbI_3$

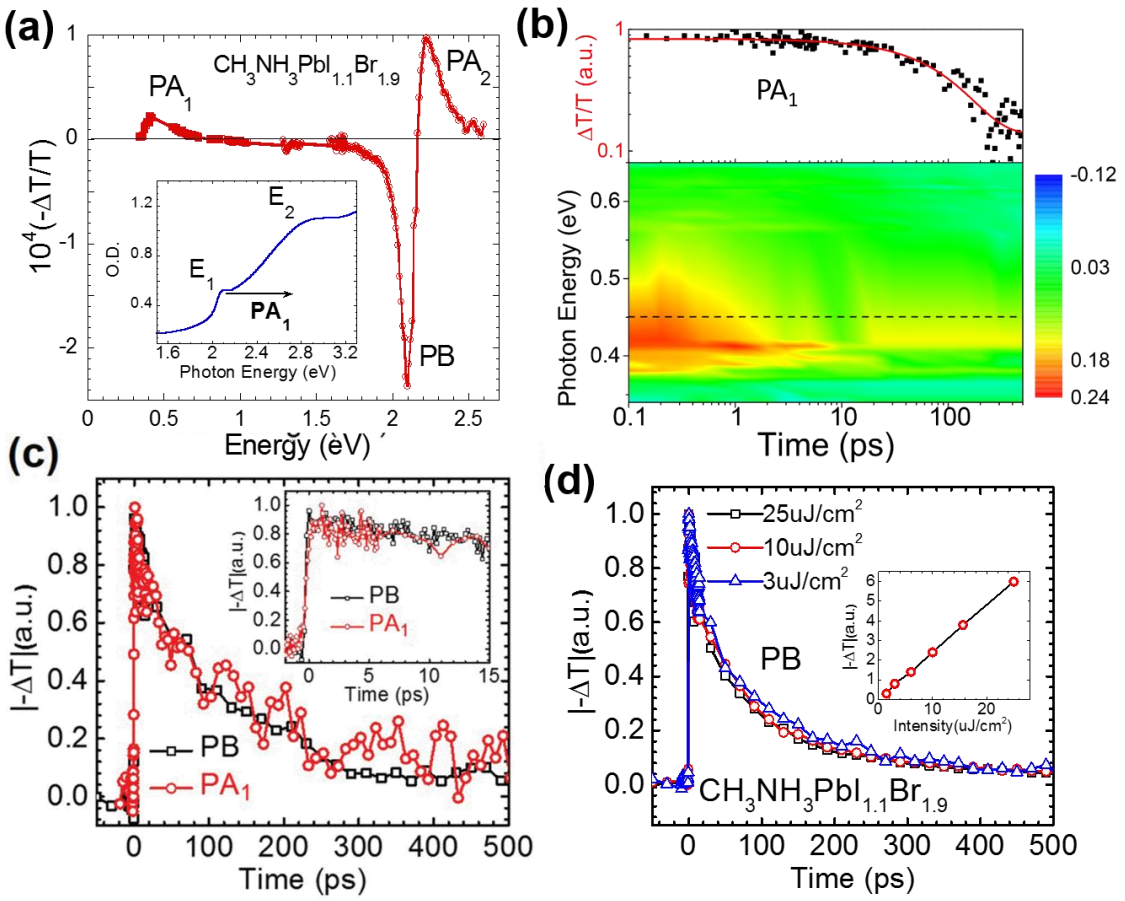

Figure 3.14. PM spectroscopy of $MAPbI_{1.1}Br_{1.9}$ film excited at 3.1eV. (a) PM spectrum at t=0 ps. The inset shows the film absorption spectrum, where two excitons, E_1 and E_2, and the interband PA_1 transition between them are assigned. (b) PA_1 decay dynamics plotted with false colors (lower panel), and at 0.45eV (upper panel) plotted on double logarithmic scale. The line through the data points in the upper panel is a fit using a single exponential decay with lifetime τ = 100 ps. (c) Decay dynamics of PB and PA_1 bands up to 15 ps (inset) and 500 ps. The similar dynamics points to a common underlying photoexcitation species that we identify as due to excitons. (d) Pump excitation intensity dependence of PB dynamics in a $MAPbI_{1.1}Br_{1.9}$ film excited at 3.1 eV. The inset shows the dependence of $\Delta T/T$ vs. the excitation intensity.

discussed in the previous section), and this generates a PB/PA_2 feature at the band-edge, in addition to PB due to phase-space filling. From the similar dynamics of all three transient PM spectral features, we thus conclude that *excitons* are the primary photoexcitations in $MAPbI_{1.1}Br_{1.9}$, consistent with the larger E_b in this hybrid perovskite (~100 meV). This is much larger than k_BT at RT, thus preventing dissociation of excitons to free carriers in this perovskite in the picosecond time domain. However, the excitons may dissociate at a later time into free carriers at native defects, impurities, and/or grain surfaces, and thus contribute to cw photocurrent in this hybrid perovskite.

We also checked the existence of transient POM in this film at PA_1 (Figure 3.15 (a)) and PB (Figure 3.15 (b)). Unlike the photoinduced POM obtained in $MAPbI_3$, there is *none* observed in this film, which suggests that this perovskite compound is *isotropic* at RT. This is consistent with the RT cubic crystal structure of this perovskite [56]. We note that the SEM image of this film also shows the existence of crystalline domains (Figure 3.1 (b)), similar to that in the $MAPbI_3$ in Figure 3.1 (a). The null result obtained for the POM in $MAPbI_{1.1}Br_{1.9}$ actually validates the observed POM for the photoexcitations in $MAPbI_3$; namely it is not an artifact of the experimental apparatus.

Although excitons are the primary photoexcitations in $MAPbI_{1.1}Br_{1.9}$, the Incident Photon to Charge Carrier Efficiency (IPCE) for $MAPbI_{3-x}Br_x$ with large x value is close to the value of $MAPbI_3$ [169]. Therefore, perovskite films in which excitons are the *primary* photoexcitations at high photoexcitation density (as required in picosecond spectroscopy) does not mean that excitons are still the major steady-state photoexcitations under sun illumination condition, where the photoexcitation density is much smaller and *thermal equilibrium* is achieved [59].

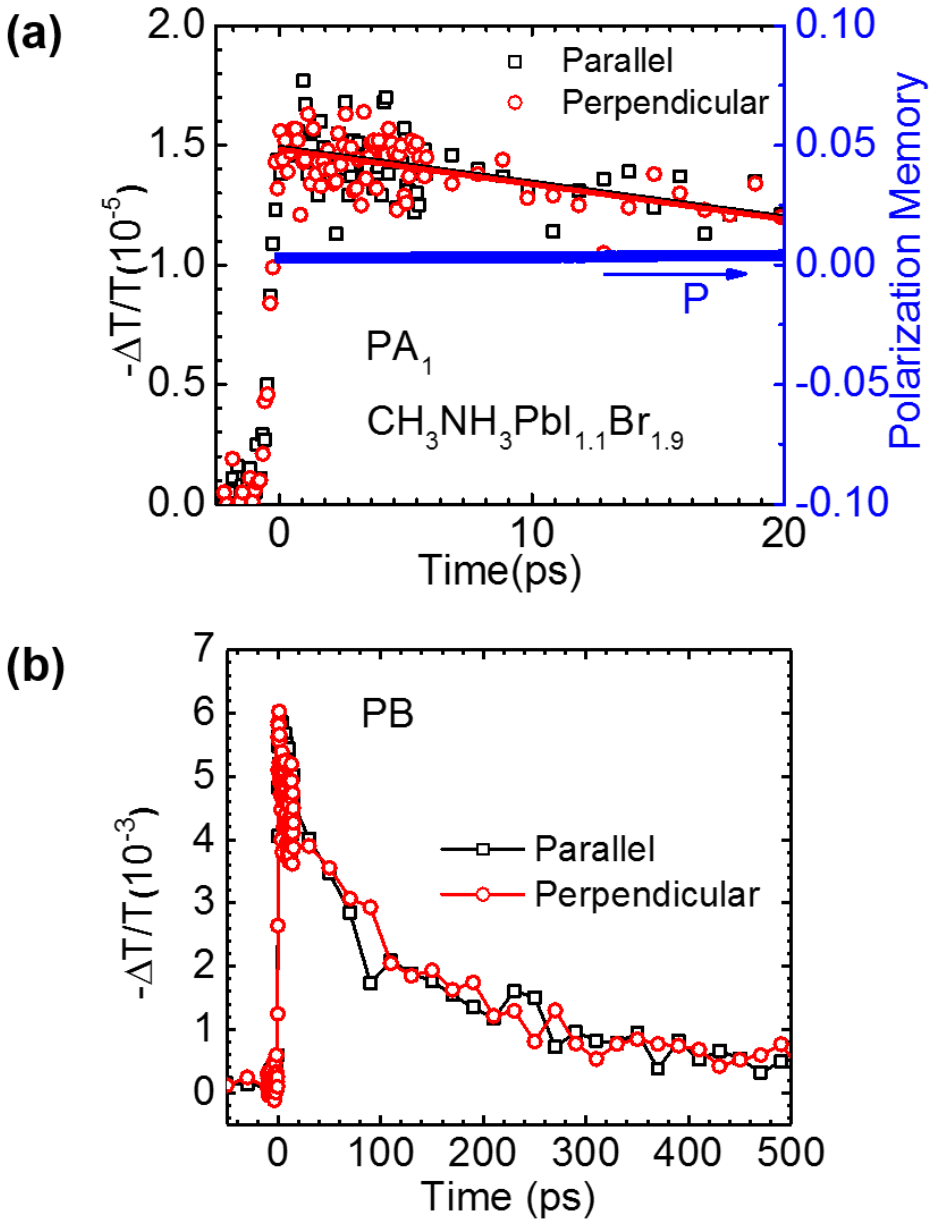

Figure 3.15. POM in $MAPbBr_3$ films. (a) Transient polarized response of $\Delta T_{\parallel}$ and $\Delta T_{\perp}$ components measured at 0.4eV (PA_1), and the resultant lack of polarization memory. (b) Transient polarized photomodulation response of the same film measured at the PB band (2.1eV); both $\Delta T_{\parallel}$ (parallel) and $\Delta T_{\perp}$ (perpendicular) components are shown.

In addition, the large exciton diffusion length in the perovskites (see above) may allow delayed photocarriers generation from excitons dissociation at grain boundaries in the film, or interfaces between the perovskite active layer and electron (hole) transport layers that are usually introduced in PV devices.

3.5 Transient Photomodulation Spectroscopy of $MAPbI_{3-x}Cl_x$ Mixed Films

This point of view is further supported by our picosecond transient measurements in a film of $MAPbI_{3-x}Cl_x$ perovskite, in which the exciton binding energy is in the range of 50 meV to 100 meV at the film surface [59, 175], i.e., also larger compared to k_BT at room temperature, but still shows an excellent IPCE value [17]. The SEM image of this film also shows the existence of crystalline domains (Figure 3.1 (c)), similar to that in the other two perovskite films (Figure 3.1 (a) and (b)). As seen in Figure 3.16 (a), the PM spectrum of this perovskite belongs to a single photoexcitation species, because the PA decay dynamics are the same across the entire PM spectrum (Figure 3.16 (b)). Since PA_1 at ~ 0.45 eV is due to exciton interband transitions according to Figure 3.16 (a) inset, we conclude that the $MAPbI_{3-x}Cl_x$ perovskite also shows mainly photogenerated excitons as the primary photoexcitation species, similar to $MAPbI_{1.1}Br_{1.9}$ shown in Figure 3.14, although this compound is abundantly used as the active layer in perovskite photovoltaic solar cells. We therefore conclude that photocarriers may still be formed in the perovskites via exciton dissociation at interfaces and grain boundaries even in cases where $E_b > k_BT$ at room temperature. Different morphology controlled by annealing temperature of the $MAPbI_{3-x}Cl_x$ perovskites and its influence on magnetic field effect (MEF) is discussed later in this chapter.

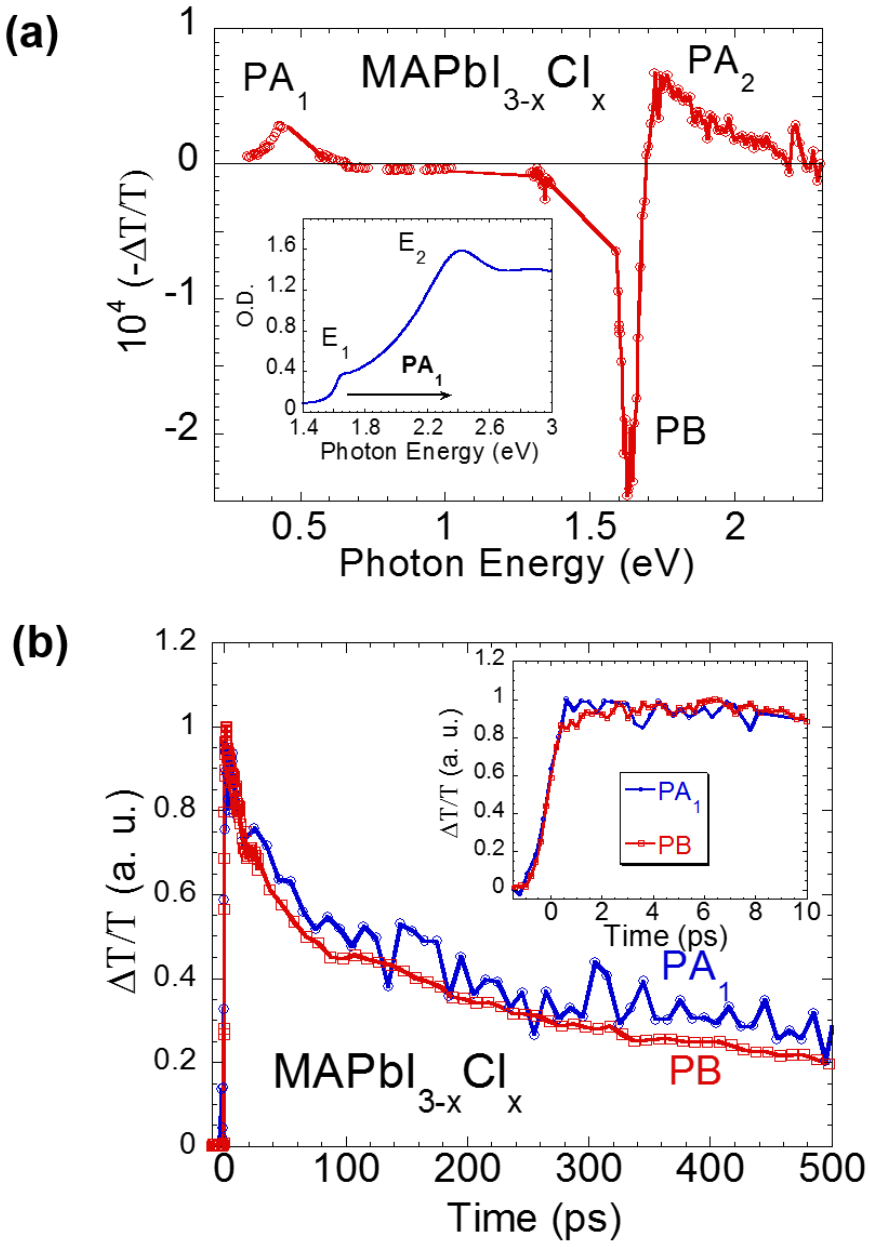

Figure 3.16. Photomodulation spectroscopy of $MAPbI_{3-x}Cl_x$ film excited at 3.1eV. (a) The transient PM spectrum measured at t = 0 ps, where various bands are assigned. Inset showes the film absorption spectrum, where two excitons, E_1 and E_2, and the interband PA_1 transition between them are assigned. (b) $PA_1(t)$ and $PB(t)$ transient dynamics up to 500 ps. The inset shows their dynamics up to 10 ps. Their similar obtained dynamics points to a common underlying photoexcitation species that we identify as due to excitons.

3.6 Morphology Dependence of Transient Photomodulation Spectroscopy in 3D Perovskite Films

3.6.1 Nano-Crystalline $MAPbBr_3$ Films

The absorption and PL spectra of representative NCP and as-cast $MAPbBr_3$ films are displayed in Figure 3.17. In the low-energy region, the scattering background is drastically reduced following NCP treatment as a result of smoother film surface and more uniform coverage due to smaller crystalline domains. For ease of comparison, the optical density (OD) at 1.91 eV (650 nm), which is 0.40 for as-cast and 0.06 for NCP films, respectively, has been subtracted off. The better NCP film quality leads to reduced optical losses, and this contributes to increased net optical gain and lower excitation threshold for laser action [122]. After subtracting off the background OD due to scattering, it appears that absorption is stronger in the NCP film. However, poor substrate coverage can lead to an apparent reduced absorption and an artificially flat spectrum as exhibited by the as-cast film [176]. We therefore interpret these differences in the absorption spectra as due to film quality rather than a change in their electronic properties. However, upon normalizing the spectra to the excitonic peak near 2.36 eV (525 nm), it is seen that this band is narrower in the NCP-treated films and slightly blue-shifted with respect to the as-cast films (Figure 3.17, inset). These results are consistent with the known increase of the optical gap upon decreasing crystal size in combination with a reduced crystal size distribution in NCP films [177] and a reduced exciton binding energy in the smaller crystallites that may also contribute to the observed blue-shift. In contrast, the PL spectra of the two films are very similar, displaying a single band with a peak at 2.30 eV (540 nm). We note, however, that the emission intensity is much stronger

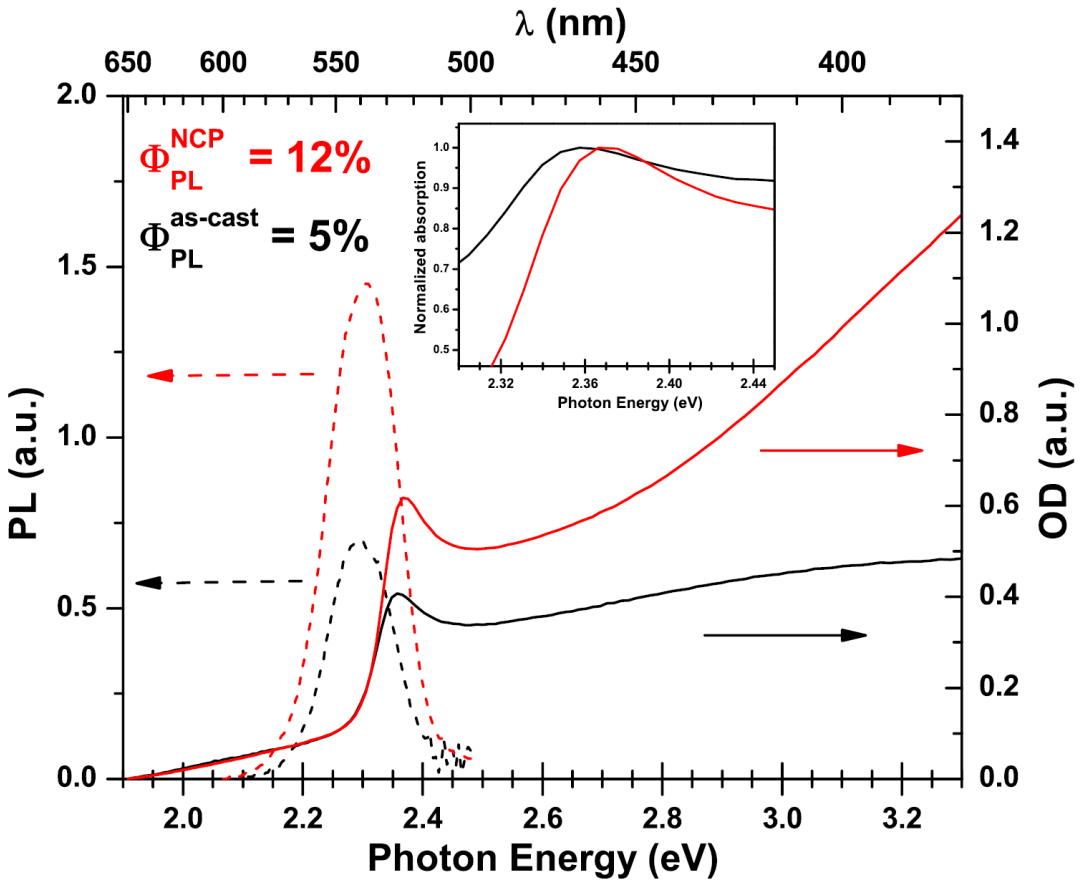

Figure 3.17. Absorption and PL spectra of as-cast (black) and NCP (red) $MAPbBr_3$ films. The contribution of scattering and reflection to the optical density at 1.91 eV (650 nm) was subtracted off to facilitate comparison. PLQE values measured for each film are included. The inset shows the respective absorption spectra normalized to the maximum of the excitonic peak.

in the NCP film. Using an integrating sphere, we measured respective PLQE of 5% and 12% (60.5%) for the as-cast MAPbBr3 film and for NCP film. The PLQE increase in the NCP films may also contribute to lower lasing threshold intensity [122, 178].

To investigate into the origin of the enhanced PLQE obtained by NCP treatment, we conducted ps transient photomodulation (PM) spectroscopy in the visible to NIR spectral range to probe the excited state dynamics. The transient PM spectra of representative films are shown in Figure 3.18. The PB/PA_2 feature is observed in both films, and we attribute this feature to due to a much larger binding energy in $MAPbBr_3$ compared to that in $MAPbI_3$ and our discuss in previous section. This is obvious in the absorption spectra, where the presence of excitons is more apparent in the NCP films.

Recently, Grancini et al. have attributed the high energy PA_2 to renormalization of the exciton energy [179]. In that work, they discussed a correlation between exciton formation and crystal grain size, where excitons are only formed in larger crystals, an effect they notably observed in $MAPbBr_3$ as well. The transient PM that we observed here in both films is consistent with the model of exciton renormalization despite the large difference in crystal grain sizes. Importantly, the transient PM of the as-cast film shows a considerable spectral red shift of the PA band at early times following pulse excitation. As the exciton-renormalization increases with the exciton density, transient PA red-shift may result from a very large initial density of excitons leading to the significant blue-shift; this is followed by fast decay of the exciton density via recombination causing a reduced renormalization and subsequent dynamic red-shift. This is in agreement with the fast PB decay of the as-cast film (Figure 3.18 (d)).

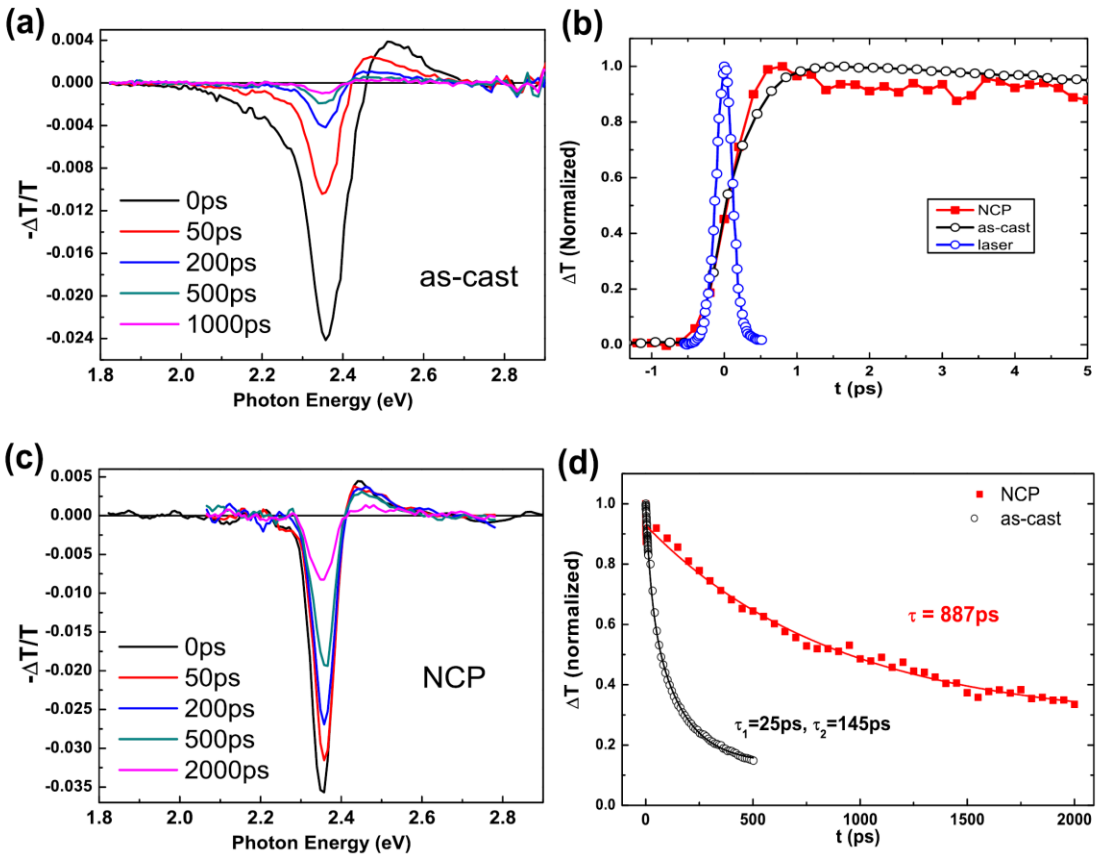

Figure 3.18. Picosecond transient photoinduced absorption spectra of the $MAPbBr_3$ as-cast film (a) and NCP film (c) at various time delays between the pump and probe pulses. (b) and (d) The transient rise (b) and decay (d) dynamics of the PB band at 2.35 eV for the as-cast and NCP film, respectively. The temporal profile of the pump beam is shown in (b) for comparison. The solid lines in (d) are fits using a single (NCP) and bi-exponential (as-cast) decay, respectively.

In contrast, the NCP film shows no-dynamic red shift of the PA_2 band at high photon energy, which is consistent with the much slower exciton population decay. Further evidence of a prolonged thermalization mechanism in as-cast films is shown in Figure 3.18 (b), where the rise time dynamics for the PB feature are displayed. The PB feature is observed to build up over a time scale of 1ps for both films. However, it is clear that the delayed ground-state depopulation occurs more slowly in the as-cast film.

The transient PB dynamics track the recovery of the photogenerated exciton population to the ground state through radiative and non-radiative decays. We found that the excited state lifetime, τ=900 ps in NCP films, is considerably longer compared to τ=150 ps in as-cast films (Figure 3.18 (d)). The excitation intensity is the same in both cases; thus, the reduction in lifetime is not due to enhanced bimolecular or Auger recombination processes [178]. In fact, we only observed evidence of these higher-order processes at higher fluence (>35 $\mu J/cm^2$) than what is used here (25 $\mu J/cm^2$). Instead, the longer PB lifetime in the NCP film indicates a reduction in non-radiative trap states that are determined by, and thus controllable by, the sample morphology. This is consistent with the observed higher PLQE, $\Phi_{PL}= \tau/\tau_{rad}$, where τ_{rad} is the intrinsic radiative decay rate of excitons. We note that the factor of six increase in exciton lifetime for the NCP films is larger than the increase of the measured PLQE (factor of two). This might be explained as due to increase reabsorption in the NCP films or change in τ_{rad}, or both. Also, the anti-correlation found between crystal grain size and excited state lifetime is not consistent with a diffusive process. This implies that the non-radiative decay is due to intra-grain trapping processes, which indicates a larger bulk defect density in as-cast films.

3.6.2 Morphology Dependence of $MAPbI_{1-x}Cl_x$ Films on Magnetic Field Effect (MEF)

In the previous work [93], we measured significant magneto-photocurrent (MPC), magneto-electroluminescence (MEL), and magneto-photoluminescence (MPL) responses in hybrid perovskite devices and thin films, where the amplitude and shape are correlated to each other through the electron–hole (e-h) lifetime, which depends on the perovskite film morphology. We attribute these responses to magnetic-field-induced spin-mixing of the photogenerated e-h pairs with different g-factor (the Δg model), which has been validated by measuring large Δg (~0.65) using field-induced circularly polarized photoluminescence. Here we measured the e-h pair lifetime using picosecond pump-probe spectroscopy and further validated the Δg model.

We first fitted our MPC(B) response in the perovskite photovoltaic cells with Lorentzian functions. In particular, we obtained both broad (MPC_B) and narrow (MPC_N) components of MPC response in a perovskite device, from which we obtained two time constants when excited at 3.1 eV, namely $\tau_1 \sim 49$ ps and $\tau_2 \sim 537$ ps; but only one time constant (τ_2) survives when excited at 1.6 eV. In addition, because $\tau_2 > \tau_1$ and assuming a robust spin-lattice relaxation time τ_{SL}, the "decreasing factor" (defined as $DF=[1-\exp(-\tau/\tau_{SL})]$) $DF_2<DF_1$ and consequently $MPC_N(B) > MPC_B(B)$, in agreement with the experiment. In fact, from the two MPC component values (0.4% and 1.8%, respectively), their individual DF values, and lifetimes extracted from the width B_0, we can calculate τ_{SL}. Using these values, we obtained $\tau_{SL} \sim 200$ ps, which is much shorter than in organic semiconductors, but longer than τ_{SL} in the perovskites at intermediate B ~100mT. This justifies the use of the "Δg mechanism" in our data analysis. See details in our previous

work in Ref. 93.

The obtained spin-pair lifetimes in the perovskite photovoltaic devices can in fact be measured more directly using the picosecond pump/probe correlation spectroscopy. The pump photon energy was set at 1.6 (3.1) eV, which is below-gap (above-gap) excitation, similar to the excitations used for the MPC measurements. As shown in Figure 3.19 (a), the photomodulation spectra excited at 1.6 eV and 3.1 eV are similar, and the entire photomodulation spectrum (1.6 to 2.2 eV) shares the same decay dynamics, indicating that it originates from the same photoexcitation species, namely photogenerated e-h pairs as discussed in Section 3.5. However, we found that the photomodulation decay dynamics strongly depend on the excitation wavelength (Figure 3.19 (b)). Exciting at 3.1 eV results in a double exponential decay that corresponds to two lifetimes of ~22 ps and ~465 ps, respectively, whereas only a longer decay of ~505 ps was observed with excitation at 1.6 eV. The excellent agreement among MFE, FICPO, and transient spectroscopy validates the model used here for interpreting the various MFE(B) responses [93].

To more directly show the existing correlation between the MPL width and amplitude in perovskite films of different morphologies (see SEM images in Figure 3.2) through the e-h pair lifetime, τ, we measured the picosecond dynamics and MPL on the same film as shown in Figure 3.19 (c) and (d), respectively. We fit the picosecond decay with an exponential function to obtain an average lifetime τ, and extracted the half-width at the half-maximum (HWHM) from the MPL(B) response. As is clearly evident, the shorter the τ, the broader and weaker the MPL(B) response.

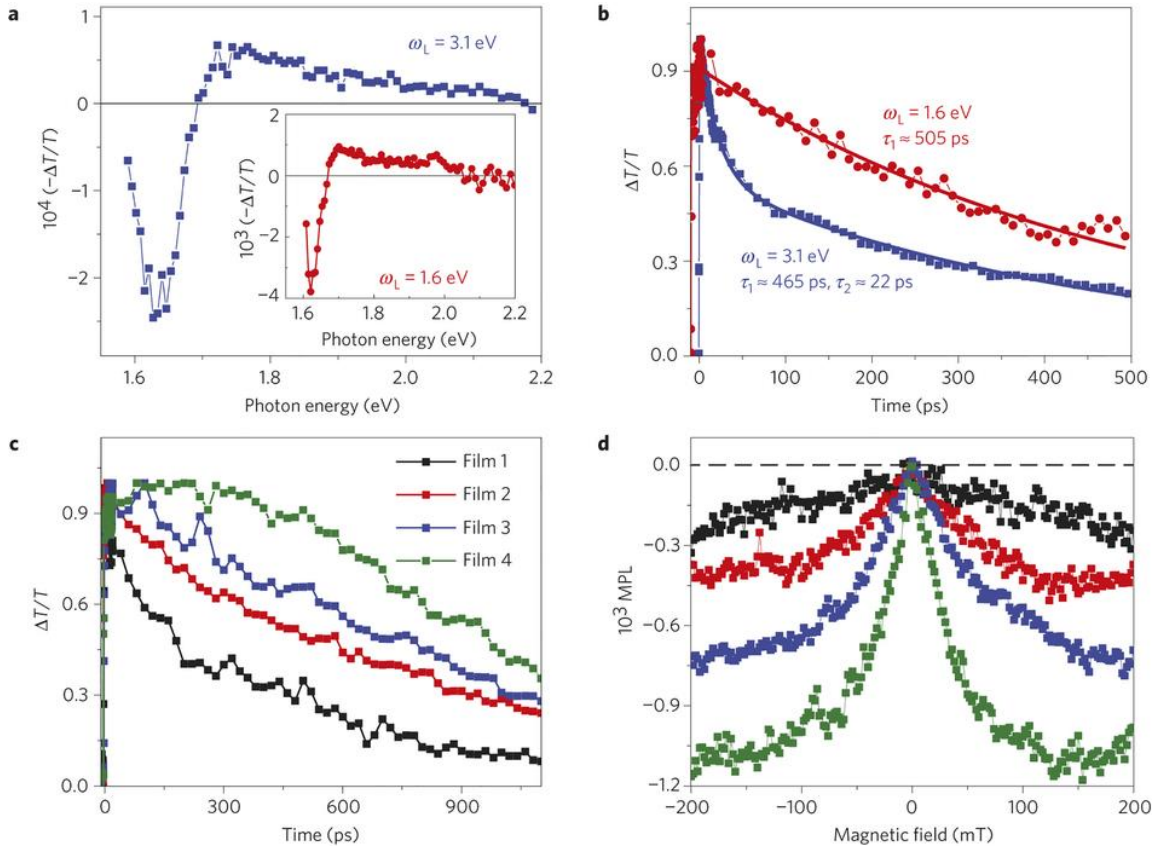

Figure 3.19. Picosecond transient response of different $MAPbI_{3-x}Cl_x$ films. (a) The photomodulation spectrum excited at 3.1 (main) and 1.6 eV (shown in the inset). (b) The photomodulation decay dynamics measured at 1.64 eV, excited at 3.1 (blue) and 1.6 eV (red). The line through the data points is an exponential (bi-exponential) fit to the decay dynamics; the various time constants τ_1 and τ_2 are denoted. (c) The photomodulation decay dynamics measured at 1.64 eV when excited at 3.1 eV for four different perovskite films (films 1–4), which were annealed at 90, 110, 120, and 130 C, respectively. The average e–h lifetime measured at 1/e of the photomodulation signal at t=0 is 280, 790, 930, and 1100 ps, respectively. (d) MPL(B) response for the same films 1–4 (marked by the corresponding colours), having a HWHM of about 100, 40, 35, and 25mT, respectively.

3.7 Conclusion

In conclusion, we identified room temperature transient PA bands in the mid-IR range that are due to photogenerated excitons in all three perovskite that we measured here, namely $MAPbI_3$, $MAPbI_{1.1}Br_{1.9}$, and $MAPbI_{3-x}Cl_x$. For $MAPbI_3$, both exciton and free carriers are photogenerated at short time, unraveling the excitons/photocarriers duality nature of neat perovskites with relatively small binding energy of less than k_BT at RT. The fraction of exciton can be significantly increased when temperature is reduced down and the phase changes from tetragonal to orthorhombic. In contrast, we found that mainly excitons are initially photogenerated in $MAPbI_{1.1}Br_{1.9}$ and $MAPbI_{3-x}Cl_x$ due to the substantially larger exciton binding energy in these two perovskites. Our work shows that the exciton binding energy in the hybrid perovskites is a crucial parameter that determines the branching ratio between the photogenerated exciton and free carriers following the thermalization process; this in turn influences the ultrafast photoexcitations spectroscopic response. The RT tetragonal crystal structure anisotropy in $MAPbI_3$ allows for a finite photoinduced transient and cw polarization memory. We used the transient polarization memory decay dynamics and the grain-like crystallite film structure of $MAPbI_3$ films to estimate the diffusion constant of excitons in this perovskite: this technique is a *bonus* in anisotropic crystalline compounds. Our results are validated by the fact that $MAPbI_{1.1}Br_{1.9}$, which is isotropic at RT, does not show any transient polarization memory. Another benefit of the polarization memory in $MAPbI_3$ is that we unambiguously identify the PL band at room temperature as due to electron-hole recombination rather than due to exciton recombination, and this justifies the existence of the magneto-PL recently observed in this perovskite. The excitons/free carriers duality

found in our studies justifies the natural dissociation of excitons into free carriers in the bulk of the hybrid perovskites with $E_b<k_BT$ at RT; in cases where $E_b>k_BT$, the long exciton diffusion length that we obtained here strongly indicates that excitons may dissociate at grain boundaries and interfaces at a later time.

We further studied the transient PM dynamics of 3D perovskite films of markedly different nano-morphologies. We observed an enhanced photoluminescence yield in $MAPbBr_3$ films with an anti-solvent-based treatment during spin-coating. NCP-treated films display smaller crystalline domains and better substrate coverage, and the transient PM study showed that the higher PLQE resulted from a decrease in non-radiative trapping and thus longer lived excitons. We have also measured the e-h pair lifetime, τ in $MAPbI_{3-x}Cl_x$ films with various morphologies using picosecond PM spectroscopy, and found that the photoexcitation dynamics are in excellent agreement with the obtained MPC(B) and MPL(B) shape and magnitude, which validates the Δg model used for interpreting the various MFE(B) responses.

Therefore, our work paves the way for photovoltic, light-emitting, lasing, and spin-related applications of the fascinating 3D perovskites.

CHAPTER 4

OPTICAL SPECTROSCOPIES IN TWO-DIMENSIONAL (2D) LAYERED HALIDE HYBRID PEROVSKITE (PEPI)

In the present chapter, we have employed a plethora of ultrafast transient pump-probe and nonlinear optical spectroscopies for studying the primary (excitons) and long-lived (free-carriers) photoexcitations in thin films of a two-dimensional (2D) layered hybrid organic-inorganic halide perovskite, namely $(C_6H_5C_2H_4NH_3)_2PbI_4$ or PEPI. The 2D layered hybrid perovskite semiconductors form natural 'multiple quantum wells' that possess strong spin-orbit coupling (SOC) due to the heavy elements (Pb and I) in their building blocks. This may lead to 'Rashba-splitting' close to the extrema in the electron bands as discussed in Chapter 1. The density functional theory calculation shows the occurrence of Rashba-splitting in the plane perpendicular to the 2D barrier as discussed in Section 1.5.2. From the electroabsorption spectrum and photoinduced absorption spectra from excitons and free-carriers, we indeed obtain a giant Rashba-splitting in this compound, with energy splitting of 40 ± 5 meV and Rashba parameter of 1.6 ± 0.1 eV·Å; these are among the highest Rashba-splitting size parameters reported so far. This finding shows that 2D hybrid perovskites have great promise for potential applications in spintronics.

4.1 Introduction

Spin-orbit coupling (SOC) can split the spin-degenerate bands of electron dispersion relation, $E(k)$, in a semiconductor with non-centrosymmetric compounds, as first realized by Dresselhaus and Rashba and discussed in Chapter 1. The two Rashba-split branches have *opposite spin sense* that influences the photoexcitations optical and magnetic properties, a situation that may benefit spintronics since it enhances the spin-to-charge conversion efficiency [97-99]. More importantly, the SOC is enhanced in reduced dimensions such as in two-dimensional (2D) semiconductors [96].

Large Rashba-splitting with splitting parameter, α_R, of a few eV·Å has been observed in only a handful of materials such as ultrathin metallic films [101], surfaces of topological insulators such as Bi_2Se_3 [102], and the polar semiconductor BiTeI [103]. We note that Rashba-splitting is very small in traditional III-V semiconductors. For example, α_R at the interface of InAlAs/InGaAs was measured to be ~0.07 eV·Å with energy splitting E_R ~1 meV [104]. In contrast, here we discovered a giant size Rashba-splitting in a 2D semiconductor, namely layered hybrid organic-inorganic perovskite.

Although there has been a tremendous advance in the power conversion efficiency (PCE) of PV solar cells based on the hybrid organic-inorganic perovskites as discussed in Chapter 1 and 3, the spin degree of freedom has not been the focus of attention in these materials. The hybrid perovskites possess strong SOC due to the heavy elements (Pb, X) that determine the electron bands near their extrema points, which may lead to large Rashba-splitting if the structure lacks inversion symmetry [105]. Even though there have been numerous theoretical predictions of Rashba-splitting in the hybrid perovskites [106], few experiments has proved this phenomenon in perovskites. In 3D perovskites, namely

$MAPbBr_3$ and $MAPbI_3$, there have been some very recent experimental proofs for Rashba-splitting using ARPES and optical spectroscopy [107-109]. The interest in the hybrid perovskites potential for spintronics applications has only recently begun, with promising spin and magnetic field phenomena [93]. Therefore, solid evidence of the existence of Rashba-splitting in these compounds would further boost this interest.

Recently, the 2D hybrid perovskites have come into focus [137, 180]. These compounds self-assemble into alternating organic and inorganic layers that form natural 'multiple-quantum wells', with outstanding optoelectronic characteristics and stability at ambient conditions as discussed in Chapter 1. Having strong SOC, high-charge mobility, and intrinsic quantum well structures with many interfaces and facile solution processability, the 2D hybrid perovskites may show Rashba-splitting and be promising candidates for room temperature spintronic applications [110]. However, there has been no experimental proof for the spin-related properties in 2D perovskites. Our work shows that these components have giant Rashba-splitting, which may further enhance their appeal for the spin-related applications.

We have employed a variety of transient and steady-state linear and nonlinear optical spectroscopies for studying the primary excitons photoexcitation in 2D hybrid perovskite films. Our spectroscopies provide compelling evidence that the continuum band-edge above the exciton level (CB bottom and/or VB top) possesses surprising optical characteristic properties that result from a large Rashba-splitting energy, $E_R \approx 40$meV. The **k·p** model calculation is used for Rashba-split bands for the first time and supports the experimental findings. Our work provides a general all-optical method for studying the Rashba-splitting effect in semiconductors.

4.2 Materials

Figure 4.1 (a) shows schematically the 2D hybrid perovskite that we studied here, namely $(C_6H_5C_2H_4NH_3)_2PbI_4$ (PEPI), where the organic ($C_6H_5C_2H_4NH_3^+$) and inorganic $[PbI_6]^{4-}$ octahedron layers form 'multiple quantum wells' with thickness of ~1nm (barrier) and ~0.64nm (well), respectively [110]. The energy gaps are 2.4eV and 4.2eV, and the dielectric constants are 6 and 2~3 in the organic barriers and inorganic well, respectively.

The 2D hybrid perovskite PEPI films were fabricated via one-step solution process as discussed in Chapter 2. We mixed R-NH_3I (where R is $C_6H_5C_2H_4$) and PbI_2 in a 2:1 molar ratio in N, N-dimethylformamide to form solutions with a concentration of 0.5 mol/ml. The solutions were spin-coated on an Oxygen plasma pretreated glass or KBr substrates at 4000 rpm and 90 s, to form 100 nm thick films; the obtained films were subsequently annealed at 100°C for 30 min. The chemicals were purchased from Sigma-Aldrich and used without further purification. All samples were prepared in a nitrogen-filled glove box with oxygen and moisture levels < 1 ppm.

Figure 4.1 (b) shows the XRD pattern of a 100nm PEPI thin film deposited on a glass substrate, which causes the bump between 20 to 30 degree. We have observed sharp peaks with equal distances between each other corresponding to the diffraction pattern from (002) up to (0024). Bragg analysis shows that the layer space is 1.64 nm, which is very consistent with those given by literature [110] and confirms the deposition of a single-phase 2D layer on the substrate. Along with the high transmission through the film (see Figure 4.1(b) inset), we conclude that our following spectroscopies are performed on high-quality films.

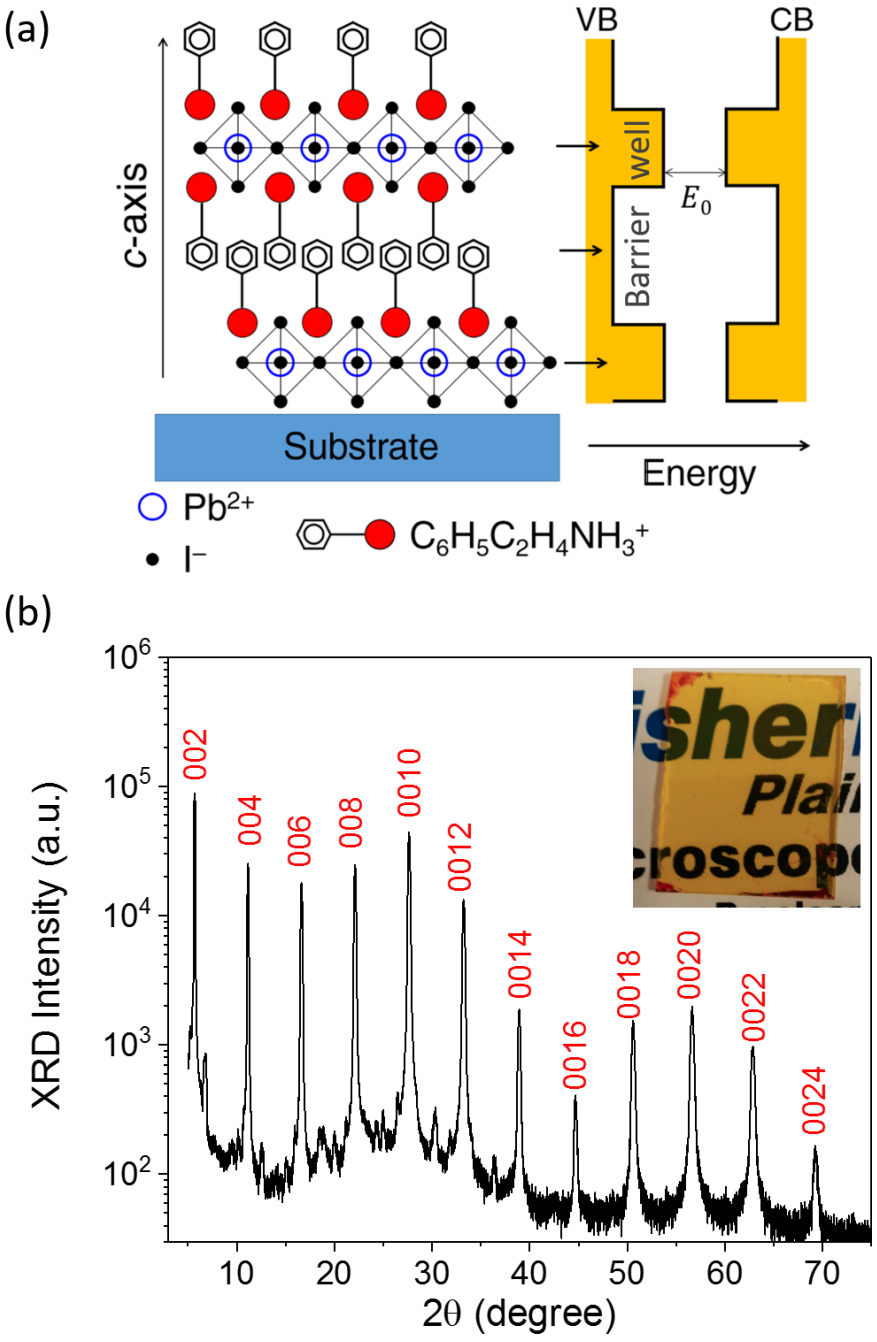

Figure 4.1. 2D perovskite structure. (a) Schematic structure of $(C_6H_5C_2H_4NH_3)_2PbI_4$ (PEPI), with alternating organic and inorganic layers, forming multiple quantum wells on the substrate with thickness of ~1nm (barrier) and ~0.64nm (well), respectively. Adapted from Ref. [110]. (b) XRD pattern of the PEPI film. Inset: the image shows high transmission through the film.

4.3 Linear Absorption and Emission

Even though the Ruddlesden-Popper 2D hybrid perovskites share some common properties with 3D perovskites, for example the Wannier exciton are delocalized in the metal-halide framework in both structures [62], the alternating organic and inorganic sheets that are akin to a quantum well superlattice give rise to quantum and dielectric confinement effects in 2D perovskites resulting in a large exciton binding energy and anisotropic charge transport [181]. The increased exciton binding energy would therefore benefit the studies of exciton properties that are concealed in the analogous 3D structures.

The room-temperature absorption and photoluminescence (PL) spectra of the 2D hybrid perovskite PEPI film are shown in Figure 4.2 (a). Unlike the 3D $MAPbI_3$ absorption shown in Figure 3.4 (a) inset, the absorption and PL in 2D PEPI film are dominated by an exciton band at ~2.4 eV with large oscillator strength, consistent with a relatively large exciton binding energy, E_B of ~0.2 eV [74]. The peak of the absorption and PL spectra centered at 2.40 eV and 2.34 eV, respectively indicates a Stokes shift of ~60 meV through vibrational relaxation.

As the PEPI film is cooled down to 10K, the absorption and PL change and more features show up, as we can see from Figure 4.2 (b). Firstly, the excitonic features become strongly enhanced in both spectra. For example, the optical density peak value increased from 0.52 to 0.91 in absorbance and more than one order in PL spectrum. Secondly, the Stokes shift reduced to ~20 meV, with the absorption and PL spectra centered at 2.37 eV and 2.35 eV, respectively. Moreover, excitonic peak splitting has been observed in both spectra and two step-like absorption edges show up in the absorption spectral range of 2.45-2.65 eV, which are discussed in the following.

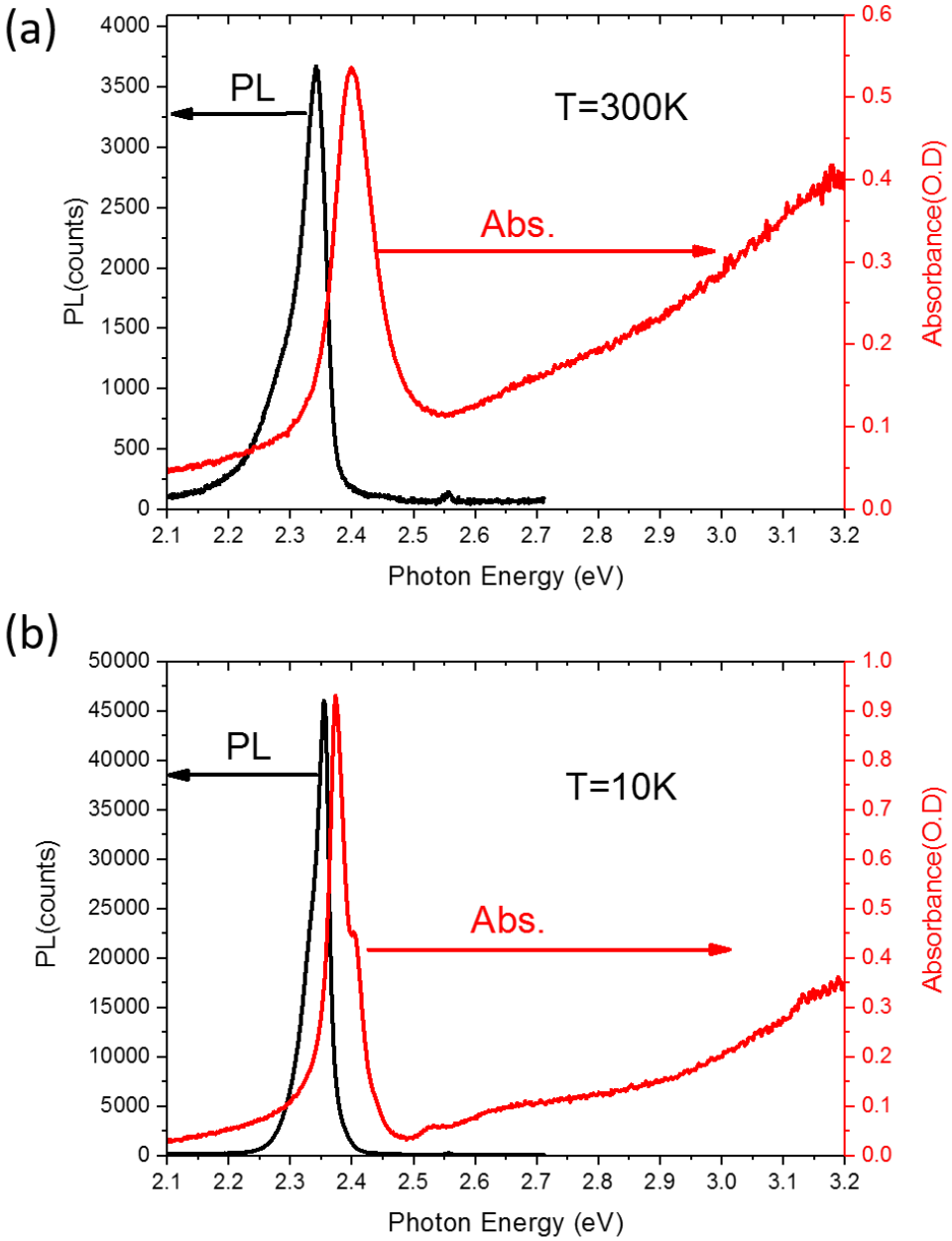

Figure 4.2 Linear absorption and photoluminescence (PL) spectra in 2D perovskites PEPI films at (a) 300K and (b) 10K. The small peak located at ~2.55eV in PL comes from the laser line at 486nm.

4.3.1 Linear Absorption

Figure 4.3 shows the linear absorption of PEPI thin film from 10K to 300K. The whole spectrum shows a blue-shift with increasing temperature, which is consistent with previous reports [181]. The spectra are expanded in the range of 2.30 eV to 2.47eV in Figure 4.3 (b) and (d) to show the evolution of 1s exciton peak with temperature. It is obvious that the excitonic absorption blue-shifts with temperature and splits into two peaks when temperature decreases. This process occurs gradually and no phase transition was observed in the PEPI 2D perovskite structure [181].

In Figure 4.4, we analyzed the excitonic absorption at 10 K and 290 K with a sum of two Gaussian distributions as

$$y = y_0 + \frac{A_1}{\sigma_1\sqrt{2\pi}}\, e^{\frac{(x-x_{c1})^2}{2{\sigma_1}^2}} + \frac{A_2}{\sigma_2\sqrt{2\pi}}\, e^{\frac{(x-x_{c2})^2}{2{\sigma_2}^2}} \qquad (4.1)$$

in which x_c is the center energy, σ is standard deviation, σ^2 is variance, and A is the amplitude. The subscripts 1 and 2 indicates peak 1 and peak 2, and y_0 is the background. The inset tables in Figure 4.4 (a) and (b) show the fitting parameters of the absorption spectra at 10K and 300K.

At 10 K as shown in Figure 4.4 (a), we obtained two peaks centered at 2.375 eV and 2.405 eV with ~30 meV spacing, and at 290K shown in Figure 4.4 (b) the two peaks shift to 2.396eV and 2.436eV, respectively, with ~40 meV spacing. The shift of the center energy x_c of each peak with temperature is show in Figure 4.4 (c), and the two parallel dot lines are drawn to guide the eyes.

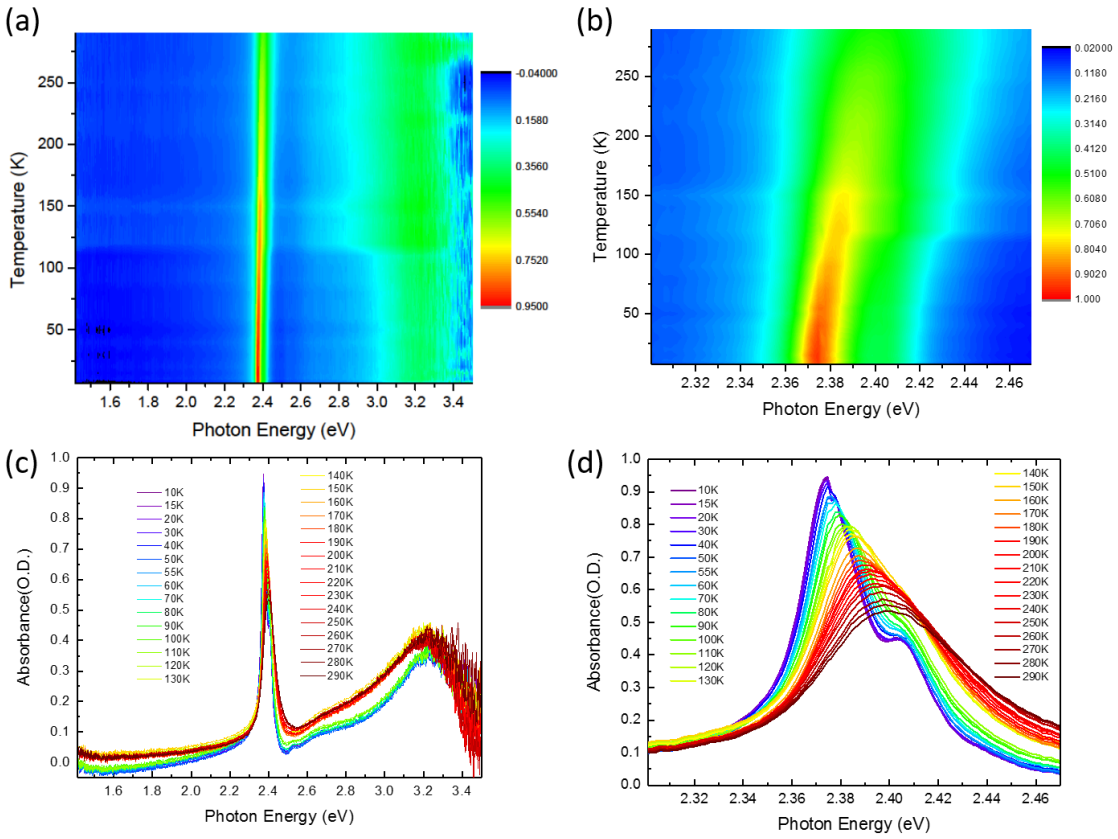

Figure 4.3. Absorption spectra of PEPI film at temperatures between 10 K and 300 K. (a) and (c) Whole spectra range measured from 1.4 eV to 3.5 eV, in which two step-like absorption edges in the spectral range of 2.45-2.65 eV show up at low temperature (T<110K). (b) and (d) Expansion of spectra from 2.30 eV to 2.47 eV to show the excitonic absorption shifting and splitting.

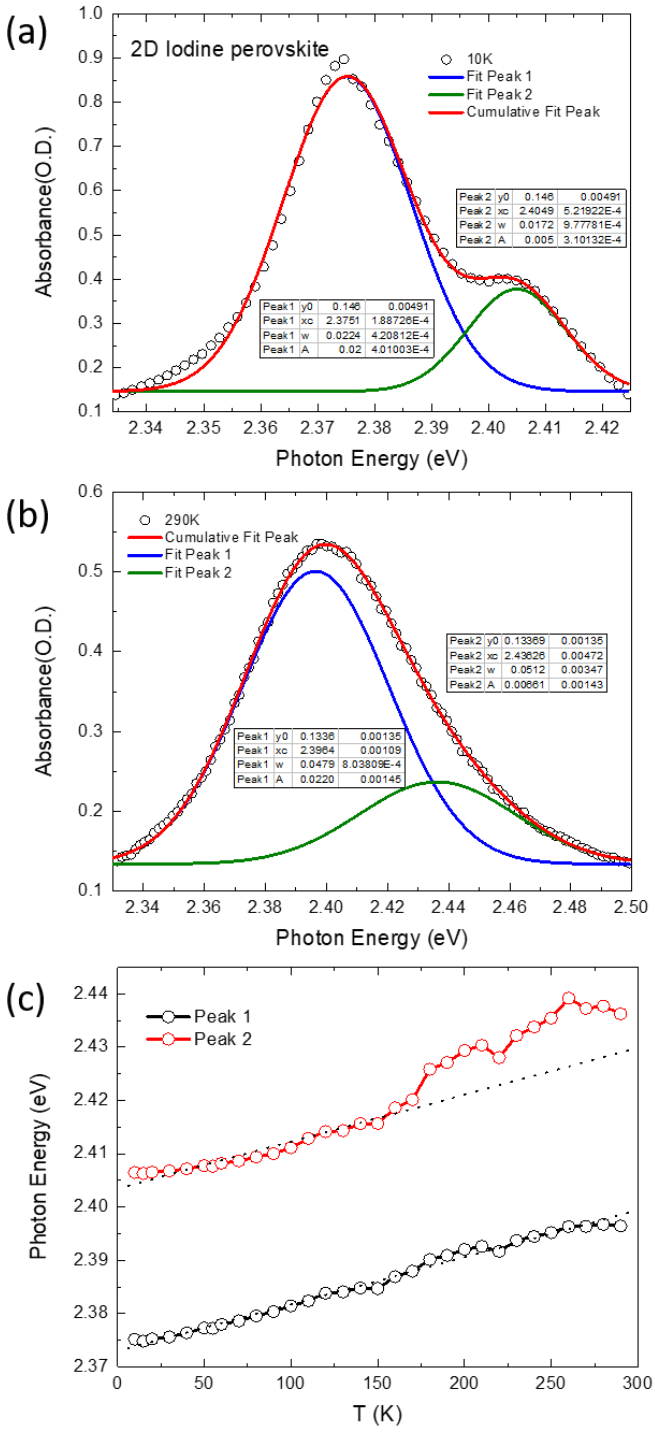

Figure 4.4. Absorption spectra of PEPI at 10K (a) and 300K (b). Red curve shows the fit of the spectrum with a sum of two Gaussian distributions, peak 1(blue) and peak 2 (green). (c) Shift of the fitted peak positions of peak 1 (black) and peak 2 (red) with temperature. The black dot lines are parallel to each other and drawn for guiding the eyes.

The fact that the main peak 1 shifts linearly with temperature and the side peak 2 follows the same trend at low temperature and keeps a constant spacing of ~30meV indicates that peak 1 originates from the 1s exciton absorption and peak 2 arises from the phonon side-band due to electron-phonon interaction. The phonon-side band of about the same values has been reported previously in both single crystals and thin films of 2D perovskites [181]. We noticed that peak 2 does not follow the linear trend at temperature above 180K. This may be because peak 2 is not well resolved above this temperature, which makes the fitting not as accurate as compared to low temperature.

Aside from the main 1s exciton absorption peak, two step-like absorption edges in the spectral range of 2.45-2.65 eV are observed in absorption spectra at low temperatures (T<110K) as shown in Figure 4.5 (a). The lowest step-like feature located at ~2.53 eV has been observed by Tanaka et al. in 2002, and assigned as the 2s exciton absorption [75]. The second step-like feature located from 2.55 eV to 2.60 eV may be interpreted as the interband (IB) transition, from which one can get the information of bandgap E_{IB} (E_g) and accordingly, the binding energy with the known exciton resonant energy. However, this feature is not sharp enough for us to extract the exact values even at 10K. We thus used a modulation spectroscopy, namely the electroabsorption (EA) in Section 4.4, to separate these delicate absorption features from the broad spectral background. Recall that the EA spectrum in neat semiconductors having intermediately large E_B usually contains two different spectral features: a Stark shift of the exciton below the continuum, and a Frank-Keldysh (FK) type oscillatory feature at the continuum band-edge [151]. In Figure 4.5 (b), we show the estimated energy levels of the excitons, E_{1s} and E_{2s}, and interband transition, E(IB), assigned with respect to the ground-state (GS).

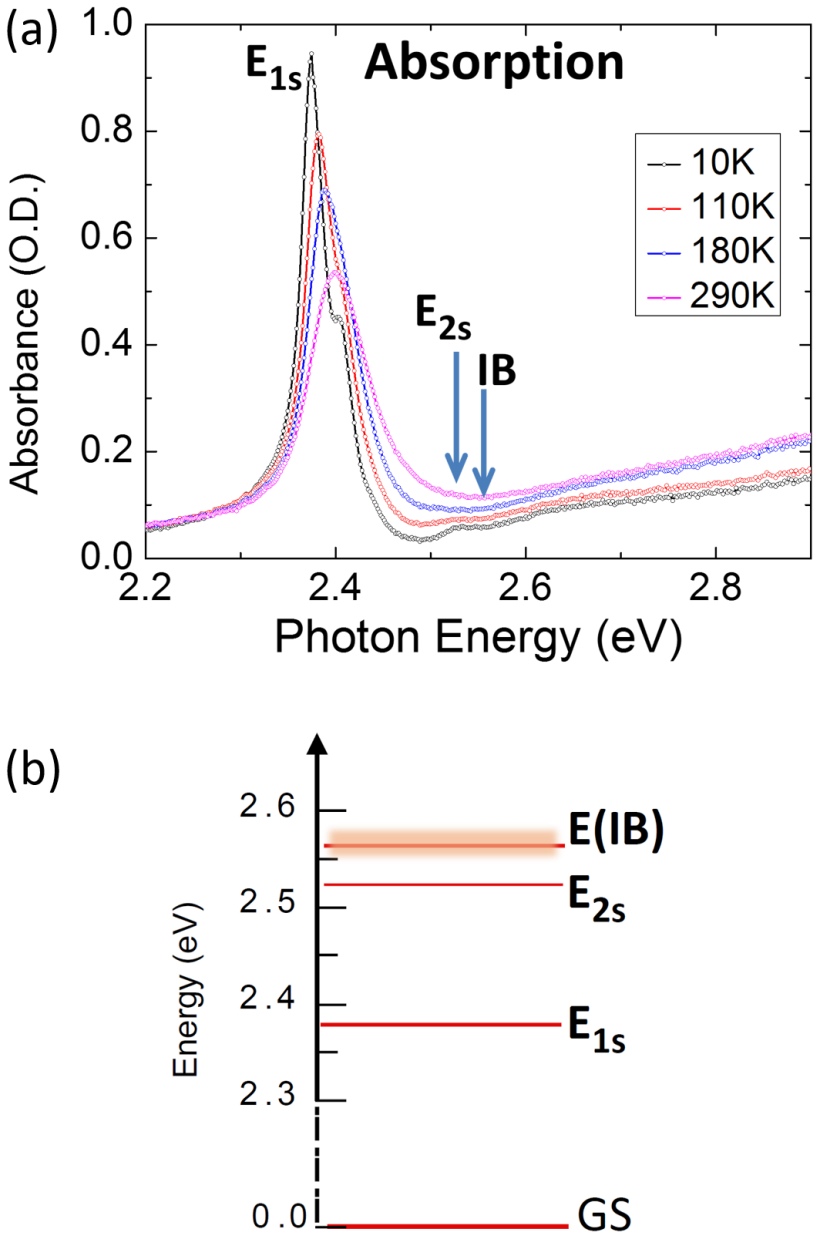

Figure 4.5. Absorption and energy levels of PEPI film. (a) Absorption spectra at 10K, 110K, 180K, and 290 K. The 1s and 2s exciton (E_{1s} and E_{2s}, respectively) and an interband transition (IB) are assigned. (b) Estimated energy levels of the excitons (E_{1s} and E_{2s}) and interband transition (E(IB)) are assigned with respect to the ground-state (GS).

4.3.2 Photoluminescence

Figure 4.6 shows the photoluminescence (PL) spectra of PEPI thin film in a temperature range from 10K to 300K pumped with a 486nm (2.55eV) solid-state laser (not in the exciton resonant energy range). A sharp main peak from ~2.3 eV to ~2.4 eV that decreases dramatically with increasing temperature is clearly observed and expansion of this spectral range is shown in Figure 4.6 (b) and (d). While the spectra blue-shift with increasing temperature, a faint shoulder is observed in the lower energy tail at ~2.34 eV. The multiple excitonic PL peaks in PEPI and other 2D perovskite films have been widely studied previously, but whether they are from free and bound excitons or phonon sidebands is still a matter of debate [181-182]. Here we believe that the free and bound excitons are the most likely attribution by the following analysis.

The PL spectra at 10K and 300K are fit with three Gaussian peaks analogous to Equation (4.1) because two-peak fitting failed to accurately fit the whole range. As shown in Figure 4.7 (a), the highest energy PL peak is located at 2.356 eV, about a 20 meV Stokes shift compared to the lowest absorption peak. The second PL peak, located 11meV lower at 2.345 eV, does not have a corresponding absorption peak. These values, however, agree well with the free and bound exciton results [182]. Additionally, the splitting between peak 1 and peak 2 gets much larger at room temperature up to ~30meV with peak 1 at 2.344 eV and peak 2 at 2.315 eV. It is clear from Figure 4.7 (c) that the two peaks are not correlated to each other and show distinct shift behavior with temperature. We therefore believe the peak 1 arises from free exciton and peak 2 arises from bound exciton. This conclusion is further supported by the fact that the contribution of free exciton emission increases with temperature.

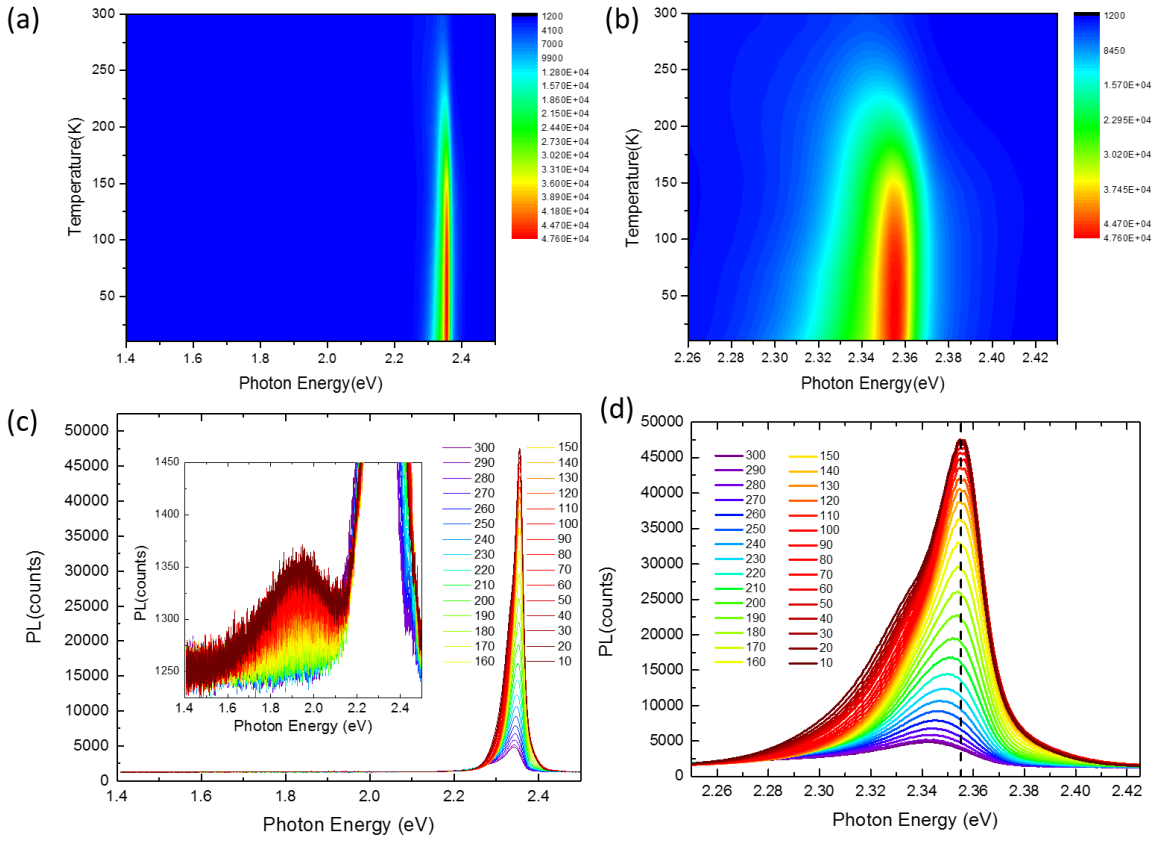

Figure 4.6. Photoluminescence (PL) of PEPI film at temperatures between 10 K and 300 K pumped at 2.55eV. (a) and (c) Whole spectra range measured from 1.4 eV to 2.5 eV, in which a main feature at 2.352eV decreases significantly with increasing temperature. The inset in (c) shows a broad PL peak ~1.93eV. (b) and (d) Expansion of spectra from 2.26 eV to 2.42 eV to show the excitonic emission shifting and splitting.

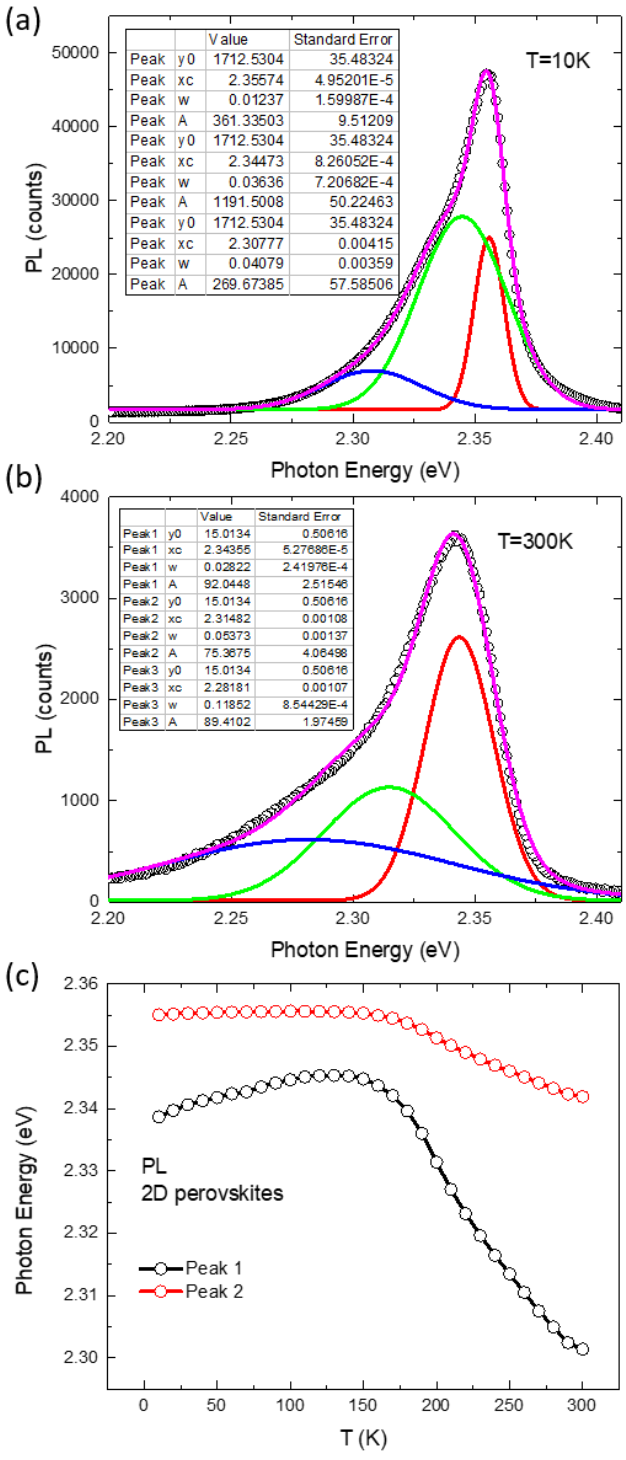

		Value	Standard Error
Peak	y0	1712.5304	35.48324
Peak	xc	2.35574	4.95201E-5
Peak	w	0.01237	1.59987E-4
Peak	A	361.33503	9.51209
Peak	y0	1712.5304	35.48324
Peak	xc	2.34473	8.26052E-4
Peak	w	0.03636	7.20682E-4
Peak	A	1191.5008	50.22463
Peak	y0	1712.5304	35.48324
Peak	xc	2.30777	0.00415
Peak	w	0.04079	0.00359
Peak	A	269.67385	57.58506

		Value	Standard Error
Peak1	y0	15.0134	0.50616
Peak1	xc	2.34355	5.27686E-5
Peak1	w	0.02822	2.41976E-4
Peak1	A	92.0448	2.51546
Peak2	y0	15.0134	0.50616
Peak2	xc	2.31482	0.00108
Peak2	w	0.05373	0.00137
Peak2	A	75.3675	4.06498
Peak3	y0	15.0134	0.50616
Peak3	xc	2.28181	0.00107
Peak3	w	0.11852	8.54429E-4
Peak3	A	89.4102	1.97459

Figure 4.7. PL spectra of PEPI at 10K (a) and 300K (b). Pink curve shows the fit of the spectrum with a sum of three Gaussian distributions, peak 1 (red), peak 2 (green), and peak 3 (blue). (c) Shift of the fitted peak positions of peak 1 (black) and peak 2 (red) with temperature.

A very broad and weak feature centered at ~1.93eV has been observed in PL spectrum decreasing with temperature as shown in Figure 4.6 (c) inset, and it does not have a corresponding absorption peak. D. B. Straus et al. have also observed this feature in the 2D PEPI thin film and assigned it as the trap-assisted recombination by PL excitation (PLE) spectroscopy [181].

4.4 Electro-Absorption (EA) Spectra

As discussed in Section 4.3.1, by electrical field modulation, the EA spectroscopy can be used to separate the delicate absorption features from the broad spectral background and provide information of energy levels.

Figure 4.8 (a) shows the EA spectra of PEPI film at room temperature with linearly increasing parallel-applied voltage V up to 200V ($F \sim 10^5$ Volt/cm) detected at second-harmonic frequency $2f$ (f = 1 kHz). The spectra show two main features, a "first-derivative -like" feature with zero crossing at 2.38 eV, which agrees with the 1s exciton absorption band. The second feature is oscillatory-like and spreads widely at energy above 2.55eV. The spectra are roughly the same over all the measured photon energy and the peak values at each band are quadratically dependent on the applied voltage V as fitted in Figure 4.8 (a) inset. According to Equation (2.20), we identify the EA mechanism as the third order nonlinear susceptibility χ^3 optical response at T=300K.

When the temperature is reduced down to 50K as shown in Figure 4.8 (b), two more features have been observed. First, the exciton phonon side band splits the negative part of the first-derivative-like feature into two peaks. Second, the peak located ~2.5eV broadens as two peaks overlap each other, in which the lower energy peak has a trend to

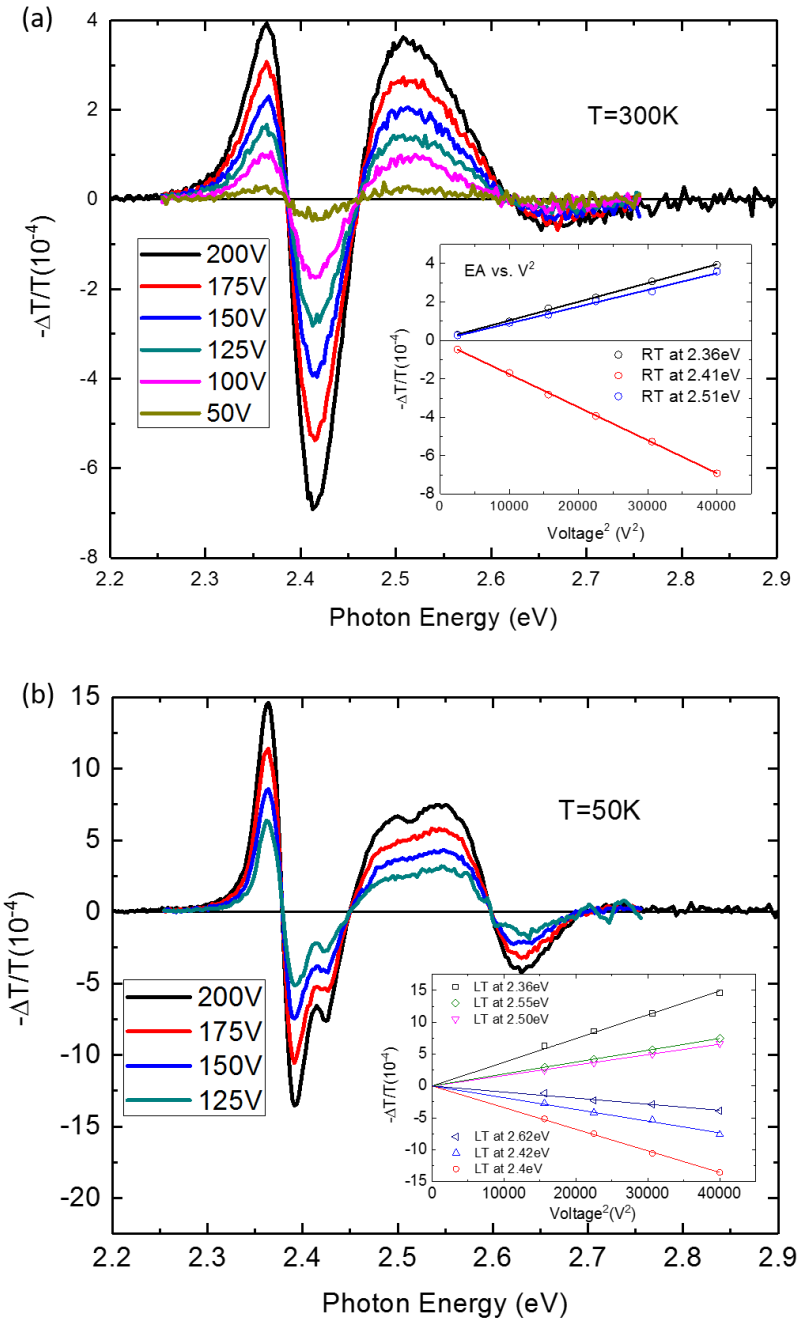

Figure 4.8. EA spectra of PEPI thin film measured at various applied electric fields up to 200V (~ the applied voltage, *V*) at (a) 300K and (b) 50K. Insets plot the linear response of EA signal vs V^2 of each band.

cross zero around the absorption energy that we have assigned to the 2s exciton (~2.53eV), but higher spectral resolution is needed to verify this [151]. Because the spectra still appear the same at voltages up to 200V and the peak values are quadratically responded to the applied voltage V as shown in Figure 4.8 (b) inset, the third order nonlinear susceptibility χ^3 optical response is also assumed at low temperature.

The χ^3 optical response is a typical electro-optical effect that is usually attributed to the excitonic quadratic Stark effect where the EA signal scales with V^2 and the EA spectrum is proportional to the derivative of the absorption with respect to the photon energy ($d\alpha=dE$) as discussed in Section 2.2.4.3. Here we assign the low-energy spectral region ($\hbar\omega<2.55$ eV) of the EA spectrum to the excitons Stark shifts, which are the 1s exciton showing the "first-derivative-like" feature consistent with zero-crossing at 2.38 eV, and the 2s exciton showing a 'trending' zero-crossing at ~2.53 eV. (The 2s exciton Stark shift peak can be more obvious with higher voltage as discussed below.)

The other possibility of χ^3 optical response is called the low-field Frank-Keldysh (FK) effect [183]. As discussed in Section 2.2.4.3, the FK effect is a type of oscillatory feature at the continuum band-edge and usually scales as a complicated function of the applied voltage. However, in the low-field limit the electro-modulation signal can be simplified to a χ^3 optical response that shows a quadratic dependence on the applied field as discovered by Aspnes and Rowe in the early 1970s [183]. We hypothesize that the large oscillatory-like EA feature at $\hbar\omega>2.55$ eV is related to the FK effect because it corresponds to the band-edge measured by linear absorption. Therefore, we applied a higher voltage up to 300V and measured the EA spectrum at slightly lower temperature for larger signal (better signal-to-noise ratio) and sharper absorption peaks.

Figure 4.9 (a) shows EA spectra of the PEPI thin film obtained at ac voltage up to 300V at T=45K and detected at 2*f* with *f*=1kHz. The 1s and 2s exciton band located at ~2.38 eV and ~2.53 eV, respectively, can be clearly identified from their derivative-like feature due to the Stark shift.

Importantly, the large oscillatory-like EA feature at ħω>2.55 eV shows multiple zero-crossings and verifies our FK oscillation hypothesis for the following reasons. First, the oscillation energy period shows "field-broadening". As we expand the EA spectra close to the zero-crossing energy from 2.66 eV to 2.74 eV as shown in Figure 4.9 (b), the high-energy oscillation (marked as "d" in Figure 4.9 (a)) clearly blue-shifts with increasing field indicating the broadening of the FK oscillation. Second, for ħω>2.55, the EA of the "b" and "d" oscillation band does not scale with V^2 and saturates at large field (see Figure 4.9 (c)).

The broadening and the EA saturation at large *V* are typical characteristic properties of the FK oscillation in the EA spectrum close to the band-edge (Interband (IB) transition in Figure 4.5), where the peak at lower energy rather than the first zero-crossing determines the energy gap [151]. We thus locate the band-edge of the PEPI film at 2.57 eV. From E(IB), E_{1s}, and E_{2s}, we can now obtain the 1s and 2s exciton binding energies: E_B(1s) = 190 (±5) meV and E_B(2s) = 45 (±10) meV, respectively, as marked in Figure 4.9 (d). These values verify the large exciton binding energy in 2D perovskites and agree well with the most recent reports of PEPI films [153]. The uncertainty originates mainly from the optical resolution of our spectrometer (2 nm entrance slit size) and the film inhomogeneity; all uncertainties are reported as one standard deviation.

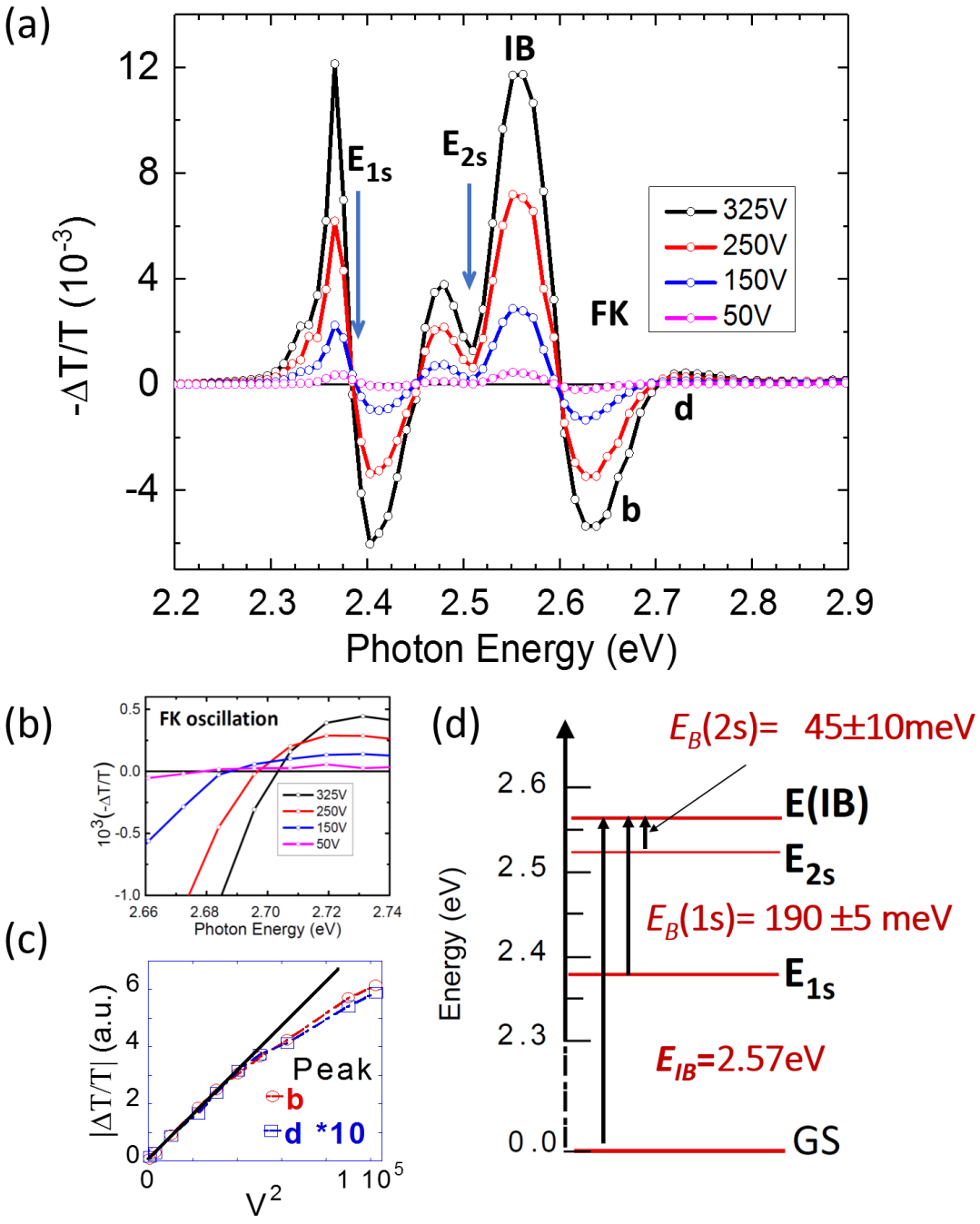

Figure 4.9. EA spectra and energy levels of PEPI film. (a) EA spectra of PEPI measured at 45K at *V* up to 300V. EA spectral features are assigned, where FK stands for the Franz-Keldysh oscillation. (b) EA spectra close to the zero-crossing energy; broadening of the FK oscillation is clearly seen. (c) The peak values of EA vs V^2 of bands 'b' and 'd', which saturate at large *V*. (d) Energy levels of the excitons E_{1s}, E_{2s}, and interband transition E(IB) with respect to the ground-state (GS). (a)-(c) were measured by Sangita Baniya.

4.5 Ultrafast Photomodulation (PM) Spectroscopy

To further investigate the excited states properties of PEPI close to the continuum band minima, we studied the primary photoexcitations using the picosecond (ps) transient photomodulation (PM) in the unique broad spectral range of 0.23 to 2.8 eV excited at 3.1 eV. At t = 0 ps, the PM spectrum contains two dominant spectral features (Figure 4.10): a photoinduced absorption (PA) in the mid-IR spectral range, denoted PA_1 at ~0.35 eV, and a PM feature in the visible spectral range centered at the PEPI exciton absorption (~2.4 eV) having both PA and photo-bleaching (PB) components; as well as a weak PA band at 1 eV denoted PA_2. We note the occurrence of "zero-sum" when adding the PA and PB bands in the PM spectrum, indicating that there are no other important photoinduced features in the spectrum. The visible PM and mid-IR PA features are discussed below.

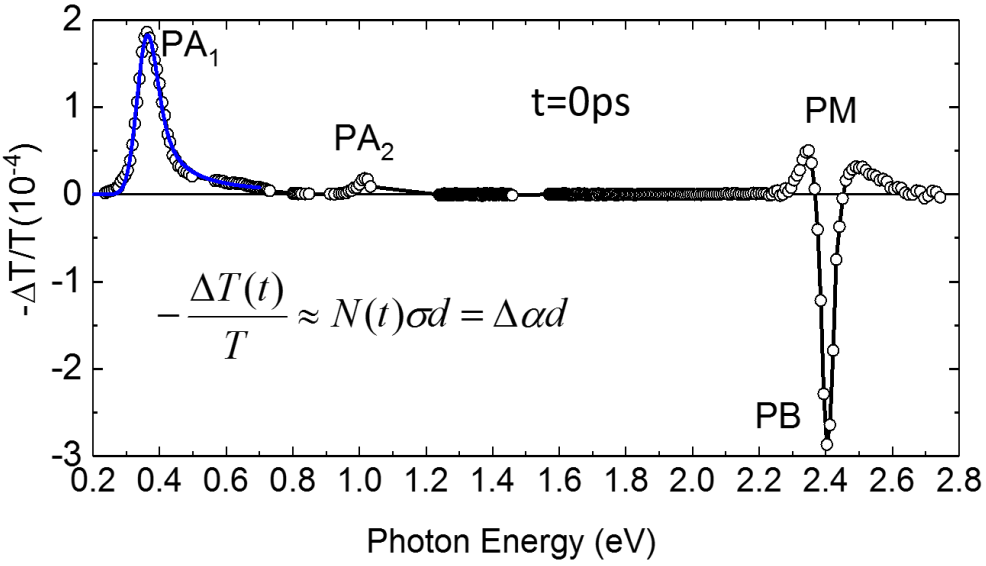

Figure 4.10. Ultrafast photomodulation (PM) spectrum of PEPI film at t = 0ps excited at 3.1 eV. PA_1, PA_2, and PM are assigned. The blue line through the data points of PA_1 is a theoretical fit using Equation (4.5).

4.5.1 Band-Filling Photomodulation (PM)

Figure 4.11 shows the transient photomodulation (PM) measured in visible range with 3.1eV pump at room temperature. The PM spectrum does not shift with time and shows similar decay rate in the whole spectral range as shown in Figure 4.11 (a). The decay dynamics of PM does not change with excitation intensity up to 3 $\mu J/cm^2$ as shown in Figure 4.11 (b), and transient spectra were measured at excitation intensity of 2.8$\mu J/cm^2$, where the $\Delta T/T$ is linearly dependent with pump intensities (Figure 4.11 (b) inset).

The PM band contains photobleaching (PB) signal at 2.4eV, the energy of the exciton line, and photoinduced absorption (PAs) signals on both sides. The PM band can be fit by linear combination of PB of the absorption spectrum, and the absorption first and second derivatives, as shown in Figure 4.11 (c). It therefore can be explained by a combination of "band-filling" due to the primary photoexcitation [60-61], photoinduced symmetry breaking process such as spatially inhomogeneous strain or photoinduced electric field [110, 152], and transient broadening [184]. From the exciton PB in the PM spectrum and strong absorption and PL emission from PEPI, we conclude that the primary transient photoexcitations in this 2D perovskite are *excitons*, mainly 1s excitons.

As the sample is cooled down to 110K, the transient PM is not significantly affected displaying a shift to lower energy and sharpening of PA bands as shown in Figure 4.12 (a), which is consistent with the feature of exciton absorption spectrum at low temperature as discussed in Section 4.1. The PEPI film does not undergo a phase transition and the PM signal decays at the same rate in room and low temperature. Therefore, the "band-filling" of 1s exciton may also be used to explain the PM spectrum at low temperature.

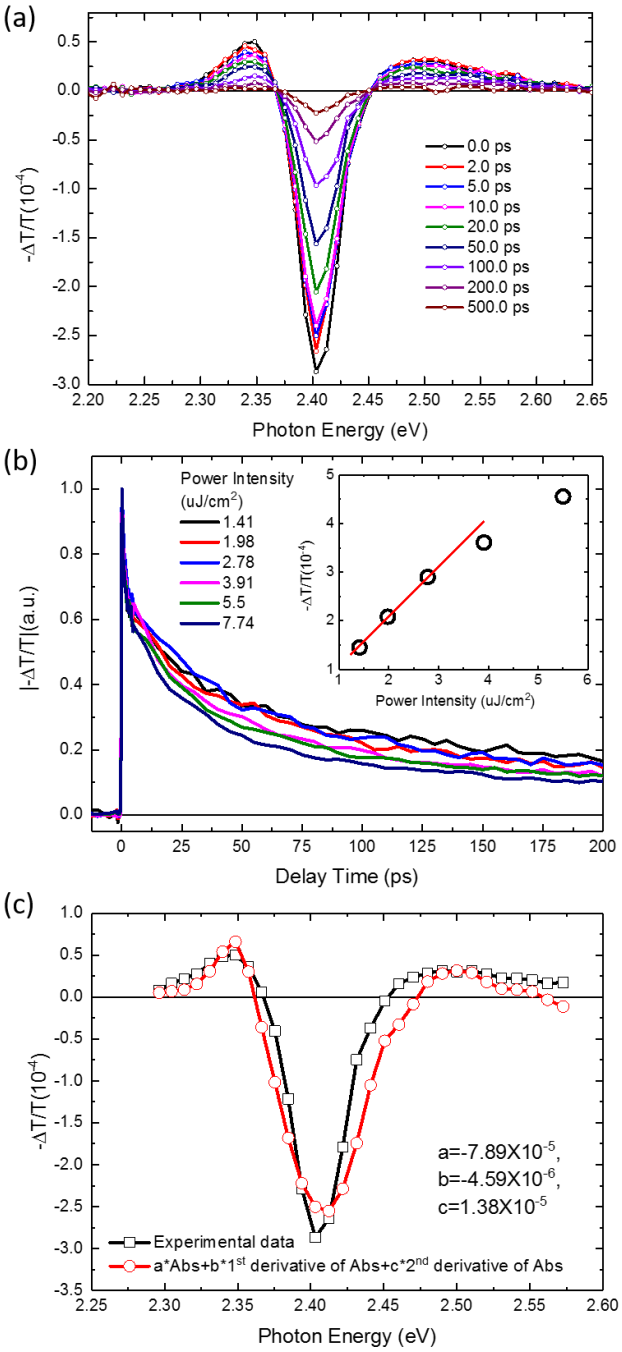

Figure 4.11. The transient PM band in the visible spectral range of a PEPI film measured at 300K. (a) PM band at various delay times. (b) The PM in a PEPI film at various excitation intensities. Inset: ΔT/T at t =0 ps vs. pump excitation intensity, circles are experimental, red line is the linear fit for first three excitation intensities. (c) PM at t=0ps and its fit using a linear combination of the absorption spectrum and its first and second derivatives.

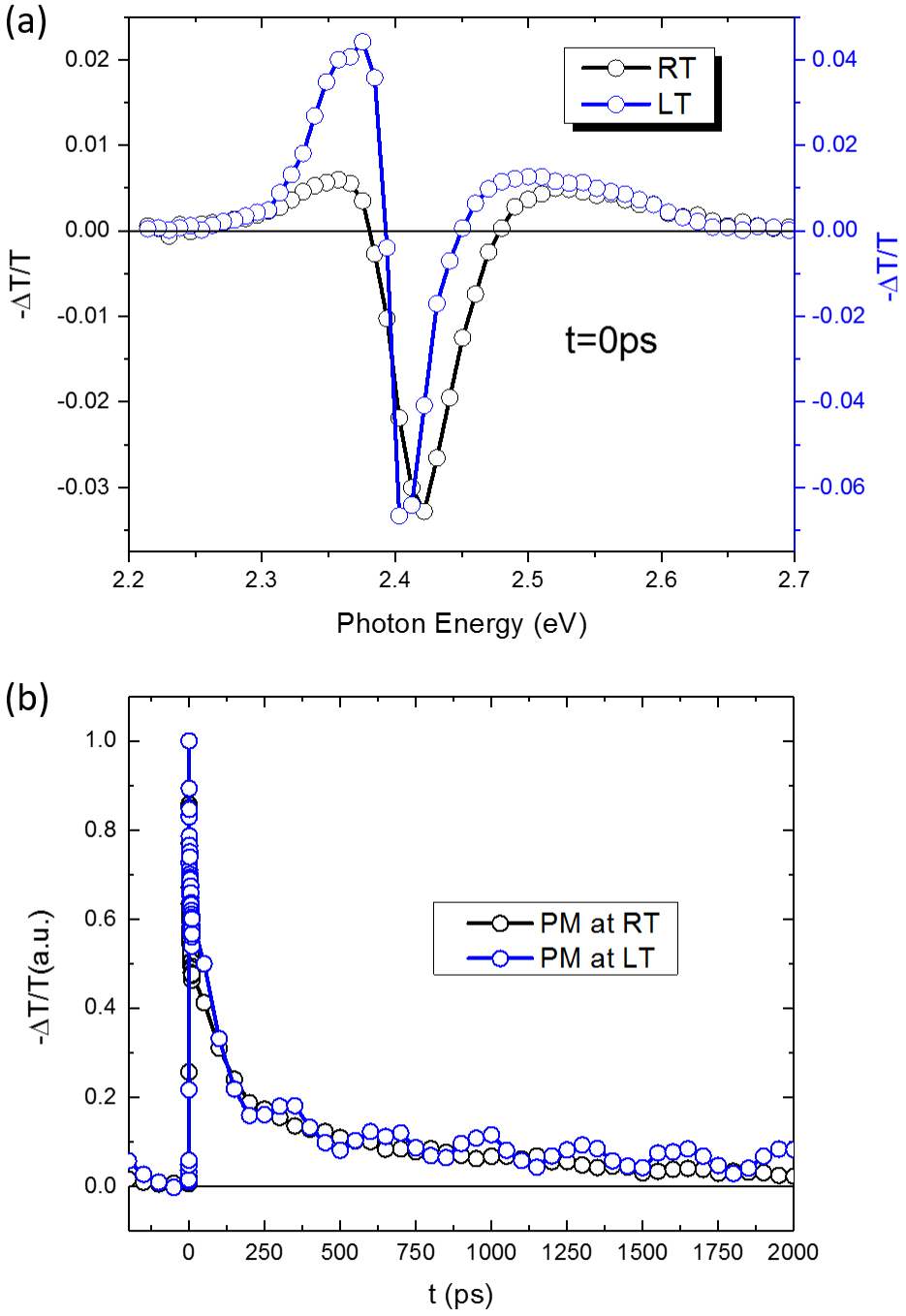

Figure 4.12. Temperature-dependence of PM in PEPI film. (a) The transient PM band in the visible spectral range of PEPI film measured at t=0ps and 300K (black) and 110K (blue). (b) PM decay dynamics up to 2000ps at 300K (black) and 110K (blue).

The existence of transient broadening in the PM band can be explained by the delocalization of excitons discussed in Section 4.5.2, indicative of high quality of naturally formed quantum wells in 2D perovskite. It is surprising to observe that the nonlinearity in the pump intensity dependence appears at a low excitation intensity of ~4 $\mu J/cm^2$ for the excitons with small Bohr radius (Figure 4.11 (b) inset). For a 100 nm 2D perovskite PEPI film, the optical density at 3.1 eV is about 0.5 as shown in Figure 4.2 (a) and the pump intensity of ~4 $\mu J/cm^2$ then results in the excitation intensity of $4\times10^{17}cm^{-3}$. For the repeat unit of PEPI quantum well at ~1.64 nm (Figure 4.1), the density of excitons in quantum well is then about $6.5\times10^{10}/cm^2$. If the interaction between excitons in neighboring quantum wells can be ignored because of the quantum well and dielectric confinement effects, the nonlinearity shown in Figure 4.11 (b) inset may originate from the interactions between excitons among the same quantum well. The distance between excitons is estimated to be 20 nm at ~4 $\mu J/cm^2$, which is consistent with the localization length of exciton from the analysis of the asymmetry of PA_1 band in the next section.

4.5.2 Photoinduced Absorption (PA) in Mid-IR

As the primary transient photoexcitations in this 2D perovskite are mainly 1s excitons, we can study the electron bands simply from the exciton transition into the adjacent continuum band(s).

Figure 4.13 (a) shows the PA features in PEPI thin film from 0.23 eV to 1.05 eV at room temperature, and the dominant spectra feature is PA_1, a band-like transition in semiconductors with large exciton binding energy. In addition, PA_1 band doesn't shift with time and PA_1 dynamics do not change with pump intensity (Figure 4.13 (a) inset).

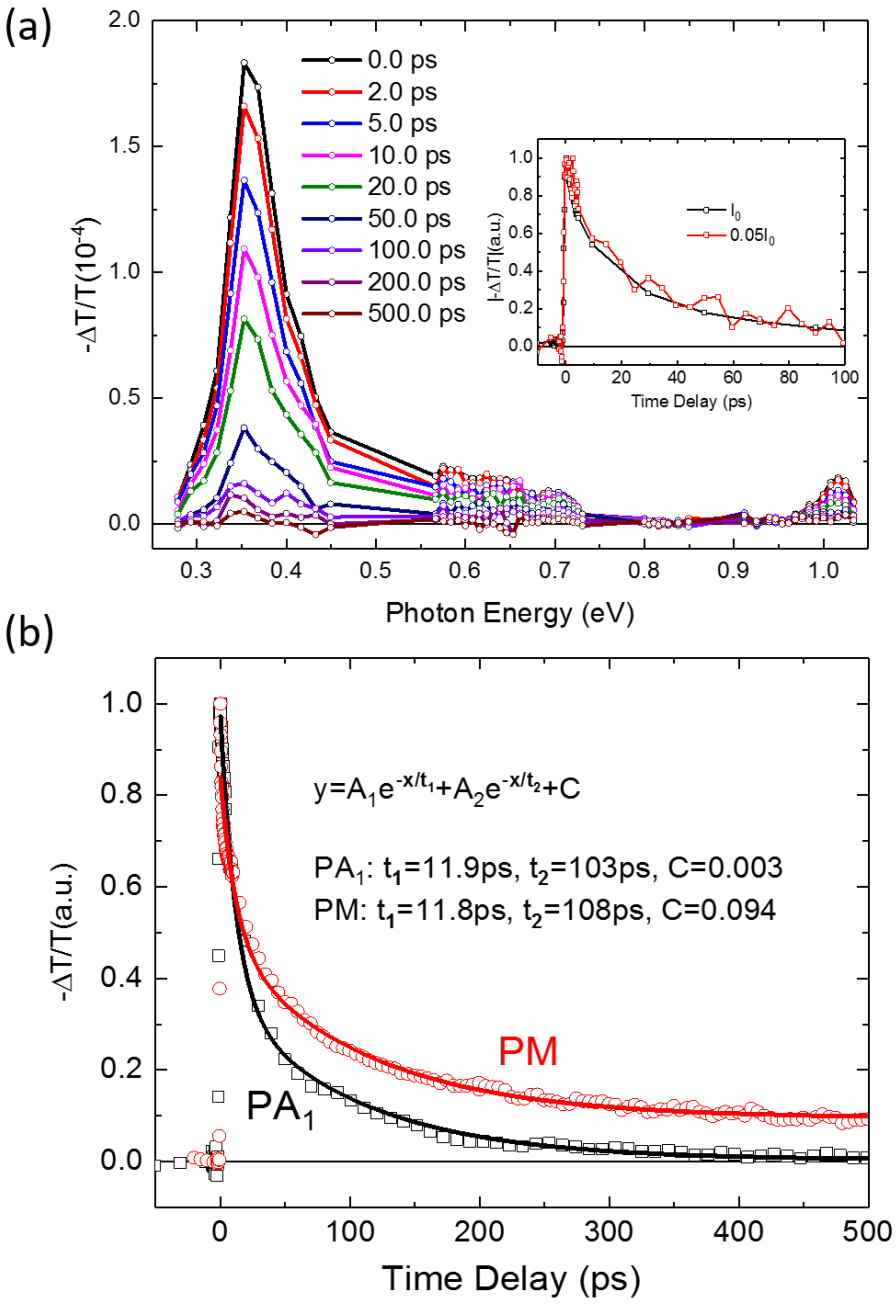

Figure 4.13. The transient PA bands in mid-IR range of PEPI film measured at 300K. (a) PA bands at various delay times. Inset: PA_1 decay dynamics at measured pump excitation intensity I_0 and 5% of I_0. (b) Decay dynamics of the PM band at 2.4 eV and PA_1 at 0.36 eV up to 500 ps. The lines through the data points show the bi-exponential decay fits and the best fit parameters are indicated.

The decay dynamics of PA_1 up to 500ps are fit and compared with PM at comparable excitation intensities as shown in Figure 4.13 (b). The bi-exponential decays ($\sim A_1 e^{-t/t1} + A_2 e^{-t/t2} + C$) are parameterized by nearly identical dynamics as t_1 =11.9 ps, 11.8 ps, t_2 = 103 ps, 108 ps, with different constants C = 0.003 and 0.094, for PA_1 and PM bands, respectively. The long-lived photoexcitations should be free-carriers since the excitons have sufficiently long time to ionize into free electrons and holes that can contribute to photocarriers. This has been verified in PV cells based on 2D perovskites that have shown power conversion efficiency larger than 10% [137]. Therefore, we conclude that the PA and PM bands originate from a *single* primary photoexcitation species.

The PA_1 band from the excitons into the continuum band peaks at 350 (±2) meV (the uncertainty comes from the 150 fs pulse duration), which cannot be ascribed to the vertical transition from the 1s exciton into the lowest continuum band, since from our EA studies, a transition into the lowest continuum band should appear at 190 meV. We therefore assign PA_1 to an optical transition from the 1s exciton to a second, upper electron continuum branch, which is split from the lower band by Rashba spin-orbit coupling, as shown schematically in Figure 4.14 (a). We have looked for a second PA band at ≈0.2 eV (i.e., into the lower continuum band), but could not find any hint of it down to 0.23 eV (see Figure 4.13 (a)). Our finding suggests that a direct optical transition from the exciton into the lower Rashba-split branch is either forbidden or much weaker compared to that in traditional semiconductors such as GaAs (78). To rationalize this result, we note that the transition from a 1s exciton to a band minimum of free electron-hole pairs is proportional to the electrical dipole moment matrix element between a conduction (valence) band state and itself.

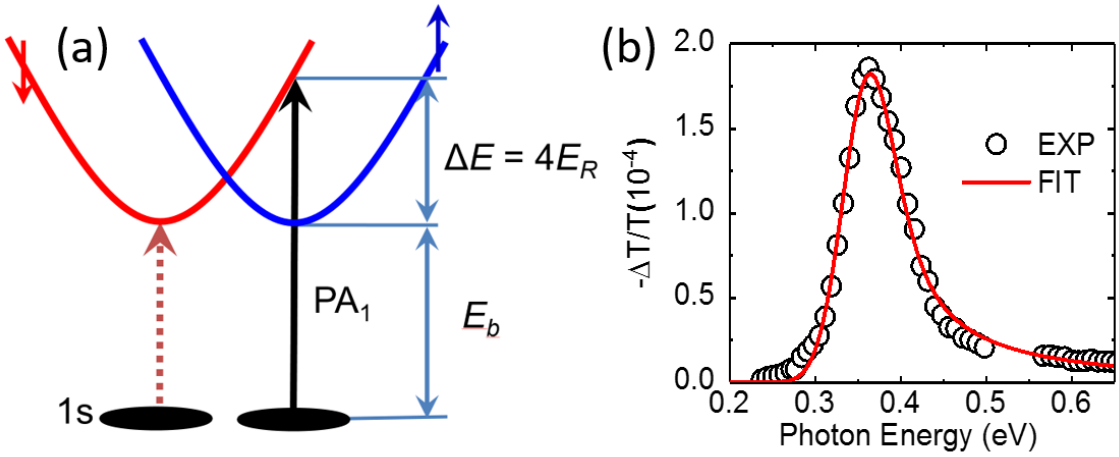

Figure 4.14. PA_1 transition in PEPI film. (a) Schematic energy diagram with Rashba-splitting that explains the PA_1 transition. The Rashba energy (E_R) may be obtained from the 1/4 of energy difference (ΔE) between PA_1 transition and the 1s exciton binding energy (E_b). (b) Asymmetric PA_1 band is fitted by "k-space extension model" in Equation (4.5), yielding the delocalization length of exciton, l~16 nm.

This is because the initial exciton includes a Bloch state of the conduction band minimum, and the final electron-hole pair includes this same Bloch state. This matrix element is nothing more than the momentum expectation value of the Bloch state, which vanishes at the band minimum. In previous analysis of the exciton-CB transition in GaAs (78), the authors replaced the free carrier wave function by a *p*-state of an unbound electron-hole pair wave function, enabling the dipole transition from exciton to continuum band. In our 2D perovskite film, disorder from point defects and grain boundaries may destroy the coherence of the unbound electron-hole pair, so that optical transitions rely solely on the properties of the Bloch wave functions. Section 1.5.2 shows the density functional theory calculation of various electrical dipole transition matrix elements, which verifies that only transitions into the upper Rashba-split conduction band

are allowed.

We therefore can readily obtain the Rashba-splitting energy, E_R, from the PA_1 band at 0.35 eV, since PA_1 should be pushed to higher energies by an energy, $\Delta E = 4E_R$ namely $E(PA_1) = E_B + 4E_R$ (Figure 4.14 (a)). Using this relation, E_B (=190 meV from the EA spectrum) and $E(PA_1)$ =350 meV (from the transient PA spectrum), we determine E_R = 40±5 meV in 2D PEPI.

We note that PA_1 band is asymmetric; this may be a result of the transition from the exciton discrete level to the continuum band, where the exciton wave function is spread in momentum ***k***-space by a '*k*-localization length' Δ*k*, as determined by its 'localization length', *l* in real space, and $\Delta k \approx 1/l$ [110].

In the ***k***-space of a quantum well, the energy-dependent absorption coefficient α(E) of an electron from the exciton state into the continuum can be expressed as,

$$\alpha(E) \propto \frac{1}{E}\int d^2k|M(k)|^2\,[f(E_{ex}(k)) - f(E_{cb}(k))]\,\delta(E_{ex}(k) - E_{cb}(k) - E), \qquad (4.2)$$

where E_{ex} and E_{cb} are the energies of the exciton and continuum band (CB or VB), respectively; *f(E)* is the Fermi-Dirac distribution function, and *M* is the matrix element for the transition.

The exciton wave function is localized in real space over a distance, *l*, and thus the exciton is not a δ-function in k-space, but instead is spread over a range, Δ*k* in *k*, where $\Delta k \approx 1/l$. Therefore, we should integrate over $k < \Delta k$, and the absorption coefficient can be expressed as the following:

$$\alpha(E) \propto \frac{1}{E}\int d^2q|M(q)|^2\,|C(q)|^2\,\delta(E_{ex}(q) - E_{cb}(q) - E), \quad (4.3)$$

where C(q) is a 'mixture function' that is spread over Δk, and determines the *k*-space extension of the exciton wavefunction. We replace the Fermi-Dirac distribution function with a step function at E_B, if the exciton temperature is low compared to the exciton binding energy, E_B.

Assuming that the exciton wave function in real space is proportional to exp$(-r/l)$, where l is the 'localization length', $C(q)$ is given by the Fourier transform of the real space extension,

$$C(q) \propto (1 + l^2q^2)^{-1} \quad (4.4)$$

Consequently, the k-space exciton extension, $\Delta k = l^{-1}$, and the absorption, α(E), for a 2D system can be then expressed by,

$$\alpha(E) \propto \frac{(E - \Delta_0)}{E}\left(\frac{1}{E - \Delta_0 + \hbar^2/2l^2m^*}\right)^2 \quad (4.5)$$

where m^* is the electron effective mass, and Δ_0 is the transition energy. We calculated the exciton PA using our DFT results $m^* = 0.25\ m_0$, where m_0 is the free electron mass, and $\Delta_0 = 0.35$ eV. The solid line through the asymmetric PA_1 data points in Figure 4.14 (b) is a fit using Equation (4.5) considering a Gaussian distribution $F(\Delta-\Delta_0)$ of Δ around Δ_0 having width $\delta\Delta$, from which we obtained the exciton localization length $l \approx 16$ nm. This

relatively large *l*-value indicates that the exciton is quite delocalized in the quantum well in a direction perpendicular to the barriers. Also, the weak PA_2 band at ~1 eV may be readily explained as the optical transition from the exciton level at ~2.4 eV into higher lying bands at ~3.3 eV, which can be clearly seen in the absorption spectrum in Figure 4.3 (c) similar to the transient PM spectra of excitons in nanotubes and in 3D $MAPbI_3$ perovskites as discussed in Chapter 3.

From the obtained E_R value, we can readily estimate the offset, k_0, in the momentum space using a parabolic dispersion relation with an electron effective mass, $m^* = 0.25m_0$, in the perovskites; we thus obtained $k_0 = (0.051 \pm 0.004)$ $Å^{-1}$. Consequently, we estimate the Rashba-splitting parameter $\alpha_R = (1.6 \pm 0.1)$ eV·Å. These values are comparable to the recently measured Rashba parameters in $MAPbBr_3$ using the surface-sensitive angle-resolved photo-electron spectroscopy (ARPES) [107].

4.6 Optical Transitions in PEPI film

As shown in Figure 4.14 (a) and discussed in Section 4.5.2, we have observed an optical transition between the 1s exciton to the upper Rashba-split band at 0.35eV, but no optical transitions between the 1s and the closest Rashba band. Here we use the **k·p** perturbation theory (Kane model) discussed in Chapter 1 to calculate the possible optical transitions in PEPI film when Rashba-splitting exists.

In general, if all quantum numbers except spin are identical for two bands, then the electric dipole optical transitions (EDOT) are forbidden because EDOT requires that the orbital quantum numbers of the initial and the final states must differ by 1 while the spin remains unchanged.

As discussed in Section 1.5.1, when considering spin-orbit (SO) coupling the Schrödinger equation in the **k·p** approximation under the influence of a periodic potential, V(**r**) may be written as

$$\left\{\frac{p^2}{2m}+V+\frac{\hbar}{m}\vec{k}\cdot\vec{p}+\frac{\hbar}{4m^2c^2}\left[\vec{\nabla}V\times\vec{p}\right]\cdot\vec{\sigma}+\frac{\hbar}{4m^2c^2}\left[\vec{\nabla}V\times\vec{k}\right]\cdot\vec{\sigma}\right\}u_k=E'u_k \quad (4.6)$$

where *E'* is defined at $E-\hbar^2k^2/2m$, and σ is the Pauli spin operator. The valence band s-wave function is denoted as |Sα> and the conduction band *p*-wave functions are |Xα>, |Yα>, |Zα>， compatible with the symmetry, with α = ↑(spin up), or ↓(spin down). The fourth term in the left-hand side (LHS) of Equation (4.6) is the atomic-like SO interaction and is *k*-independent. The Rashba-splitting stems from the linearly *k*-dependent SO interaction term (the fifth term in the LHS of Equation (4.6)). First, we ignore this linear *k*-dependence SO term.

Taking, for simplicity, k||z and following the procedure outlined in Ref. [6] we obtain for small values of *k,* three parabolic conduction bands and one valence band each with a characteristic mass,

$$E_{c_1}(k)=E_g+\Delta+\frac{\hbar^2k^2}{2m} \quad (4.7)$$

$$E_{c_2}(k)=E_g+\Delta+\frac{\hbar^2k^2}{2m}+\frac{2P^2k^2}{3E_g}\equiv E_g+\Delta+\frac{\hbar^2k^2}{2m_{le}} \quad (4.8)$$

$$E_{SO}(k)=E_g+\frac{\hbar^2k^2}{2m}+\frac{2P^2k^2}{3(E_g+\Delta)}\equiv E_g+\Delta+\frac{\hbar^2k^2}{2m_{SO}} \quad (4.9)$$

$$E_v(k) = -\frac{\hbar^2 k^2}{2m} - \frac{P^2 k^2}{3}\left(\frac{2}{E_{c_1}} + \frac{1}{E_{c_1} + \Delta}\right) \equiv -\frac{\hbar^2 k^2}{2m_v} \tag{4.10}$$

where P is the Kane parameter, E_g is the energy gap between the valence band (VB) and the lowest conduction band (CB), Δ is the SO splitting energy, and m_{SO} and m_{le} are the respective effective masses. The lowest conduction band, E_{SO}, is the split-off band that is shifted downward by the SO interaction. Each band is doubly spin degenerate.

Except for the highest band, which is a pure p-wave function, the wave functions for the other bands are mixtures of s- and p-wave functions,

$$\phi_{j\alpha} = a_j\left|iS\downarrow> + b_j|(X - iY)\uparrow>/\sqrt{2}\right| + c_j|Z\downarrow> \tag{4.11}$$

$$\phi_{j\beta} = a_j\left|iS\uparrow> + b_j|-(X + iY)\downarrow>/\sqrt{2}\right| + c_j|Z\uparrow> \tag{4.12}$$

The index *j* refers to the bands *v*, *c2*, *SO*. a, b, c are the mixture coefficients,

$$a_j = kP\left(E_j + \frac{\hbar^2 k^2}{2m} + \frac{2\Delta}{3}\right)/N \tag{4.13}$$

$$b_j = \left(\frac{\sqrt{2}\Delta}{3}\right)\left(E_j + \frac{\hbar^2 k^2}{2m} - E_g - \Delta\right)/N \tag{4.14}$$

$$c_j = \left(E_j + \frac{\hbar^2 k^2}{2m} - E_g - \Delta\right)\left(E_j + \frac{\hbar^2 k^2}{2m} - E_g - \frac{\Delta}{3}\right)/N \tag{4.15}$$

where N is a normalization constant. The optical transitions between the various bands are proportional to $|P|^2$.

When the Rashba-splitting term (Equation (4.6)) is not ignored, then the spin degeneracy is removed. In particular, the lowest conduction band, SO, is split into two Rashba-split bands,

$$E_{SO_\alpha} = E_g + \frac{\hbar^2 k^2}{2m_{SO}} + \alpha_R k \tag{4.16}$$

$$E_{SO_\beta} = E_g + \frac{\hbar^2 k^2}{2m_{SO}} - \alpha_R k \tag{4.17}$$

where α_R is the Rashba-splitting parameter. The minimum of the band is offset by $k_0 = m_{so}\alpha_R/\hbar^2$. These two bands are shown in Figure 1.10. Ignoring the small effect of the Rashba term on the wave functions, Equations (4.11) to (4.15) with k replaced by $k \pm k_0$, represent well the wave functions of the two Rashba-split bands.

We first check if there is EDOT between two Rashba bands, so called inter-Rashba optical transitions. For EDOT, the transition probability is proportional to the square of the Kane parameter P between the initial and final states. Consequently, optical transitions are non-zero only when the wave function content of the initial and final states have contributions from both the conduction band (*p*-like) and valence band (*s*-like) character. We now consider a vertical optical transition from the minimum of the lowest Rashba-split band at $k=-k_0$ to the other Rashba-split band at the same k. The transition energy equals $4E_R$, as shown in Figure 4.14 (a). Using Equations (4.11) to (4.15) with k replaced by $k \pm k_0$ and conserving spin, we conclude that non-zero optical matrix elements between the two Rashba-split bands are proportional to the product of the coefficients $|a_j(k)^* b_j(k1)|^2$, where $k1$ is at the minimum of the band shifted by $k=2k_0$.

It is seen that for finite k, the optical transition probabilities between these two Rashba-split bands are finite, while for k =0, the transition probability is zero.

This analysis also explains the optical transitions between the 1s exciton level and the Rashba bands as we observed in Figure 4.13 (a). The electron wave function of the 1s exciton is composed mainly of the wave functions of the CB minimum (at $k=k_0$) of the closest Rashba-split band. Since at the band minimum the wave functions are purely p-like (Equations (4.11) to (4.15)), no optical transitions are possible between the 1s and the closest Rashba band. On the other hand, the dipole operator couples p and s states if the transition is into the upper Rashba-split band (Figure 4.14 (a)). This explains the experimentally observed PA_1 band shown in Figure 4.13 (a).

4.7 Conclusion

In conclusion, we investigated the Rashba-splitting effect in 2D perovskite material PEPI using a variety of cw and ps transient optical spectroscopies. From absorption and PL spectra as well as the EA measurements, we locate the band-edge of the PEPI film at 2.57 eV, and the binding energies of 1s and 2s exciton as E_B(1s) = 190 (±5) meV and E_B(2s) = 45 (±10) meV, respectively. These values verify the large exciton binding energy in 2D perovskites caused by the quantum confinement effects.

Strong spin-orbit coupling in the 2D perovskite PEPI causes Rashba-splitting in the continuum band, where the spin-degenerate parabolic band splits into two branches with opposite spin-aligned electronic states. This causes both the optical transitions of excitons into the continuum band to acquire an additional energy term of $4E_R$. In ultrafast PM spectra, we found a strong photoinduced transition from an exciton state to a continuum

state at energy of 0.35 eV which is about 0.15eV higher than the binding energy of excitons, from which we have determined the Rashba-splitting energy, E_R= 40 ± 5 meV and Rashba-splitting parameter α_R= 1.6 ± 0.1 eV·Å in PEPI 2D hybrid perovskite, which is among the highest values reported so far. Instead of angle-resolved photoelectron spectroscopy (ARPES), which is used extensively to measure Rashba-splitting but is an exclusively surface sensitive technique, our work supplies a comprehensive, all-optical method for studying the Rashba-splitting effect in semiconductors. Our methods may be extended to other bulk semiconductors such as GaAs upon consideration of the proper spectral range.

CHAPTER 5

ULTRAFAST SPECTROSCOPY OF PHOTOEXCITATONS IN HALIDE HYBRID PEROVSKITE SINGLE CRYSTALS

In this chapter, we studied the electron-hole recombination in a solution processed inorganic-organic hybrid lead-trihalide perovskites $MAPbBr_3$ single crystal using picosecond transient photoinduced modulation (PM) spectroscopies. Compared to thin films, perovskite single crystals have greater advantage for the study of intrinsic properties and optoelectronic applications due to reduced defects. However, their bulk and surface photophysics are still under debate, especially how to discern the contribution from each other. Here we used a picosecond laser to pump a $MAPbBr_3$ single crystal at 400nm that has short penetration depth and mainly excites the near-surface region, and studied photoexcitation recombination in this material. We observed the buildup of a broad photoinduced absorption (PA) band together with corresponding decay of a photobleaching (PB) band on the same time scale up to ~100 ps, which becomes faster at higher excitation concentration. Additionally, a long-lived photoluminescence (PL) tail has been observed at delay time longer than 2ms with spectral red-shifting compared to that measured immediately. Both of our results suggests the diffusion of photoexcited carriers from the surface to the interior of the crystal.

5.1 Introduction

The organic-inorganic hybrid perovskites showing long carriers lifetime, high optical absorption coefficients, and low cost solution processing have been intensively studied for optoelectronic applications such as photovoltaics, lasing, and light emission, and their poly-crystalline thin films have been discussed in previous chapters. Recently, the ability to grow larger size single crystals of such materials like methylammonium lead iodide ($MAPbI_3$), bromide ($MAPbBr_3$), and chloride ($MAPbCl_3$) at low cost have enabled more advantages of perovskites optoelectronics [52, 84, 160]. Single crystals, compared with their counterpart thin films, show significantly lower defect densities, and therefore higher mobility, lower electron-hole recombination rate, and longer carrier diffusion length [84, 185].

On the other hand, the high absorption of perovskites limits the light penetration depth to less than 100nm in single crystal materials, and the influence from the surface on the bulk properties cannot be neglected, because the surface usually contains a lot of dangling bonds, chemical impurities, trapping states, and so on [148]. Furthermore, a recent study has shown that the surface state density of the $MAPbBr_3$ perovskites crystals has ultrahigh sensitivity to the environmental gas, which leads to different PL properties in different gases. While the surface regions have been extensively studied via various optical techniques such as time-resolved photoluminescence (TRPL), time of flight (TOF), and photocurrent spectroscopy [84, 148, 185], the question as how to separately study the coexisting surface and bulk photoexcited species, and how one diffuses to the other, are still open.

In this study, we used picosecond transient photoinduced modulation (PM)

spectroscopy and investigated the electron-hole recombination in the $MAPbBr_3$ perovskites single crystal within the near-surface region. We observed a broad photoinduced absorption (PA) band that builds up with the decay of a photobleaching (PB) band on the same time scale up to about 100 ps indicating the surface recombination and diffusion. The rising time of the PA band becomes shorter at higher pump pulse energy that manifests faster diffusion at higher photoexcitation concentration. Additionally, a red-shifted and long-lived photoluminescence (PL) signal has been observed at delay time longer than 2ms that also states the diffusion of photoexcited carriers from the surface to the interior of the crystal.

5.2 Materials

The $MAPbBr_3$ single crystals (crystal structure shown in Figure 1.5) were grown by solution-processing solvent vapor exchange method as discussed in detail in Chapter 2. By tuning of fabrication parameters like boiling point and miscibility, the size of crystal can be tuned from ~μm up to "Macro" crystals of mm dimensions as shown in Figure 5.1.

To get sufficient transmission of the white light continuum (WLC) probe beam in transient pump and probe measurement, small and thin crystals at size around 2mm×2mm×0.2mm were selected. All measurements have been done in air to study the surface properties of the $MAPbBr_3$ single crystal, which have been shown to have ultrahigh sensitivity to environmental gases [186].

A thin layer of polydimethylsiloxane (PDMS) film was used on a pretreated glass substrate to set the single crystals. PDMS is an optically clear polymeric organosilicon compound and has no effect on the ultrafast optical measurement in vis/NIR range [61].

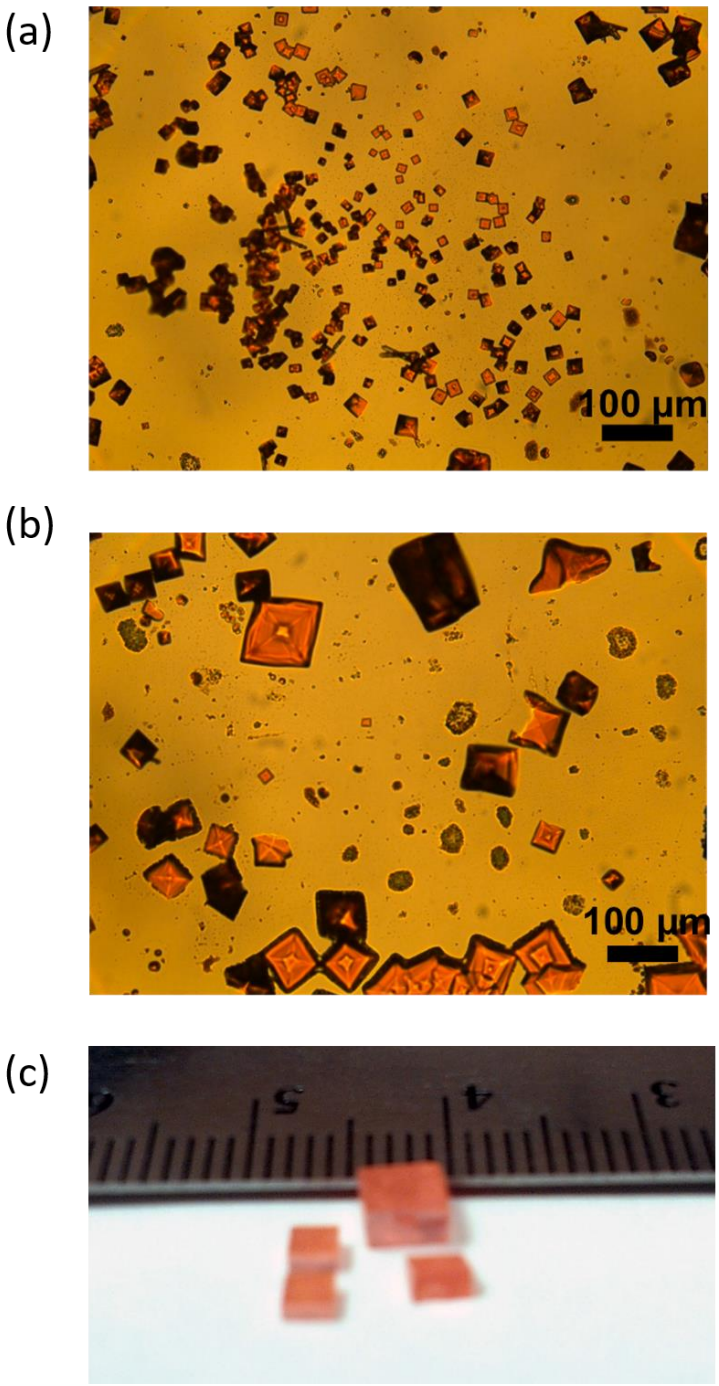

Figure 5.1. $MAPbBr_3$ single crystals grown by solvent vapor exchange. The size of crystal can be tuned through parameters like boiling point and miscibility from ~µm (a) up to "Macro" crystals of mm dimensions (c). For transient PM measurement, small and thin crystals were selected to ensure the transmission of the probe beam.

5.3 Ultrafast Photomodulation (PM) Spectroscopy in $MAPbBr_3$ Single Crystals

To investigate the surface and bulk recombination kinetics in $MAPbBr_3$ single crystal, we performed picosecond ultrafast photomodulation (PM) spectroscopy on the $MAPbBr_3$ single crystal in air. The pump wavelength was chosen to be at 400 nm (3.1eV) with low pulse intensity at around $15\mu J/cm^2$ to study the near-surface region. The penetration depth under such an experimental condition is assumed to be about 80nm.

Figure 5.2 shows the measured transient PM results in visible spectral range from 1.6eV to 2.3eV. Even though our probe white light continuum (WLC) provides a wide spectrum up to 2.8 eV, no PM signal has been detected in the thick $MAPbBr_3$ single crystal (about 0.2mm) because of its great absorption.

The transient PM spectra at early delay time of 1 ps, 10 ps, and 100 ps are shown in Figure 5.2 (a). Two features can be identified from the spectra, a strong and fast photobleaching (PB) tail at photon energy higher than 2.1 eV and a very broad and weak photoinduced absorption (PA) band almost isobestically at lower energy with a blue-shift and rise at longer time. The PB band has also been observed in $MAPbBr_3$ thin film samples as shown in Figure 3.18 and discussed in Section 3.6.1. The PB peak in the polycrystalline thin film is located at about 2.35 eV and assigned to the band filling or stimulated emission effect, which also explains the PB feature in the single crystal here even though only a tail can be seen. The PA peak located at lower energy and rising in the first 100 ps (Figure 5.2 (a)), however, was not observed in polycrystalline thin films (neither the as-cast nor NCP-treated film) and bulk crystal [148]. It is a distinct phenomenon in the near-surface region of the single crystal.

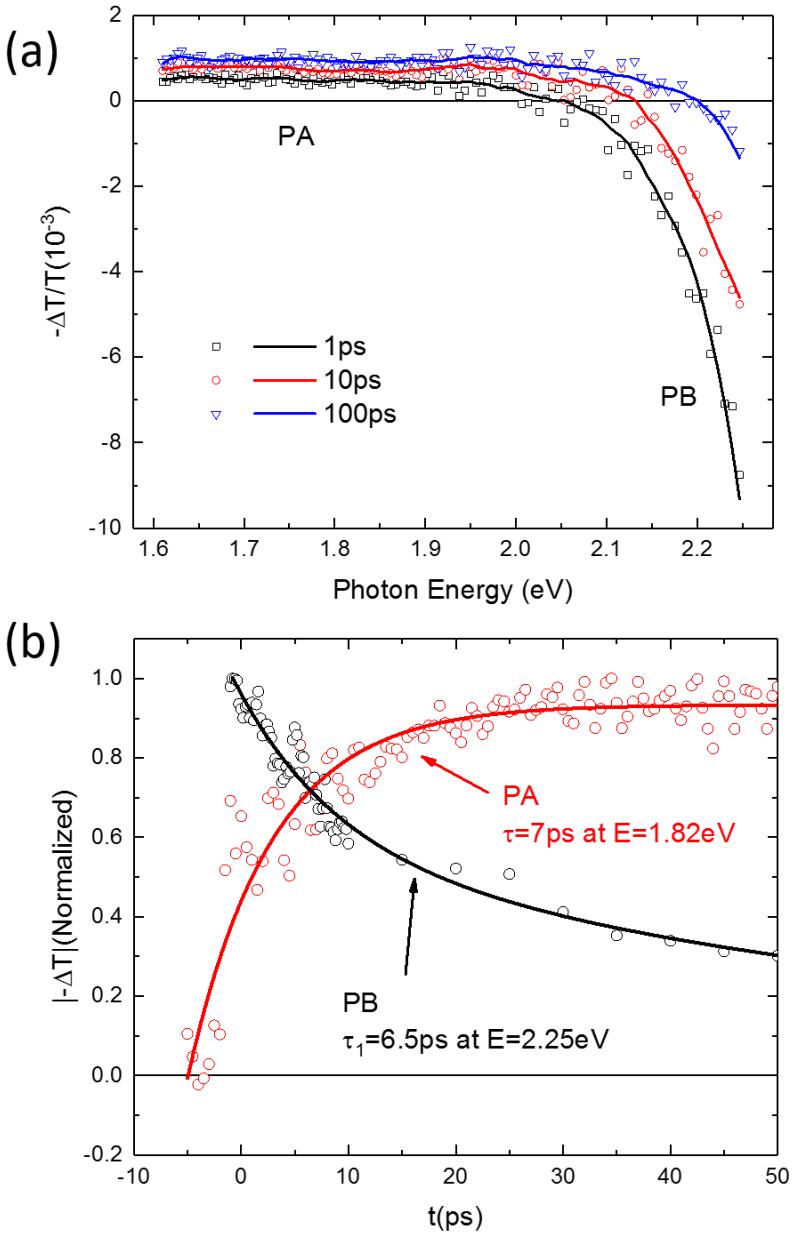

Figure 5.2. Transient PM spectra in $MAPbBr_3$ single crystals at early time (< 100ps). (a) PM spectra at different time delay, 1ps (black), 10ps (red), and 100ps (blue). Two features are observed, a low-energy broad photoinduced absorption PA and a high-energy photobleaching PB. (b) The early time dynamics up to 50 ps. The rapid decay of PB (~7 ps) is correlated with the rise time of PA (~6.5 ps).

According to previous studies, the PA band may come from the transition of the photoexcitation to higher states [148] or sub-bandgap trap state absorption [186]. These effects may be neglected in thin film with ~100nm thickness but greatly enhanced in thick single crystal at mm scale.

Figure 5.2 (b) shows the decay dynamics and the fits of PB and PA in the first 50 ps. The PB recombination rate is fit with a bi-exponential decay

$$y = A_1 e^{-\frac{t}{\tau_1}} + A_2 e^{-\frac{t}{\tau_2}} + C, \tag{5.1}$$

in the time scale up to 2000ps as the longer decay is discussed later. The PA band within 50 ps is fit with an exponential rise equation

$$y = C - A_1 e^{-\frac{t}{\tau_1}}. \tag{5.2}$$

The fits result in a rapid decay of PB (~7 ps) and a correlated rise time of PA (~6.5 ps), which along with the blue-shift of the spectrum indicates that the surface excitation diffuses very efficiently in $MAPbBr_3$ single crystals.

The transient PM spectra at time longer than 100 ps are shown in Figure 5.3 (a), in which the solid lines are the smoothed data using 10 points average and external boundary to guide the eyes. It is clear to see that the PB peak has disappeared at ~200 ps and the PA band decays in nanosecond scale. The PB and PA decay dynamics and the fits up to 2000ps are shown in Figure 5.3 (b). The lifetime of PB extracted from the fit is about 53ps, while that of the PA is about 1ns.

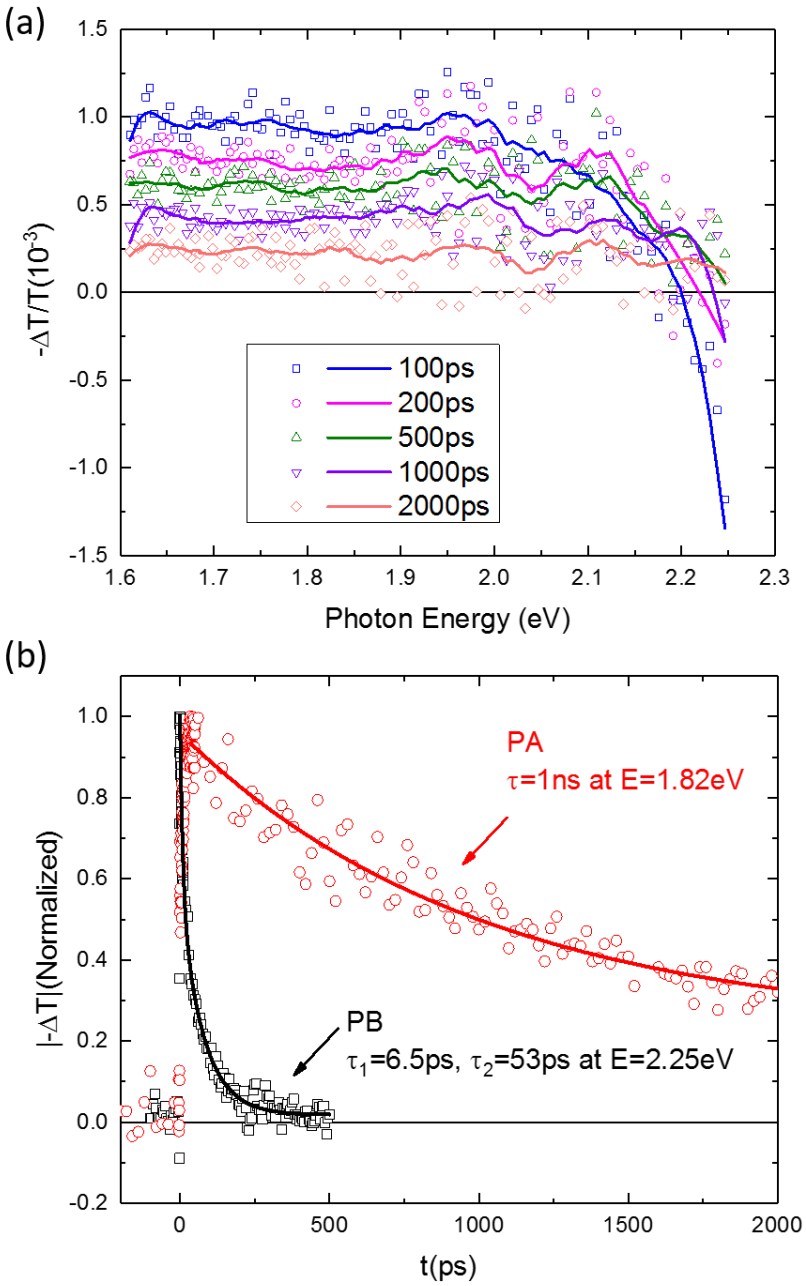

Figure 5.3. Transient PM spectra in $MAPbBr_3$ single crystals from 100ps to 2000ps. (a) PM spectra at different time. The high-energy photobleaching PB disappears. (b) The decay dynamics of PA (red) and PB (black) up to 2000 ps. PB_2 decays fast with the fit life time ~6.6 ps and ~53 ps, which matches the life of PB in the polycrystalline thin film of $MAPbBr_3$ studied in Chapter 3 (see Figure 3.8 (d)).

As the rising PA is attributed to the surface photoexcitation diffusion, the rising time should be able to be tuned by changing the excitation concentrations. In Figure 5.4, we show the PA decay dynamics at various pump intensity from 5 $\mu J/cm^2$ up to 100 $\mu J/cm^2$ and observed significant change of the PA dynamics.

Figure 5.4 (a) shows PA dynamics up to 2000ps (log scale) in the linear recombination range where the decay rate does not depend on the pump intensity. The rising time, however, becomes greatly shorter at higher excitation intensity, which indicates a much faster diffusion due to higher excitation concentration. The build-up time at low excitation intensity (~5 $\mu J/cm^2$) is up to 100 ps, and this agrees well with the previously reported results. In the similar work done by Wu et al. [148], they estimated a diffusion length of about 48 nm from this build-up time and claimed that the value represents the average propagation distance of the excited species away from the surface photoexcited region into the bulk as the distribution equilibrates.

As the pump fluence is increased significantly to the nonlinear region at 100 $\mu J/cm^2$, as shown in Figure 5.4 (b), the PA signal is generated immediately within the time resolution of our system and higher-order recombination shows up as expected from a very high photoexcitation concentration.

In the WLC system as discussed in Chapter 2, the pump beam is modulated at 500Hz; therefore, all the photoexcitations that live longer than 2ms are accumulated and show as a background in the transient spectroscopy. Since most of the photoexcitations cannot live so long, we do not usually see the background signal in WLC system. However, in materials with high PL efficiency such as the $MAPbBr_3$ single crystal studied here, the tail of the long-lived PL signal can show as the background (see Figure 5.5).

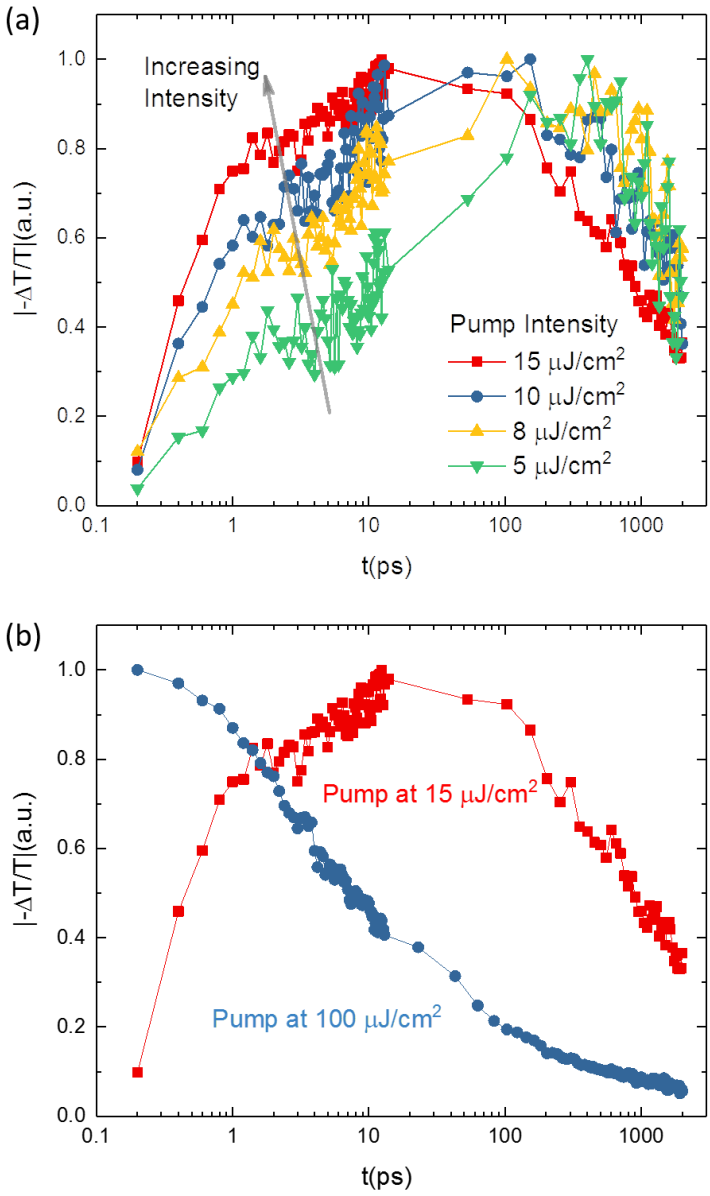

Figure 5.4. The dependence of the decay dynamics on pump intensity of PA band in $MAPbBr_3$ single crystals up to 2000ps. (a) The decay dynamics of PA in linear recombination range at various pump intensities (5 to 15 $\mu J/cm^2$); the faster diffusion rate causes shorter rising time at higher intensity. (b) Higher-order recombination shows up when pump intensity is increased to 100 $\mu J/cm^2$.

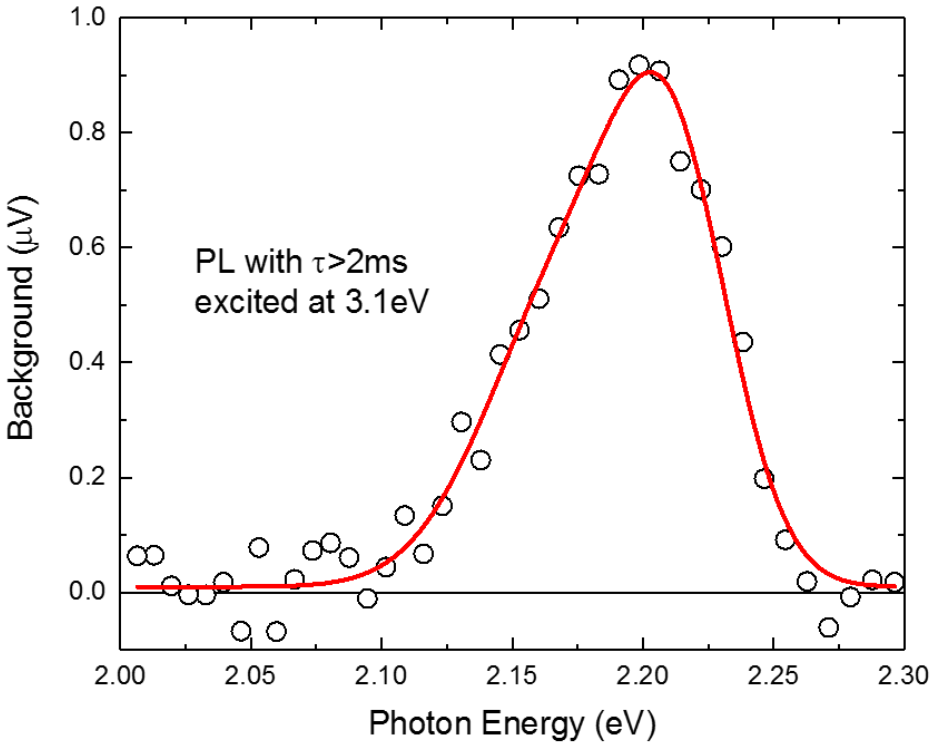

Figure 5.5. Background signal measured by ultrafast pump beam at 3.1eV (400nm) and modulated at 500Hz. It comes from the long-lived PL at lifetime τ>2ms.

Under 400nm (3.1eV) excitation, the penetration depth of the laser pulse in the crystal is only ~80 nm [148]. The PL signal shown in Figure 5.5 was measured under transmission through a 0.2mm thick $MAPbBr_3$ single crystal, and therefore, it comes from the photocarriers recombination in the near-surface region and diffusion to the interiors of the bulk because of their long diffusion length. A recent study shows that the PL peak can be redshifted from 546 to 560 nm in about 25 ns when excited at 400nm due to the carrier diffusion [186]. This agrees with our PL tail spectrum measured with this method that is located at 2.2eV (563nm).

5.7 Conclusion

In conclusion, we measured picosecond transient photoinduced modulation (PM) spectroscopies by near-surface excitation at 400nm in a solution processed inorganic-organic hybrid lead-trihalide perovskite $MAPbBr_3$ single crystal. We observed rise of a photoinduced absorption (PA) band on the same time scale of corresponding decay of a photobleaching (PB) band. The much faster rising time and higher-order recombination process have been observed at higher excitation concentration. Additionally, a long-lived and red-shifted photoluminescence (PL) tail has been observed at delay time longer than 2ms. Our findings reveal the photoexcitation recombination on the surface and diffusion process to the interiors of the bulk.

CHAPTER 6

CONCLUSIONS

In this dissertation, we employed a variety of ultrafast transient, nonlinear optical spectroscopies, and theoretical calculations for studying the excitons and free-carriers photoexcitations in the organic/inorganic hybrid perovskite systems, including three- (3D) and two- (2D) dimensional thin films and 3D $MAPbBr_3$ single crystals, which were synthesized via one (two)-step solution process and a liquid state reaction, respectively.

The transient pump-probe photomodulation (PM) spectroscopy in a broad spectral range from mid-IR to visible (namely 0.2-2.8eV) with 300 fs time resolution is realized via two laser systems based on a Ti: Sapphire oscillator, which are a low power (energy/pulse ~0.1 nJ) high repetition rate (~80 MHz) laser for the mid-IR spectral range, and a high power (energy/pulse ~10 μJ) low repetition rate (~1 kHz) laser for the near-IR/visible spectral range. Continuous-wave (CW) optical measurements such as linear absorption, photoluminescence (PL), electroabsorption (EA) spectroscopy, and related techniques have been adapted to monitor long-lived photoexcitations.

In 3D hybrid perovskites, we observed a transient photoinduced absorption (PA) band in mid-IR range at room temperature in all three perovskite films that we measured here, namely $MAPbI_3$, $MAPbI_{1.1}Br_{1.9}$, and $MAPbI_{3-x}Cl_x$, and we identified these PA features as due to photogenerated excitons. Both excitons and free carriers are photogenerated in

lead iodine $MAPbI_3$ films, which is consistent with the small exciton binding energy (E_b) less than k_BT at RT and the resulting excitons/photocarriers duality nature of the neat $MAPbI_3$ perovskites. As the temperature was reduced down to liquid nitrogen level, the structure phase of this perovskites changes from tetragonal to orthorhombic, in which the E_b are believed to be larger. In this phase, a much faster decay of photoexcitations was observed indicating the fraction of excitons are significantly increased. On the other hand, due to the substantially larger E_b, the primary photoexcitations in the other two perovskites $MAPbI_{1.1}Br_{1.9}$ and $MAPbI_{3-x}Cl_x$ were found to be mainly excitons. These results show that the branching ratio between the photogenerated excitons and free carriers, and therefore the ultrafast photoexcitations spectroscopic response, are determined by the exciton binding energy in the hybrid perovskites.

At room temperaure, the lead iodine perovskites $MAPbI_3$ possess anisotropic tetragonal crystal structure, but the other two, $MAPbI_{1.1}Br_{1.9}$ and $MAPbI_{3-x}Cl_x$, have isotropic cubic structure. We used a polarized transient PM spectroscopy and measured the polarization memory (POM) dynamics in both excitons and free carriers in the $MAPbI_3$ films. From the lifetime of exciton POM and the grain-like crystallite film structure of $MAPbI_3$ films, we estimated the exciton diffusion length at ~150nm in this perovskite. For free carriers, however, the POM decays at a much longer time, indicating that free carriers do not easily cross the boundary between neighboring crystalline grains, which suggests that grain boundaries are an important factor that may limit the charge mobility in the perovskites. In $MAPbI_{1.1}Br_{1.9}$ and $MAPbI_{3-x}Cl_x$, we didn't observe any POM, which validated that the effect arises from the structural anisotropy in teragonal $MAPbI_3$ films.

The excitons/free carriers duality found in our studies justifies the natural dissociation of excitons into free carriers in the bulk of the 3D hybrid perovskites with $E_b < k_B T$ at RT; in cases where $E_b > k_B T$, the long exciton diffusion length that we obtained here strongly indicates that excitons may dissociate at grain boundaries and interfaces at a later time.

We further studied the transient PM dynamics in 3D perovskite films with markedly different nano-morphologies. We have observed a much longer lifetime of excitons in nano-crystal pining (NCP)-treated $MAPbBr_3$ films with smaller crystalline domains, and this agrees with the enhanced PL yield implying a significant decrease of non-radiative trapping in NCP treated films. We have also measured the exciton lifetime in $MAPbI_{3-x}Cl_x$ films with various morphologies, and found that the dynamics are in excellent agreement with the lifetime obtained from magnetic field effects (MFE(B)), which validates the Δg model used for interpreting the various MFE(B) responses.

In 2D hybrid perovskite $(C_6H_5C_2H_4NH_3)_2PbI_4$ or PEPI, we found a very strong photoinduced transition from an exciton state to continuum state at energy of 0.35 eV which is about 0.15eV higher than binding energy of excitons. Density functional theory (DFT) calculations predicted strong spin orbit coupling can cause Rashba-splitting in the continuum band in the 2D perovskite, where the spin-degenerate parabolic band splits into two branches with opposite spin-aligned electronic states. This causes both the optical transitions of excitons into the continuum band to acquire an 'add-on' energy term of $4E_R$. Therefore, we assign the PA transition at 0.35 eV as the photoexcitation from the primary exciton state to the upper branch of the Rashba-splitting band, from which we have determined the Rashba-splitting energy, $E_R = 40 \pm 5$ meV, and Rashba-splitting parameter, $\alpha_R = 1.6 \pm 0.1$ eV·Å, in PEPI 2D hybrid perovskite, which is among the highest

values reported so far. Our study offers an all optical method of measuring the Rashba-splitting effect in semiconductors, which is essential for spin-related applications.

We have extended our measurement to lead-trihalide perovskites single crystals, which have much lower trap state densities and longer exciton lifetimes in the bulk than the film samples. The $MAPbBr_3$ single crystal was pumped at 400nm with a short penetration depth of ~80nm that limits the excitation to the near-surface regime. We observed a fast decaying photobleaching (PB) band and the corresponding rise of a PA band on the same time scale. Moreover, higher excitation concentration leads to much faster PA rise time and higher-order recombination processes, which reveals the photoexcitation recombination on the surface and diffusion process to the interior of the bulk.

Therefore, our work on various perovskites paves the way for photovoltic, light-emitting, lasing, and spin-related applications of the these fascinating materials.

REFERENCES

[1] M. Bazilian, I. Onyeji, M. Liebreich, I. MacGill, J. Chase, J. Shah, D. Gielen, D. Arent, D. Landfear, and S. Zhengrong, Renewable Energy. **53**, 329 (2013).

[2] W. Palz, *Solar Power for the World: What You Wanted to Know about Photovoltaics*. (CRC Press, Florida, 2013).

[3] R. M. Swanson, Science **324**, 5929 (2009).

[4] A. Smee, *Elements of Electro-Biology,: or The Voltaic Mechanism of Man of Electro-Pathology, Especially of the Nervous System and of Electro-Therapeutics*. (London: Longman, Brown, Green, and Longmans,1849).

[5] S. K. Deb, *Recent Developments in High Efficiency PV cells*. (NREL, Colorado, 2000).

[6] J. Yu, Y. Zheng, and J. Huang, Polymers **6**, 2473 (2014).

[7] Y. Sun, G. C. Welch, W. L. Leong, C. J. Takacs, G. C. Bazan, and A. J. Heeger, Nature Materials **11**, 44 (2011).

[8] U. Wurfel, M. Thorwart, E. Weber, *Quantum Efficiency in Complex Systems, Part II: From Molecular Aggregates to Organic Solar Cells: Organic Solar Cells* (Elsevier, London, 2011).

[9] N. -G. Park, M. Grätzel, and T. Miyasaka, *Organic-Inorganic Halide Perovskite Photovoltaics: From Fundamentals to Device Architectures* (Springer, Switzerland, 2016).

[10] A. Walsh, J. Phys. Chem. C 119, 5755 (2015).

[11] Ossila Ltd, https://www.ossila.com/pages/perovskites-and-perovskite-solar-cells-an-introduction, accessed: May 2016.

[12] H. J. Snaith, J. Phys. Chem. Lett. **4**, 3623 (2013).

[13] M. A. Green, A. Ho-Baillie, H. J. Snaith, Nature Photon. **8**, 506 (2014).

[14] A. Kojima, K. Teshima, Y. Shirai, T. Miyasaka, J. Am. Chem. Soc. **131**, 6050 (2009).

[15] J.-H. Im, C.-R. Lee, J.-W. Lee, S. W. Park, N.-G. Park, Nanoscale **3**, 4088 (2011).

[16] H.-S. Kim, C.-R. Lee, J.-H. Im, K.-B Lee, T. Moehl, A. Marchioro, S.-J. Moon, R. Humphry-Baker, J.-H. Yum, J. E. Moser, M. Grätze, and N.-G. Park, Sci. Rep. **2**, 591 (2012).

[17] M. M. Lee, J. Teuscher, T. Miyasaka, T. N. Murakami, H. J. Snaith, Science **338**, 643 (2012).

[18] M. Liu, M. B. Johnston, H. J. Snaith, Nature **501**, 395 (2013).

[19] J. Burschka, N. Pellet, S.-J. Moon, R. Humphry-Baker, P. Gao, M. K. Nazeeruddin, M. Grätzel, Nature **499**, 316 (2013).

[20] J. H. Heo, S. H. Im, J. H. Noh, T. N. Mandal, C.-S. Lim, J. A. Chang, Y. H. Lee, H.-J. Kim, A. Sarkar, M. K. Nazeeruddin, M. Grätzel, S. II Seok, Nature Photon. **7**, 486 (2013).

[21] O. Malinkiewicz, A. Yella, Y. H. Lee, G. M. Espallargas, M. Graetzel, M. K. Nazeeruddin, H. J. Bolink, Nature Photon. **8**, 128 (2014).

[22] A. Mei, X. Li, L. Liu, Z. Ku, T. Liu, Y. Rong, M. Xu, M. Hu, J. Chen, Y. Yang, M. Grätzel, H. Han, Science **345**, 295 (2014).

[23] R.F. Service, Science **344**, 458 (2014).

[24] National Renewable Energy Laboratory (NREL), Research Cell Efficiency Records, https://www.nrel.gov/pv/assets/images/efficiency-chart.png, accessed: May. 2016.

[25] Z. K. Tan, R. S. Moghaddam, M. L. Lai, P. Docampo, R. Higler, F. Deschler, M. Price, A. Sadhanala, L. M. Pazos, D. Credgington, F. Hanusch, T. Bein, H. J. Snaith, and R. H. Friend, Nature Nanotech. **9**, 687 (2014).

[26] H. Zhu, Y. Fu, F. Meng, X. Wu, Z. Gong, Q. Ding, M. V. Gustafsson, M. T. Trinh, S. Jin, X.-Y. Zhu, Nature Mater. **14**, 636 (2015).

[27] Y. Mei, C. Zhang, Z. V. Vardeny, O. D. Jurchescu, MRS Communications **5**, 297 (2015).

[28] Y. Hsiao, T. Wu, M. Li and B. Hu. Adv. Mater. **27**, 2899 (2015).

[29] H. R. Wenk and A. Bulakh, *Minerals: Their Constitution and Origin*. (Cambridge

University Press, New York, 2004).

[30] X. Wu, Ph. D thesis, Columbia University (2015).

[31] L. A. Kosyachenko, *Solar Cells - New Approaches and Reviews*, (InTech, Croatia, 2015).

[32] T. Baikie, Y. Fang, J. M. Kadro, M. Schreyer, F. Wei, S. G. Mhaisalkar, M. Grätzel, and T. J. White, Journal of Materials Chemistry A **1**, 5628 (2013).

[33] T. Hahn, *International Tables for Crystallography*, Volume A. (Kluwer Academic, The Netherland, 1995).

[34] T. Oku, Nanotechnology Reviews **1**, 389 (2012).

[35] N. Onoda-Yamamuro, T. Matsuo, H. Suga, J. Phys. Chem. Solids **51**, 1383 (1990).

[36] A. Poglitsch, D. J. Weber, Chem. Phys. **87**, 6373 (1987).

[37] C. C. Stoumpos, D. H. Cao, D. J. Clark, J. Young, J. M. Rondinelli, J. I. Jang, J. T. Hupp, and M. G. Kanatzidis, Chem. Mater. **28**, 2852 (2016).

[38] J. C. Blancon, H. Tsai, W. Nie, C. C. Stoumpos, L. Pedesseau, C. Katan, M. Kepenekian, C. M. M. Soe, K. Appavoo, M. Y. Sfeir, et al. Science **355**, 1288 (2017).

[39] H. Hu, T. Salim, B. Chen, Y. M. Lam, Scientific Reports **6**, 33546 (2016)

[40] De Angelis, F. Modeling, Acc. Chem. Res. **47**, 3349 (2014).

[41] M. A. Green, A. Ho-Baillie, H. J. Snaith, Nat. Photonics **8**, 506 (2014).

[42] H. P. Zhou, Q. Chen, G. Li, S. Luo, T. B. Song, H. S. Duan, Z. R. Hong, J. B. You, Y. S. Liu, Y. Yang, Science **345**, 542 (2014).

[43] P. Gao, M. Gratzel, M. K. Nazeeruddin, Energy Environ. Sci. **7**, 2448 (2014).

[44] L. Etgar, P. Gao, Z. Xue, Q. Peng, A. K. Chandiran, B. Liu, M. K. Nazeeruddin, M. Grätzel, J. Am. Chem. Soc. **134**, 17396 (2012).

[45] J. Calabrese, N. L. Jones, R. L. Harlow, N. Herron, D. L. Thorn, Y. Wang, J. Am. Chem. Soc. **113**, 2328 (1991).

[46] X. Wu, M. T. Trinh, D. Niesner, H. Zhu, Z. Norman, J. S. Owen, O. Yaffe, B. J. Kudisch, X. Y. Zhu, J. Am. Chem. Soc. **137**, 2089 (2015).

[47] W. Shockley and H. J. Queisser, J. Appl. Phys. **32**, 510 (1961).

[48] J. M. Ball, S. D. Stranks, M. T. Hörantner, S. Hüttner, W. Zhang, E. J. W. Crossland, I. Ramirez, M. Riede, M. B. Johnston, R. H. Friend and H. J. Snaith, Energy Environ. Sci. **8**, 602 (2015).

[49] D. Bi, W. Tress, M. I. Dar, P. Gao, J. Luo, C. Renevier, K. Schenk, A. Abate, F. Giordano, J.-P. C. Baena, et al. Sci. Adv. **2**, e1501170 (2016).

[50] S. De Wolf, J. Holovsky, S.-J. Moon, P. Löper, B. Niesen, M. Ledinsky, F.-J. Haug, J.-H. Yum, and C. Ballif, J. Phys. Chem. Lett. **5**, 1035 (2014).

[51] D. M. Jang, K. Park, D. H. Kim, J. Park, F. Shojaei, H. S. Kang, J.-P. Ahn, J. W. Lee, and J. K. Song, Nano Lett. **15**, 5191 (2015).

[52] L. Wang, G. D. Yuan, R. F. Duan, F. Huang, T. B. Wei, Z. Q. Liu, J. X. Wang, and J. M. Li, AIP Advances **6**, 045115 (2016).

[53] C.H. Henry, J. Appl. Phys. **51**, 4494 (1980).

[54] S. Albrecht, M. Saliba, J. P. C. Baena, F. Lang, L. Kegelmann, M. Mews, L. Steier, A. Abate, J. Rappich, L. Korte, et al. Energy Environ. Sci. **9**, 81 (2016).

[55] J.P. Mailoa, C. D. Bailie, E. C. Johlin, E. T. Hoke, A. J. Akey, W. H. Nguyen, M. D. McGehee, and T. Buonassisi, Appl. Phys. Lett. **106**, 121105 (2015).

[56] P. Löper, S.-J. Moon, S. M. de Nicolas, B. Niesen, M. Ledinsky, S. Nicolay, J. Bailat, J.-H. Yum, S. De Wolfa, and C. Ballif, Phys. Chem. Chem. Phys. **17**, 1619 (2014).

[57] Josh Holt, Ph.D thesis, University of Utah (2009).

[58] E. Edri, S. Kirmayer, S. Mukhopadhyay, K. Gartsman, G. Hodes, D. Cahen, Nat. Commun. **5**, 3461 (2014).

[59] V. D'Innocenzo, G. Grancini, M. J. P. Alcocer, A. R. S. Kandada, S. D. Stranks, M. M. Lee, G. Lanzani, H. J. Snaith, A. Petrozza, Nat. Commun. **5**, 3586 (2014).

[60] C.-X. Sheng, C. Zhang, Y. Zhai, K. Mielczarek, W. Wang, W. Ma, A. Zakhidov, and Z. V. Vardeny, Phys. Rev. Lett **114**, 116601 (2015).

[61] Y. Zhai, C.-X. Sheng, C. Zhang, and Z. V. Vardeny, Adv. Funct. Mater. **26**, 1617 (2016).

[62] J. I. Pankove, *Optical Processes in Semiconductors* (Dover, New York, 1971).

[63] C. C. Stoumpos, C. D. Malliakas, M. G. Kanatzidis, Inorg. Chem. **52**, 9019 (2013).

[64] A. Miyata, A. Mitioglu, P. Plochocka, O. Portugall, J. T.-W. Wang, S. D. Stranks, H. J. Snaith, R. J. Nicholas, Nature Phys. **11**, 582 (2015).

[65] C. Kittel, *Introduction to Solid State Physics*, *8th Edition* (Wiley, New Jersey, 2004).

[66] C. F. Klingshirn, *Semiconductor Optics* (Springer, Berlin, 2006).

[67] S. Y. Sun, T. Salim, N. Mathews, M. Duchamp, C. Boothroyd, G. Xing, T. C. Sumbce, Y. M. Lam, Energy Environ. Sci. **7**, 399 (2014).

[68] M. Hirasawa, R. Ishihara, T. Goto, K. Uchida, N. Miura, Phys. B **201**, 427 (1994).

[69] K. Tanaka, T. Takahashi, T. Ban, T. Konda, K. Uchida, N. Miura, Solid State Commun. **127**, 619 (2003).

[70] I. B. Koutselas, L. Ducasse, G. C. Papavassiliou, J. Phys.: Condens. Matter **8**, 1217 (1996).

[71] J. Even, L. Pedesseau, C. Katan, J. Phys. Chem. C **118**, 11566 (2014).

[72] Y. Yamada, T. Nakamura, M. Endo, A. Wakamiya, Y. Kanemitsu, IEEE J. Photovolt. **5**, 401 (2015).

[73] M. Shimizu, J.-I Fujisawa, and Ishi-Hayase, Phys. Rev. B **71**, 205306 (2005).

[74] X. Hong and T. Ishihara, Nurmikko, Phys. Rev. B **45**, 6961 (1992).

[75] K. Tanaka, F. Sano, T. Takahashi, T. Kondo, R. Ito, and K. Ema, Solid State Commun. **122**, 249 (2002).

[76] C.-X. Sheng, Z. V. Vardeny, A. B. Dalton, R. H. Baughman, Phys. Rev. B **71**, 125427 (2005).

[77] C.-X. Sheng, M. Tong, S. Singh, Z. V. Vardeny, Phys. Rev. B **75**, 085206 (2007).

[78] R. A. Kaindl, M. A. Carnahan, D. Hägele, R. Lövenich, D. S. Chemla, Nature **423**, 734 (2003).

[79] S. D. Stranks, G. E. Eperon, G. Grancini, C. Menelaou, M. J. P. Alcocer, Tomas Leijtens, L. M. Herz, A. Petrozza, and H. J. Snaith, Science **342**, 341 (2013).

[80] G. Xing, N. Mathews, S. Sun, S. S. Lim, Y. M. Lam, M. Grätzel, S. Mhaisalkar,

T. C. Sum, Science **342**, 344 (2013).

[81] T. J. Savenije, C. S. Ponseca, Jr., L. Kunneman, M. Abdellah, K. Zheng, Y. Tian, Q. Zhu, S. E. Canton, I. G. Scheblykin, T. Pullerits, A. Yartsev, V. Sundström, J. Phys. Chem. Lett. **5**, 2189 (2014).

[82] C. S. Ponseca, Jr., T. J. Savenije, M. Abdellah, K. Zheng, A. Yartsev, T. Pascher, T. Harlang, P. Chabera, T. Pullerits, A. Stepanov, et al., J. Am. Chem. Soc. **136**, 5189 (2014).

[83] C. Wehrenfennig, M. Liu, H. J. Snaith, M. B. Johnston, I. Herz, Energy, Environ. Sci. **7**, 2269 (2014).

[84] Q. Dong, Y. Fang, Y. Shao, P. Mulligan, J. Qiu, L. Cao, J. Huang, Science **347**, 967 (2015).

[85] E. Edri, S. Kirmayer, A. Henning, S. Mukhopadhyay, K. Gartsman, Y. Rosenwaks, G. Hodes, and D. Cahen, Nano Lett. **14**, 1000 (2014).

[86] Y. Vaynzof, A. A. Bakulin, S. Gélinas, and R. H. Friend, Phys. Rev. Lett. **108**, 246605 (2012).

[87] H.-W. Chen, N. Sakai, M. Ikegami, T. Miyasaka, J. Phys. Chem. Lett. **6**, 164 (2014).

[88] Z. Fan, J. Xiao, K. Sun, L. Chen, Y. Hu, J. Ouyang, K. P. Ong, K. Zeng, and J. Wang, J. Phys. Chem. Lett. 1155 (2015).

[89] T. Etienne, E. Mosconi, and F. De Angelis, J. Phys. Chem. Lett. **7**, 1638 (2016).

[90] F. Zheng, L. Z. Tan, S. Liu, and A. M. Rappe, Nano Lett. **15**, 7794 (2015).

[91] W.-J. Yin, T. Shi, Y. Yan, Adv. Mater. **26**, 4653 (2014).

[92] Z. Xiao, Q. Dong, C. Bi, Y, Shao, Y. Yuan, J. Huang, Adv. Mater. **26**, 6503 (2014).

[93] C. Zhang, D. Sun, C-X. Sheng, Y. Zhai, K. Mielczarek, A. Zakhidov, Z. V. Vardeny, Nat. Phys. **11**, 427 (2015).

[94] E. I. Rashba, Sov. Phys. Solid State **2**, 1109 (1960).

[95] G. Dresselhaus, A. Kip, C. Kittel, Phys. Rev. **95**, 568 (1954).

[96] Y.A. Bychkov and E.I. Rashba, JETP Lett. **39**, 78 (1984).

[97] A. Manchon, H. C. Koo, J. Nitta, S. M. Frolov, and R. A. Duine, Nature Materials **14**, 871 (2015).

[98] E. Lesne, Y. Fu, S. Oyarzun, J. C. Rojas-Sánchez, D. C. Vaz, H. Naganuma, G. Sicoli, J.-P. Attané, M. Jamet, E. Jacquet, et al, Nature Materials **15**, 1261(2016).

[99] P. Yu and M. Cardona, *Fundamentals of Semiconductors: Physics and Materials Properties, 3rd Edition* (Springer, Berlin, 2015).

[100] C. Kittel, *Quantum Theory of Solids, 2nd Edition* (Wiley, New York, 1987).

[101] E. Frantzeskaikis, S. Pons, H. Mirhosseini, J. Henk, C. R. Ast, and M. Grioni, Phys. Rev. Lett. **101**, 196805 (2008).

[102] P. D. C. King, R. C. Hatch, M. Bianchi, R. Ovsyannikov, C. Lupulescu, G. Landolt, B. Slomski, J. H. Dil, D. Guan, J. L. Mi, et al., Phys. Rev. Lett. **107**, 096802 (2011).

[103] K. Ishizaka, M. S. Bahramy, H. Murakawa, M. Sakano, T. Shimojima, T. Sonobe, K. Koizumi, S. Shin, H. Miyahara, A. Kimura, et al., Nat. Materials **10**, 521 (2011).

[104] J. Nitta, T. Akazaki, H. Takayanagi, and T. Enoki, Phys. Rev. Lett. **78**, 1335 (1997)

[105] Z. G. Yu, Sci. Reports, **6**, 28576 (2016).

[106] M. Kepenekian, R. Robles, C. Katan, D. Sapori, L. Pedesseau, and J. Even, ACS Nano **9**, 11557 (2015)

[107] D. Niesner, M. Wilhelm, I. Levchuk, A. Osvet, S. Shrestha, M. Batentschuk, C. Brabec, and T. Fauster, Phys. Rev. Lett. **117**, 126401 (2016).

[108] E. M. Hutter, M. C. Gélvez-Rueda, A. Osherov, V. Bulovic, F. C. Grozema, S. D. Stranks, and T. J. Savenije, Nature Materials **16**, 115 (2017).

[109] T. Wang, B. Daiber, J. M. Frost, S. A. Mann, E. C. Garnett, A. Walsh, and B. Ehrler, Energy Environ. Sci. **10**, 509 (2017).

[110] D. Giovanni, W. K. Chong, H. A. Dewi, K. Thirumal, I. Neogi, R. Ramesh, S. Mhaisalkar, N. Mathews, and T. C. Sum, Science Advance **2**, e1600477 (2016).

[111] W. Zhang, G. E. Eperon and H. J. Snaith, Nature Energy **1**, 16048 (2016).

[112] H. J. Snaith, A. Abate, J. M. Ball, G. E. Eperon, T. Leijtens, N. K. Noel, S. D. Stranks, J. T.-W. Wang, K. Wojciechowski, and W. Zhang, J. Phys. Chem. Lett.

5, 1511 (2014).

[113] E. L. Unger, E. T. Hoke, C. D. Bailie, W. H. Nguyen, A. R. Bowring, T. Heumüller, M. G. Christoforo, and M. D. McGehee, Energy Environ. Sci. **7**, 3690 (2014).

[114] S. van Reenen, M. Kemerink, H. J Snaith, J. Phys. Chem. Lett. **6**, 3808 (2015).

[115] W. S. Yang, J. H. Noh, N. J. Jeon, Y. C. Kim, S. Ryu, J. Seo, and Sang II Seok, Science **348**, 1234 (2015).

[116] J. H. Heo, H. J. Han, D. Kim, T. K. Ahn, S. H. Im, Energy Environ. Sci. **8**, 1602 (2015).

[117] Y. Shao, Z. Xiao, C. Bi, Y. Yuan, J. Huang, Nature Commun. **5**, 5784 (2014).

[118] S. Brittman, G. W. P. Adhyaksa, and E. C. Garnett, MRS Communications **5**, 7 (2015).

[119] D. P. McMeekin, G. Sadoughi, W. Rehman, G. E. Eperon, M. Saliba, M. T. Hörantner, A. Haghighirad, N. Sakai, L. Korte, B. Rech, M. B. Johnston, L. M. Herz, H. J. Snaith, Science **351**, 151 (2016).

[120] M. Era, S. Morimoto, T. Tsutsui, S. Saito, Appl. Phys. Lett. **65**, 676 (1994).

[121] X. Hong, T. Ishihara, A. V. Nurmikko, Solid State Commun. **84**, 657 (1992).

[122] H. Cho, S.-H. Jeong, M.-H. Park, Y.-H. Kim, C. Wolf, C.-L. Lee, J. H. Heo, A. Sadhanala, N. Myoung, S. Yoo, et al., Science **350**, 1222 (2015).

[123] J. Wang, N. Wang, Y. Jin, J. Si, Z.-K. Tan, H. Du, L. Cheng, X. Dai, S. Bai, H. He, et al., Adv. Mater. **27**, 2311 (2015).

[124] Z. Xiao, R. A. Kerner, L. Zhao, N. L. Tran, K. Min Lee, T.-W. Koh, G. D. Scholes, B. P. Rand, Nature Photonics **11**, 108 (2017).

[125] N. K. Kumawat, A. Dey, A. Kumar, S. P. Gopinathan, K. L. Narasimhan, and D. Kabra, ACS Appl. Mater. Interfaces **7**, 13119 (2015).

[126] A. Sadhanala, S. Ahmad, B. Zhao, N. Giesbrecht, P. M. Pearce, F. Deschler, R. L. Z. Hoye, K. C. Gödel, T. Bein, P. Docampo, et al., Nano Lett. **15**, 6095 (2015).

[127] S. Yakunin, L. Protesescu, F. Krieg, M. I. Bodnarchuk, G. Nedelcu, M. Humer, G. De Luca, M. Fiebig, W. Heiss, and M. V. Kovalenko, Nature Commun. **6**, 8056 (2015).

[128] S. D. Stranks, S. M. Wood, K. Wojciechowski, F. Deschler, M. Saliba, H. Khandelwal, J. B. Patel, S. J. Elston, L. M. Herz, M. B. Johnston, et al., Nano Lett. **15**, 4935 (2015).

[129] F. Deschler, M. Price, S. Pathak, L. E. Klintberg, D.-D. Jarausch, R. Higler, S. Hüttner, T. Leijtens, S. D. Stranks, H. J. Snaith, et al., J. Phys. Chem. Lett. **5**, 1421 (2014).

[130] Q. Zhang, S. T. Ha, X. Liu, T. C. Sum, Q. Xiong, Nano Lett. **10**, 687 (2014).

[131] Q. Liao, K. Hu, H. Zhang, X. Wang, J. Yao, H. Fu. Adv. Mater. **27**, 3405 (2015).

[132] M. Saliba, S. M. Wood, J. B. Patel, P. K. Nayak, J. Huang, J. A. Alexander-Webber, B. Wenger, S. D. Stranks, M. T. Hörantner, J. T.-W. Wang, Adv. Mater. **28**, 923 (2016).

[133] D. Giovanni, H. Ma, J. Chua, M. Grätzel, R. Ramesh, S. Mhaisalkar, N. Mathews, and T. C. Sum, Nano Lett. **15**, 1553 (2015).

[134] D. Sun, C. Zhang, M. Kavand, K. J. van Schooten, H. Malissa, M. Groesbeck, R. McLaughlin, C. Boehme, and Z. V. Vardeny, arXiv:1608.00993 [cond-mat.mtrl-sci].

[135] Y. Yang and J. You, Nature **544**, 155 (2017).

[136] M. Saliba, T. Matsui, J.-Y. Seo, K. Domanski, J.-P. Correa-Baena, M. K. Nazeeruddin, S. M. Zakeeruddin, W. Tress, A. Abate, A. Hagfeld, and M. Grätzel, Energy Environ. Sci. **9**, 1989 (2016).

[137] H. Tsai, W. Nie, J.-C. Blancon, C. C. Stoumpos, R. Asadpour, B. Harutyunyan, A. J. Neukirch, R. Verduzco, J. J. Crochet, S. Tretiak, L. Pedesseau, J. Even, M. A. Alam, G. Gupta, J. Lou, P. M. Ajayan, M. J. Bedzyk, M. G. Kanatzidis, A. D. Mohite, Nature **536**, 312 (2016).

[138] A. Babayigit, A. Ethirajan, M. Muller, B. Conings, Nature Mater. **15**, 247 (2016).

[139] C. C. Stoumpos, L. Frazer, D. J. Clark, Y. S. Kim, S. H. Rhim, A. J. Freeman, J. B. Ketterson, J. I. Jang, and M. G. Kanatzidis. J. Am. Chem. Soc. **137**, 6804 (2015).

[140] T. Krishnamoorthy, H. Ding, C. Yan, W. L. Leong, T. Baikie, Z. Zhang, M. Sherburne, S. Li, M. Asta, N. Mathews, and S. G. Mhaisalkar, J. Mater. Chem. A **3**, 23829 (2015).

[141] Q. Chen, H. Zhou, Z. Hong, S. Luo, H.-S. Duan, H.-H. Wang, Y. Liu, G. Li and Y. Yang, J. Am. Chem. Soc. **136**, 622 (2013).

[142] J.-H. Im, H.-S. Kim and N.-G. Park, APL Mater. **2**, 081510 (2014).

[143] S. Pang, H. Hu, J. Zhang, S. Lv, Y. Yu, F. Wei, T. Qin, H. Xu, Z. Liu, and G. Cui, Chem. Mater. **26**, 1485 (2014).

[144] T.-B. Song, Q. Chen, H. Zhou, C. Jiang, H.-H. Wang, Y (M.). Yang, Y. Liu, J. You, and Y. Yang, J. Mater. Chem. A **3**, 9032 (2015).

[145] D. Shi, V. Adinolfi, R. Comin, M. Yuan, E. E. Alarousu, A. Buin, Y. Chen, S. Hoogland, A. Rothenberger, K. Katsiev, Y. Losovyj, X. Zhang, P. A. Dowben, O. F. Mohammed, E. H. Sargent, O. M. Bakr, Science **347**, 519 (2015).

[146] H. Zhu, K. Miyata, Y. Fu, J. Wang, P. P. Joshi, D. Niesner, K. W. Williams, S. Jin, X.-Y. Zhu, Science **353**, 1409 (2016).

[147] M. I. Saidaminov, A. L. Abdelhady, B. Murali, E. Alarousu, V. M. Burlakov, W. Peng, I. Dursun, L. Wang, Y. He, G. Maculan, A. Goriely, T. Wu, O. F. Mohammed, O. M. Bakr, Nat. Commun. **6**, 7586 (2015).

[148] B. Wu, H. T. Nguyen, Z. Ku, G. Han, D. Giovanni, N. Mathews, H. J. Fan, and T. C. Sum, Adv. Energy Mater. **6**, 1600551 (2016).

[149] M. T. Asaki, C.-P. Huang, D. Garvey, J. Zhou, H. C. Kapteyn, and M. M. Murnane, Opt. Lett. **18**, 977 (1993).

[150] F. Schindler, J. M. Lupton, J. Müller, J. Feldmann, and U. Scherf. Nat. Mat. **5**, 141 (2006).

[151] L. Sebastian and G. Weiser. Physical Review B **46**, 1156 (1981).

[152] G. S. Kanner, S. Frolov, Z. V. Vardeny, Phys. Rev. Lett. **74**, 1685 (1995).

[153] B. Anand, S. Sampat, E. O. Danilov, W. Peng, S. M. Rupich, Y. J. Chabal, Y. N. Gartstein, and A. V. Malko, Phys. Rev. B **93**, 161205(R) (2016).

[154] Z. V. Vardeny, J. Tauc, Phys. Rev. Lett. **46**, 1223 (1981).

[155] A. A. Bakulin, H. J. Bakker, Z. Sun, Z. Chen, Proc. of SPIE **9165**, 91650U-1 (2014).

[156] H. Fröhlich, Proc. R. Soc. Lond. A **215**, 291 (1952).

[157] Z. V. Vardeny, J. Tauc, *Semiconductors Probed by Ultrafast Laser spectroscopy*, (Academic, Orlando, 1984).

[158] Y. C. Chen, N. R. Raravikar, L. S. Schadler, P. M. Ajayan, Y.-P. Zhao, T.-M. Lu,

G.-C. Wang, and X.-C. Zhang, Appl. Phys. Lett. 81, 975 (2002).

[159] Z. V. Vardeny, J. Strait, D. Pfost, J. Tauc, and B. Abeles, Phys. Rev. Lett. **48**, 1132 (1982).

[160] S. Schmitt-Rink, D. S. Chemla, D. A. B. Miller, Phys. Rev. B **32**, 6601 (1985).

[161] L. Lüer, S. Hoseinkhani, D. Polli, J. Crochet, T. Hertel, G. Lanzani, Nature Phys. **5**, 54 (2009).

[162] J. J. Choi, X. Yang, Z. M. Norman, S. J. L. Billinge, J. S. Owen, Nano Lett. **14**, 127 (2014).

[163] S. Frolov, Ph.D. thesis, University of Utah, 1997.

[164] A. Marchioro, J. Teuscher, D. Friedrich, M. Kunst, R. van de Krol, T. Moehl, M. Grätzel, J.-E. Moser, Nature Photon. **8**, 250 (2014).

[165] Q. Chen, H. Zhou, Z, Hong, S. Luo, H.-S. Duan, H.-H. Wang, Y. Liu, G. Li, Y. Yang, J. Am. Chem. Soc. **136**, 622 (2014).

[166] M. Saba, M. Cadelano, D. Marongiu, F. Chen, V. Sarritzu, N. Sestu, C. Figus, M. Aresti, R. Piras, A. G. Lehmann, C. Cannas, A. Musinu, F. Quochi, A. Mura, G. Bongiovanni, Nat. Commum. **5**, 5049 (2014).

[167] Y. Yamada, T. Nakamura, M. Endo, A. Wakamiya, Y. Kanemitsu, J. Am. Chem. Soc. **136**, 11610 (2014).

[168] S. D. Stranks, Phys. Rev. Appl. **2**, 034007 (2014).

[169] S. De Wolf, J. Holovsky, S.-J. Moon, P. Löper, B. Niesen, M. Ledinsky, F.-J. Haug, J.-H. Yum, C. Ballif, J. Phys. Chem. Lett. **5**, 1035 (2014).

[170] H. Wang, L. Whittaker-Brooks, and G. R. Fleming, J. Phys. Chem. C **119**, 19590 (2015).

[171] N. Onoda-Yamamuro, T. Matsuo, H. J. Suga, Phys. Chem. Solids, **53**, 935 (1992).

[172] C. Quarti, E. Mosconi, J. M. Ball, V. D'Innocenzo, C. Tao, S. Pathak, H. J. Snaith, A. Petrozza and F. De Angelis, Energy Environ. Sci. **9**, 155 (2016).

[173] J. H. Noh, S. H. Im, J. H. Heo, T. N. Mandal, S. Seok, Nano Lett. **13**, 1764 (2013).

[174] N. Kitazawa, Y. Watanabe, Y. Nakamura, J. Mater. Sci. **37**, 3585 (2002).

[175] W. Zhang, M. Saliba, S. D. Stranks, Y. Sun, X. Shi, Nano Lett. **13**, 4505 (2013).

[176] Y. Tian and I. G. Schleblykin, J. Phys. Chem. Lett. **6**, 3466 (2015).

[177] L. C. Schmidt, A. Pertegas, S. Gonzalez-Carrero, O. Malinkiewicz, S. Agouram, G. M. Espallargas, H. J. Bolink, R. E. Galian, and J. Perez-Prieto, J. Am. Chem. Soc. **136**, 850 (2014).

[178] E. Lafalce, C. Zhang, Y. Zhai, D. Sun, and Z. V. Vardeny, J. Appl. Phys. **120**, 143101 (2016).

[179] G. Grancini, A. R. S. Kandada, J. M. Frost, A. J. Barker, M. D. Bastiani, M. Gandini, S. Marras, G. Lanzani, A. Walsh, and A. Petrozza, Nat. Photonics **9**, 695 (2015).

[180] D.H. Cao, C. C. Stoumpos, O. K. Farha, J. T. Hupp, and M. G. Kanatzidis, J. Am. Chem. Soc.**137**, 7843 (2015).

[181] D. B. Straus, S. Hurtado Parra, N. Iotov, J. Gebhardt, A. M. Rappe, J. E. Subotnik, J. M. Kikkawa, and C. R. Kagan, J. Am. Chem. Soc. **138**, 13798 (2016).

[182] J. Fujisawa and T. Ishihara, Phys. Rev. B **70**, 205330 (2004).

[183] M. E. Ziffer, J. C. Mohammed, and D. S. Ginger, ACS Photonics **3**, 1060 (2016).

[184] K. Abdel-Baki, et al., J. Appl. Phys. **119**, 064301 (2016)

[185] W. Y. Nie, H. H. Tsai, R. Asadpour, J. C. Blancon, A. J. Neukirch, G. Gupta, J. J. Crochet, M. Chhowalla, S. Tretiak, M. A. Alam, H. L. Wang, A. D. Mohite, Science **347**, 522 (2015).

[186] H.-H. Fang, S. Adjokatse, H. Wei, J. Yang, G. R. Blake, J. Huang, J. Even, M. Antonietta Loi, Sci. Adv. **2**, e1600534 (2016).